Development of Components for Solid-State Batteries and their Characterization

Dissertation zur Erlangung des naturwissenschaftlichen
Doktorgrades der Julius-Maximilians-Universität Würzburg

vorgelegt von
Matthias Rumpel
aus Würzburg

Würzburg, September 2023

Fraunhofer
ISC

Eingereicht bei der Fakultät für Chemie und Pharmazie am

15.09.2023

Gutachter der schriftlichen Arbeit

1. Gutachter: Prof. Dr. Gerhard Sextl

2. Gutachter: Prof. Dr. Julien Bachmann

Prüfer des öffentlichen Promotionskolloquiums

1. Prüfer: Prof. Dr. Gerhard Sextl
2. Prüfer: Prof. Dr. Julien Bachmann
3. Prüfer: Prof. Dr. Lutz Nuhn

Datum des öffentlichen Promotionskolloquiums

19.12.2023

Doktorurkunde ausgehändigt am

____

List of Publications

First-Authorship

Thermal stabilities of Mn-based active materials in combination with the ceramic electrolyte LATP for ASSB bulk cathodes

M. Rumpel, F. Nagler, L. Appold, W. Stracke, A. Flegler, O. Clemens and G. Sextl

Mater. Adv., 2022, 3, 4015-4025 DOI: https://doi.org/10.1039/D2MA00158F

How interdiffusion affects the electrochemical performance of $LiMn_2O_4$ thin films on stainless steel

M. Rumpel, M. Machhaus, J. Sastre, S. Ziegler, X. Chen, A. Flegler, Y.E. Romanyuk and G. Giffin

Mater. Adv., 2021, 2, 2289-2298 DOI: https://doi.org/10.1039/D0MA00893A

Impact of the Sintering Additive Li_3PO_4 on the sintering behavior, microstructure and electrical properties of the ceramic LATP electrolyte

M. Rumpel, L. Appold, J. Baber, W. Stracke, A. Flegler and G. Sextl

Mater. Adv., 2022, 3, 8157-8167 DOI: https://doi.org/10.1039/d2ma00655c

Co-Authorship

Photonic methods for rapid crystallization of $LiMn_2O_4$ cathodes for solid-state thin-film batteries

X. Chen, J. Sastre, M. Rumpel, A. Flegler, A. Singhania, J.B. Bonner, P. Hoffmann and Y.E. Romanyuk

Journal of Power Sources, 2021, 495, 229424 DOI: https://doi.org/10.1016/j.jpowsour.2020.229424

Avoiding voltage-induced degradation in PET-ITO-based flexible electrochromic devices

S. Macher, M. Rumpel, M. Schott, U. Posset, G. Giffin and P. Löbmann

ACS Appl. Mater. Interfaces, 2020, 12(32), 36695 - 36705 DOI: https://doi.org/10.1021/acsami.0c07860

Toward an all-ceramic cathode-electrolyte interface with low-temperature pressed NASICON LAGP electrolyte

A. Paolella, W. Zhu, G. Bertoni, A. Perea, H. Dremers, S. Savoie, G. Girard, N. Delaporte, A. Guerfi, M. Rumpel, H. Lorrmann, G.P. Demopoulos, K. Zaghib

Advanced Material Interfaces, 2020, 7(12), 2000164 DOI: https://doi.org/10.1002/admi.202000164

Unlocking Stable Multi-Electron Cycling in NMC811 Thin-Films between 1.5 – 4.7 V

A. Aribia, J. Sastre, X. Chen, M.H. Futscher, M. Rumpel, A. Priebe, M. Döbeli, N. Osenciat, A.N. Tiwari, Y.E. Romanyuk

Advanced Energy Materials, 2022, 4, 2201750 DOI: https://doi.org/10.1002/aenm.202201750

Table of Contents

List of Publications .... **I**

Table of Contents .... **III**

List of Abbreviations .... **VII**

List of Symbols .... **IX**

1 Motivation and Scope of Thesis **1**

Motivation *1*
Scope of Thesis *2*

2 Fundamentals **4**

2.1 Thermodynamics of Lithium-Ion Batteries | LiBs 4

Electrochemical Fundamentals *4*
Cathode Active Materials *8*
Anode Active Materials *13*
Liquid Electrolytes *14*

2.2 All Solid-State Batteries | ASSBs 15

Perspective, Concept and Application Profile *15*
Bulk vs. Thin-Film Approach *18*
Solid-State Electrolyte Materials | SSE Materials *19*
Description of SSE Materials used in this Study *22*

2.3 Sintering, Liquid Phase Sintering and Microstructure 25

Solid Phase Sintering *25*
Liquid Phase Sintering *26*

2.4 Interdiffusion, Intermixing and Decomposition of Composites 28

Interdiffusion *28*
Intermixing and Decomposition *29*

2.5 Ion Diffusion and Ionic Conductivity in Ceramics 30

Ion Diffusion through a Crystal Lattice *30*
Ion Diffusion through a Polycrystalline Material / Brick-Layer Model *31*

3 Instruments and Methods **33**

3.1 X-Ray Diffraction | XRD 33

Theoretical Background *33*
Rietveld Refinement and Quantification of Phase Fractions in Composites *35*
XRD Set-Up *35*

3.2 Thermal-Optical Measurement Device | TOM 36

3.3 Time-of-Flight Secondary Ion Mass Spectroscopy | ToF-SIMS 37

3.4 Electrical and Electrochemical Impedance Spectroscopy | EIS 38

Electrical Impedance Spectroscopy of Li-Ion Conduction in SSEs *39*
Electrochemical Impedance Spectroscopy of Battery Cells *41*

3.5 Galvanostatic Cycling with Potential Limits | GCPL 43

Fundamentals of GCPL *43*
Rate Capability Tests & Long-Term Cycling Tests *45*

4 Thermal Stabilities of the LATP SSE in Combination with various Mn-based Active Materials ... 46

4.1 Introduction and Status Quo ... 47

4.2 Experimental Approach ... 49

4.3 Characterization of Starting Powders ... 50

4.4 Thermal Stability of LMO-s and LATP Powder Mixture ... 51

- *DSC-TG and MS Measurements ... 51*
- *HT-XRD Measurements and Rietveld Refinements ... 52*
- *SEM Images and EDS Analyses ... 55*
- *Correlation and Summary ... 55*

4.5 Thermal Stability of LMO-l and LATP Powder Mixture ... 57

- *DSC-TG and MS Measurements ... 57*
- *HT-XRD Measurements and Rietveld Refinements ... 58*
- *SEM Images and EDS Analyses ... 60*
- *Correlation and Summary ... 60*

4.6 Thermal Stability of LMP and LATP Powder Mixture ... 63

- *DSC-TG and MS Measurements ... 63*
- *HT-XRD Measurements and Rietveld Refinements ... 63*
- *SEM Images and EDS Analyses ... 65*
- *Correlation and Summary ... 65*

4.7 Comparison of the Powder Mixtures ... 67

4.8 Thermal Stability of LMP and LATP Powder Mixture with Ag ... 70

- *DSC-TG and MS Measurements ... 70*
- *HT-XRD Measurements and Rietveld Refinements ... 71*
- *SEM Images and EDS Analyses ... 73*
- *Correlation and Summary ... 73*

4.9 Summary and Conclusion of the Investigation into Thermal Stabilities ... 74

5 Impact of the Sintering Additive Li_3PO_4 on the Sintering Behavior, Microstructure and Electrical Properties of LATP ... 76

5.1 Introduction and Status Quo ... 77

5.2 Experimental Approach ... 79

5.3 Investigations of Sintering Behavior and Microstructure ... 80

- *Crystalline Phases and Secondary Phases ... 80*
- *Thermal Diffusivity, Shrinkage and Porosity ... 81*
- *Microstructure and Grain Size ... 85*

5.4 Investigation of Electrical Properties ... 87

- *Data Analysis and Fitting ... 87*
- *Bulk Conductivity ... 88*
- *Grain Boundary Conductivity ... 89*
- *Grain Boundary Capacitance ... 91*
- *Arrhenius Plots and Activation Energies ... 92*

5.5 Correlation of Sintering Behavior, Microstructure and Electrical Properties ... 94

- *$LiTiOPO_4$ and $AlPO_4$ formation ... 95*
- *Pore Elimination, Densification and Shrinkage ... 96*
- *Grain Growth and Grain Size Distribution ... 98*
- *Crack Formation ... 100*

5.6 Summary and Conclusion of the Investigation into Sintering Additives 101

6 TF-SSB | Engineering Current Collector/Cathode Interface 103

6.1 Introduction and Status Quo 104

6.2 Experimental Approach 106

6.3 Structural Investigation of the Interdiffusion Barriers Pt, Au and ITO 107

Morphology of the LMO Thin Films and Interlayers *107*
Interdiffusion Processes *109*
Crystalline Phases *112*
Changes in Oxidation States *113*

6.4 Electrochemical Investigation of the Interdiffusion Barriers Pt, Au and ITO 115

Galvanostatic Cycling with Potential Limits (GCPL) *115*
Electrochemical Impedance Spectroscopy *119*

6.5 Discussion and Correlation of Structural and Electrochemical Results 123

Impact of Interdiffusion Processes on Electrochemical Performance *123*
Changes in Morphology and Crystallinity of LMO *125*
Irreversible Side Reaction of the Pt samples *125*
Oxide Layer Formation *126*

6.6 Optimization of the ITO Interlayer 126

ITO Layer Thickness and LMO Morphology *127*
Electrochemical Performance *128*

6.7 Summary and Conclusion of the Investigation into the Current Collector/Cathode Interface 133

7 TF-SSB | Engineering Cathode/SSE Interface 135

7.1 Introduction and Status Quo 136

7.2 Experimental Approach 138

7.3 Functionality of TiO_2 and LTO Coatings on LMO in Liquid Electrolyte Cells 139

Morphology of TiO_2 and LTO coatings *139*
Crystallinity of TiO_2 and LTO coatings *140*
Electrochemical Characterization: Rate Capability Tests *141*
Electrochemical Characterization: Long-Term Cycling Test *144*
Conclusion and Summary *148*

7.4 Functionality of TiO_2 and LTO Interlayers in LIPON|Interlayer|LMO Full Cells 149

Electrochemical Characterization: Rate Capability Tests *149*
Electrochemical Characterization: Long-Term Cycling Test *152*
Conclusion and Summary *154*

7.5 TiO_2 and LTO as Interdiffusion Barriers in Ga-LLZO|Interlayer|LMO Cells 155

Crystalline Phases *155*
Cross-Sections *157*
Interdiffusion Processes *157*
Electrochemical Characterization: 1. Formation Cycles at 5 $\mu A/cm^2$ *159*
Electrochemical Characterization: 2. Cycling Test at 1 $\mu A/cm^2$ *162*
Discussion of Electrochemical Results *168*

7.6 Summary and Conclusion of the Investigation into the SSE/Cathode Interface 173

8 Summary and Conclusion of Ph.D. Thesis and Outlook 176
8.1 English Summary, Conclusion and Outlook 176
Summary and Conclusion 176
Outlook 180
8.2 Deutsche Zusammenfassung, Fazit und Ausblick 181
Zusammenfassung und Fazit 181
Ausblick 185
9 Experimental Part 187
9.1 Experimental Part of Study on Thermal Stabilities of LATP in Combination with various Mn-based Active Materials 187
Powder Synthesis 187
Powder Mixtures, Pellet Preparation and Form Integrity Tests 188
HT-XRD incl. Rietveld Refinement 188
DSC-TG incl. MS 188
SEM/EDS 188
9.2 Experimental Part of Study on the Sintering Additive Li_3PO_4 for LATP 189
Powder Synthesis 189
Adding of Li_3PO_4, Preparation of Pellets and Sintering 189
XRD 189
TOM and Water Saturation (Archimedes Principle) 189
SEM/EDS 190
EIS 190
9.3 Experimental Part of Study on the Current Collector/Cathode Interface 190
Preparation of Substrate and Interlayers 190
Preparation of LMO Thin-Films 191
SEM 191
ToF-SIMS 191
GIXRD 191
XPS 192
Cell Assembly 192
GCPL & EIS 192
Optimization of Preparation and ITO Interlayers 192
9.4 Experimental Part of Study on the Cathode/SSE Interface 193
Preparation of LMO Double-Layer Thin-Films and LTO or TiO_2 Coatings 193
LIPON Preparation 193
Ga-LLZO Preparation 194
SEM 194
GIXRD 194
ToF-SIMS 194
Cell Assembly 194
Electrochemical Characterization of coated LMO and LIPON Full Cells 195
Electrochemical Characterization of Ga-LLZO Cells 195
10 Appendix 196
10.1 List of Figures 196
10.2 List of Tables 205
11 References 207
12 Acknowledgments 225

List of Abbreviations

AM	Active material
ASSB	All solid-state battery
Au	Gold
CEI	Cathode electrolyte interphase
Co	Cobalt
CPE	Constant phase element
CPE_{CT}	Constant phase element of charge transfer in battery cell corresponding to double layer formation
CPE_{In}	Constant phase element of insulating layer in battery cell
CVD	Chemical vapor deposition
DMC	Dimethyl carbonate
DSC-TG	Differential scanning calorimetry and thermal gravimetric analysis
EC	Ethylene carbonate
EDS	Energy dispersive X-ray spectroscopy
EIS	Electrical/electrochemical impedance spectroscopy
Ga-LLZO	$Li_{6.25}Ga_{0.25}La_3Zr_2O_{12}$, Lithium gallium lanthanum zirconium oxide
GCPL	Galvanostatic cycling with potential limits
GIXRD	Grazing incidence X-ray diffraction
HT-XRD	High-temperature X-ray diffraction
ITO	Indium tin oxide
LATP	$Li_{1.3}Al_{0.3}Ti_{1.7}(PO_4)_3$, lithium aluminum titanium phosphate
LGPS	$Li_{10}GeP_2S_{12}$, lithium germanium thiophosphate
Li	Lithium
LiB	Li-ion battery
$LiClO_4$	Lithium perchlorate
$LiMO_2$	Lithium metal oxide with M = transition metal element (Co, Ni, Mn etc.)
$LiPF_6$	Lithium hexafluorophosphate
LIPON	Lithium phosphorous oxynitride
LISICON	Li super ionic conductor
LLZO	$Li_7La_3Zr_2O_{12}$, lithium lanthanum zirconium oxide
LMO, LMO-s	$LiMn_2O_4$, spinel lithium manganese oxide

LMO-l	$LiMnO_2$, layered lithium manganese oxide
LMP	$LiMnPO_4$, lithium manganese phosphate
LTO	$Li_4Ti_5O_{12}$, lithium titanate
LTP	$LiTi_2(PO_4)_3$, lithium titanium phosphate
M	3d transition metal such as Co, Mn, Ni, Fe
Mn	Manganese
MS	Mass spectroscopy
NASICON	Na super ionic conductor
Ni	Nickel
Pt	Platinum
PVD	Physical vapor deposition
SEI	Solid electrolyte interphase
SEM	Scanning electron microscopy
SHE	Standard hydrogen electrode
Si	Silicon
SSE	Solid-state electrolyte
StSt	Stainless-steel
TF-SSB	Thin-film solid-state battery
TiO_2	Titanium dioxide
ToF-SIMS	Time-of-flight secondary ion mass spectroscopy
TOM	Thermal-optical measurement device
XPS	X-ray photoelectron spectroscopy
XRD	X-ray diffraction

List of Symbols

A	Cross-sectional area of component	cm^2
$A_{Eletrodes}$	Area of electrodes	cm^2
A_{hkl}	Absorption factor	--
a_{Li}	Activity of Li-metal (usually $a_{Li} = 1$)	mol/cm^3
a_{Li+}	Activity of Li-ion	mol/cm^3
ASR_i	Area-specific resistance	Ω/cm^2
C	Capacitance	F
c_0	Concentration of redox species in bulk electrolyte	mol/cm^3
C_{gb}	Capacitance of grain boundaries	F
c_{Li+}	Concentration of Li-ions	mol/cm^3
c_s	Concentration of redox species at surface	mol/cm^3
d	Length of component	cm
D	Diffusivity or Diffusion coefficient	cm^2/s
d_g	Thickness of grain	cm
d_{gb}	Thickness of grain boundary	cm
d_{hkl}	Distance between lattice planes	m
D_{Li}	Diffusivity of Li-ions	cm^2/s
d_{Pellet}	Thickness of pellet	cm
E	Cell potential	V
E_0	Standard Electromotive force of electrochemical cell	V
$E_{a,b}$	Bulk activation energy for ion migration in crystal lattice	J
$E_{a,gb}$	Grain boundary activation energy for ion transfer through grain boundary	J
E_d	Energy of defect formation	J
E_m	Potential barrier for ion migration in crystal lattice	J
F	Faraday constant: $F = 96{,}485.33$ C/mol	C/mol
F_{hkl}	Structure factor	--
i	current	A
$I(t)$	Alternating current as a function of time t	A
I_A	Amplitude of alternating current	A
I_{hkl}	Intensity of X-ray reflections	--
iR	iR loss as specified term for overpotential η_{iR} induced by ohmic resistances R and current i	V
j	Current density	A/cm^2
j_0	Exchange current density at equilibrium potential	A/cm^2
j_a	Anodic current density	A/cm^2
j_c	Cathodic current density	A/cm^2
j_{lim}	Limiting current density by mass transport	A/cm^2

$k_{0,a}$	Standard rate constant of anodic redox reaction	1/s
$k_{0,c}$	Standard rate constant of cathodic redox reaction	1/s
k_B	Boltzmann constant: k_B = 1.380649 E-23 J/K	J/K
k_c	Rate constant of cathodic redox reaction	1/s
l	Jump length	cm
L	Inductance	H
LP	Lorentz-Polarization factor	--
M	Molar mass	g/mol
M_{hkl}	Multiplicity factor	--
M_P	Molar mass per formula unit	g/mol
n	Charge passed per atom	--
n_d	Number of defects	--
n_i	Number of mols of element i	mol
p	Pressure	Pa
P_{hkl}	Preferred orientation factor	--
q	Charge	C
q_{th}	Theoretical specific capacity of active material	mAh/g
R	Universal gas constant: R = 8.31432 J/Kmol	J/Kmol
R	Ohmic Resistance	Ω
R_b	Bulk resistance of Li-ion conduction through grains	Ω
R_{CT}	Resistance of charge transfer in battery cell	Ω
R_{gb}	Grain boundary resistance of Li-ion conduction through grain boundaries	Ω
R_{In}	Resistance of insulating layer in battery cell	Ω
R_Ω	Ohmic resistance of battery cell	Ω
S	Entropy	J/K
s	Scaling factor	--
T	Temperature	K
t	Time	s
V	Volume	cm^3
$V(t)$	Alternating voltage as a function of time t	V
V_A	Amplitude of alternating voltage	V
V_P	Volume of unit cell	cm^3
W_0	Warburg Impedance	Ω
w_p	Phase fraction	wt%
$Z(\omega)$	Impedance as a function of angular frequency ω	Ω
Z^*	Complex number of Impedance	Ω
Z'	Real part of complex impedance Z^*	Ω
Z''	Imaginary part of complex impedance Z^*	Ω

Z_c	Capacitive Impedance	Ω
Z_L	Inductive Impedance	Ω
Z_P	Number of formula units per unit cell	--
Z_R	Electrical Resistance	Ω
Z_{SSB}	Total device impedance	Ω
α	Charge transfer coefficient of redox process	--
β	Correction factor for capacitance in constant phase elements	--
γ	Incidence angle for GIXRD set-up	degree
ΔG_0	Standard Gibbs free energy change in a chemical process	J/mol
$\Delta G_{0,c}$	Standard activation energy of cathodic redox reaction at equilibrium conditions	J/mol
ΔG_c	Activation energy of cathodic redox reaction	J/mol
$\Delta\varphi_0$	Potential difference at electrolyte-electrode interface	V
ε_0	Vacuum permittivity ε_0 = 8.854188 E-12 F/m	F/m
ε_{gb}	Grain boundary permittivity	F/m
η_C	Concentration polarization or concentration overpotential	V
η_{CT}	Charge transfer polarization or charge transfer overpotential	V
η_{iR}	Ohmic overpotential induced by ohmic resistances and current flow	V
θ	Incident angle	degree
ϑ	Geometric factor of crystal lattice	--
λ	Wavelength	m
μ	Chemical potential	J/mol
μ_i	Chemical potential of species *i*	J/mol
μ_{Li}	Chemical potential of Li	J/mol
μ_{Li+}	Chemical potential of Li-ion	J/mol
ξ	Ionic mobility	cm^2/Vs
σ	Specific conductivity	S/cm
σ_b	Bulk conductivity	S/cm
σ_{el}	Electrical conductivity	S/cm
σ_{gb}	Grain boundary conductivity	S/cm
υ	Jump frequency for ion migration in crystal lattice	1/s
υ_C	Reaction rate of cathodic redox reaction	$mol/s\cdot cm^3$
φ	Electrode potential	V
Φ	Phase difference of alternating voltage and current	--
φ_0	Standard electrode potential or equilibrium electrode potential	V
ω	Angular frequency	1/s or Hz

1 Motivation and Scope of Thesis

Motivation

Nowadays, batteries are permanent companions in our all daily lives. The successful development of Li-ion batteries (LiBs) as an energy source for mobile devices such as smartphones and laptops has significantly changed our information and communication culture. In addition, batteries play a key role in the transformation of the energy and transport sectors toward a sustainable and ecological future. Two technological responses to the challenges of climate change are the transition to an energy supply by 100 % renewable energy technologies, such as solar cells and wind turbines, and the electrification of combustion engine cars. In both cases, batteries are a crucial factor either as an energy storage system to buffer energy peaks during sunny or windy days or as a power source for electrical vehicles. The application profiles of batteries differ for both application fields since electrical vehicles provide limited space for the battery and require fast charging to be competitive with combustion engine cars. Thus, a high energy density for long driving ranges and high power density for fast charging in addition to safety, costs as well as long calendar and cycling lives are the key performance measures for batteries in the field of electromobility. Particularly in terms of energy density, LiBs are the only battery technology used in commercially available electrical vehicles so far, as lithium is the third lightest existing element and also in combination with the electrode materials, lithium metal oxides (cathode) or graphite (anode) are much lighter than lead and lead oxide in lead-acid batteries or sodium metal oxides and hard carbon in sodium-ion batteries. Since the commercialization of LiBs in 1991 the energy density of standard cylindrical 18650 batteries based on metal oxide cathodes, graphite anode and an organic liquid electrolyte has increased by almost a factor of four to nowadays values of ca. 770 Wh/l (270 Wh/kg).[1] However, the theoretical limit is almost reached, so that new designs and material concepts need to be considered to guarantee a further enhancement of LiBs and by that the competitiveness of electrical vehicles. The straightforward approach is the increase of the cell working voltage by high voltage cathode materials (> 4 V vs. Li/Li^+) and the use of a Li-metal anode, which has a factor ten higher specific capacity than commercially used graphite anodes. However, the high cathode potentials cause degradation of the organic liquid electrolyte and Li-metal anodes tend to form Li dendrites by electro-decomposition, which results in short circuits, heating of the cell and finally bursting under the pressure of the evaporated liquid electrolyte.[2–4]

One promising approach to address these safety hazards is the concept of an all solid-state battery (ASSB). Due to the substitution of the liquid electrolyte by a ceramic solid-state electrolyte (SSE), the operating temperature range can be significantly increased, which might increase the power density due to faster charge transfer kinetics at high temperatures, and the out-gassing at high temperatures is highly inhibited. Furthermore, the dendrite growth is expected to be suppressed by stiff and mechanically stable ceramic SSE separators in contrast to the commercially used porous plastic separators impregnated with liquid electrolyte. These characteristics would enable the safe implementation of Li-metal anodes in commercial batteries.[1,5–9] In addition, some ceramic solid-state electrolytes show high intrinsic electrochemical potential windows (up to 5 V vs. Li/Li^+)[10], which would enable the use of high voltage cathodes. The increase of the cell potential from 4.2 V to 5 V would increase the energy density by approx. 20 %. The additional integration of Li-metal anodes could result in a further estimated increase by 70 % in energy density.[1] However, these promising improvements are far from realization and further developments have to be made for the successful integration of ceramic SSEs in LiBs. Even though the technological readiness level (TRL) is above four for the single components and most of the cathode active materials and SSEs are already commercially available, the overall TRL of a functional ASSB is less or equal to three since the fabrication and operation of ASSB batteries differ significantly from commercial liquid electrolyte LiBs. Further obstacles regarding thermal stabilities as well as electrochemical, mechanical and structural requirements have to be overcome to obtain a competitive ASSB in comparison to already commercialized liquid electrolyte LiBs.

Scope of Thesis

This Ph.D. thesis addresses the currently most significant issue for ASSBs on the cathode side: the thermal stability during manufacturing of the ceramic active material in combination with a ceramic SSE and its impact on electrochemistry.

After introducing the thermodynamical background of LiBs and explaining the benefits and drawbacks of Li-metal batteries (**Chapter 2.1**), the concept of a ceramic ASSB is elucidated (**Chapter 2.2**). In both cases, the redox process at the cathode active material is the insertion/extraction of Li-ions into/out of its crystal lattice. Thus, good electrochemical performance requires a firmly bonded contact between active material and electrolyte to guarantee a fast charge transfer and to maximize the electrochemically active area. This is easily given by the wettability of a liquid electrolyte. However, the implementation of a ceramic SSE requires sintering processes to obtain a firm bonding between the ceramic active material and the ceramic SSE. Consequently, the exchange of the liquid electrolyte with a ceramic SSE involves a change in the manufacturing processes. The target system is a ternary composite cathode consisting of active material, SSE and an electrically conductive additive, which has to fulfill electrochemical, chemical, mechanical and structural requirements (**Chapter 2.2**). However, the sintering of a particulate powder mixture of the single components can cause interdiffusion and the formation of mixed phases (**Chapter 2.4**). Non-conductive or electrochemically inactive mixed phases impair significantly the cell performance and finally result in the malfunction of the battery cell.

In the first part (**Chapter 4**), this Ph.D. thesis investigates the thermal stability of Mn-based active materials in combination with the ceramic SSE lithium aluminum titanium phosphate ($Li_{1.3}Al_{0.3}Ti_{1.7}(PO_4)_3$, LATP, **Chapter 2.2**). The three chosen active materials are $LiMn_2O_4$, $LiMnO_2$ and $LiMnPO_4$, which represent each active material class categorized by the lattice structure (**Chapter 2.1**). Powder mixtures are pressed into pellets and investigated by high-temperature X-ray diffraction measurements (HT-XRD) and Rietveld refinement to determine the development of mixed phase formation during a heating ramp between 500 °C and 1000 °C. Differential scanning calorimetry and thermal gravimetric analysis including mass spectroscopy (DSC-TG incl. MS) as well as microstructural analyses by scanning electron microscopy (SEM) including energy dispersive X-ray spectroscopy (EDS) complement the thermal stability investigation. As the combination of $LiMnPO_4$ and LATP exhibits good thermal stability, silver (Ag) was added as an electrical conductor.

The second part deals with the impact of the sintering additive Li_3PO_4 on the sintering behavior, microstructure and electrical properties of the ceramic SSE LATP (**Chapter 5**). The scope of this approach is to reduce the sintering temperature of LATP due to liquid phase sintering (**Chapter 2.3**) to reduce mixed phase formation and interdiffusion in combination with active materials. The sintering behavior of pure LATP and LATP with various amounts of Li_3PO_4 is investigated by means of a thermal-optical measurement device (TOM, **Chapter 3.2**). The impact of Li_3PO_4 on the microstructure is analyzed by SEM. Finally, the differences in the electrical properties such as ionic conductivity and activation energy (**Chapter 2.5**) of the samples with and without sintering additive as a function of the sintering temperature are analyzed by electrical impedance spectroscopy (EIS, **Chapter 3.4**). Hereby, correlations between sintering behavior, microstructure and electrical properties can be discussed.

In the third and fourth parts of the thesis, the concept of a thin-film solid-state battery (TF-SSB) is used to investigate the impact of interdiffusion processes on the electrochemical performance. Firstly, thin layers (< 1 µm) of $LiMn_2O_4$ (LMO) are deposited and crystallized on a stainless-steel current collector (StSt). Platinum (Pt), gold (Au) and indium tin oxide (ITO) interlayers are tested as probable interdiffusion barriers between LMO and StSt (**Chapter 6**). The thin-film approach gives the possibility to examine the interdiffusion by means of time-of-flight secondary ion mass spectroscopy (ToF-SIMS, **Chapter 3.3**). Grazing-incidence X-ray diffraction spectroscopy (GIXRD) and X-ray photoelectron spectroscopy (XPS) give information about the changes in the crystal lattice of LMO. Finally, the impact of interdiffusion on the electrochemical performance is investigated by galvanostatic cycling with potential limits (GCPL, **Chapter 3.5**) and electrochemical impedance spectroscopy (EIS, **Chapter 3.4**).

The best performing material combination is used afterward to deposit and crystallize the ceramic SSE gallium lithium lanthanum zirconium oxide ($Li_{6.25}Ga_{0.25}La_3Zr_2O_{12}$, Ga-LLZO, **Chapter 2.2**) on top of it (**Chapter 7**). Titanium dioxide (TiO_2) and lithium titanate ($Li_4Ti_5O_{12}$, LTO) are tested as interdiffusion barriers between LMO and Ga-LLZO by the same techniques as in the previous chapter. The general functionality of these interlayers is tested in TF-SSB full cells with the amorphous lithium phosphorous oxynitride (LIPON, **Chapter 2.2**) SSE.

2 Fundamentals

2.1 Thermodynamics of Lithium-Ion Batteries | LiBs

Electrochemical Fundamentals

The principal function of rechargeable LiBs is the reversible transformation of chemical energy into electrical energy and vice versa. A battery cell of a commercial LiB (also called full cell) consists of two electrodes defined as cathode (positive electrode, e.g. $LiMO_2$ with M = transition metal element such as Co, Mn or Ni) and graphite anode (C, negative electrode) immersed in an organic liquid solvent such as ethylene carbonate (EC) or dimethyl carbonate (DMC) with a Li-salt such as lithium hexafluorophosphate ($LiPF_6$) or lithium perchlorate ($LiClO_4$), which forms the electrolyte and enables the Li-ion transfer between the electrodes during charge and discharge. Electron flow is possible due to connecting the electrodes with a wire (**Fig. 2.1**). The term for an electrochemical lab-cell with a Li-metal anode is half cell. The transformation of chemical energy into electrical energy takes place due to redox reactions at the electrodes. During discharge, the cathodic reaction is the lithiation of the $Li_{1-x}MO_2$, which is an insertion reaction of Li^+ into the crystal lattice accompanied by the reduction of the transition metal. The counterpart is the anodic deintercalation of Li^+ between the graphene layers of the graphite. In the case of a Li-metal anode, the oxidation of metallic Li^0 to Li^+ takes place by stripping. The driving force for these redox processes is the difference in the chemical potentials of the Li^+ in the electrode and the Li^+ in the electrolyte. During the charge step of the battery, an external electrical force generated by applying a current or voltage causes reverse redox reactions.[2–4]

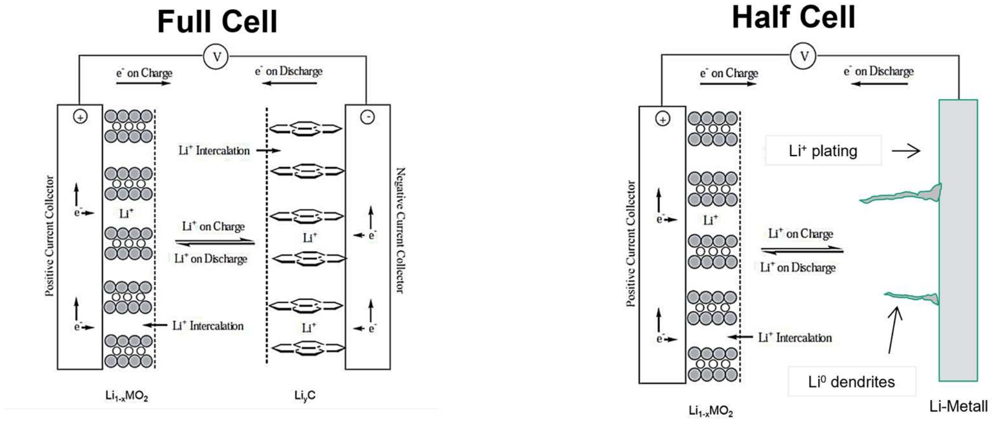

$$LiMO_2 \rightleftarrows Li_{1-x}MO_2 + xLi^+ + xe^-$$
$$C + yLi^+ + ye^- \rightleftarrows Li_yC$$
$$LiMO_2 + \frac{x}{y}C \rightleftarrows \frac{x}{y}Li_yC + Li_{1-x}MO_2$$

$$LiMO_2 \rightleftarrows Li_{1-x}MO_2 + xLi^+ + xe^-$$
$$xLi^+ + xe^- \rightleftarrows xLi^0$$
$$LiMO_2 \rightleftarrows Li_{1-x}MO_2 + xLi^0$$

Fig. 2.1 Schematics of LiBs consisting of $LiMO_2$ (M = transition metal such as Mn, Ni, Co) as cathode and graphite in full cell design as well as Li-metal in half cell design as anodes. The listed redox reactions are insertion/extraction reactions for the $LiMnO_2$ and graphite as well as Li plating and stripping on the Li-metal. Adapted from T. B Reddy and D. Linden: Linden's handbook of batteries (2011, 4th ed., McGraw-Hill).[4]

The maximum electrical energy, which can be delivered by the redox couple of the system, is given by the change in the standard Gibbs free energy ΔG_0, which is given by the standard electromotive force E_0 of the system and the charge passed is defined by n as the number of electrons passed per atom and F as the Faradaic constant, which describes the charge on a mole of electrons:

$$\Delta G_0 = -nFE_0 \qquad \textbf{Eq. 2.1}$$

The standard electromotive force E_0 is the ideal potential difference between the two electrodes induced by the redox reactions. Its value can be deduced from the Nernst Equation (**Eq. 2.3**), which describes the standard redox potential of a single electrode. Considering a Li-metal in a Li-salt electrolyte without the possibility of current flow, the chemical potentials μ_{Li+} of Li^+ in the electrolyte and the electrode might differ and the system aims at equilibrium conditions. If μ_{Li+} in the electrolyte is higher than in the electrode, Li^+ will diffuse to the electrode surface and will form an electrochemical double-layer. The accumulation of positive charged Li-ions at the neutral charged Li-metal surface results in an electrical potential difference $\Delta\varphi_0$ at the interface:

$$\begin{aligned}\Delta\varphi_0 &= \varphi_{electrode} - \varphi_{electrolyte} = \\ &= \frac{{\mu^0}_{Li^+,electrolyte} - {\mu^0}_{Li^+,electrode}}{nF} + \frac{RT}{nF} ln\left(\frac{a_{Li^+}}{a_{Li}}\right)\end{aligned} \qquad \textbf{Eq. 2.2}$$

a_{Li+} and a_{Li} are the chemical activities or concentrations of the Li^+ in the electrolyte and the Li-metal (a of metals is defined as 1). R is the universal gas constant and T is the temperature.

The electrochemical equilibrium is reached when the potential difference is equal to the difference of the chemical potentials in dependency on the concentration of Li^+. **Eq. 2.2** at the equilibrium state leads to the Nernst equation of the redox potential φ_0 of a single electrode:

$$\varphi_0 = \varphi_{00} + \frac{RT}{nF} ln(a_{Li^+}) \qquad \textbf{Eq. 2.3}$$

By applying the Nernst equation to both electrodes, the difference in the obtained redox potential defines the ideal cell potential or standard electromotive force E_0 of an electrochemical cell:

$$E_0 = \varphi_{0,cathode} - \varphi_{0,anode} \qquad \textbf{Eq. 2.4}$$

However, the actual cell potential E differs during the operation of the cell due to polarization effects and ohmic resistances induced by current flow.

$$E = E_0 - \eta_{CT} - \eta_C - iR \qquad \textbf{Eq. 2.5}$$

The three loss mechanisms are i) the charge transfer polarization η_{CT}, ii) concentration polarization η_C and iii) the iR loss. The charge transfer polarization depends on the kinetics of the redox reaction. Concentration polarization is induced by mass transport limits between the electrode surface and bulk electrolyte. The *iR* loss is the sum of all ohmic resistances such as the ionic resistance of the electrolyte and active material and the electrical resistance of all components of the cell set-up. Their impact on the cell voltage *E* by increasing the operating current is demonstrated in **Fig. 2.2**.[3,4,11,12]

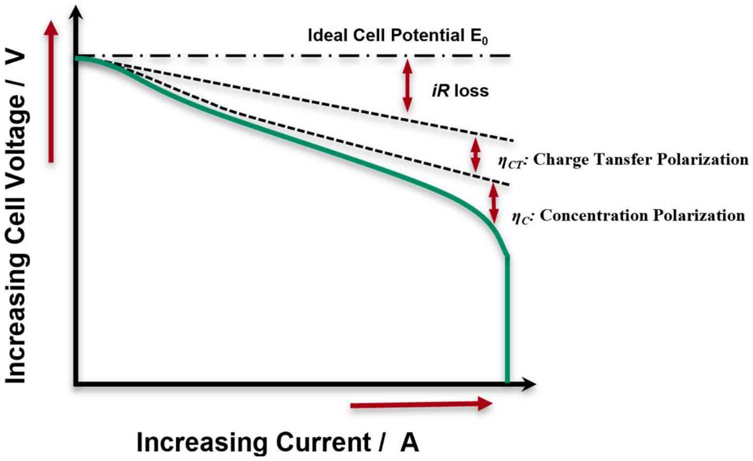

Fig. 2.2 Cell voltage as a function of operating current including the fractions of the three loss mechanisms. Adapted from T. B Reddy and D. Linden: Linden's handbook of batteries (2011, 4th ed., McGraw-Hill).[4]

i) Charge Transfer Polarization η_{CT}

The charge transfer polarization is based on the reaction rate of the redox process. Considering the example of the cathodic Li^+ plating on the Li-metal, the reaction rate of the cathodic reaction υ_C is defined by the concentration of Li^+ c_{Li+} at the surface and the rate constant k_c:

$$\upsilon_c = c_{Li^+}k_c = c_{Li^+}k_{0,c}\exp\left(-\frac{\Delta G_0, c}{RT}\right) \qquad \textbf{Eq. 2.6}$$

The rate constant can be written in its Arrhenius form with $k_{0,c}$ as the standard rate constant and $\Delta G_{0,c}$ as the activation energy of the reduction of Li^+. When the redox reaction takes place in an electrochemical cell, it generates a current flow, which disturbs the equilibrium state and shifts the equilibrium electrode potential φ_0 to φ by the so-called overpotential or charge transfer polarization η_{CT}:

$$\eta_{CT} = \varphi - \varphi_0 \qquad \textbf{Eq. 2.7}$$

This leads also to a shift of the energy of the elements in the electrochemical double layer to $nF\varphi$ and it leads to a change in the activation energy of the reaction. However, the change of the activation energy to ΔG_c does not happen to the same degree as the change of electrode potential:

$$\Delta G_c = \Delta G_{0,c} + \alpha nF\varphi \qquad \textbf{Eq. 2.8}$$

The charge transfer coefficient α ($0 \leq \alpha \leq 1$) describes the fraction of the potential change, which influences the activation energy. The equations **Eq. 2.6**, **Eq. 2.7** and **Eq. 2.8** combined with the relation between current density j_c and reaction rate υ_c gives the cathodic part of the Butler-Volmer equation:

$$j_c = nF\upsilon_c = nFc_{Li^+}k_{0,c}exp\left(-\frac{\alpha nF(\eta_{CT} - \varphi_0)}{RT}\right) \qquad \textbf{Eq. 2.9}$$

Applying the same derivation on the anodic Li plating reaction, the anodic part of the anodic current density j_a can be included in the final Butler-Volmer Equation:

$$j = j_a + j_c = j_0\left[exp\left(\frac{(1-\alpha)nF}{RT}\eta_{CT}\right) - exp\left(-\frac{\alpha nF}{RT}\eta_{CT}\right)\right] \qquad \textbf{Eq. 2.10}$$

where j_0 is the exchange current density, thus, the current density at the equilibrium potential with zero overpotential:

$$j_0 = nFc_{Li^+}k_{0,c}exp\left(-\frac{\alpha nF}{RT}\varphi_0\right) = nFc_{Li}k_{0,a}exp\left(\frac{(1-\alpha)nF}{RT}\varphi_0\right) \qquad \textbf{Eq. 2.11}$$

The Butler-Volmer equation describes the relation between the current density and charge transfer polarization η_{CT} as a function of concentration and rate constant. By that, a material-specific examination can be done and the conclusions of the electrochemical mechanisms can be obtained. That makes the equation one of the most important relations in electrochemistry.[11,12]

ii) Concentration Polarization η_C

The concentration polarization, also called concentration overpotential, η_C appears, when the proper mass transport of the reacting species or reacted species between the electrode surface and the bulk electrolyte is not guaranteed. That happens mostly when the reaction kinetic is much faster than the ion flow to the electrode surface. Considering the case of a low ionic current flow of the reacting species to the electrode, the concentration of the species at the surface c_s is lower than its concentration in the bulk electrolyte c_0, which generates a concentration profile at the electrode surface. By applying the Nernst Equation (**Eq. 2.3**) to both concentrations the potential difference results in the relation for the concentration polarization η_C:

$$\eta_C = \varphi_0(c_s) - \varphi_0(c_0) = \frac{RT}{nF}ln\left(\frac{c_s}{c_0}\right) = \frac{RT}{nF}ln\left(1 - \frac{j}{j_{lim}}\right) \qquad \textbf{Eq. 2.12}$$

$$j = j_{lim}\left(1 - exp\left(\frac{nF}{RT}\eta_C\right)\right) \qquad \textbf{Eq. 2.13}$$

The concentration polarization can be set in relation to the electrochemical current density j and a limiting current density j_{lim} can be defined, at which the concentration at surface c_s becomes 0. Reaching this case, the electrochemical cell just polarizes, since η_c tends to infinity. That happens at high overpotentials when the electrochemical charge transfer (Butler-Volmer equation, **Eq. 2.10**) is much faster than the mass transport. Here, concentration polarization is the dominating loss mechanism. At low overpotentials, mass transport is guaranteed and the state of $c_s \approx c_0$ can be maintained since the chare transfer reaction is slow. Thus, the charge transfer polarization η_{CT} is the main loss mechanism in this potential region.

Considering the voltage-current profiles of a redox-reaction in an experimental cell set-up, it is difficult to separate the charge transfer polarization from the concentration polarization, since both polarizations' effects depend on each other. Consequently, the measured voltage-current correlation is always an overlay of **Eq. 2.10** and **Eq. 2.13** which ratio can also change with measurement duration.[11,12]

iii) *iR* Loss

The *iR* loss is the sum of all ohmic resistances induced by the electrical and ionic conductivities of all components of the electrochemical cell. It follows Ohm's law with the linear course of the current $i = \eta_{iR}/R$ (η_{iR}: voltage loss due to ohmic resistance and current flow). The ohmic resistance R related to the conductivity σ due to the length d of the component and its cross-sectional area A:

$$\mathrm{R} = \frac{1}{\sigma}\frac{d}{A} \qquad \textbf{Eq. 2.14}$$

The *iR* loss becomes important for ASSBs, because of the low ionic conductivities of most ceramic SSEs in comparison to commercially used liquid electrolytes, which have factor 100 higher ionic conductivities.[4,11,12]

Cathode Active Materials

The redox reaction at the cathode is an insertion during discharge and extraction during charge of Li-ions into and out of the crystal lattice of a lithium metal oxide or phosphate, whereby the transition metal ion is reduced or oxidized, respectively. 3d transition metals M such as Mn, Co and Ni are the commonly used transition metals in lithium metal oxides, and Fe is preferred in lithium metal phosphates. The most common active materials are categorized by their crystal structure in layered ($LiMO_2$), spinel (LiM_2O_4) and phosphatic olivine ($LiMPO_4$) materials (**Fig. 2.3**).[2–4,13,14] A few representatives are summarized in **Table 2.1**. The theoretical capacities q_{th} can be calculated by assuming that all Li-ions take part in the redox reaction:

$$q_{th} = \frac{1}{M} nF \qquad \textbf{Eq. 2.15}$$

where M is the total molar mass of the cathode material.[2–4]

Table 2.1 Electrochemical characteristics of selected cathode active materials adapted from Nitta et al.[14]

Crystal Structure	Active Material	Redox	Specific Capacity theoretical | experimental	Average Potential vs. Li/Li$^+$
Layered	$LiMnO_2$	Mn^{3+} / Mn^{4+}	285 mAh/g | 140 mAh/g	3.3 V
	$LiCoO_2$	Co^{3+} / Co^{4+}	274 mAh/g | 148 mAh/g	3.8 V
Spinel	$LiMn_2O_4$	Mn^{3+} / Mn^{4+}	148 mAh/g | 120 mAh/g	4.0 V
	$LiNi_{0.5}Mn_{1.5}O_4$	Ni^{2+} / Ni^{4+}	148 mAh/g | 120 mAh/g	4.7 V
Olivine	$LiFePO_4$	Fe^{2+} / Fe^{3+}	170 mAh/g | 165 mAh/g	3.4 V
	$LiMnPO_4$	Mn^{2+} / Mn^{3+}	171 mAh/g | 168 mAh/g	3.8 V

The experimentally obtained specific capacities, which guarantee long cycling life, are significantly lower than the theoretical specific capacities. The host crystal structure can become unstable by ongoing Li extraction, by which an irreversible crystal structure conversion can occur along with oxygen release.[3,13] The three types of active materials also differ in their Li-ion diffusivity D_{Li} and electrical conductivity σ_{el} (**Fig. 2.3**).[15] The redox potential difference between $LiMnO_2$ and $LiMn_2O_4$ is significantly high, even though the same Mn^{3+}/Mn^{4+} redox process takes place, which can be explained by the different occupation sites of Li in the crystal structure. In general, two main factors determine the redox potential of the cathode material: i) the fermi level of the transition metal and ii) the activation energy for the Li^+ diffusion through the cathode material.[3] Since 3d transition metals M are used, the fermi level is defined by electron occupation of the d-orbitals. The fermi level of the degenerated d-orbitals generally increases with the atomic number, thus, the number of d-orbitals electrons.[3,16] However, the transition metals M are sixfold coordinated and form MO_6 octahedrons with O^{2-} atoms in all three crystal structure types (**Fig. 2.3**).[3,13] The interaction of the positively charged M with the free electrons of the six surrounding O^{2-} atoms results in a splitting of the five degenerated d-orbital energy levels in two separate energy levels t_{2g} and e_g (**Fig. 2.4a**), which is described by the crystal field theory.[3,17,18] Two configurations are possible for the occupation of the d-orbitals with electrons depending on the pairing energy of putting two electrons in the same orbital. If the pairing energy, thus the repulsion of two electrons, is lower than the energy difference between e_g and t_{2g}, the t_{2g}-orbitals are filled primarily and completely with electrons, which is referred to the low-spin configuration. In the opposite case, every orbital of e_g and t_{2g} is filled with one electron before forming electron pairs, which is called the high-spin configuration.[3,17,18] This is important in order to understand the origin of the different redox potentials of the various cathode active materials, which will be discussed in detail in the following. In addition, the nature of the crystal structures will have an influence on the thermal stabilities and their tendencies to decompose.

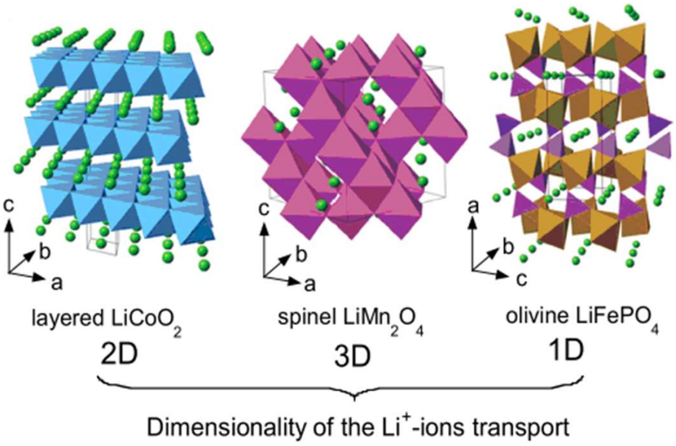

	D_{Li} [cm²/s]	σ_{el} [S/cm]
Layered		
	10^{-10} to 10^{-8}	10^{-4}
Spinel		
	10^{-11} to 10^{-9}	10^{-6}
Olivine		
	10^{-15} to 10^{-14}	10^{-9}

Fig. 2.3 Crystal structures reprinted from Julien et al.[13] (published under CC-BY license in MDPI: *inorganics* 2014) of the three common active material types on the left: the Li-ions in green and the MO_6 octahedrons in blue for $LiCoO_2$, in purple for $LiMn_2O_4$ and in brown for $LiFePO_4$. On the right: the value ranges of the Li diffusivity D_{Li} and electrical conductivity σ_{el}.[15]

Layered Active Materials $LiMO_2$

$LiCoO_2$ crystallizes in the rhombohedral lattice structure ($R\overline{3}m$ space group) and $LiMnO_2$ has an orthorhombic lattice structure ($Pmmn$ space group).[3,13] In both, the O^{2-} ions form a cubic structure. The M^{3+} transition metal ions occupy half of the octahedral sites and the other half is filled with Li-ions (**Fig. 2.3**). The edge-sharing MO_6 octahedrons form a layered structure. In between the Li-ions can diffuse in two dimensions. The average electrode potential of $LiCoO_2$ is about 3.8 V vs. Li/Li^+ and higher than the electrode potential of $LiMnO_2$ (ca. 3.3 V vs. Li/Li^+, **Table 2.1**). The large difference is based on the electronic configuration of both materials. The Co^{3+} ion exhibits a low-spin configuration, where the five electrons fill the t_{2g}-orbitals.[3,13,16,19,20] In contrast, Mn^{3+} has a high-spin configuration, so that the forth electron occupies an e_g-orbital.[20–22] The higher energy level of the e_g-orbital results in a lower fermi level, so the thermodynamic work to add or extract an electron is lower for the $LiMnO_2$ in comparison to $LiCoO_2$. This causes the lower electrode potential of $LiMnO_2$.

Spinel Active Materials LiM_2O_4

Spinels crystallize in a cubic lattice structure. The $LiMn_2O_4$ exhibits a crystal lattice with a $Fd\overline{3}m$ space group, in which the O^{2-} ions on the 32e sites form a cubic closed-pack structure. The Mn^{3+} and Mn^{4+} ions are situated in half of the 16d octahedral sites and the Li-ions occupy 1/8 of the 8a tetrahedral sites. The MnO_6 octahedrons are arranged three-dimensionally, which provides tunnels for Li diffusion in all three dimensions (**Fig. 2.3**).[3,13] The Li-ions are more stabilized on the tetrahedral sites than on the octahedral sites. The thereby obtained higher diffusion activation energy for the Li-ions explains the lower Li diffusivity for spinel than for layered active materials (**Fig. 2.3**) as well as the higher average potential of $LiMn_2O_4$ at ca. 4.0 V vs. Li/Li^+ compared with the 3.3 V for $LiMnO_2$ (**Table 2.1**), even though the change of the oxidation state from Mn^{3+} to Mn^{4+} by Li^+ extraction is the same.[3,20] Additionally, the

$LiMn_2O_4$ can be overlithiated by discharging below 3 V vs. Li/Li^+ (**Fig. 2.4b**). Hereby, additional Li-ions are inserted into the crystal lattice on the 16c octahedral sites and $Li_{1+x}Mn_2O_4$ ($0 < x \leq 1$) is formed. Because of the lower binding energies for the Li-ion on the octahedral sites, the potential of this redox reaction is at ca. 3 V vs. Li/Li^+. This reaction goes along with a reversible change to a tetragonal $Li_2Mn_2O_4$ crystal structure.[3,19,23,24] A further feature induced by the Li diffusion is the two-step redox process observable in the voltage profile at ca. 4 V vs. Li/Li^+ (**Fig. 2.4b**) so that two voltage plateaus at ca. 3.95 V and ca. 4.1 V can be seen. This can be explained by the slight change in the diffusion activation energies of the Li-ion by reaching a composition of $Li_{0.5}Mn_2O_4$ (in **Fig. 2.4b** at ca. 60 mAh/g). At a composition of $x < 0.5$ for $Li_xMn_2O_4$, the Li-ion diffusion from one 8a tetrahedral site to another 8a tetrahedral site is along an energetically unfavorable 16c octahedral site, which increases the diffusion activation energy and by that the redox potential to 4.1 V vs. Li/Li^+.[13,15,23]

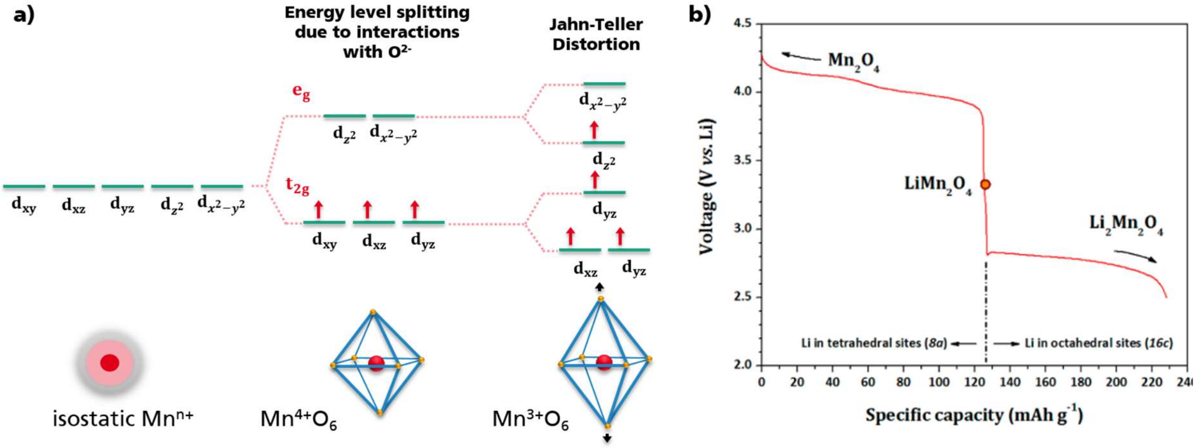

Fig. 2.4 a) d-orbital splitting regarding the crystal field theory including the corresponding $Mn^{4+}O_6$ and $Mn^{3+}O_6$ octahedrons, latter exhibits Jahn-Teller distortion, which induces further splitting of the e_g and t_{2g} energy levels. **b)** Discharge profile of $Li_xMn_2O_4$ for the lithiation between $0 < x < 2$ reprinted with permission from Goodenough et al.[19]. © American Chemical Society 2013.

The oxidation states of the Mn transition metal are half 3+ and half 4+ in $LiMn_2O_4$. The electronic configurations of both oxidation states are shown in **Fig. 2.4a**. Mn^{3+} exhibits a high-spin configuration, which causes a Jahn-Teller distortion of the $Mn^{3+}O_6$ octahedrons in the crystal lattice.[3,13,20] The Jahn-Teller distortion describes the change in the binding length of two opposite ligands, so that the octahedron is distorted, which causes a further splitting of the e_g and t_{2g} energy levels (**Fig. 2.4a**).[17] The Jahn-Teller effect can induce the disproportionation of Mn^{3+} into Mn^{2+} and Mn^{4+}. Hereby, the Mn^{2+} ion will dissolve into the liquid electrolyte and the Mn^{4+} remains in the crystal structure and a blocking layer for charge transfer is formed at the surface due to the depletion of Mn^{3+} and the formation of $Li_{1+\delta}Mn_{2-\delta}O_4$. This results in ongoing capacity fade with cycle life.[3,13] The Jahn-Teller distortion has a higher impact when discharging the cell below 3 V vs. Li/Li^+ since all Mn-ions have an oxidation state of 3+ in $Li_2Mn_2O_4$. Consequently, $LiMn_2O_4$ cells are usually cycled with a minimum potential limit of 3.1 V vs. Li/Li^+ in order to avoid the overlithiation at 3 V.[3,13] The Mn depletion at the surface is the major disadvantage of spinel active materials in practical battery application, however, two approaches address this issue. Firstly, coatings such as TiO_2 or LTO are used to inhibit the Mn^{2+} dissolution.[13,25–27] Secondly, Mn^{3+} can be substituted by Ni^{2+} forming the spinel $LiNi_{0.5}Mn_{1.5}O_4$, in which all Mn-ions have an oxidation state of 4+.[3,13,19] Thus, the Jahn-Teller distortion does not occur. The redox reaction is the oxidation of Ni^{2+} to Ni^{4+} involving two electrons so that the theoretical specific capacity is comparable with that of the $LiMn_2O_4$ spinel (**Table 2.1**). Furthermore, the fermi level of Ni is higher than for Mn due to its higher atomic number. This in combination with the high diffusion activation energy of Li-ions on the 8a tetrahedral sites results in an average electrode potential of 4.7 V vs. Li/Li+ (**Table 2.1**), which makes $LiNi_{0.5}Mn_{1.5}O_4$ a promising high voltage cathode material for future battery applications.

Olivine Active Materials $LiMPO_4$

The crystal structure of olivine $LiMPO_4$ is orthorhombic with the space group $Pnma$. The oxygen framework is a hexagonal closed-packed structure occupied with Li-ions and M^{2+} ions on half of the octahedral sites and P-ions on 1/8 of the tetrahedral sites. The LiO_6 octahedrons form an edge-sharing chain surrounded by corner-linked FeO_6 octahedrons, which are also bridged by the PO_4 tetrahedrons. This results in one-dimensional channels for Li diffusion (**Fig. 2.3**), which explains the low Li diffusivity (**Fig. 2.3**).[3,13] The average electrode potentials of $LiFePO_4$ and $LiMnPO_4$ are 3.4 V and 3.8 V vs. Li/Li^+, thus, higher than expected (**Table 2.1**).[14] This is caused by the low Li diffusivity and gets supported by the reduction of the M-O bond due to the strong P-O bond of the neighboring PO_4 tetrahedrons, whereby the energy levels of the d-orbitals of M^{2+} are reduced, which increases the fermi level and electrode potential.[3] The strong P-O bonds result additionally in a lower tendency of oxygen release at high potentials or high temperatures, which makes the olivine active materials safer than the lithium metal oxides in cases of short circuits and malfunction of the battery cell.[3] Since Fe^{2+} has a higher atomic number than Mn^{2+}, a higher electrode potential for $LiFePO_4$ is expected. However, a lower potential can be observed in experiments. This is caused by the different electronic configurations of Mn^{2+} and Fe^{3+}. The fifth electron of the high-spin Mn-ion, which is involved in the Mn^{2+}/Mn^{3+} redox reaction, occupies the fifth d-orbital. In contrast, the electron involved in the Fe^{2+}/Fe^{3+} redox reaction is the sixth electron of the Fe-ion. Since the Fe-ion also exhibits the high-spin configuration, all five d-orbitals are already occupied and the sixth electron has to overcome the pairing energy for a double occupation of a t_{2g}-orbital. This lowers the electrode potential of $LiFePO_4$.[16,28,29]

Anode Active Materials

Graphite is the commercially used anode active material in LiBs. Its theoretical specific capacity is 372 mAh/g and the redox reaction is a multiple-step intercalation/deintercalation process of Li-ion into/out the space between the graphene layers in the range of 0.20 V and 0.07 V vs. Li/Li^+.[3,30] By that, six Li^+ can be stored for one carbon atom (**Fig. 2.1**). Further anode materials, which are under investigation, are the insertion material LTO[3,14,31,32] and the alloy-forming Si[3,14,32,33], with theoretical specific capacities of 175 mAh/g at 1.55 V vs. Li/Li^+ and 4200 mAh/g at in the range of 0.21 V and 0.05 V vs. Li/Li^+, respectively. LTO is an interesting material due to no volume changes during the intercalation process and due to the high electrode potential so that the decomposition of the liquid electrolyte can be avoided. However, the high electrode potential results in low cell energies, which makes LTO not feasible for high-energy LiBs.[3,31,32] The decomposition of the liquid electrolyte occurs for all anode materials operating below 1 V vs. Li/Li^+. The decomposition results in the formation of a solid electrolyte interphase (SEI), which is capable of Li^+ diffusion but electrical non-conductive, so that the decomposition stops at sufficient SEI thickness.[2–4] However, the Li-Si alloy formation causes a volume change of up to 400 %, which results in high mechanical stress inducing the cracking of Si particles, thus, contact loss and cracking of the SEI layer. That results in low coulombic efficiencies, since the SEI has to be formed in every new cycle, as well as an ongoing capacity fade, so that lab-cells are usually cycled with maximal half the theoretic capacity. Consequently, further developments in electrolyte and anode formulations are required.[32,33]

The holy-grail of all anode materials is the Li-metal anode. Its specific capacity is about 3860 mAh/g and it has the lowest standard electrode potential of - 3.04. vs. SHE (standard hydrogen electrode). The redox reaction is an electro-decomposition process due to plating during discharge and striping during charge of Li on/off the Li-metal surface (**Fig. 2.1**).[3,32,34,35] Major drawback of the Li-metal anode is the dendrite formation. After the nucleation of Li on the Li-metal surface, potential peaks appear at these nucleation sites, which makes them more favorable for further Li plating. This leads to the growth of dendrites (**Fig. 2.1**) and by that to the cracking of the SEI layer, thus, a decrease in the coulombic efficiency.[3,34,35] Moreover, if the dendrites reach the cathode, it causes a short-circuit, so that the whole energy of the battery cell discharges by electron flow through the thin dendrite needles. This heats the cell and causes liquid electrolyte decomposition and the thermal runaway of the cathodic lithium metal oxide material including oxygen release. Under high pressure due to gas formation, the battery cell can burst. The flammability of the liquid electrolyte and the strong reaction of Li-metal with oxygen leads to significant fire hazards so that Li-metal is not used in commercial LiBs.[3,32,34,35]

Liquid Electrolytes

The liquid electrolyte consists of an organic solvent and a Li-salt. Its function is the Li transport between cathode and anode; thus, the Li-ion conductivity is the crucial factor to obtain high current densities and power densities. In commercial LiBs (**Fig. 2.1**) the liquid electrolyte is impregnated in the porous cathode and anode layers as well as in a plastic or glassy porous separator, which separates the cathode from the anode in order to avoid short circuits.[2–4] Consequently, the ionic conductivity is also affected by the porosity and tortuosity of the single components.[36] Ethylene carbonate (EC), dimethyl carbonate (DMC), propylene carbonate (PEC) or diethyl carbonate (DEC) are often used as organic solvents. $LiPF_6$ or $LiClO_4$ are common lithium salts.[3,4] Considering the pure liquid electrolyte, its Li-ion conductivity depends on the dielectric constant of the organic solvent, which affects the ionic dissociation and association of the lithium salt. Dielectric constants above 20 are recommended for sufficient salt dissolution.[3] However, a high dielectric constant also leads to increased viscosities, which also affects the Li-ion diffusivity. In addition, the melting temperature is increased, which lowers the operationally possible temperature range. To solve this issues, mixtures of organic solvents are used. For instance, EC has a dielectric constant of 89.6 F/m but a melting point of 39 °C. DMC has a low dielectric constant of 0.5 F/m but a melting point of 0.5 °C. The mixture of both results in good ionic conductivities of 1.16 E-2 S/cm and a broader operation temperature range.[3] However, the temperature range for organic solvents is limited between 0 °C and 50 °C due to the melting point and the high vapor pressure.[3] That can lead to safety issues, when the cell bursts under the gas pressure and the energy activates the ignition of organic solvent in contact with air since the flash points of liquid electrolytes are < 50 °C (25 °C for EC:DMC).[37] Further gas evolution can be generated by the oxidation of the solvent at the cathode during cell operation.[3,38,39] Most liquid electrolytes have an oxidation onset of about 4.0 V vs. Li/Li^+. Its oxidation leads to the formation of a polymeric cathode electrolyte interphase (CEI) along with the formation of CO_2 or O_2.[38,39] EC, for instance, reacts to polyethylene glycol along with gas evolution.[38,39] According to the Butler-Volmer equation (**Eq. 2.10**), the reaction increases exponentially with cell voltage so that high voltage cathode materials such as $LiNi_{0.5}Mn_{1.5}O_4$ cannot be used safely in commercial LiBs. Due to the volume change of the cathode active material and the gas evolution, the CEI can crack and will be formed each cycle.[3] Liquid electrolytes are also initially unstable on the anode side. The reduction on the graphite surface or the surface of Li-metal causes the formation of the so-called solid electrolyte interphase (SEI) but without gas release.[2–4,38] The SEI is Li-conductive but electrically isolating so that the reaction stops at sufficient layer thickness. To address the above-mentioned issues, current research focusses on electrolyte additives such as anode SEI additives, overcharge protectors, ionic conductivity enhancers and flame retardants.[3]

2.2 All Solid-State Batteries | ASSBs

Perspective, Concept and Application Profile

All solid-state batteries (ASSBs) are a promising approach to overcome the safety hazards caused by liquid electrolyte decomposition and the implementation of Li-metal anodes or high voltage cathode materials. The concept of ASSBs is based on the exchange of the liquid electrolyte with a ceramic or polymeric SSE. Since this thesis focuses on ceramic SSEs, a further discussion on polymeric SSEs is omitted and can be found elsewhere.[40–44] Many remarkable review articles about ceramic ASSBs can be found in the literature.[1,5–9,45–51]

The ceramic SSEs are stable at elevated temperatures and their mechanical rigidity may prevent dendrite growth so that short circuits can be avoided. Furthermore, ceramic SSEs are single-ion conductors so that no bulk polarization induced by the Li-salt anions in liquid electrolytes occurs.[1,6] These properties might result in higher energy density, higher power density, higher safety and longer cycle life. The implementation of high voltage cathodes and Li-metal anodes might increase the energy density by about 70 %.[1] The absence of bulk polarization due to the concentration gradient of the electrolyte anions may allow higher current densities, which enhances the power density.[1,6] The high-temperature stability of most SSEs and by that the lower tendency of gas evolution increases the battery safety and might allow higher operating temperatures, which would increase the power density. Furthermore, no leakage and combustion of the liquid electrolyte can occur.[1,5,6] Whether longer cycle lives are possible, depends on electrochemical and mechanical properties as well as the integration of ceramic SSEs into the battery cell. A promising proof of concept is given by Li et al.[52], who realized a thin-film solid-state battery (TF-SSB, < 1 µm layer thickness) based on the $LiNi_{0.5}Mn_{1.5}O_4$ cathode, LIPON SSE and Li-metal anode with a cycle life of > 10,000 cycles, which is more than three times higher than the cycle lives of the reference liquid electrolyte cells.[52]

However, commercial LiBs have a cathode loading of 2 - 3 mAh/cm² (cathode capacity per cathode area), which corresponds to a layer thickness of up to 130 µm for the porous cathode layer.[53] In order to achieve these high loadings for ASSBs, ternary composite cathodes consisting of cathode active material, ceramic SSE and electrically conductive additive must be accomplished (**Fig. 2.5** and **Fig. 2.8**). The ternary composite must fulfill several requirements with regard to electrical and electrochemical, chemical, mechanical and structural properties (**Fig. 2.6**).[1,6,8,47]

The ion conduction in a ceramic crystal lattice is the diffusion over interstitial sites or vacancies described as the hopping of a Li-ion from one site to another by overcoming an activation energy (**Fig. 2.5**), which will be discussed in more detail later in this thesis (**Chapter 2.5**). On a microscopic and macroscopic scale, ceramics are polycrystalline microstructures consisting of grains with different crystal lattice orientations (**Fig. 2.5**). The contact interface of two grains is called grain boundary and because of the misalignment of the two grain's lattices, the Li-ion hopping requires high activation energies, thus, the ionic conduction is hindered from one grain to another. The grain boundary conductivity σ_{gb} is usually the limiting factor of intrinsic Li-ion diffusion. A percolation network for Li-ion migration based on grains can be defined, which depends on grain lattice orientation, grain boundary alignment and amount of contact areas for Li-ion hopping from one grain to another (**Fig. 2.5**, Macro).[6] The total ionic conductivities of ceramic SSEs depend on the material class and are usually by a factor of 10 to 1,000 lower than the ionic conductivity of liquid electrolytes (**Fig. 2.9a**). On a device scale, percolation is also important in ternary composite cathodes. The cathode active material in the whole cathode layer must be supplied with Li-ions from the Li-metal anode and electrons from the current collector in order to guarantee an effective Li-ion insertion redox reaction and to achieve high utilization of the cathode.[6] Consequently, the composition, ratio and particle size distribution of the single components are crucial factors in accomplishing efficient percolation networks for Li-ion and electron supply to the cathode active material.[54] Cracks and pores interrupt the percolation network so that very dense microstructures need to be realized. This particularly applies to the contact area between SSE and cathode active material. Without a firm bonding, Li-ion transfer is not possible. Cracks and pores at the interface cause a decrease in the contact area and gain the area-specific resistance for the charge transfer (**Fig. 2.5**, Device, *ASR*).[6]

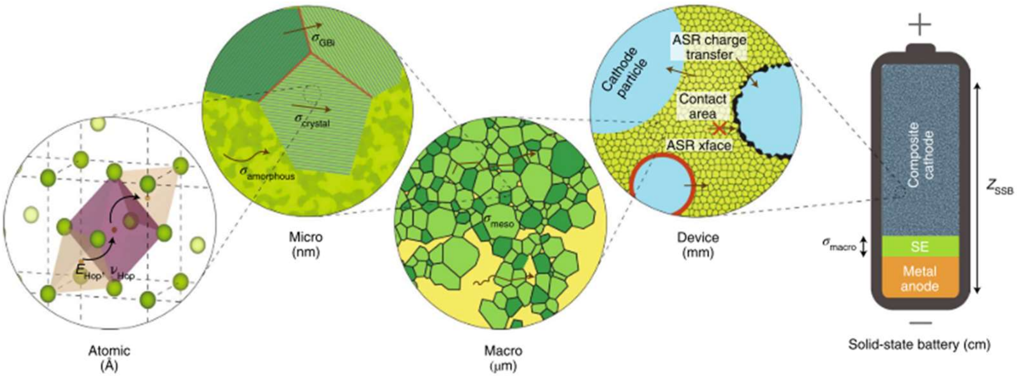

Fig. 2.5 Scheme of the ASSB concept regarding the various ionic conductivities σ_i of the SSE on the atomic, micro and macro scale as well as the interaction of the cathode particles and SSE defined by the area-specific resistances (ASR_i) and contact losses (pores in black) on the device scale. These resistances are summed up in the total device impedance (Z_{SSB}) of the ASSB. Reprinted by permission from Springer Nature: Nature Materials, Famprikis et al.[6] (2019): © Springer Nature 2019.

A common approach to densify a particulate composite is sintering at high temperatures. Consequently, the thermal stability of the materials combination has to be guaranteed. Intermixing and decomposition can occur, which results in interdiffusion, the formation of non-conductive or electrochemically non-active mixed phases and the dissolution of the initial components. If non-conductive mixed phases are formed at the interface of the cathode and SSE, the charge transfer is hindered and the area-specific resistance increases (**Fig. 2.5**, Device, *ASR xface*).[1,6,8] The formation of interphases can also be induced electrochemically, when the intrinsic electrochemical window of the SSE is lower or higher than the cathode or anode potential, respectively (**Fig. 2.7a**).[1,6,8,10,55–57] Interphase formation is enhanced by the accumulation and opposite depletion of Li-ions at the two electrodes forming space charge layers (**Fig. 2.7a**). Accumulation and depletion of positive charge could induce reduction or oxidation of the further elements in the lattice and by that the decomposition to new crystal phases.[1,6,8,55] If the formed interphases are electrically and ionically conductive, the interphases might grow in their thickness and consume continuously the initial components. However, three functional interfaces are thinkable: i) the intrinsically stable interface shows no reaction; ii) the kinetically stabilized interface, which means the formation of a Li-ion conductive but electron-blocking interphase so that the redox reaction stops at sufficient interphase thickness; iii) the artificially protected interface due to implementation of an electrochemically stable interlayer (**Fig. 2.7b**).[6,55] The implemented interlayer is meant to extend the potential window of the SSE. Such interlayers might additionally help to inhibit interdiffusion processes during the high-temperature manufacturing process. Consequently, various interlayers such as LTO, $LiNbO_3$, Li_3PO_4, etc. are currently under investigation as probable interdiffusion barriers and protection layers against electrochemical decomposition.[10,49,55]

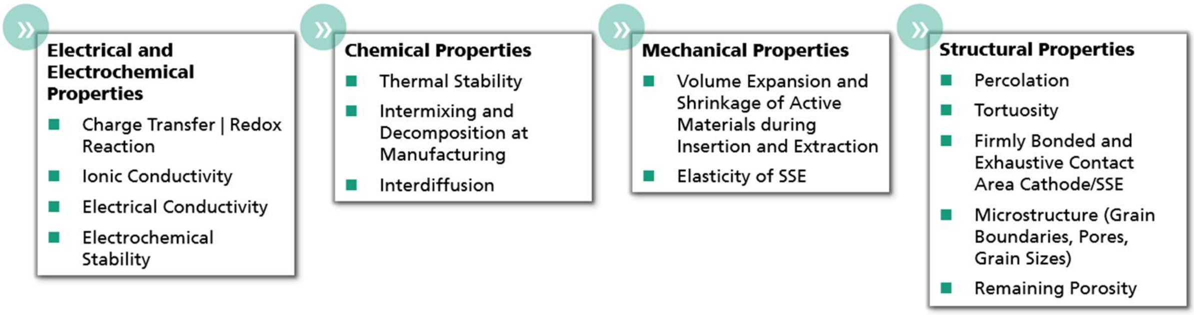

Fig. 2.6 Important properties of ternary composite cathodes consisting of cathode active material, ceramic SSE and electrically conductive additive.

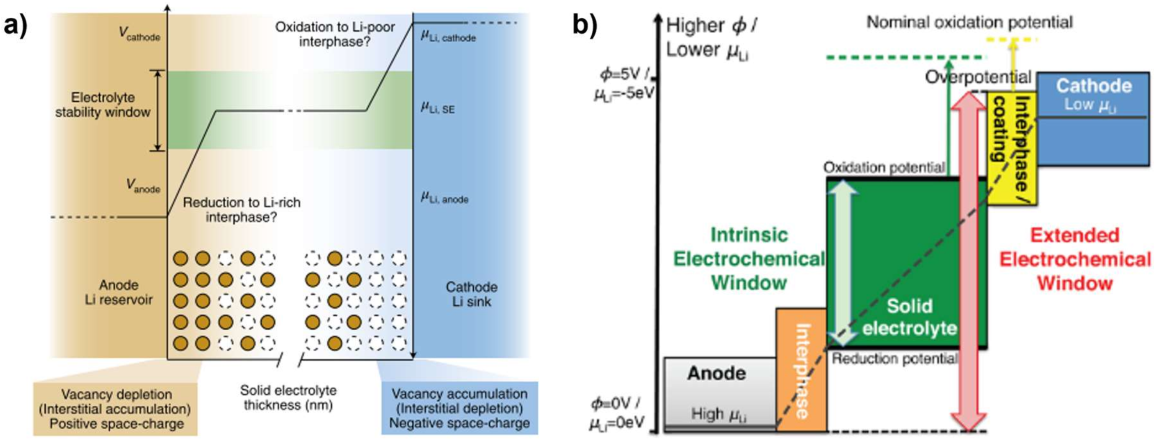

Fig. 2.7 a) Evolution of the chemical potential of Li μ_{Li} (right axis) and the corresponding electrode potentials (V, left axis) across the SSE in contact with anode and cathode. Accumulation and depletion of Li-ions (opposite of vacancy depletion and accumulation) form space-charge layers (comparable to double layer formation in liquid electrolytes) and concentration gradients, which can directly lead to decomposition of the SSE and/or reaction with the electrodes. Reprinted by permission from Springer Nature: Nature Materials, Famprikis et al.[6] (2019): © Springer Nature 2019.
b) Concept of accomplishment of an extended electrochemical window by the implementation of interlayers between SSE and electrodes. Reprinted from Zhu et al.[55] (open access article published under an ACS AuthorChoice License for free reuse in non-commercial publications).

A further electrochemically induced issue is the volume expansion and shrinkage of the cathode active material during Li-ion insertion and extraction, respectively. Layered active materials such as $LiCoO_2$ exhibit a volume change of 2 %, spinel active materials about 7 % (e.g., $LiMn_2O_4$) and olivine materials 5 % (e.g., $LiFePO_4$).[58] Here, the elasticity of the SSE is important. If the SSE material is too stiff, cracks will form at the interface of the cathode and SSE, so that the electrochemically active area is decreased and the charge-transfer inhibited.[1,6]

The combination of the ohmic resistances induced by the effective ionic and electrical conductivities interfered by cracks, pores and percolation efficiency and the area-specific resistances of the charge transfer depending on chemically and electrochemically interphase formation as well as cracks at the interface cathode and SSE results in the total device impedance (**Fig. 2.5**, Z_{SSB}).[6] The challenge is to minimize the discussed failure mechanisms, thus, to decrease the total device impedance in order to accomplish competitive ASSBs.

Bulk vs. Thin-Film Approach

The above-discussed requirements and failure mechanisms refer to the bulk ternary composite cathodes (**Fig. 2.8**). These bulk approach ASSBs are the target systems since they theoretically exhibit higher energy density and higher power density than thin-film solid-state batteries (TF-SSBs). The layer thickness of the ternary composite cathode depends on the requested cathode loading and is meant to be between 40 µm to 150 µm.[56] The layer thickness of the Li-metal anode depends on the cathode loading, however, because of the lower density and high specific capacity of Li-metal, it is less than half of the cathode thickness. The separator is also a SSE material and its thickness is supposed to be < 40 µm, depending on its capability to suppress dendrite growth.[56] The aspired manufacturing process is the roll-to-roll deposition of a particle slurry on a current collector followed by a sintering process. Then, the SSE separator is deposited and sintered. Finally, the Li-metal anode will be processed. In contrast, the TF-SSB is mainly manufactured by physical or chemical vapor deposition under vacuum (PVD & CVD), since layer thicknesses of less than 5 µm are requested.[47,49,56] The absence of electrically conductive additives and SSEs in the cathode layer limits the layer thickness, because of the low ionic and electrical conductivities of the cathode active material (**Fig. 2.3**). A breakthrough in TF-SSB research was made in the 1990s by the successful implementation of a lithium phosphorus oxynitride (LIPON) in a $LiCoO_2$|LIPON|Li-metal TF-SSB at the Oak Ridge National Laboratory.[59] After further research[60–62], these cells could be commercialized and have been used primarily for microelectronics, for instance, by direct fabrication on microchips.[47] In contrast, a ceramic bulk ASSB is still far from realization and further research has to be done. Especially, the densification of the ternary cathode composite by sintering is the major challenge in processing an ASSB.[1,6,56] The benefit of LIPON is that it is an amorphous and vitreous SSE, which is deposited by sputtering and does not require a further heating step afterward. However, considering oxidic and phosphatic SSEs (see next section), no sufficient bulk ASSB as well as TF-SSB could be demonstrated so far. Comprehensive summaries of the current ASSB lab-cells are given by Randau et al.[9] and Yang et al.[49]

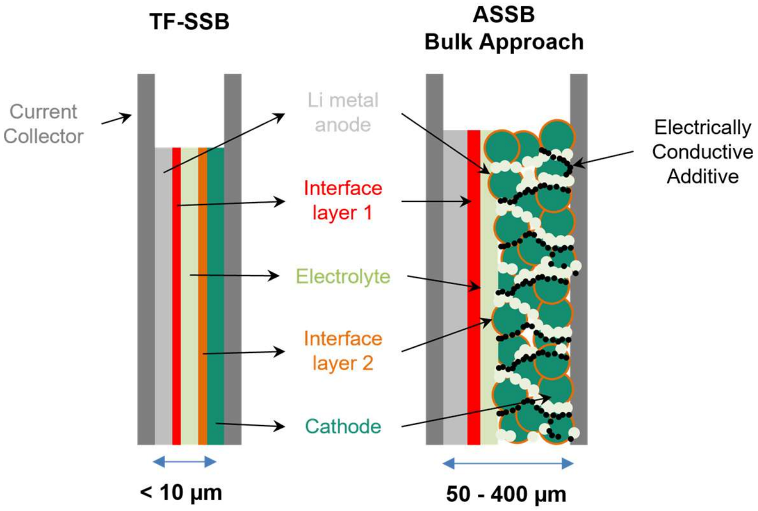

Fig. 2.8 Schemes of a thin-film solid-state battery (TF-SSB, left) and a bulk ASSB (right) including protecting interlayer (Interface layer) against electrochemical or chemical decomposition and intermixing. Given cell thicknesses are without current collectors.

Solid-State Electrolyte Materials | SSE Materials

SSEs can be categorized into organic and inorganic materials (**Table 2.2**). Inorganic SSEs can be differentiated into ceramic, crystalline SSEs and vitreous, amorphous SSEs. Some ceramic SSEs exhibit higher ionic conductivities than organic or amorphous SSEs, depending on the material class and modification of the crystal lattice by cation substitution. The main inorganic SSEs being investigated are sulfide-type (also thio-LISICON-type: Li super ionic conductors), NASICON-type (NASICON: Na super ionic conductors), perovskite-type and garnet-type materials (**Table 2.2**). The ion valency and size of the host structure elements significantly influence the Li-ion conductivity (**Fig. 2.9a**). Stronger interactions between host structure elements and Li-ions decrease the Li-ion diffusivity, thus, higher activation energies for Li-ion transport through the host structures are required. LISICON-like materials, for instance, are based on the crystalline lattice structure of γ-Li_3PO_4 (orthorhombic unit cell with $Pnma$ space group).[63] The substitution of O^{2-} with S^{2-} (Li_3PS_4, thio-LISICON) increases the ionic conductivity, as the S^{2-} exhibits a larger ionic size and a higher polarization capability, which results in large tunnels for Li-ion diffusion in the host structure and weaker interactions of Li^+ with S^{2-} than with O^{2-}.[49] Further optimization by cation substitution has resulted in the development of $Li_{10}GeP_2S_{12}$ (LGPS), which exhibits total ionic conductivities of up to 10^{-2} S/cm, thus, comparable with liquid electrolytes (**Fig. 2.9a**). Here, it is important to understand, that the total conductivity is limited by the grain boundaries in the polycrystalline structure. Thus, cation modification in the host structure has to enhance both the Li-ion transport in the host crystal lattice as well as at the grain boundaries, which are formed during the densification process. A further effect of the high polarization of S^{2-} is that it results in a higher ductility so that cold-pressing at temperatures below 80 °C is possible in order to manufacture ternary cathode composites. However, thio-LISICON materials have very small electrochemical windows

(**Fig. 2.9b**), which causes significant degradation during cell operation. Moreover, one side product of decomposition is the highly toxic H_2S gas, which can lead to significant safety hazards with cell malfunctioning.

Table 2.2 Summary of SSE materials. Reprinted by permission from Springer Nature: Nature Materials, Manthiram et al.[46] (2017): © Springer Nature 2017.

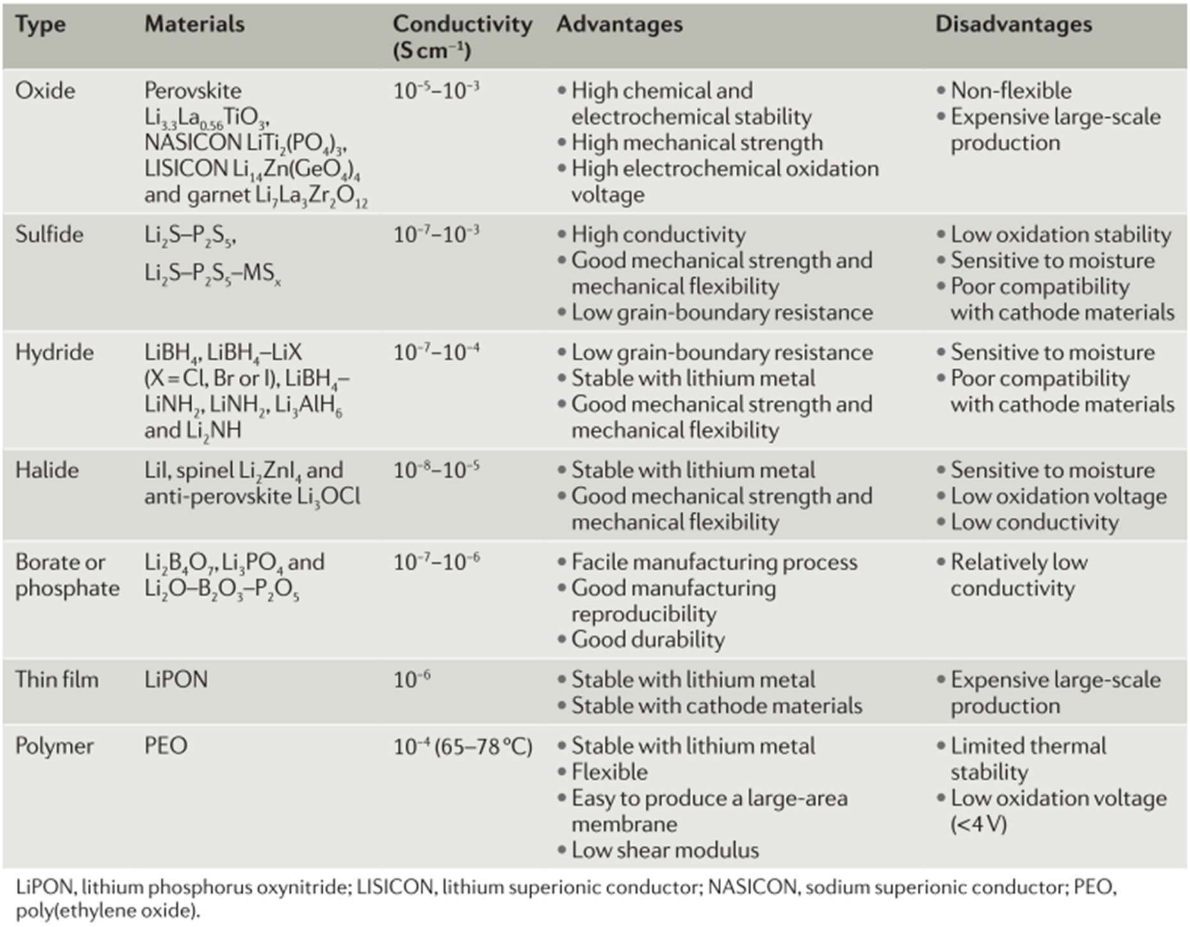

Type	Materials	Conductivity ($S\,cm^{-1}$)	Advantages	Disadvantages
Oxide	Perovskite $Li_{3.3}La_{0.56}TiO_3$, NASICON $LiTi_2(PO_4)_3$, LISICON $Li_{14}Zn(GeO_4)_4$ and garnet $Li_7La_3Zr_2O_{12}$	10^{-5}–10^{-3}	• High chemical and electrochemical stability • High mechanical strength • High electrochemical oxidation voltage	• Non-flexible • Expensive large-scale production
Sulfide	Li_2S–P_2S_5, Li_2S–P_2S_5–MS_x	10^{-7}–10^{-3}	• High conductivity • Good mechanical strength and mechanical flexibility • Low grain-boundary resistance	• Low oxidation stability • Sensitive to moisture • Poor compatibility with cathode materials
Hydride	$LiBH_4$, $LiBH_4$–LiX (X = Cl, Br or I), $LiBH_4$–$LiNH_2$, $LiNH_2$, Li_3AlH_6 and Li_2NH	10^{-7}–10^{-4}	• Low grain-boundary resistance • Stable with lithium metal • Good mechanical strength and mechanical flexibility	• Sensitive to moisture • Poor compatibility with cathode materials
Halide	LiI, spinel Li_2ZnI_4 and anti-perovskite Li_3OCl	10^{-8}–10^{-5}	• Stable with lithium metal • Good mechanical strength and mechanical flexibility	• Sensitive to moisture • Low oxidation voltage • Low conductivity
Borate or phosphate	$Li_2B_4O_7$, Li_3PO_4 and Li_2O–B_2O_3–P_2O_5	10^{-7}–10^{-6}	• Facile manufacturing process • Good manufacturing reproducibility • Good durability	• Relatively low conductivity
Thin film	LiPON	10^{-6}	• Stable with lithium metal • Stable with cathode materials	• Expensive large-scale production
Polymer	PEO	10^{-4} (65–78 °C)	• Stable with lithium metal • Flexible • Easy to produce a large-area membrane • Low shear modulus	• Limited thermal stability • Low oxidation voltage (<4 V)

LiPON, lithium phosphorus oxynitride; LISICON, lithium superionic conductor; NASICON, sodium superionic conductor; PEO, poly(ethylene oxide).

That is why phosphatic and oxidic SSEs are still of high interest since they exhibit a larger electrochemical window. Particularly, the tendency of oxidation is lower than for polymers and sulfides (**Fig. 2.9b**). One phosphatic and one oxidic candidate can be highlighted in this context: the NASICON-type SSE lithium aluminum titanium phosphate (LATP, $Li_{1+x}Al_xTi_{2-x}(PO_4)_3$) and the garnet-type SSE lithium lanthanum zirconium oxide (LLZO, $Li_7La_3Zr_2O_{12}$). LATP exhibits the highest intrinsic oxidation onset at 4.31 V vs. Li/Li^+ with a calculated decomposition energy of 0.03 eV/atom. In comparison, LGPS has an intrinsic oxidation onset of 2.15 V vs. Li/Li^+. The decomposition energy at this potential is 0.02 eV/atom but increases linearly to 1.12 eV/atom at 5 V vs. Li/Li^+. LATP exhibits a decomposition energy of 0.06 eV/atom at 5 V. This low decomposition energy might result in a high overpotential of the decomposition reaction so that a stable electrochemical window up to 5 V vs. Li/Li^+ is expected in practical operation (**Fig. 2.9b**, LATP, dashed lines). However, the drawback of LATP is its electrochemical instability against Li-metal. The reduction onset is at 2.16 V vs. Li/Li^+. It goes along with the reduction of Ti^{4+}, which causes electrical conduction. Consequently, the redox reaction continues until the short circuit of the cell occurs.[64] The perovskite-type SSEs, such as $Li_{3x}La_{2/3-x}TiO_3$ (LLTO), suffer from the same issue. On the contrary, LLZO can be considered electrochemically stable against Li-metal. Its calculated reduction onset is at 0.05 V vs. Li/Li+ along with the formation of an electrically isolating SEI and a low decomposition energy of 0.01 eV/atom. Consequently, LLZO is the most promising separator material in ASSBs. However, the oxidation onset is at 2.91 V vs. Li/Li^+ (0.01 eV/atom) going along with the formation of Li-ion blocking interphases. The calculated decomposition energy increases to a high value of 0.53 eV/atom at 5 V vs. Li/Li^+ so that high voltage cathode materials are difficult to realize. As discussed before, current research focuses on interlayer materials, which are meant to inhibit these decomposition processes.

The stronger interactions of the lattice elements in oxidic SSEs have also an impact on the mechanical strength of the material. The higher rigidity of these materials might result in a better inhibition of dendrite growth. However, it also leads to higher sintering temperatures of > 800 °C. Decomposition and intermixing are thermodynamic processes so that high temperatures accelerate these reactions, which makes oxidic materials difficult to integrate into ternary composite cathodes.

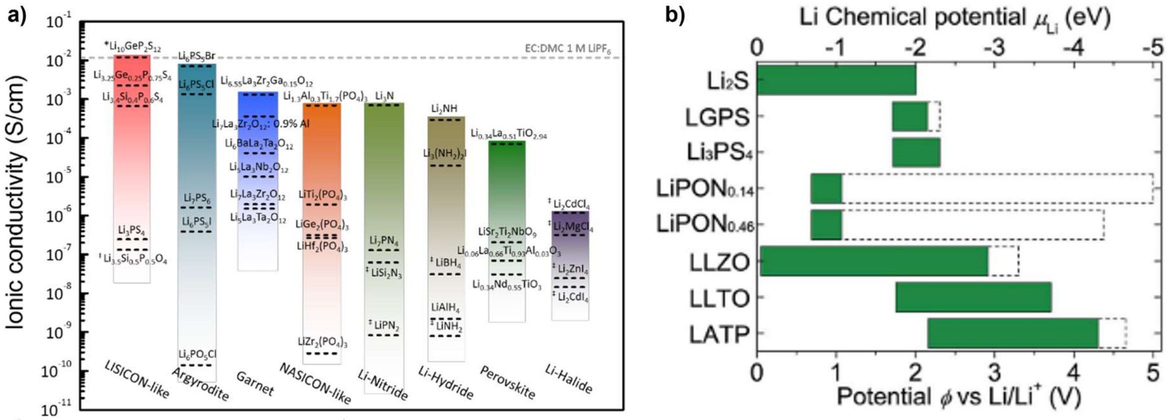

Fig. 2.9 a) Total ionic conductivities of the various SSE material classes. Ionic conductivity of a liquid electrolyte (EC:DMC, 1 M $LiPF_6$) marked with the dashed line. Reprinted with permission from Bachman et al.[63] (2016). © 2016 American Chemical Society.
b) Intrinsic electrochemical windows of various SSE materials. Dashed lined extension marks the potential to fully delithiate the SSE, which results in an acceleration of the decomposition process. Reprinted with permission from Zhu et al.[10] (2016). © 2016 The Royal Society of Chemistry.

Description of SSE Materials used in this Study

NASICON-type LATP

The general formula of a NASICON-type material is $LiM_2(PO_4)_3$ (M = Ti, Ge, Hf, Zr; **Fig. 2.9a**). It crystallizes in a rhombohedral structure (space group $R\overline{3}c$, **Fig. 2.10a**). MO_6 octahedrons and PO_4 tetrahedrons form the $M_2(PO_4)_3$ framework. The Li-ions are located between two MO_6 octahedrons on the M1-sites, with distorted octahedral coordination. Further Li-ions can be introduced in the M3-sites by substitution of M^{4+}, for instance, Ti^{4+}, with a lower valance element such as Al^{3+} leading to the formula $Li_{1+x}Al_xTi_{2-x}(PO_4)_3$ ($0 < x < 0.5$, LATP). M1-sites are located along the c-axis and M3-sites are perpendicular to the c-axis (**Fig. 2.10a**).[64–66] Their connection results in 3D tunnels for Li-ion diffusion. The three-dimensional Li-diffusion possibility increases significantly the probability of adequately aligned lattice planes of two grains at the grain boundaries. That explains the significant increase in the total ionic conductivity up to 10^{-3} S/cm of LATP in comparison to $LiTi_2(PO_4)_3$ (LTP) with conductivities of 10^{-7} S/cm to 10^{-5} S/cm (**Fig. 2.9a**).[64] That becomes clearer by considering the bulk conductivity, which is about 10^{-3} S/cm for LTP and by that comparable with LATP.[64,67,68] Consequently, the sintering ability is a crucial factor for ceramic SSEs. It could be shown that the use of sintering additives like Li_2O improves the density of the polycrystalline microstructure of LTP, which leads to an increase in the total conductivity up to 10^{-4} S/cm.[64,69,70] This means that the total ionic conductivity depends significantly on the sintering conditions and behavior. The purity of the initial powder, the density of the sintered sample as well as impurity phases can have an impact on the total conductivity so that various values can be found in the literature.[65] The ratio of Al in LATP has also an impact on the ionic conductivity. A ratio of Al of $0.4 \leq x \leq 0.5$ in LATP ($Li_{1+x}Al_xTi_{2-x}(PO_4)_3$) can lead to the formation of $AlPO_4$.[65,71] However, this impurity phase can have a positive effect on the ionic conductivity due to higher densification of the sintered sample. But at higher amounts of $AlPO_4$, the blocking characteristics for Li-ion diffusion leads to a reduction of the total ionic conductivity.[64,65,71] At an Al ratio of $x \leq 0.2$, a depletion of Li on the M3-sites could be observed at the grain surface, which decreases the grain boundary conductivity, thus, the total ionic conductivity of LATP.[71] It could be shown, that a compromise between these two effects could be found at $x = 0.3$. Crystalline LATP has a high sintering temperature starting at 900 °C, which makes it challenging to integrate LATP in ternary composites.[72,73] Besides the sintering of already crystalline LATP in a sintering furnace, many other preparation techniques such as microwave-assisted sintering, rapid annealing, etc. are reported in the literature.[65] Sintering duration, temperature and technique affect the polycrystalline microstructure in terms of grain size, density, cracks, etc., which all impact the total ionic conductivity.[73]

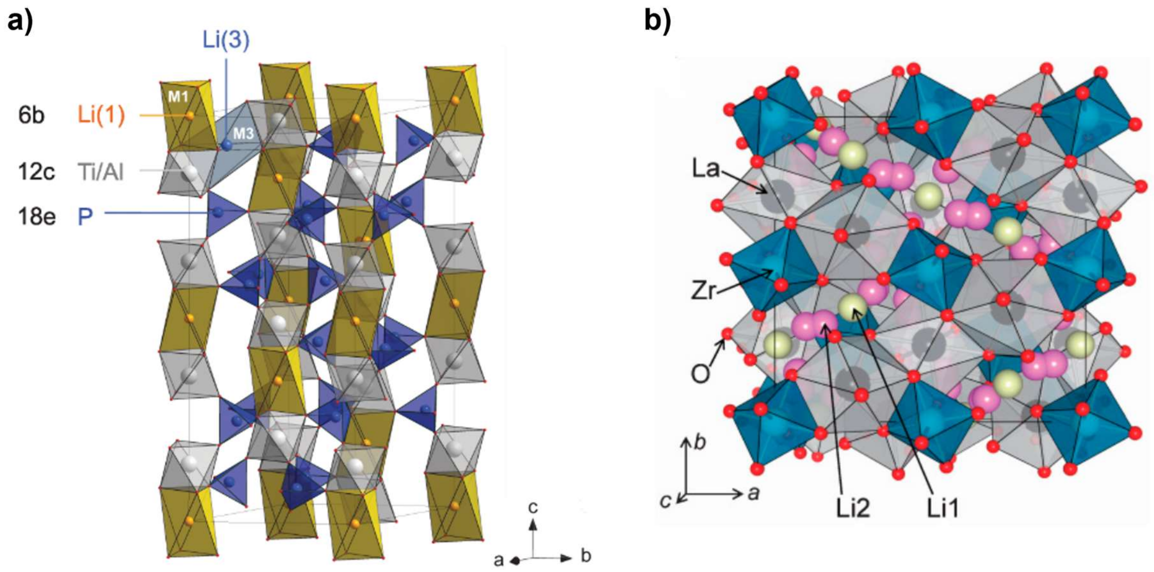

Fig. 2.10 a) Crystal lattice structure of rhombohedral LATP. Reprinted with permission from Epp et al.[66] (published under CC BY 3.0 license in Royal Society of Chemistry: *Phys. Chem. Chem. Phys.* 2015).
b) Crystal lattice structure of cubic LLZO. Reprinted with permission from Raju et al.[74] (published under CC BY license in MDPI: *electrochem* 2021).

Garnet-type Ga-LLZO

Garnet-type materials follow usually the formula $A_3B_3C_2O_{12}$, where A, B and C can be various cations. However, LLZO has the formula $Li_7La_3Zr_2O_{12}$ with 7 instead of 3 Li atoms. These structures are called Li-stuffed garnets, which can exhibit two different phases: a tetragonal phase (space group $I4_1/acd$) and a cubic phase (space group $Ia\overline{3}d$, **Fig. 2.10b**).[64,74] The structural framework of both phases consists of eightfold oxygen-coordinated La and sixfold oxygen-coordinated Zr. However, the Li distributions differ. In the tetragonal phase, Li-ions occupy the tetrahedral 8a and the octahedral 16f and 32g sites. In the cubic phase, Li-ions occupy two different sites: the tetrahedral 24d-sites and the octahedral 96h-sites (Li1 and Li2, respectively, in **Fig. 2.10b**).[74] Hereby, it appears that in the tetragonal phase all possible sites are occupied with Li atoms, whereas the cubic phase has still free sites or vacancies for Li-ion migration. Consequently, the ionic conductivity of tetragonal LLZO is 10^{-6} S/cm and significantly lower than that of cubic LLZO, which exhibits ionic conductivities in the order of 10^{-4} S/cm.[64,74,75] The transition appears due to heat treatment between 150 °C and 650 °C, depending on preparation and synthesis.[76,77] Since the tetragonal LLZO is thermodynamically more stable at room temperature, a stabilization of the cubic LLZO is required. This can be achieved by modification of the LLZO lattice with Al^{3+} and Ga^{3+}.[64,74,78] The stabilization effect improves the total ionic conductivity up to 3 E-3 S/cm, even though the Al and Ga substitute Li-atoms in the crystal lattice.[74] As discussed in the previous section, the total ionic conductivities in literature depend on the sintering technique and conditions since these determine the polycrystalline microstructure.[74] However, it could be shown that Ga-modification also improves the densification process.[64,74] The sintering temperatures of modified and unmodified

LLZO are about 1200 °C and higher than for LATP.[74] Ga-LLZO is used in this study as a thin-film (< 1 µm) and it was prepared by direct crystallization of a sputtered and amorphous film on top of the substrate in collaboration with and following the preparation of Sastre et al.[78,79] He could achieve total ionic conductivities of 1.91 E-4 S/cm for Ga-LLZO with a crystallization temperature of 700 °C in a dry oxygen atmosphere.[78] Dry oxygen atmosphere for sintering or crystallization is important since LLZO tends to undergo a Li^+/H^+ exchange in contact with adsorbed H_2O. Hydrogen goes into the LLZO lattice and the remaining LiOH can react to Li_2CO_3 in combination with CO_2. Both effects can reduce the grain boundary conductivity.[64,80,81] Another issue in LLZO synthesis is the possibility of Li_2O evaporation, which can result in non-conductive impurity phases such as $La_2Zr_2O_7$. That's why a proper amount of excess Li must be provided during sintering and synthesis.[64,74,78,79]

Vitreous LIPON

LIPON is an amorphous and vitreous SSE. The term LIPON concludes all compounds regarding the formula $Li_xPO_yN_z$.[49,82] Its preparation is usually done by magnetron sputtering of a Li_3PO_4 target in combination with a reactive N_2 gas. Subsequent heat treatment is not required. Stoichiometry has an impact on the ionic conductivity. The Li-ion conductivity increases by the incorporation of N due to the substitution of O in the phosphate structure.[51,82,83] The strong bonding between N and P causes weaker interactions with Li^+ and enhances the ionic conductivity.[84] However, the reported ionic conductivities are in the order of 10^{-6} S/cm, thus by a factor of 100 to 1,000 lower than LATP and LLZO.[49,51] The highest ionic conductivity, reported by Suzuki et al.[85], is 6.4 E-6 S/cm. It could be achieved by sputtering with an additional Li_2O target, thus a high Li amount in the LIPON thin-film. The low ionic conductivity and the preparation via vapor deposition techniques make LIPON solely feasible in TF-SSBs. The major advantage of LIPON is the large electrochemical window.[10,83] In contact with Li-metal, LIPON forms a protective SEI layer consisting of Li_3PO_4, Li_3P, Li_3N and Li_2O, which is Li-conductive but electrically isolating, so that a stabilization of the interface can be achieved.[10,82] On the cathodes side, the computational calculations of Zhu et al.[10] show an oxidation onset at 1.07 V vs. Li/Li^+ but a neglectable decomposition energy for that oxidation. By that, the electrochemical window is extended up to 5 V vs. Li/Li^+ (**Fig. 2.9b**). This could be confirmed by electrochemical experiments, where a limit of 5.5 V vs. Li/Li^+ was determined.[83] Moreover, Li et al.[52] demonstrated in a remarkable study about a $LiNi_{0.5}Mn_{1.5}O_4$|LIPON|Li TF-SSB cell the oxidation stability of LIPON in combination with high voltage active materials. As discussed before, the average voltage potential of $LiNi_{0.5}Mn_{1.5}O_4$ is about 4.7 V vs. Li/Li^+. The realized TF-SSB showed a cycle life of over 10,000 cycles with a capacity retention of 90.6 % and coulombic efficiency of almost 100 %.[52]

2.3 Sintering, Liquid Phase Sintering and Microstructure

Solid Phase Sintering

Sintering describes the solidification of a ceramic powder during heat treatment. To obtain the wished shape of the ceramic component, ceramic powder is pressed into green bodies, which exhibit a porosity of ca. 30 - 40 %. During a sintering process, the green body undergoes a densification process via diffusion and mass transport between the particles. The relative density, which is inverse to the porosity (relative density = 1 - porosity), of the ceramic component increases during sintering and the microstructure undergoes significant changes, which can be differentiated into three sintering stages with different dominating mechanisms (**Fig. 2.11**). The driving force for sintering is the reduction of the Gibbs free energy by reduction of the surface energy of the particles and later the interface energy of grains in contact. This goes along with the growth of the grains due to mass transport and so the decrease of the surface area.[86–89]

In the first sintering stage, a particle rearrangement takes place, whereby the particles form a closed packing and get in contact with each other. At the contact points, surface diffusion, volume diffusion and interface diffusion of the lattice elements result in the formation of sinter necks between the particles. This is the start of grain boundary formation. Densification and grain growth do not happen in this stage and the microstructure has still a high porosity. The grain size distribution is still in the range of the particle size distribution of the starting powder. The component is still fragile. The SEM image in **Fig. 2.11** (at the bottom) shows such a microstructure in the first sintering stage.[86–89]

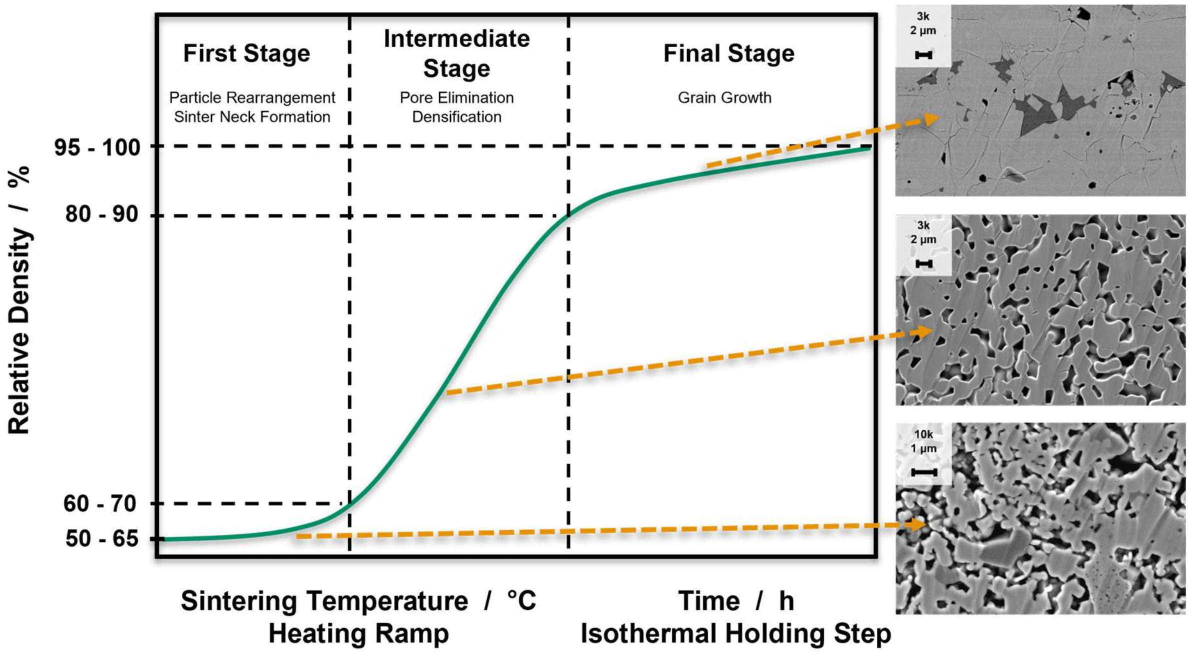

Fig. 2.11 Curve of relative density during the sintering process consisting of the heating ramp and subsequent isothermal holding step at maximum temperature.[86] SEM images represent microstructures of the three sintering stages. Three SEM images, which demonstrate appropriately the sintering stages, are chosen carefully from **Chapter 5**.

In the intermediate sintering stage, ongoing mass transport causes the densification. This goes along with pore elimination and shrinkage of the ceramic component. Particle growth already occurs. Sinter necks transform to broader grain boundaries separating grains with different grain lattice orientations. The middle SEM image in **Fig. 2.11** shows a microstructure in the middle of the intermediate stage. The grains already grow to 4 - 8 μm and have pronounced grain boundaries. The porosity is still high and is characterized by open pore channels through the component. The end of the intermediate stage is defined as the end of significant densification at porosities between 10 % and 20 % (**Fig. 2.11**).[86–89]

In the final sintering stage, grain growth is the dominating process. Larger grains grow by assimilating smaller grains, which is also called Ostwald ripening. This often leads to microstructures of large grains surrounded by smaller ones. Since pore elimination is almost finished, further densification is a side effect of the grain growth leading to rest porosities between 0 % and 5 % consisting of mainly closed pores. The upper SEM image in **Fig. 2.11** shows such a microstructure. Linear and broad grain boundaries are connecting the single grains with grain sizes of 5 - 15 μm. However, excessive grain growth can also lead to pore and crack formation due to internal stresses through the microstructure.[86–89]

Grain growth is kinetically dependent on the sintering temperature. To avoid intensive grain growth and crack formation, the sintering process is usually controlled by introducing an isothermal holding step after the heating ramp slightly above the transition point between the intermediate stage and the final stage. By controlling the final sintering temperature and the holding step duration as well as the initial particle size distribution, highly dense ceramic components with fewer cracks and pores can be obtained. Furthermore, the grain size distribution and grain boundaries can be adjusted very precisely.[86–89]

Liquid Phase Sintering

By adding small amounts of a sintering additive with a lower melting temperature than the sintering temperature of the host material, the densification process can be accelerated due to liquid phase sintering. The main difference is the mass transport through the melted liquid phase. Instead of a solid phase diffusion during solid phase sintering, the elements of the particles dissolute in the melted phase, which accelerates the diffusion process and lowers the starting temperature for mass transport, thus, the sintering temperature. In addition to the driving forces of surface energy reduction and interface energy reduction, a difference in chemical potential between additive and host material benefits the dissolution and also leads to precipitation and sinter neck formation in the first sintering stage. Chemically similar additives should be chosen to minimize the probability of mixed phase formation or phase reformation as well as to facilitate the dissolution of the host material elements. The liquid phase sintering process can also be described by the three sintering stages but exhibit small differences due to the melted phase.[86–89]

The first sintering stage starts with the melting of the additive. The liquid phase wet the particle surfaces of the host material. The capillary forces accelerate the particle rearrangements. Menisci are formed at the contact areas of neighboring particles, which supports the sinter neck formation.[86–89]

The intermediate sintering stage is dominated by the mass transport process, thus, dissolution and precipitation, which leads also to densification, pore elimination and shrinkage. Grain growth and the formation of grain boundaries take place, however, the lack of space due to the additive as well as locally occurring equilibria of the chemical potentials between the liquid phase and host material hinder the grain growth. The grains start to form a three-dimensional solid phase skeleton connected by grain boundaries and the liquid phase starts to accumulate in the pores.[86–89]

In the final sintering stage, grain growth is again the dominating process. Grain boundaries are already formed and the liquid phase is accumulated at the triple-points of the grains so that the grain growth is mainly supported by the solid phase diffusion process through grain boundaries. The sintering additive can prevent intensive grain growth, as it simply occupies the space in the pores. The internal stresses, which arise from the interaction of missing space and forced grain growth can result in crack and pore formation. These formations can also occur during the cooling process, when the sintering additive and host material exhibit different thermal expansion coefficients.[86–89]

In conclusion, sintering additives, which initiate liquid phase sintering, reduce the sintering temperature of the host material as well as give new possibilities to control the microstructure development.

2.4 Interdiffusion, Intermixing and Decomposition of Composites

Composites are multi-component systems consisting of various materials. In the case of ceramic and/or metallic composites, these materials differ in elemental composition and lattice structure. Heat treatment is the primary manufacturing process to obtain dense composites. In accordance with sintering, the initial components tend to reduce the Gibbs free energy of the system by reduction of the surface and interface energies. However, in multi-component systems, further possibilities to reduce the Gibbs free energy are given: interdiffusion, intermixing and decomposition. Hereby, the components change their composition and structure. The additional driving forces of these processes are the decrease in volume V of the crystal phases due to phase transformation to denser crystal structures, the increase in entropy S (e.g., gas evolution) and the balancing of the chemical potentials μ_i of the elemental species i by diffusion processes, so that the differential form of the Gibbs equation is given by:[90–94]

$$\delta G = V\delta P + \sum \mu_i \delta n_i - S\delta T \qquad \textbf{Eq. 2.16}$$

where V is the volume, which changes correlate with changes in the pressure p within the system. The change of the number of moles n_i of element i occurs during heat treatment due to diffusion processes along the concentration gradients between the different components of the composite until equilibrium conditions are reached. Consequently, diffusion mechanisms and reaction kinetics are the defining processes describing whether interdiffusion, intermixing or decomposition takes place. These processes are temperature-dependent and can occur in parallel during the heat treatment of the multi-component composite manufacturing. If the initial materials maintain without phase and composition changes during the heating process, the material combination is called chemically or thermally stable.[90,91]

Interdiffusion

Considering two ceramic or metallic materials with different elemental compositions in contact, interdiffusion processes can occur during heat-treatment in order to reach an equilibrium state for the chemical potentials. Hereby, elements of one material diffuse along concentration gradients in the other material and vice versa, whereby the compositions of the host structures are changed. The lattice structure is not changed so that the impurity elements occupy interstitial sites of the host material or substitution of elements in the host structure occurs. The latter can be described as substitutional solid solutions and the probability of interdiffusion can be estimated by means of the Hume-Rothery rules:[90]

1. Size factor: The difference in the ionic radii of the diffusing elements should be < 15 %. If the difference is higher, either the diffusion does not take place or the substitution of a host structure element results in the transformation of the crystal lattice.
2. Valance factor: This is mainly important for ceramic materials due to the required electroneutrality of the cation- and anion-based crystal structure. To maintain

electroneutrality, the substituting element requires the same oxidation state as the element in the host structure.

3. Chemical affinity: It describes the tendency of two chemical species to form a new compound or mixed phase. If it is thermodynamically more favorable to form a new phase by changes in composition and crystal lattice, interdiffusion will stop and phase transition and reaction occur.
4. Structure type: The more similar the lattice structures of the two components are the greater the solubility of the interdiffusing elements.

These rules are true for metallic and ceramic materials except for the valence factor. In metallic materials, the Hume-Rothery rules are one part to describe the alloy formation. However, if saturation of the solubility is reached or the rules cannot be followed, the material combination remains chemically stable or intermixing and decomposition takes place.[90,91]

Intermixing and Decomposition

Intermixing occurs due to chemical reactions at the phase boundaries of two different materials. Hereby, the elements of both materials form a new mixed phase with different composition and crystal lattice than the initial components. Diffusion of the reacting elements from the bulk material to the phase boundary takes place along the concentration gradient. If interdiffusion does not occur and the new mixed phase is thermodynamically more favorable than maintaining the initial crystal phases (**Eq. 2.16**), the reaction takes place by forming a new crystal phase differing in the crystal lattice structure and composition. This can be supported by gas evolution, which increases significantly the entropy of the system and lowers the Gibbs free energy. Considering oxidic ceramics, oxygen release is mostly observed, which also allows the reduction of the host structure elements.[90,91]

Oxygen evolution is also the main process of the intrinsic decomposition of an oxidic initial material. Hereby, one initial component starts to degrade by losing oxygen anions in the host structure and the accompanying reduction of the cations. This results in the transition of the crystal structure of the host material. The increase in entropy and the formation of thermodynamically more stable phases are the driving forces of decomposition processes (**Eq. 2.16**).[90–94]

2.5 Ion Diffusion and Ionic Conductivity in Ceramics

As introduced in **Chapter 2.2**, the ion conduction in ceramic SSEs can be distinguished in the ion diffusion through the crystal lattices of the grains and additionally through the polycrystalline microstructure by overcoming grain boundaries (**Fig. 2.5**). On the atomic scale, the Li-ion diffusion depends on the number of defect sites in the crystal lattice. On a micro-scale, the nature of the grain boundaries is the limiting characteristic for Li-ion conduction.

Ion Diffusion through a Crystal Lattice

Point defects such as vacancies and interstitials in the crystal lattice of the ceramic material enable ion diffusion. Considering a perfect crystal lattice, in which every atom is located in the correct position in the host structure, the space between the atoms is called interstice. If an atom of the host structure occupies an interstice, then the atom is interstitial and it left behind a vacancy in the host structure because of electroneutrality. This point defect is called the Frenkel defect. If a cation and an anion (with the same charge to maintain electroneutrality) are missing in the host structure, two vacancies are formed, which is called a Schottky defect. Along these defect sites, the diffusion of the ions of the material can occur, which is the basis of the mass transport during sintering, interdiffusion or intermixing as well as for the Li-ion conductivity of SSEs. The number of defects n_d is crucial for the diffusion process and it is thermally activated:[90,95]

$$n_d = n_0 exp\left(-\frac{E_d}{2k_BT}\right) \qquad \textbf{Eq. 2.17}$$

where n_0 is the possible number of defects, k_B is the Boltzmann constant and E_d is the energy required to form a point defect. In addition to E_d, a further potential barrier E_m must be overcome for ion migration, which can be described as a jump between two energetic minima of the ion in the crystal lattice (**Fig. 2.12**). The so-called jump frequency υ defines the diffusivity D:[90]

$$D = \vartheta l^2 \upsilon = \vartheta l^2 \upsilon_0 exp\left(-\frac{E_m}{k_BT}\right) \qquad \textbf{Eq. 2.18}$$

where ϑ is a geometric factor depending on the crystal structure and l is the jump length between the two minima. The ionic conductivity σ_b can finally be described by the charge q, the number of defect sites available for ion diffusion n_d and its ionic mobility ξ, which is defined by the Nernst-Einstein relation:[15,90,96]

$$\xi = \frac{qD}{k_BT} \qquad \textbf{Eq. 2.19}$$

$$\sigma_b = q\xi n_d = \frac{\vartheta q^2 l^2 \upsilon_0 n_0}{k_BT} exp\left(-\frac{E_m + E_d/2}{k_BT}\right) = \frac{A}{T} exp\left(-\frac{E_{a,b}}{k_BT}\right) \qquad \textbf{Eq. 2.20}$$

Consequently, the ionic conductivity σ_b through the crystal lattice, which is also called bulk conductivity, exhibits an Arrhenius behavior and its activation energy $E_{a,b}$ consists of the formation of a point defect E_d and the ion hopping from one minimum to another E_m. The formation energies of Frenkel or Schottky defects depend on the crystal host structure and composition so that in some structures Frenkel defects are favored and in others Schottky defects.[90] In general, the interstitial movement has a lower activation energy for the ion hopping, since no vacancy movement takes part in the conduction process. That's why the transport mechanism of Li-ions in highly conductive SSEs is mainly along the interstitial sites of the host structure enabled by the small ionic radius and low charge of Li^+.[15]

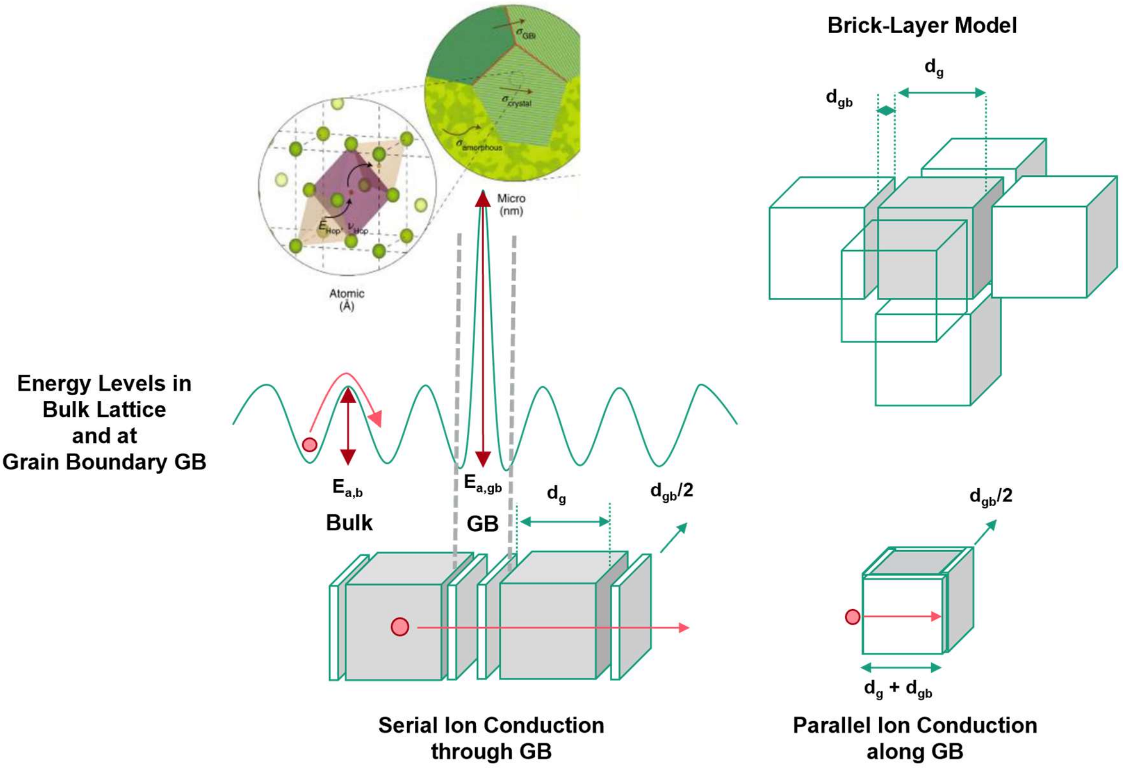

Fig. 2.12 Ion conduction through crystal lattice and grain boundaries (GB) including simplified energy levels and activation energies $E_{a,b}$ and $E_{a,gb}$ for ion hopping within the crystal lattice and over grain boundaries, respectively. Brick-Layer model for ion conduction representing grains with thickness d_g and grain boundaries with thickness d_{gb}. Serial conduction through grains and grain boundaries on the right bottom. Parallel conduction along grain boundaries on the left bottom. Adapted from E. Barsoukov and J. R. Macdonald: Impedance Spectroscopy (2005, 2nd ed., Wiley-Interscience).[97]

Ion Diffusion through a Polycrystalline Material / Brick-Layer Model

On a microscopic scale, ceramic SSEs exhibit polycrystalline microstructures with grains of various lattice orientations. At the contact area of two grains, grain boundaries are formed, at which the two lattices meet under a particular angle. Low-angle to high-angle grain boundaries are described in the literature.[86] Low-angle grain boundaries exhibit a better alignment of two neighboring grain lattices, thus, they have a lower grain boundary energy than high-angle grain boundaries.[86] The degree of misalignment affects the grain boundary activation energy $E_{a,gb}$ for Li-ion transfer from one grain to another (**Fig. 2.12**).[98] Consequently, the Li-ion conduction through grain boundaries has a higher activation energy than the bulk conduction (**Fig. 2.12**), thus, the grain boundary conductivity σ_{gb} is lower than the bulk conductivity σ_b. The angle between two grain lattice orientations also affects the thickness of the grain boundary regime. High-angle grain boundaries usually form a thicker grain boundary region defined by a high number of dislocations and defects. A sufficient thick grain boundary regime can result in a further ion conduction process along the grain boundaries instead of through the grain boundaries.[86,97,98]

A theoretical approach to describe the ion conduction in parallel with and through the grain boundaries is the Brick-Layer model (**Fig. 2.12**).[97] It has been used for computationally calculations of the grain boundary processes in literature.[99–108] Grains are assumed as cubes (Bricks, **Fig. 2.12**) with grain thickness d_g and grain boundaries are seen as separate layers between these cubes with thickness d_{gb}. Bouchet et al.[99], for instance, used this model to calculate the parallel and perpendicular ion conduction by varying the d_{gb}/d_g ratio and alternating the ionic conductivities. The results have shown, that the ionic conductivity parallel to grain boundaries increases by smaller grain thicknesses d_g. These results might explain unexpected observations, such as the constant ionic conductivities despite the increase of the amount of non-conductive B_2O_3 in nanocrystalline Li_2O:B_2O_3 composites, as a high degree of conduction goes along the grain boundaries.[109]

However, the exact processes within the microstructure of real SSEs are difficult to distinguish in experimental set-ups. Additionally, it must be considered that both processes take place at the same time and the measured value for the grain boundary conductivity is an average of parallel and perpendicular ion conduction. However, the Li-ion conduction in ceramic SSEs is assumed to be through grain boundaries, because of the usually large grains compared with the much smaller grain boundary regions.[15,96,97,99] That’s why, in the analysis of impedance spectroscopic measurements, serial ion conduction is used as the basis for the consideration of equivalent circuits.[96,97] Hereby, the Brick-Layer model helps to illustrate the conduction process and to deduce the exact equivalent circuit, which will be explained in more detail in **Chapter 3.4**.

3 Instruments and Methods

3.1 X-Ray Diffraction | XRD

Theoretical Background

X-ray diffraction (XRD) is a method to investigate the nature and type of crystal lattices of crystalline materials. X-rays are diffracted at the lattice planes of the crystal lattice, as their wavelength is in the range of the atomic distances (order of 1 Å). The periodicity of the atoms in a crystal lattice results in many periodically ordered scattering centers. The scattered electromagnetic X-ray waves can interfere constructively or destructively. The constructive interfered waves can be detected and so give information about the lattice nature. The requirements for constructive interference can be deduced by means of the consideration of Bragg, who described the diffraction of X-rays at lattice planes (**Fig. 3.1a**). The incident X-rays with wavelength λ got multiply diffracted at a set of equal lattice planes defined by the Miller's indices (h k l) and with spacing distance d_{hkl}. If the path difference of the scattered waves is equal to an integer multiple n of the wavelength λ, the requirement of constructive interference is given. This happens only at particular angles θ and also depends on the lattice plane spacing d_{hkl}, which leads to Bragg's law:[110–112]

$$n\lambda = 2d_{hkl}\sin(\theta) \qquad \textbf{Eq. 3.1}$$

The many differently orientated lattice planes (**Fig. 3.1b**) of the crystal lattice result in various diffraction angles so that a material-specific diffraction pattern can be obtained by scanning through a spectrum of incident angles and detecting the constructively interfered waves. Such a diffraction pattern is shown for the spinel $LiMn_2O_4$ in **Fig. 3.1c.** The lattice planes depend on the lattice structure and their spacing distance d_{hkl} depends on the positions and distances of the atoms in the unit cell as well as the Miller's indices. Consequently, different crystal lattices and crystal compositions cause different diffraction patterns, so that material classes can be distinguished and information about the crystal lattice can be obtained.[110–112]

The intensities and shapes of the detected reflections I_{hkl} depend additionally on the crystal composition:[110–114]

$$I_{hkl} = s \cdot |F_{hkl}|^2 \cdot M_{hkl} \cdot P_{hkl} \cdot A_{hkl} \cdot LP \cdot \Pi(\theta) + \gamma_B \qquad \textbf{Eq. 3.2}$$

where s is a scaling factor depending on measurement time and phase fraction regarding composites; F_{hkl} is a structure factor; M_{hkl} is a multiplicity factor; P_{hkl} describes a preferred orientation function; A_{hkl} is an absorption factor; LP is a factor for the Lorentz-polarization; $\Pi(\theta)$ is called the reflection profile function corresponding to the impact of the measurement set-up and γ_B takes the background of the measurement into account.[110–114]

The structure factor F_{hkl} describes the sum of all electromagnetic waves diffracted by all unit cell's atoms for a set of lattice planes defined by the Miller's indices. It includes also an atomic form factor, which is element-specific so that different compositions can be distinguished by XRD.[110–112]

The multiplicity factor M_{hkl} takes the symmetrically equivalent lattice planes into account. For instance, the lattice plane (0 0 1) is equal to (0 1 0) and (1 0 0) so that their reflections overlap.[110–112]

The preferred orientation function P_K considers ununiform crystals, such as needles or platelets, which exhibit mostly a deviation from a random particle distribution due to agglomeration in a preferred direction (e.g., side by side along the length for needles).[110–112,115]

The absorption coefficient A_{hkl} is also element-specific and additionally a function of crystallite size. It describes the amount of not absorbed radiation due to the material.[110–112]

The Lorentz-factor LP results from the dispersion of the wavelength of the incident beam partly depending on the geometry of the measuring device as well as the partial polarization of the scattered radiation.[110–114]

The reflection profile function $\Pi(\theta)$ summarizes all device-specific impacts including X-ray distribution of the source or irregularities along the beam path etc. The reflection profile function can easily be determined by measuring a standard reference, such as LaB_6 with very defined sample properties.[110–114]

The background intensity γ_B of the measurement is caused by diffuse scattering of the source beam at the surface or edges of the sample. [110–114]

In conclusion, the angle of the reflection as well as its intensity is material-specific and depends on the crystal structure and composition. Measured diffractograms can be compared with databases so that quality management of synthesis (impurity phases, crystallinity) is possible or the composition of composites can be determined. The latter is supported by the Rietveld analysis.

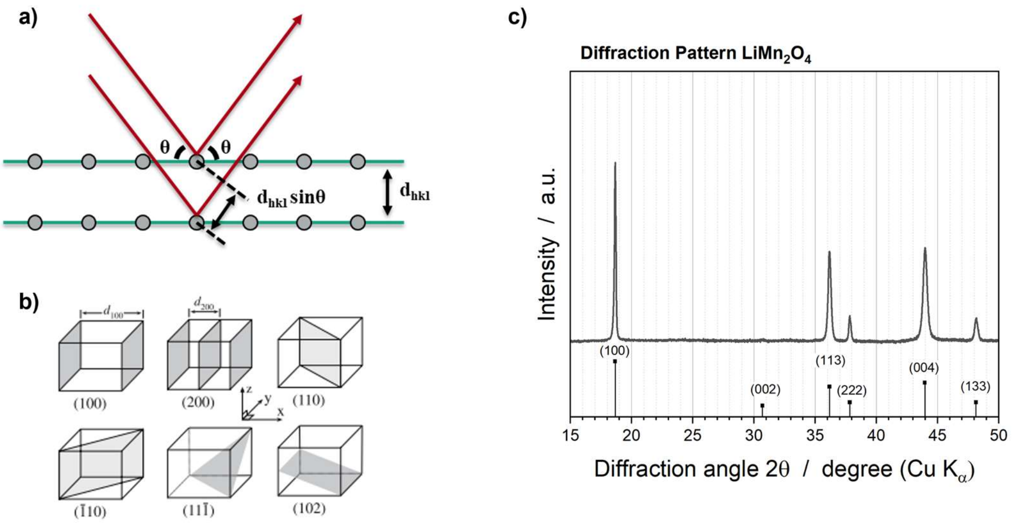

Fig. 3.1 a) Diffraction of X-rays at lattice planes of a unit cell. **b)** Various orientations for lattice planes adapted from Carter and Norton (2007).[90] **c)** X-ray diffraction pattern of $LiMn_2O_4$ (ICSD 85398).

Rietveld Refinement and Quantification of Phase Fractions in Composites

Rietveld refinement is a method to fit the diffraction pattern and by that material-specific parameters such as unit cell dimensions and volumes, crystal structures or the compositions of composites can be determined in a very precise manner. Structural models based on the knowledge of crystal structure, lattice parameters, atomic position, etc. are used to calculate a theoretical diffractogram following **Eq. 3.2** as a function of θ, which includes all crystal lattice information. By refining the fit by means of the measured diffractogram, the structural parameters of the sample can be accurately determined.[110–119]

The obtained structural parameters can be used to quantify the phase fractions of various phases in crystalline multi-component composites. If all phase compositions are known, the Rietveld refinement leads to a precise fit of the diffraction data and the phase fraction of every single existing phase w_p can be calculated by:[114]

$$w_p = \frac{s_P Z_P M_P V_P}{\sum_i s_i Z_i M_i V_i} \qquad \textbf{Eq. 3.3}$$

where s_p is the scaling factor of the phase p; Z_p is the number of formula units per unit cell of phase p; M_P is the molar mass per formula unit of phase p and V_P is the unit cell volume of phase p. The product of these parameters divided by the sum of all existing phases i results in the phase fraction w_p.[110–119]

XRD Set-Up

Two XRD geometries are used in this study (**Fig. 3.2**). The Bragg-Brentano geometry defined by a moveable X-ray source and detector is usually used for powder samples. The incident and scattered angle are equal to θ. The grazing-incidence geometry (GIXRD) is used to measure thin-films with thicknesses in the nm and µm range. A low fixed incidence angle γ of < 5° is chosen to increase the intensity of the thin-film reflections, as the penetration depth is minimized avoiding high intensities of the substrate as well as a larger cross-sectional sample area is measured, which increases the thin-film signal.[110–112]

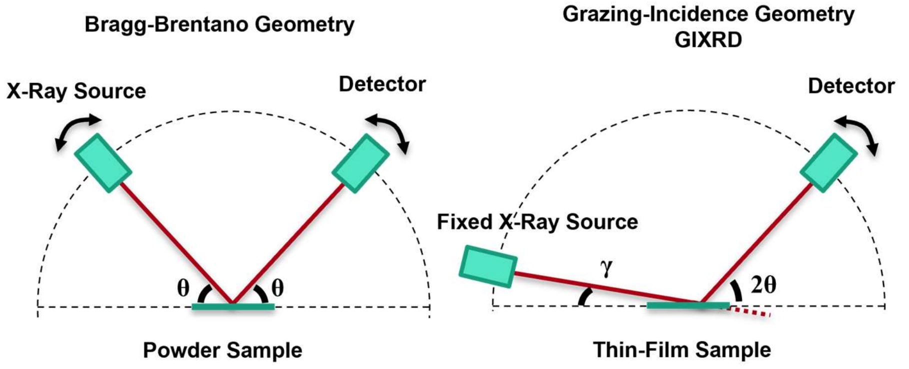

Fig. 3.2 Bragg-Brentano Geometry usually used for powder samples as well as grazing-incidence geometry with fixed incidence angle γ for thin-film samples.

3.2 Thermal-Optical Measurement Device | TOM

Thermal-optical measurement devices (TOM) are an effective technique to determine in-situ the development of shrinkage and thermal diffusivity of a pressed sample pellet of a powder during sintering. The TOM device used in this study has been developed by the group of F. Raether[120–124], from whom a detailed description was published in 1998 (Raether et al.[120]). The TOM set-up consists of an optical dilatometer, a CO_2 laser and pyrometer and a furnace (**Fig. 3.3a**).

The sample pellet is placed in the furnace and various temperature-programs can be performed in various atmospheres. The shrinkage of the pellet can be observed by means of a CCD camera and a halogen lamp, which illuminates the sample (**Fig. 3.3b**). According to **Chapter 2.3**, shrinkage is a measure of the pore elimination during sintering so that an in-situ determination of the sintering process can be obtained. [120–124]

The heat flow through the sample can be determined by a laser-flash technique. A CO_2 laser is used to generate a short laser pulse, which heats the front site of the pellet. A pyrometer measures the delayed temperature change at the back site of the pellet (**Fig. 3.3a**). The increase in surface temperature is only about 1 K and the pulse duration is about 100 ms to 500 ms so that it has no significant impact on the sintering processes.[120,121,125] However, the temperature change during the heating ramp superposes the laser-flash signal, which is considered in the computational analysis of the signal. This together with the delayed increase in temperature at the backside of the pellet and the sample thickness, obtained from the dilatometer measurement, is used to determine the thermal diffusivity of the sample.[125] The course of the thermal diffusivity is a measure of the sintering stage of the sample since the heat flow is benefited by sinter necks and more grain-to-grain contacts due to pore elimination and formation of grain boundaries.[120–122,125]

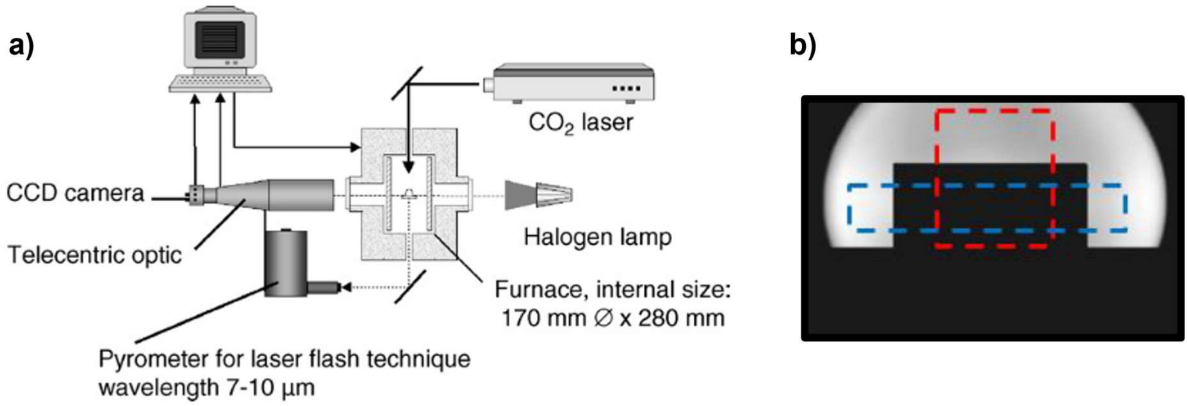

Fig. 3.3 a) Set-up of a thermal-optical measurement device. Reprinted by permission from Elsevier: Journal of European Ceramic Society, Baber et al.[121] (2007) © Elsevier 2007. **b)** Determination of shrinkage of sample pellet by means of the CCD camera.

3.3 Time-of-Flight Secondary Ion Mass Spectroscopy | ToF-SIMS

Time-of-flight secondary ion mass spectroscopy (ToF-SIMS) is a surface-sensitive method to analyze the elemental composition of a few monolayers at the surface of a flat sample. Ultrahigh vacuum systems are required. A scheme of the ToF-SIMS set-up is shown in **Fig. 3.4a**. A pulsed analyzing ion beam (primary ion beam) is used to remove secondary ions from the surface of the sample. These secondary ions are electrostatically accelerated into a time-of-flight mass spectrometer. The accelerated secondary ions enter a field-free drift region with a particular kinetic energy. Lighter ions will have a higher velocity than heavier ions so that the lighter ions reach the detector faster than the heavier ions, by which an elemental differentiation by mass and charge of the secondary ion can be obtained.[126–129]

Compositional depth profiles of the sample can be obtained by using a further ion source for sputtering between the analysis pulses (**Fig. 3.4a**). The benefit of the second ion beam is that it can be optimized for sputtering with respect to low energy and high dose for high spatial resolution. Cs^+, O_2^+ or Ar^+ are often used for sputtering. Whereas, Bi^+, Au^+ or Ga^+ ion beams with high energy and low dose for high mass resolution are used for analysis. Additionally, the sputtering area should be larger than the measuring area (**Fig. 3.4b**) in order to avoid edge effects. After each sputtering step and before the pulsed analysis beam is performed, an electron flood gun is used to provide charge neutralization of the surface (**Fig. 3.4a**).[126–129]

Compositional depth profiles are usually plotted as a function of sputtering time. The exact sputter depth in nanometers can be calculated by the knowledge of the sputter yield of the material in combination with the characteristics of the used ion beam. Multilayer systems of various materials exhibit different sputter yields for each material layer so that a determination of the sputter depth is more complicated.[126–129]

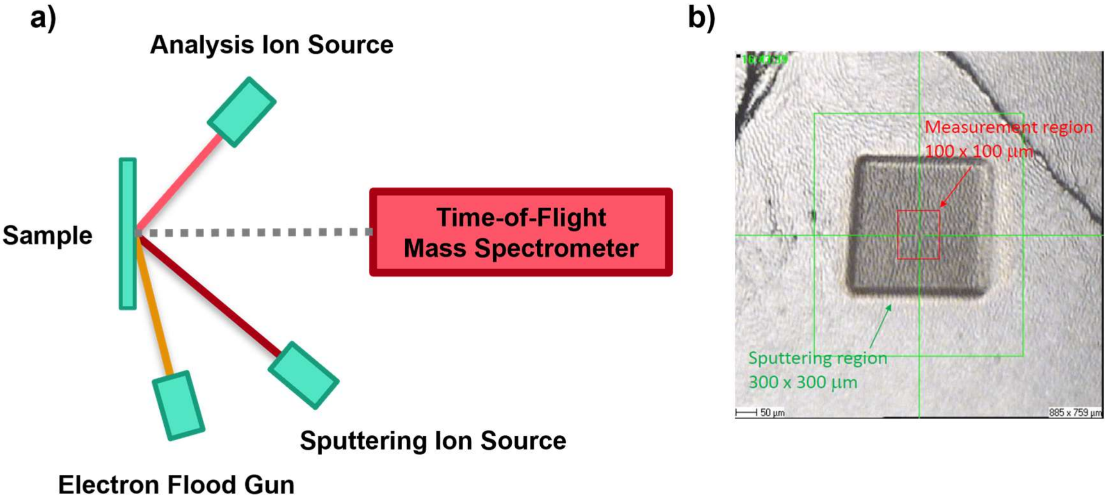

Fig. 3.4 a) Scheme of ToF-SIMS set-up. **b)** SEM image of sputtering crater via sputtering ion beam and measurement region via analysis ion beam.

3.4 Electrical and Electrochemical Impedance Spectroscopy | EIS

Impedance spectroscopy is used to measure ohmic, capacitive and inductive impedances of single materials (such as SSEs) or electrical as well as electrochemical systems of several components (battery cells). The prefix electrical is given for electrical systems and the prefix electrochemical for electrochemical systems. The abbreviation of both is EIS and is used in literature and this study without further distinction since the concept of the measurement is the same: An alternating voltage is induced and the current response of the material or system is measured (**Fig. 3.5a**). Due to the interaction of the material with the alternating voltage $V(t)$ with the amplitude V_A, the response of the alternating current $I(t)$ with the amplitude I_A has a phase difference of Φ (**Fig. 3.5a and b**). The impedance of the system $Z(\omega)$ as a function of the angular frequency ω can be obtained by introducing Ohm's law:[3,11,12,97]

$$Z(\omega) = \frac{V(t)}{I(t)} = \frac{V_A \cdot \sin(\omega t)}{I_A \cdot \sin(\omega t + \Phi)} = Z_A \cdot \frac{\sin(\omega t)}{\sin(\omega t + \Phi)} \qquad \textbf{Eq. 3.4}$$

This can be rewritten by using complex numbers:

$$Z^* = Z_A \cdot (\cos \Phi - i \cdot \sin \Phi) = Z' + i \cdot Z'' \qquad \textbf{Eq. 3.5}$$

where i is the imaginary unit, Z' is the real part of Z^* and Z'' is the imaginary part. The real part is the resistance Z_R and the imaginary part is the reactance defined by the impedances Z_C and Z_L of the capacitance C and inductance L:[3,11,12,97]

$$Z_R = R \; and \; Z_C = \frac{1}{i\omega C} \; and \; Z_L = i\omega L \qquad \textbf{Eq. 3.6}$$

The electrical and electrochemical processes in real systems can be correlated to these impedances. For instance, the Li-ion conduction in ceramic SSEs has a resistance due to the activation energy for Li-ion hopping (**Fig. 2.12**), which goes along with the polarization processes of the Li-ion in the energy environment of the crystal lattice described by the capacitance. Another example is the charge transfer during the redox process, which takes place in parallel to the double-layer formation (**Chapter 2.1**). The charge transfer has a particular resistance and the double-layer formation exhibits capacitive characteristics. Both cases will be explained in more detail in the next sections, however, both can be described as a parallel circuit consisting of a resistor and a capacitor (**Fig. 3.5c**). The total impedance of the so-called RC component can be described as:[3,11,12,97]

$$\frac{1}{Z^*} = \frac{1}{Z_R} + \frac{1}{Z_C} = \frac{1}{R} + i\omega C \qquad \textbf{Eq. 3.7}$$

$$Z^* = \frac{\frac{1}{R}}{\left(\frac{1}{R}\right)^2 + (\omega C)^2} + i \cdot \frac{(-\omega C)}{\left(\frac{1}{R}\right)^2 + (\omega C)^2} = Z' + iZ'' \qquad \textbf{Eq. 3.8}$$

The EIS measurement is performed by choosing a minor voltage amplitude V_A mostly below 100 mV in order to not interfere with the measurement by activating further material-specific processes, such as redox reactions, at higher or lower potentials. By doing so, quasi-stable conditions of the system can be obtained. The angular frequency ω is altered step by step during the measurement in a common range between 1 MHz and 1 mHz. The total impedance depends on ω, particularly the capacitive part. The real part vs. imaginary part of Z^* can be plotted as so-called Nyquist plots. In the case of the RC component, the Nyquist plot results in a semicircle (**Fig. 3.5c**).[3,11,12,97]

However, real systems are much more complex than a RC component and consist of many further effects. The choice of the correct equivalent circuit is the major challenge of fitting and interpreting the Nyquist plots of electrical and electrochemical systems, which requires a good knowledge of the system.

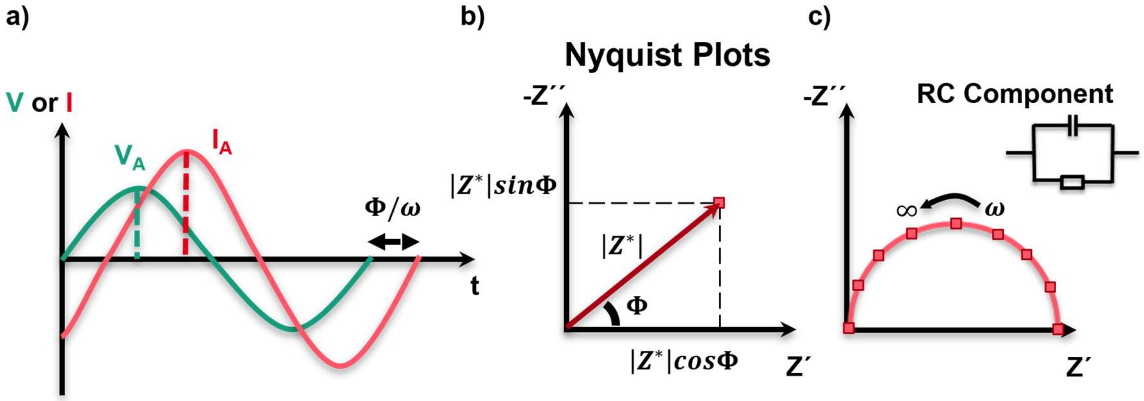

Fig. 3.5 a) Alternating voltage and phase-shifted (Φ) alternating current response. **b)** Nyquist plot of impedance Z^* in imaginary numbers at particular ω. **c)** Nyquist plot of RC component obtained by scanning through ω.

Electrical Impedance Spectroscopy of Li-Ion Conduction in SSEs

As described in **Chapter 2.5**, the Li-ion conduction through polycrystalline ceramic SSEs consists of the Li-ion migration through the crystal lattice and through the grain boundaries with different activation energies (**Fig. 2.12**). This results in different activation frequencies for the two hopping processes. The RC component can be used to describe the Li-ion conduction consisting of a resistive part for the Li-ion transfer and a capacitive part for the polarization of the Li-ion within the crystal lattice energy minimum or at the grain boundary. The serial description of Li-ion conduction is commonly used (**Fig. 2.12**), which is represented by the equivalent circuit consisting of two RC components for bulk conduction and grain boundary conduction in series (**Fig. 3.6b**).[97] The measurement is performed on sintered pellets of the ceramic SSE by sputtering blocking electrodes at both sides (**Fig. 3.6a**). Blocking electrodes do not react with the material or allow redox reactions, in other words, no charge transfer takes place so that they can be seen as a capacitor, with a capacitive impedance. This leads to a final serial equivalent circuit of two RC components for Li-ion conduction and a capacitor for the blocking electrodes (**Fig. 3.6b**).[97] Consequently, the Nyquist plot shows two semicircles for the bulk conduction at high frequencies and the grain boundary conduction at lower frequencies. The blocking electrodes just show an imaginary impact due to the capacitance at low frequencies (**Fig. 3.6b**). The intercept of the semicircles with the real Z′ axis represents the resistances for the Li-ion conduction in the bulk R_b and through the grain boundaries R_{gb}. The bulk conductivity σ_b and grain boundary conductivity σ_{gb} can be calculated by means of the pellet thickness d_{Pellet} and the electrode area $A_{Electrodes}$ (**Fig. 3.6a**):[97]

$$\sigma_b = \frac{1}{R_b} \cdot \frac{d_{Pellet}}{A_{Electrodes}} \quad and \quad \sigma_{gb} = \frac{1}{R_{gb}} \cdot \frac{d_{Pellet}}{A_{Electrodes}} \qquad \textbf{Eq. 3.9}$$

However, the reality is much more complex than theory. In **Fig. 3.6c** the experimentally obtained Nyquist plot of a LATP pellet is shown including the used equivalent circuit for fitting. The first semicircle for the bulk conduction is not shown and can only be measured at very low temperatures below - 100 °C, however, the intercept with the Z′ axis still correlates with the resistance of the bulk conduction.[96] The second semicircle for the grain boundary conduction appears compressed and the increase at low frequencies for the capacitive blocking electrodes exhibits a slope. The compressed semicircle is caused by the grain size distribution and the variation in grain boundary regimes and thicknesses of the polycrystalline microstructure of the SSE, since the capacitance of the grain boundary C_{gb} can be deduced by means of the Brick-Layer model (**Fig. 2.12**):[97,99,101]

$$C_{gb} = \varepsilon_{gb}\varepsilon_0 \cdot \frac{{d_g}^2}{d_{gb}} \qquad \textbf{Eq. 3.10}$$

where ε_0 is the vacuum permittivity and ε_{gb} is the permittivity of the grain boundary regime. Consequently, variations of the grain thickness d_g and grain boundary thickness d_{gb} result in variations in the capacitance through the polycrystalline materials, which causes a compressed semicircle in the Nyquist plot. The slope of the imaginary part introduced by the blocking electrodes can be explained by imperfect electrode interfaces due to the surface roughness of the pellet. That is why a constant phase element (CPE) is introduced for practical use:[97]

$$CPE = \frac{1}{(i\omega C)^\beta} \qquad \textbf{Eq. 3.11}$$

where β (0.5 < β < 1) is a correction factor describing the width of material property distribution. If β is equal to 1, a perfect capacitor is described.[97]

Computer software supports fitting the Nyquist plot by means of the equivalent circuit. By doing so, the resistances of the bulk conduction R_g and grain boundary conduction R_{gb} as well as the grain boundary capacitance C_{gb} can be determined. Furthermore, temperature-dependent measurements make it possible to determine the activation energy $E_{a,gb}$ for the Li-ion conduction by means of the Arrhenius equation **Eq. 2.20**:[97]

$$\sigma_{gb} = \frac{A}{T} exp\left(-\frac{E_{a,gb}}{k_B T}\right) \Rightarrow ln\, \sigma_{gb} T = -\frac{E_{a,gb}}{k_B} \cdot \frac{A}{T} \qquad \textbf{Eq. 3.12}$$

This is also true for the bulk conduction σ_b. Plotting ln($\sigma_{gb}T$) *versus* $1/T$ results in a linear course, which slope is - $E_{a,gb}/k_B$, so that the activation energy can be obtained by linear fitting.[97]

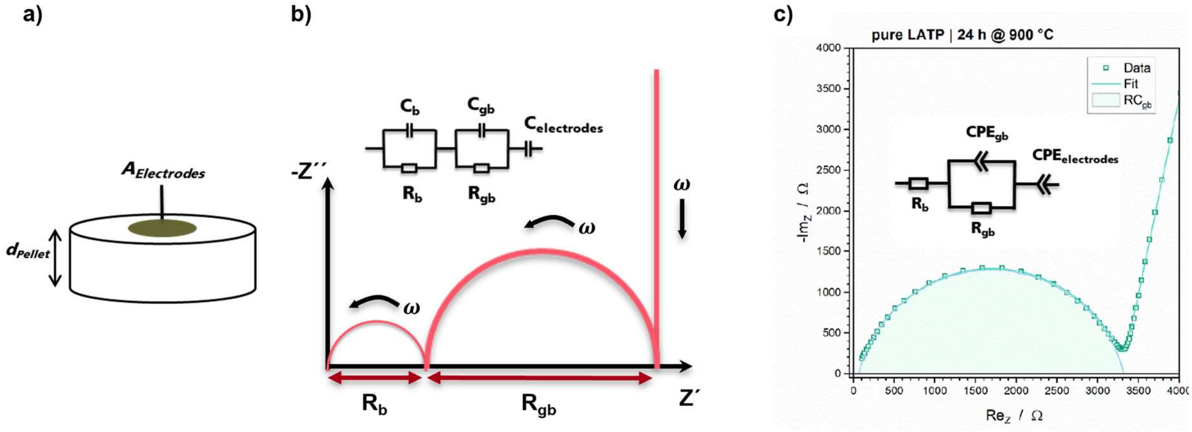

Fig. 3.6 a) Dimensions of SSE pellet required for the determination of the ionic conductivity. **b)** Theoretical Nyquist plot consisting of two semicircles for bulk and grain boundary conduction of Li-ions in ceramic SSEs. **c)** Experimentally obtained Nyquist plot of a LATP SSE pellet measured at room temperature.

Electrochemical Impedance Spectroscopy of Battery Cells

Electrochemical systems such as battery cells are defined by redox reactions during operation. EIS measurements can be used to determine the internal resistance R_Ω of the cell, the charge transfer resistance R_{CT} of the redox reaction and the probable impact of an insulating layer R_{In}.[97]

The internal resistance R_Ω includes all ohmic resistances of the cell induced by the electrical conductivity of wires, current collectors, active materials, additives, etc. and the ionic conductivity of the electrolyte and active materials. It corresponds to the *iR* loss in **Eq. 2.5**.[97]

The charge transfer resistance correlates with the kinetics, thus, the Butler-Volmer equation (**Eq. 2.10**) and charge transfer polarization as well as the concentration polarization (**Eq. 2.5**). Charge transfer goes along with the formation of an electrochemical double-layer, which is the accumulation or depletion of charge at the cathode or anode surfaces. This can be described by a capacitor CPE_{CT}, so that a RC component can be used to describe the redox process (**Fig. 3.7**). The RC component is often extended by the Warburg impedance W_0, which correlates to diffusion processes in the electrolyte.[97]

As described in the previous chapters, side reactions can cause the formation of insulating layers, such as the CEI formation by degradation of the electrolyte (**Chapter 2.1**: Liquid Electrolytes), Mn depletion of LMO (**Chapter 2.1**: Cathode Active Materials) or the electrochemical decomposition of SSEs (**Chapter 2.2**: SSE Materials). This results in an additional resistance induced by the insulating layer R_{In}, which also has a polarization component due to the Li-ion conduction described by a capacitor CPE_{In}.[97]

These impacts in series results in the equivalent circuit and Nyquist plot demonstrated in **Fig. 3.7**. The capacitors are represented as *CPE*s due to the material property distribution, such as porosity, particle size distribution, surface roughness, etc. EIS measurements are mostly performed at the fully charged or discharged state of the cell since the charge transfer resistance changes with the amount of incorporated Li in the insertion material lattice. Quasi-stable conditions must be reached for accurate measurements. That means, that a constant current flow should be present during the whole EIS measurement since an altering current influences the impedance determination (**Eq. 3.4**). That is why constant voltage steps are introduced before the EIS measurement in order to guarantee a fully charged or discharged state.[3,97]

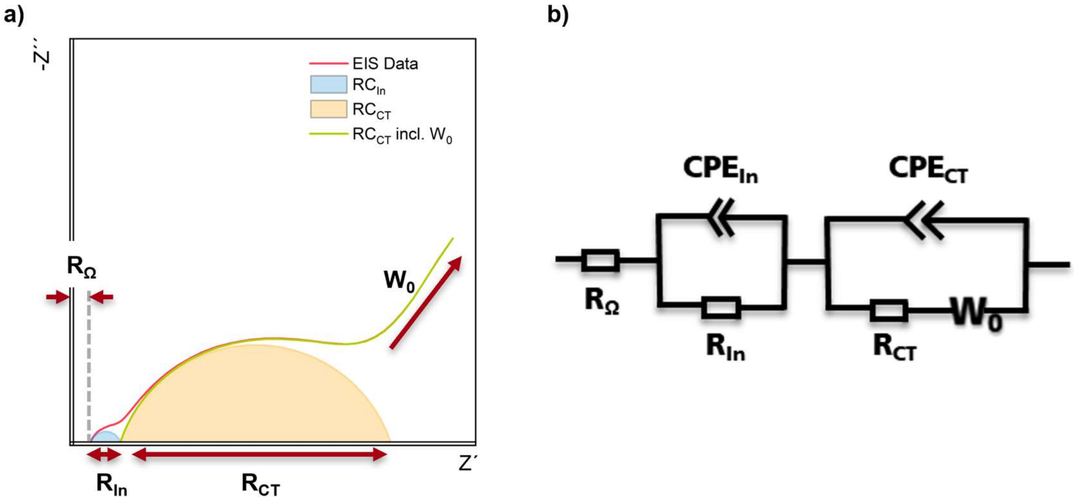

Fig. 3.7 a) Nyquist plot of a battery cell with the internal resistance R_{Ω}, the semicircles of the RC components for the insulating layer (corresponding to R_{In}) and for the charge transfer (corresponding to R_{CT}) as well as the Warburg impedance W_0. **b)** The corresponding equivalent circuit.

3.5 Galvanostatic Cycling with Potential Limits | GCPL

The method of galvanostatic cycling with potential limits (GCPL) is the most widely used method to investigate battery cells and their characteristics. The capacity of the cell, redox potentials and overvoltages of the active materials, side-reactions, cycle life and rate capability of the cell can be determined with this method.

Fundamentals of GCPL

A battery cell is charged and discharged with a constant current (CC) and the voltage of the cell is measured. The battery cell polarizes until a redox reaction (Li insertion or extraction reactions, **Chapter 2.1**) takes place. When this happens a plateau at the redox potential of the active material reaction occurs (**Fig. 3.8a and b**). As soon as the active material is fully charged or discharged (fully Li extraction or insertion), the cell further polarizes. In order to avoid further side reactions such as intensive electrolyte decomposition or degradation of the active material at high potentials, the potential range of the measurement is limited. A charge step (positive current) and a discharge step (negative current) gives a cycle. By repeating the charge and discharge of the cell, cycling tests can be performed, which give information about ongoing side reactions, further loss mechanisms and cycle stability. If the focus of the investigation is on the discharge behavior, constant voltage steps (CV) after the charge step can be introduced in order to guarantee a fully charged cell.[2–4]

A $LiMn_2O_4$ thin-film half cell from this study is used here as an example. In **Fig. 3.8a**, the voltage signal and the applied current are plotted vs. time. The potential limits are set at 3.2 V and 4.4 V vs. Li/Li^+. A CV step at 4.4 V vs. Li/Li^+ is performed after the CC charge step. During the CV step, the current is measured. This gives information on whether further redox reactions take place (faradaic trend of current) or the cell has just polarized (capacitive trend of current). In **Fig. 3.8a** the current rapidly drops to zero, which represents a capacitive behavior of the cell and the cell can be assumed to be fully charged. [2–4]

The current multiplied with time gives the charge which is consumed during cell operation. The totally transformed charge is equal to the capacity of the cell. The cell voltage as a function of the capacity gives the voltage profile (**Fig. 3.8b**). The charge step begins at 3.2 V vs. Li/Li+ with the polarization of the cell until the redox reaction of the Li extraction starts. Here, two plateaus (as described in **Chapter 2.1**: Cathode Active Materials) for the Li extraction redox reaction of the $LiMn_2O_4$ appear. As soon as the extractions are finished, the cell polarizes again and goes over in the CV step. The capacity at the end of the charge step is the charge capacity. During the CC discharge step, the $LiMn_2O_4$ active material is lithiated and its redox reaction occurs again as two plateaus. The end value of the capacity is the discharge capacity.[2–4]

By performing several cycling steps, the trend of the charge and discharge capacity elucidates loss mechanisms during cell operation. The capacities can be plotted as a function of the cycle number (**Fig. 3.8c**). Discharge capacity fade, for instance, indicates, among others, an increase of the internal resistance due to insulating layers caused by electrolyte decomposition or it indicates a degradation of the active material with cycle number. A quantitative measure for redox side reactions is the coulombic efficiency, which describes the ratio of capacity between the charge and discharge step of one cycle:[2–4]

$$Coulombic\ Efficiency\ of\ Cycle = \frac{Discharge\ Capacity\ of\ Cycle}{Charge\ Capacity\ of\ Cycle} \qquad \textbf{Eq. 3.13}$$

If the coulombic efficiency is below 100 %, an additional side reaction during charge can be assumed. For instance, the charge capacity in **Fig. 3.8c** decreases in the first 8 cycles and the discharge capacity remains constant, which results in an increase of the coulombic efficiency. The extra charge during the charge steps of these cycles is most likely used to form the SEI at the anode interface and partly the formation of CEI at the cathode interface (**Chapter 2.1**: Liquid Electrolytes).[2–4]

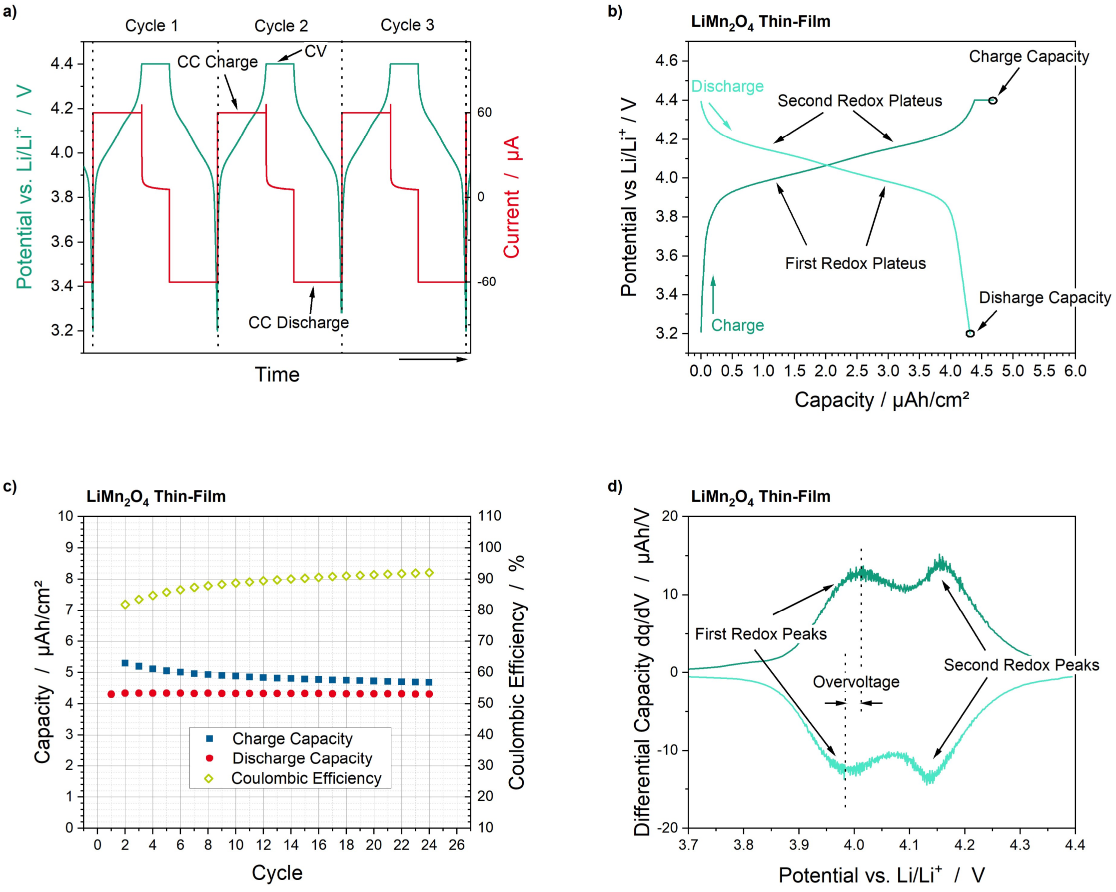

Fig. 3.8 Plots obtained from GCPL analysis of a $LiMn_2O_4$ thin-film cell with liquid electrolyte and Li-metal anode. **a)** Potential and current as a function of time **b)** Voltage profile of one cycle. **c)** Charge and discharge capacities as well as coulombic efficiencies as a function of cycle number. **d)** Differential capacity plots of the voltage profile presented in **b)**.

The differential capacity plot (**Fig. 3.8d**) is used to determine the exact redox plateau positions and it gives insights into the polarization processes and internal resistances of the cell. As described in **Chapter 2.1**, the charge transfer polarization and concentration polarization are the main loss mechanisms during cell operation (**Eq. 2.5**) shifting the redox potential to higher potentials during charge and lower potentials during discharge. The difference in the peak potentials can be defined as overvoltage, which gives a quantitative measure of the loss mechanisms and can be qualitatively compared with other samples. The formation of CEIs, Mn depletion during cycling of $LiMn_2O_4$ or further side reactions can enhance polarization effects so that higher overvoltages will be measured.[2–4]

Rate Capability Tests & Long-Term Cycling Tests

Rate capability tests describe GCPL measurements with varying constant currents for a set of cycles. As described in **Chapter 2.1**, the current affects the polarization processes and the internal resistance. High currents increase the polarization effects (**Eq. 2.10** and **Eq. 2.13**) and might result in premature polarization of the cell without complete charging or discharging. The ratio of the capacities of the cell at two different currents is a measure of the dominance of the polarization effects. Consequently, it gives information about insulating layers and further loss effects. The maximum possible operating current can be determined.[2–4]

Long-term cycling tests are GCPL measurements over > 500 cycles. The trend of the cell capacity gives information about the ongoing side reactions or active material degradation. These side effects result in an increase of the polarization effects and internal resistance so that a capacity fade with cycle number occurs. The cycle life of the cell can be determined and compared within various samples. The cycle life is defined as the cycle number at which 80 % of the initial capacity is reached.[2–4]

4 Thermal Stabilities of the LATP SSE in Combination with various Mn-based Active Materials

All solid-state batteries with high energy densities require particulate, ternary composite cathodes consisting of active material, solid-state electrolyte and an electrically conductive component. The solid-state electrolyte and the electrical conductor supply the active material with Li-ions and electrons, respectively. In this way, the redox reaction can take place in the active material due to the insertion or extraction of Li-ions in or out of the crystal lattice of the ceramic active material accompanied by electron flow and reduction or oxidation of the active material’s transition metal. Thus, charge transfer is an important process for good battery performance. To enhance the charge transfer, the electrochemically active area needs to be increased and the Li-ion transfer between electrolyte and active material needs to be improved. First can be realized by densification of the particulate cathode green body, which maximizes the contacts between the three components. Secondly, the charge transfer of Li-ions requires firmly bonded grain-to-grain contacts with low grain boundary energies, so that the barrier for Li-ion hopping is minimized. Since the active material and the solid-state electrolyte are ceramics, sintering at high temperatures is necessary to achieve firmly bonded contacts. However, side effects at high temperatures like interdiffusion and decomposition processes could result in non-conductive and electrochemically inactive mixed phases and the dissolution of the initial components, which significantly reduces the battery performance. Consequently, a thermally stable material combination needs to be found. Furthermore, the atomic processes during high-temperature treatment are supposed to be described and understood, so that the selection can be simplified or the heat treatment can be optimized.

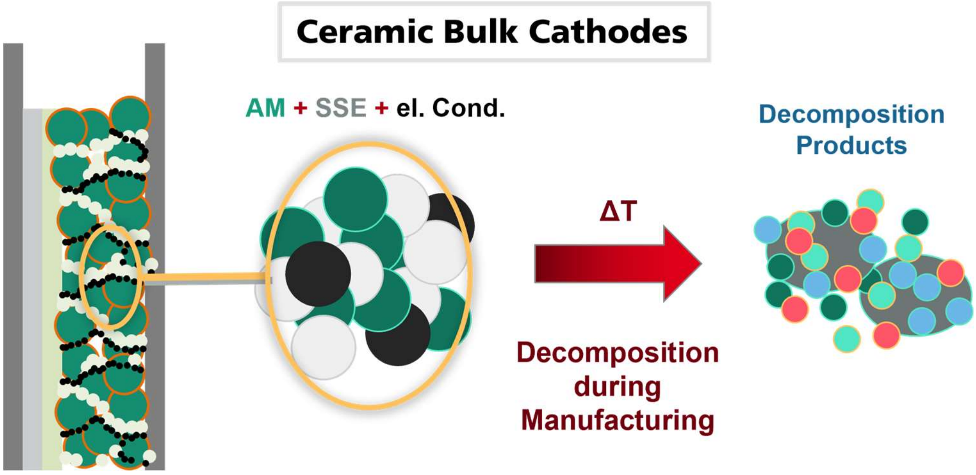

Fig. 4.1 Manufacturing of bulk cathode composites can result in decomposition and intermixing of the initial components. AM = active material; SSE = solid-state electrolyte.

For that purpose, the ceramic solid-state electrolyte LATP has been tested on its thermal stability in combination with the active materials $LiMn_2O_4$ (LMO-s), $LiMnO_2$ (LMO-l) and $LiMnPO_4$ (LMP). Each chosen active material represents an active material class categorized by its lattice structure. Since LATP and LMP showed a thermally stable behavior, silver (Ag) was added as an electrical conductor. The powder mixture of active material and LATP were pressed into pellets and analyzed via high-temperature XRD (HT-XRD) and Rietveld refinement in order to determine the mixed phases and their development during the heating ramp. HT-XRD and Rietveld analysis have been done within the master thesis of Felix Nagler ("Investigation on component stabilities within cathode composites of novel battery systems" 2020) in collaboration with the group of Prof. Oliver Clemens at the Technical University Darmstadt. Additionally, DSC-TG measurements including mass spectroscopy (MS) have been done to determine oxidation and reduction processes. SEM-EDS analyses reveal the microstructure and mixed phases. Some of these results are summarized in the project works of Lavinia Appold ("Untersuchung der thermischen Stabilität von LATP mit verschiedenen Aktivmaterialien" 2020) and Katharina Nuss ("Thermische Stabilität von Mischungen aus LATP und LMP" 2018). The author developed the experimental plans and managed the collaboration with the TU Darmstadt. Data analyses, discussions and interpretation had taken place under my supervision.

The study has been published in the Journal *Materials Advances* of the Royal Society of Chemistry:

M. Rumpel, F. Nagler, L. Appold, W. Stracke, A. Flegler, O. Clemens, and G. Sextl, "Thermal stabilities of Mn-based active materials in combination with the ceramic electrolyte LATP for ASSB bulk cathodes," Mater. Adv. **3** (9), 4015–4025 (2022).[130]

4.1 Introduction and Status Quo

The thermal stability of multi-component ceramics can be described by thermodynamics since the most stable phases are the ones with the lowest Gibbs free energy.[90–94] As described in **Chapter 2.4**, the differences in chemical potential of the elements between the components as well as the increase of entropy (i.e. gas formation) mainly define if element diffusion, phase transition or chemical reaction takes place or not. These processes are temperature-dependent. A system with various chemical potentials aims to equilibrium conditions due to diffusion processes along the concentration gradient.[90–94] One way to reach equilibrium is the solution of the diffusing elements in the crystal lattice of the second material. These interdiffusion processes are described by the Hume-Rothery rules, which consider the size of the elements, valence factor regarding electroneutrality as well as chemical affinity and structure type of the lattices (**Chapter 2.4**).[90] If the solution of the elements is not possible, the multi-component ceramics maintain thermally stable or chemical reactions cause mixed phases and gas formation in order to reduce the total Gibbs free energy.[90]

Considering the valance factor, chemical affinity and structure type, the active materials $LiMn_2O_4$ (LMO-s), $LiMnO_2$ (LMO-l) and $LiMnPO_4$ (LMP) differ in these parameters, so that different reactions during heat treatment in combination with LATP can be expected. LMO-s crystallizes in a spinel structure, LMO-l represents the layered materials and LMP has an olivine structure (**Chapter 2.1**: Cathode Active Materials). Their lattice structures differ by their Li-ion diffusion pathways and Li-ion diffusivity. LMO-s, LMO-l and LMP have 3D, 2D and 1D channels for Li-ion diffusion, respectively. Additionally, the oxidation states of Mn are 3+ and 4+ for LMO-s, 3+ for LMO-l and 2+ for LMP.[13,14] Since LATP crystallizes in a NASICON structure type with the oxidation states 3+ for Al and 4+ for Ti,[64] the combinations of these active materials and the electrolyte are supposed to cause different conditions for the thermodynamic consideration.

First principle studies on the chemical stability of ceramic electrolytes based on thermodynamic calculations considering the chemical potentials have been done by Miara et al.[131] and Zhu et al.[10,55] Although they focused on the electrochemical potential window, the trends might be transferred to the thermal stability. The calculated reaction energies of LATP show the highest intrinsic chemical stability and good stability with $LiCoO_2$.[10] Experimental studies had been done by Miara et al.[132] and Gellert et al.[133] Miara et al.[132] tested three spinel materials ($LiCoMnO_4$, $LiNi_{0.5}Mn_{1.5}O_4$ and $LiFe_{0.5}Mn_{1.5}O_4$) in combination with LATP and demonstrated the decomposition and formation of mixed phases for all material combinations starting at 700 °C. Gellert et al.[133] could show the most thermally stable combinations of olivine active materials (i.e. $LiCoPO_4$) in combination with LATP. However, a deeper consideration of the reaction mechanisms has not been done.

Recapitulating the previous research, this study is simplified to Mn-based active materials of the three common active material classes in combination with LATP. A more detailed insight into decomposition processes and mixed phase formation can be revealed by using HT-XRD with Rietveld analyses, DSC-TG with MS and SEM/EDS.

4.2 Experimental Approach

This subchapter gives a short overview of the experimental plan (**Fig. 4.2**). Detailed information can be found in the experimental section (**Chapter 9.1**).

$Li_{1.3}Al_{0.3}Ti_{1.7}(PO_4)_3$ (LATP) powder as well as $LiMn_2O_4$ (LMO-s) and $LiMnPO_4$ (LMP) powders were synthesized via sol-gel formulations. The crystallization temperatures and durations were particularly chosen in order to obtain particle sizes less than 1 µm. Since $LiMnO_2$ (LMO-l) and nano-sized Ag particles could not be synthesized, these powders were purchased from Sigma Aldrich® (LMO-l: < 1 µm) and Nanografi® (Ag: 48 - 78 nm).

Powder mixtures of 1:1 vol% of LATP and active material were mixed in a mortar. In the case of LMP + LATP + Ag the ratio was 1:1:1 vol%.

Pellets of 0.25 g of the powder mixtures were pressed with 90 kN for the HT-XRD measurements. The maximum temperature was determined by a form integrity test in order to identify the maximum temperature without significant deformation of the pellets. For the HT-XRD measurements, the pellets were heated up in an argon atmosphere with 3 K/min to 500 °C and the first XRD scan was performed. Afterward, the heating rate was 3 K/min and XRD scans were performed every 25 °C. During the 15 min XRD scans, the temperature was kept constant. The maximum temperature was held for 1 h followed by a cooling process with 3 K/min and XRD scans every 25 °C. The XRD patterns were analyzed via Rietveld refinement with the TOPAS software (Bruker®). The lattice parameters and crystalline size parameters were only fitted.

DSC-TG measurements with MS were performed on 20 mg of each powder mixture in an argon atmosphere. Alumina crucibles were used and the heating rate was 10 K/min up to 1000 °C.

SEM/EDS measurements were performed on polished cross sections of pellets of the powder mixtures annealed in an argon atmosphere at 800 °C for 2 h. The heating rate was 5 K/min.

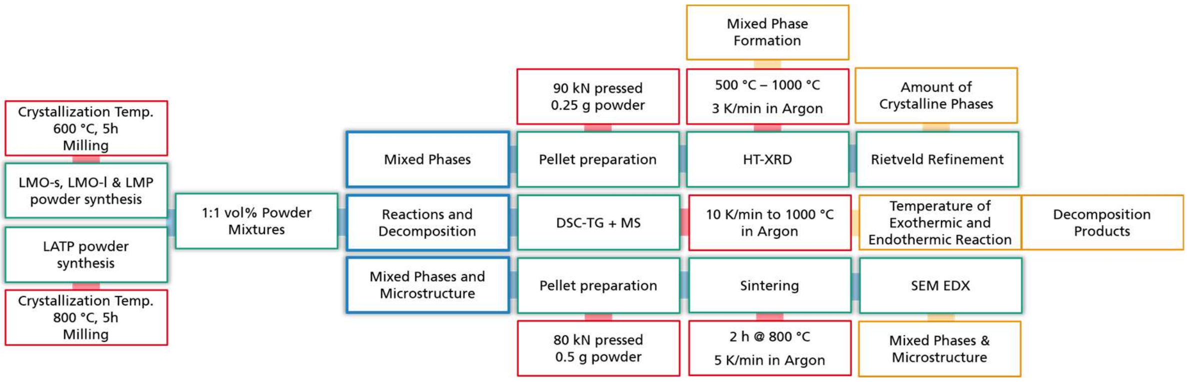

Fig. 4.2 Experimental plan of the investigation of the thermal stabilities of LATP in combination with various Mn-based active materials. Experimental steps (green), parameters (red) and measured properties (orange).

4.3 Characterization of Starting Powders

SEM images of the synthesized LATP, LMO-s and LMP powders as well as the purchased LMO-l powder are demonstrated in **Fig. 4.3**. The particle size distributions of all powders are comparable and the particle sizes are less than 1 µm. The purchased LMO-l powder has occasionally particles > 1 µm, but the majority is below 1 µm. This is important for the following HT-XRD and DSC-TG measurements since a homogeneous mixture of the powders results in a maximum number of contacts between the materials. Consequently, the signal of the reactions and mixed phase formation is more accurate.

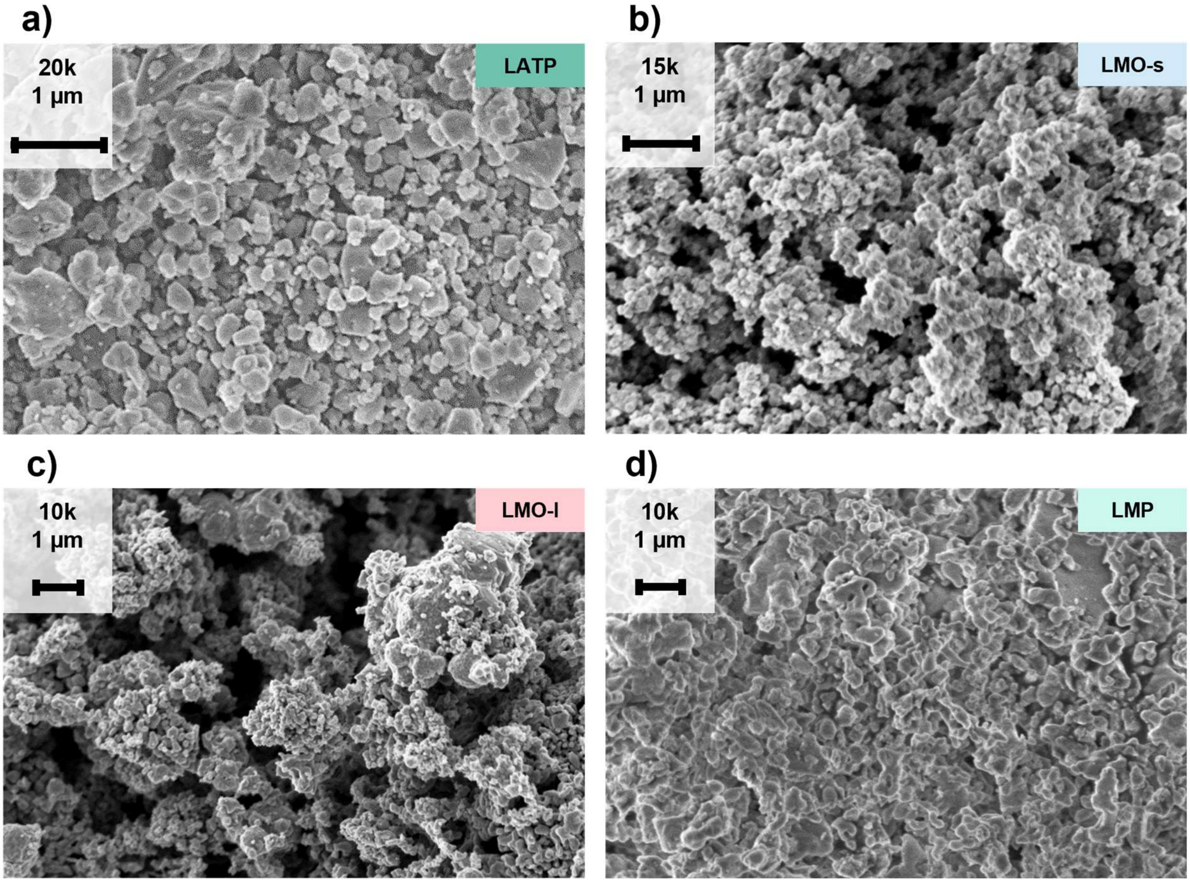

Fig. 4.3 SEM images of the starting powders: **a)** LATP, **b)** LMO-s, **c)** LMO-l and **d)** LMP. Particle size distributions are comparable and particle sizes are < 1 µm. Published by and reprinted from Rumpel et al.[130] (published under CC-BY license in Royal Society of Chemistry: *Materials Advances* 2022).

The XRD patterns of all materials show no impurity phases (**Fig. 4.4a**). The patterns are in perfect accordance with the references known from the literature: LATP (ICSD 95979), LMO-s (ICSD 85398), LMO-l (ICSD 81051) and LMP (ICSD 25834).

The DSC-TG profiles of the pure powders demonstrate no significant mass loss for the LATP, LMO-l and LMP samples up to 1000 °C (**Fig. 4.4b**). The DSC curves of LATP and LMO-l also show no reactions. The LMP sample shows an endothermic peak at 921 °C, which indicates a decomposition process. In contrast, LMO-s demonstrates mass loss to finally 93.5 % starting at ca. 550 °C with two slopes at 821 °C and 850 °C, which corresponds to the minimum of two endothermic peaks shown in the DSC curve. Consequently, LMO-s is not intrinsically stable in argon atmosphere.

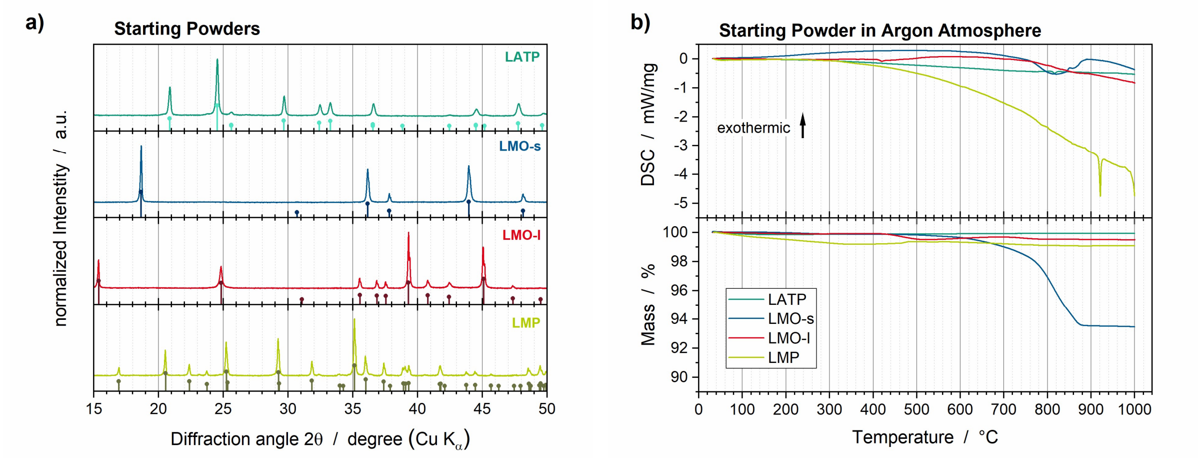

Fig. 4.4 Characterization of starting powders LATP (dark green), LMO-s (blue), LMO-l (red) and LMP (light green): **a)** XRD patterns and **b)** DSC-TG profiles. Published by and reprinted from Rumpel et al.[130] (published under CC-BY license in Royal Society of Chemistry: *Materials Advances* 2022).

4.4 Thermal Stability of LMO-s and LATP Powder Mixture

DSC-TG and MS Measurements

The DSC-TG and MS data of the 1:1 vol% LMO-s + LATP powder mixture is demonstrated in **Fig. 4.5**. At the beginning of heating, H_2O and CO_2 gassing can be detected, which goes along with a mass loss of 0.9 %. This can be related to the adsorption of humidity and formation of carbonates during storage of the material[134,135] as well as residues of the sol-gel syntheses. Since the pure LMO-s is not stable in argon atmosphere (**Fig. 4.4b**), reactions in the powder mixture of LMO-s and LATP are expected. Consequently, the DSC curve (**Fig. 4.5**) of this mixture shows five endothermic peaks with peak positions at 564 °C (P_1), 645 °C (P_2), 803 °C (P_3), 862 °C (P_4) and 916 °C (P_5). The reactions are accompanied by oxygen formation and mass loss. The highest mass loss of 4.6 % to 94.5 % is between ca. 500 °C and ca. 670 °C. The temperature derivation of the mass shows two rates for the mass loss in this temperature range, which correspond to the endothermic peaks at 564 °C and 645 °C. Afterward, the rate of oxygen formation and mass loss decreases between ca. 670 °C and ca. 780 °C (mass = 93.8 %) and it increases again between ca. 780 °C and ca. 900 °C (mass = 92.7 %). At 1000 °C, the mass was reduced to 92.3 % of the initial mass. In general, oxygen formation indicates reduction processes of the initial material. The first two endothermic peaks at 564 °C and 645 °C are probably comparable with the reactions of the pure LMO-s represented by the endothermic peaks at 821 °C and 850 °C (**Fig. 4.4b**). The decrease in the reaction temperature can be explained by the presence of LATP particles, which can function as reaction seeds due to the reduction of the surface energy of the LMO-s particles, which results in a decrease of the reaction activation energy.[90,93] Finally, it must be considered that the DSC measurement is a dynamic measurement method, which correlates to the kinetics of the reactions. That means, lower heating rates can shift the peak position of the reactions to lower temperatures.[136,137]

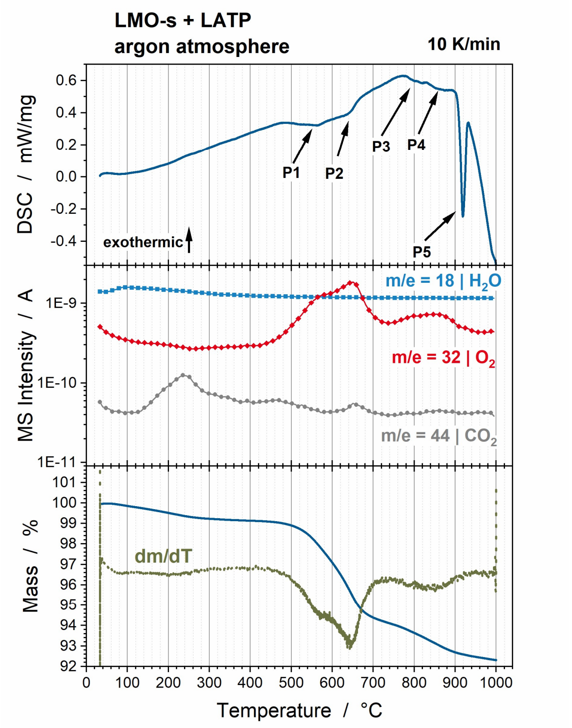

Fig. 4.5 Results of the DSC-TG and MS analyses of a 1:1 vol% LMO-s + LATP powder mixture measured in argon atmosphere with 10 K/min. Published by and reprinted from Rumpel et al.[130] (published under CC-BY license in Royal Society of Chemistry: *Materials Advances* 2022).

HT-XRD Measurements and Rietveld Refinements

A selection of XRD patterns incl. the Rietveld refinements of the LMO-s + LATP sample is demonstrated in **Fig. 4.6**. The form integrity test showed a maximum temperature without deformation of 900 °C, thus, it is set as the maximum temperature for the HT-XRD measurements. The XRD patterns demonstrate already at 500 °C the formation of several mixed phases and the decomposition of the starting materials LMO-s and LATP. The detected reflections significantly change at 700 °C and 900 °C. The Rietveld refinement could be properly done and the deduced weight percentages as a function of annealing temperature are shown in **Fig. 4.7**. The starting values of the 1:1 vol% mixture of LMO-s and LATP are 58 wt% (LMO-s) and 42 wt% (LATP). LMO-s decreases already at 500 °C and vanishes completely at 650 °C. This goes along with a significant increase in Mn_3O_4 up to 56 wt% at 650 °C. Additionally, Mn_2O_3 can be detected. The amount of LATP is also reduced at 500 °C and vanishes completely at 800 °C. It decomposes to Li_3PO_4 and TiO_2 at 500 °C and $LiTiOPO_4$ between 650 °C and 850 °C. At 500 °C the first reaction product (low amounts of $Mn_2P_2O_7$) with LMO-s can be detected. Furthermore, at 600 °C the formation of $LiMnPO_4$ is demonstrated and it increases afterward to 36 wt% at 850 °C. Further reaction products are $MnTiO_3$ appearing at 725 °C and $Li(Mn,Ti)_2O_4$

appearing at 875 °C. Their formations run parallel to the decrease of Mn_3O_4 and the disappearance of Mn_2O_3 at 800 °C. During the holding step of 1 h at 900 °C, 7 wt% of a cristobalite M-PO_4 (M = Ti^{3+} or Mn^{3+}) phase can be detected, which completely vanishes at the beginning of the cooling step at 875 °C. Its formation goes along with a drop of Li_3PO_4 from 8 wt% to 2 wt% and a further decrease of Mn_3O_4 from 28 wt% to 12 wt% during the holding step. Since the Ti-containing phases such as $MnTiO_3$ and $Li(Ti,Mn)_2O_4$ increase from 16 wt% to 27 wt% or 2 wt% to 6 wt% during the holding step, the M-PO_4 phase is most likely a Mn-rich cristobalite phase. This interpretation is supported by the increase of $LiMnPO_4$ from 34 wt% to 38 wt% accompanied by the disappearance of the M-PO_4 phase with the start of the cooling step. However, since Mn^{3+} is Jahn-Teller active, particularly on the tetrahedral sides of the lattice, it is unlikely to be stabilized in the cristobalite phase. The decrease of Mn_3O_4 containing Mn^{3+} and the increase of the $MnTiO_3$ containing Mn^{2+} can also lead to the assumption that the Mn in the cristobalite lattice has the oxidation state of 4+ due to the disproportionation of Mn_3O_4. In this case, lower valent ions, such as Li^+ and Al^{3+}, are necessary to be incorporated in the cristobalite lattice with the resulting formula $Li_{x/2}Mn_xAl_{1-3x/2}PO_4$. Since the cristobalite phase is only high-temperature stable and vanishes at 875 °C during cooling, a further detailed compositional analysis is not possible.

Nevertheless, during the cooling to 500 °C, no further significant changes can be detected. Between 500 °C and 30 °C, the phases of $Mn_2P_2O_7$, TiO_2 and $Li(Mn,Ti)_2O_4$ disappear. The remaining powder finally consist of 47 wt% $LiMnPO_4$, 28 wt% $MnTiO_3$, 17 wt% Mn_3O_4 and 8 wt% Li_3PO_4 (**Fig. 4.7**).

Summarizing these results, it can be deduced that at the beginning of the annealing, LMO-s transforms to Mn_2O_3 and Mn_3O_4 and LATP transforms to Li_3PO4 and TiO_2 as well as $LiTiOPO_4$. First reactions between LMO-s and LATP cause the formation of $Mn_2P_2O_7$ and $LiMnPO_4$ until the starting powders are completely decomposed. At elevated temperatures, these decomposition products react to $MnTiO_3$ and $Li(Mn,Ti)_2O_4$ as well as the cristobalite M-PO_4, which is only stable at high temperatures. Crystalline phases including Al could not be detected. Since their amount is very low, Al is expected to solute in the other phases by substitution of Mn^{3+} or their formed phases are below the resolution limit.

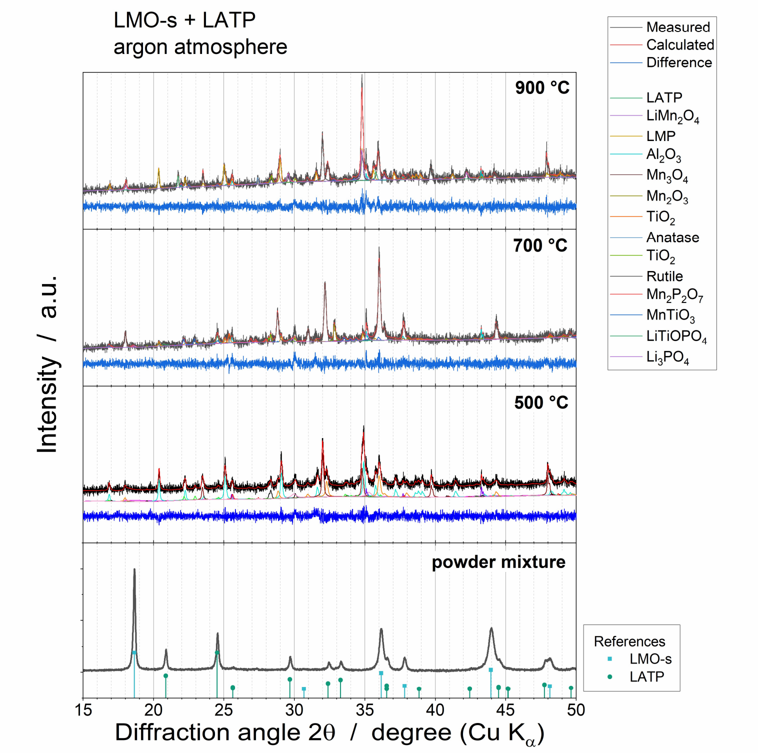

Fig. 4.6 Selected HT-XRD patterns and their Rietveld refinements of the LMO-s + LATP pellet sintered in argon atmosphere at 500 °C, 700 °C and 900 °C. Additionally, the XRD pattern of the pristine LMO-s + LATP powder is presented. Published by and reprinted from Rumpel et al.[130] (published under CC-BY license in Royal Society of Chemistry: *Materials Advances* 2022).

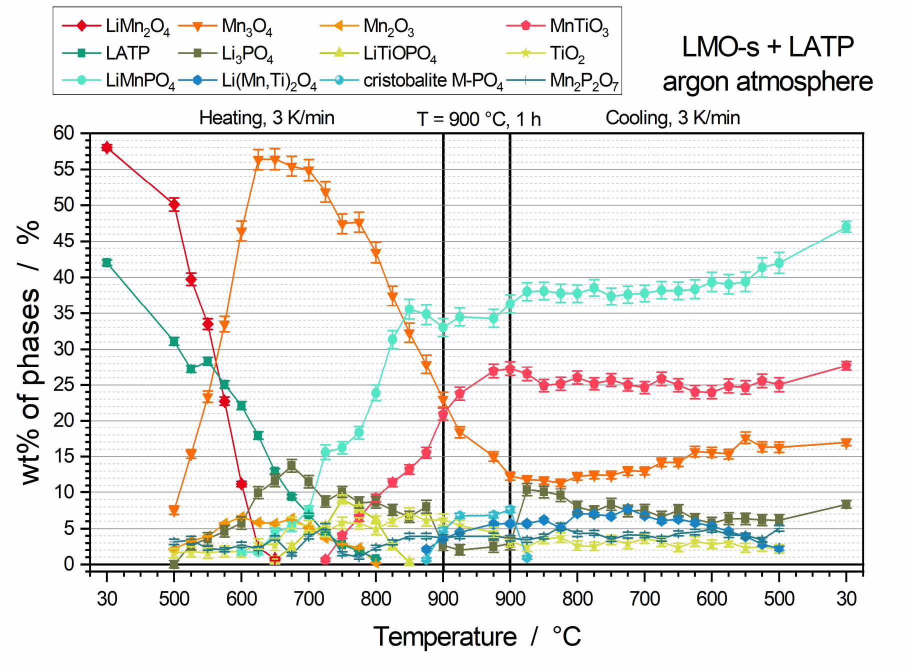

Fig. 4.7 Weight percentages wt% of crystalline phases obtained by Rietveld refinement of the LMO-s + LATP pellet as a function of the annealing temperature. Heating up to 900 °C with 3 K/min, holding step at 900 °C for 1 h, and afterward cooling with 3 K/min to 30 °C. Published by and reprinted from Rumpel et al.[130] (published under CC-BY license in Royal Society of Chemistry: *Materials Advances* 2022).

SEM Images and EDS Analyses

The cross-section of the LMO-s + LATP pellet annealed at 800 °C for 2 h in an argon atmosphere shows a porous microstructure with grains in the size of a few 100 nm (**Fig. 4.8a**). Four different contrasts can be detected. Their EDS analyses (**Fig. 4.8b**) reveal regions with only Mn and O elements (**Fig. 4.8a**, position 1), which corresponds to Mn_3O_4 detected via XRD. Further accordance with the remaining components determined via XRD (**Fig. 4.7**) can be found in the positions 2, 3 and 4. Position 2 belongs to $MnTiO_3$. Additionally, Al can be detected here, which confirms the assumption that Al is dissolved in the $MnTiO_3$ lattice. Positions 3 and 4 correspond to $LiMnPO_4$ and Li_3PO_4, respectively.

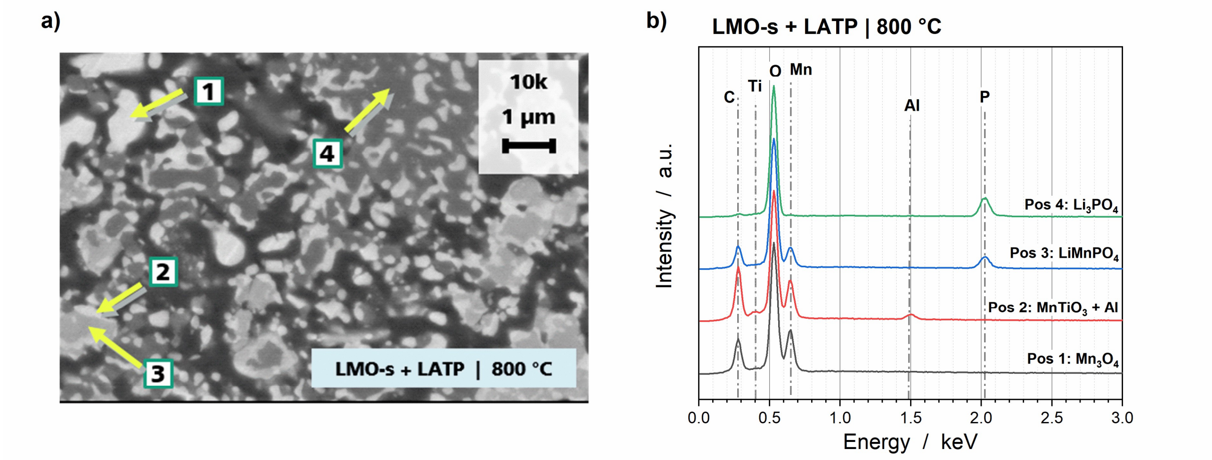

Fig. 4.8 a) SEM cross-section and **b)** EDS analyses of a LMO-s + LATP pellet sintered for 2 h at 800 °C in argon atmosphere. Published by and reprinted from Rumpel et al.[130] (published under CC-BY license in Royal Society of Chemistry: *Materials Advances* 2022).

Correlation and Summary

The powder mixture of LMO-s and LATP is thermally not stable in argon atmosphere even at 500 °C. The correlations of the analyses of HT-XRD and DSC-TG incl. MS are summarized in **Table 4.1**. LMO-s endothermically reacts to Mn_2O_3 and Mn_3O_4, which means the reduction of Mn^{3+} and Mn^{4+} in LMO-s to Mn^{3+} as well as Mn^{2+} and Mn^{3+} in Mn_2O_3 and Mn_3O_4, respectively. The reduction of Mn is accompanied by the oxidation of O^{2-} to O_2 and correlates to the endothermic peaks P1 and P2 (**Fig. 4.5**). This results in the complete decomposition of LMO-s at 650 °C (**Fig. 4.7**) so that in this temperature range the highest mass loss can be detected (**Fig. 4.5**). Meanwhile, the decomposition of LATP to Li_3PO_4, TiO_2 and $LiTiOPO_4$ takes place, which is not associated with reduction or oxidation processes. The oxidation state of Ti is 4+ in all Ti-containing species. LATP is completely decomposed at 800 °C. This decomposition goes along with the first reactions between LMO-s and LATP to $Mn_2P_2O_7$ and $LiMnPO_4$, which also indicates a further reduction of Mn since the oxidation states of Mn in both species are 2+. The formation of $LiMnPO_4$ starts at 600 °C (**Fig. 4.7**) so that it likely corresponds with the endothermic peak P3 and a lower oxygen loss (**Fig. 4.5**) since Mn_3O_4 with similar oxidation states can also be the educt of this reaction. $MnTiO_3$ formation starts at 725 °C and runs parallel to the disappearance of $LiTiOPO_4$ and Mn_2O_3. This temperature range is in accordance with P4. Additionally, low amounts of Al^{3+} are dissolved in the $MnTiO_3$ lattice (**Fig. 4.8b**). Finally, $Li(Mn,Ti)_2O_4$ is formed at 875 °C (corresponds to P5, **Fig. 4.5**), which causes a further decrease of Mn_3O_4 and TiO_2 and a low mass loss due to oxygen formation is detected. Most phases are just stable at temperatures > 500 °C. The final composition after cooling to 30 °C consists of $LiMnPO_4$ (47 wt%), $MnTiO_3$ (28 wt%), Mn_3O_4 (17 wt%) and Li_3PO_4 (8 wt%), which can also be detected in the EDS measurements (**Fig. 4.8b**). Additionally, the oxygen formation causes a porous microstructure (**Fig. 4.8a**).

Table 4.1 Summary of the results and findings of the analyses of the thermal stability of LMO-s and LATP. DSC Peak positions: 564 °C (P1), 645 °C (P2), 803 °C (P3), 862 °C (P4) and 916 °C (P5).
Published by and reprinted from Rumpel et al.[130] (published under CC-BY license in Royal Society of Chemistry: *Materials Advances* 2022).

Detected Phases	Valence of Transition Metals	Temperature Range and Trend	Possible Educts	Possible corres-ponding DSC Peaks	Expected Oxygen Formation and Mass Loss	Final Composition
$LiMn_2O_4$ (LMO-s)	Mn^{3+} and Mn^{4+}	Decrease already < 500 °C Disappearance at 650 °C	--	--	--	--
$Li_{1.3}Al_{0.3}Ti_{1.7}(PO_4)_3$ (LATP)	Al^{3+} and Ti^{4+}	Decrease already < 500 °C Disappearance at 800 °C	--	--	--	--
Mn_2O_3	Mn^{3+}	Detectable between 500 °C and 800 °C	LMO-s	P1 and P2	Yes	--
Mn_3O_4	Mn^{2+} and Mn^{3+}	Formation already < 500 °C Strong increase up to 625 °C, afterwards steady decrease to 900 °C, during cooling constant	LMO-s	P1 and P2	Yes	17 wt%
Li_3PO_4	--	Detectable during heating and cooling	LATP	--	No	8 wt%
TiO_2	Ti^{4+}	Detectable during heating and cooling	LATP	--	No	--
$LiTiOPO_4$	Ti^{4+}	Detectable between 650 °C and 850 °C	LATP	--	No	--
$Mn_2P_2O_7$	Mn^{2+}	Detectable during heating and cooling	LMO-s and LATP	P1 and P2	Yes	--
$LiMnPO_4$	Mn^{2+}	Formation at 600 °C, strong increase to 850 °C, afterwards slight increase during cooling	LMO-s, Mn_2O_3, Mn_3O_4 and LATP	P3	Yes	47 wt%
$MnTiO_3$	Mn^{2+} and Ti^{4+} + Al^{3+} (dissolved)	Formation at 725 °C, strong increase to 900 °C, afterwards constant during cooling	Mn_2O_3, Mn_3O_4 and $LiTiOPO_4$, TiO_2	P4	Yes	28 wt%
$Li(Mn,Ti)_2O_4$	Mn^{3+} and Ti^{4+}	Formation at 875 °C, increase to 900 °C, afterwards decrease during cooling	Mn_3O_4 and TiO_2	P5	No	--
Cristobalite Phase M-PO_4	n/a	Detectable during holding step at 900 °C	Mn_3O_4 and Li_3PO_4	P5	No	--

4.5 Thermal Stability of LMO-l and LATP Powder Mixture

DSC-TG and MS Measurements

The DSC-TG and MS measurements of the 1:1 vol% LMO-l and LATP powder mixture (**Fig. 4.9**) show a mass loss of 1.6 % up to 400 °C related to the evaporation of humidity and the decomposition of carbonates. Four endothermic peaks can be identified: P1 at 662 °C, P2 at 707 °C, P3 at 816 °C and P4 at 915 °C. The highest mass loss of 2.1 % between ca. 625 °C and ca. 700 °C is related to P1 and goes along with O_2 and CO_2 formation. The subsequent mass loss is 0.3 % up to ca. 770 °C. Between ca. 770 °C and ca. 860 °C, the rate of mass loss increases again and oxygen formation along with a mass loss of 0.8 % can be detected. This temperature range is in good accordance with the broad endothermic region of the P3 peak. At 916 °C (P4) a low signal of oxygen can be seen in the MS data. The accompanied mass loss is 0.4 % to a total relative mass of 94.8 % at 1000 °C.

Since the DSC-TG curves of the pure starting powders LMO-l and LATP show no reactions and mass losses (**Fig. 4.4b**), it is evident that the powder mixture is thermally not stable. Oxygen formation indicates reduction processes between LMO-l and LATP. The large CO_2 signal, particularly up to 400 °C (mass loss 1.6 %), suggests a high amount of carbonates or residues from the synthesis of the purchased LMO-l powder.

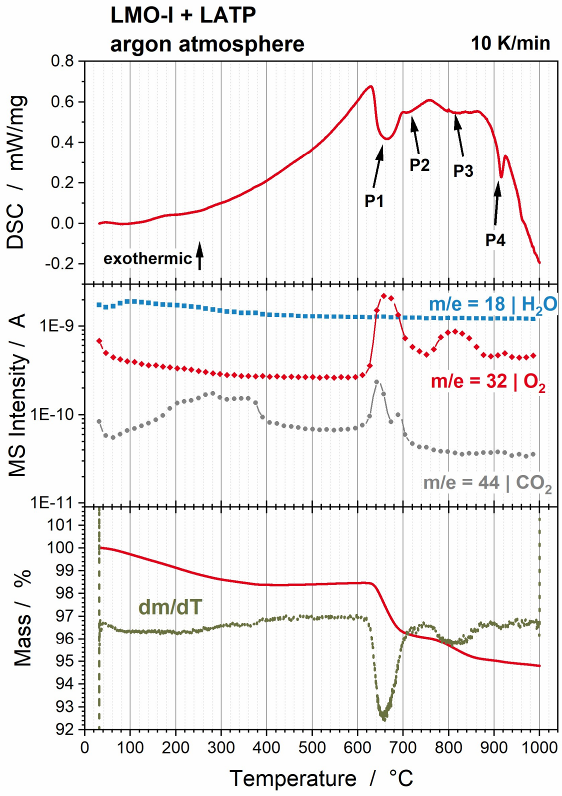

Fig. 4.9 Results of the DSC-TG and MS analyses of a 1:1 vol% LMO-l + LATP powder mixture measured in argon atmosphere with 10 K/min. Published by and reprinted from Rumpel et al.[130] (published under CC-BY license in Royal Society of Chemistry: *Materials Advances* 2022).

HT-XRD Measurements and Rietveld Refinements

The form integrity test of the LMO-l + LATP pellet showed no deformation up to 1000 °C so that 1000 °C was chosen as the maximum temperature for the HT-XRD measurements. The XRD patterns incl. the Rietveld refinements show the formation of mixed phases already at 500 °C (**Fig. 4.10**) and a subsequent change in the reflection profiles at 700 °C and 1000 °C. The Rietveld refinements were highly accurate and the results of the calculated weight percentages are shown in **Fig. 4.11** as a function of temperature. The 58 wt% of LMO-l is already decreased to 16 wt% at 500 °C. This decrease and the subsequent vanishing of LMO-l at 650 °C go along with the formation and subsequent increase of $LiMn_2O_4$ (LMO-s) and Mn_3O_4. LMO-s strongly decreases at 650 °C and disappears at 700 °C, which is accompanied by a strong increase in Mn_3O_4 to a maximum of 44 wt% at 700 °C. The decomposition of LATP to Li_3PO_4 and TiO_2 starts at 525 °C and is finalized at 775 °C. At 725 °C the maximum of Li_3PO_4 is 38 wt% and of TiO_2 is 8 wt%. $LiTiOPO_4$ is additionally formed at 675 °C and goes along with a slight decrease of the Li_3PO_4 and TiO_2 amounts. The formation of the first reaction products of LMO-l and LATP can be detected at 500 °C ($LiMnPO_4$, LMP), 575 °C ($Li(Mn,Ti)_2O_4$) and 700 °C ($MnTiO_3$). The amount of LMP significantly increases from 2 wt% at 675 °C to 16 wt% at 875 °C, which goes along with the vanishing of $LiTiOPO_4$ at 875 °C. In parallel, the amount of $MnTiO_3$ increases to 24 wt% at 850 °C. The source of Mn is Mn_3O_4, since the reaction to $LiMnPO_4$ and $MnTiO_3$ is accompanied by a significant decrease of Mn_3O_4. The formation of $Li(Mn,Ti)_2O_4$ at 575 °C goes along with the reduction of LMO-s and remains quite constant at ca. 5 wt% up to 950 °C. At 875 °C the formation of a cristobalite M-PO_4 (M = Ti^{3+} or Mn^{3+}) can be detected. The trend is comparable with the LMO-s + LATP sample discussed before. The M-PO_4 formation is accompanied by significant drops in the amounts of Li_3PO_4 to 3 wt% and $LiMnPO_4$ to 5 wt% during the holding step. Meanwhile, the amounts of $MnTiO_3$ and $Li(Mn,Ti)_2O_4$ increase to 38 wt% and 14 wt%, respectively, during the holding step at 1000 °C. Since, the Ti-containing species increases parallel to M-PO_4, the transition metal in the M-PO_4 phase is most likely Mn or is represented by the formula $Li_{x/2}Mn_xAl_{1-3x/2}PO_4$ as discussed in the LMO-s + LATP section. The amount of M-PO_4 is 28 wt% during the holding step. In the subsequent cooling, M-PO_4 vanishes again at 875 °C. After that, the amount of LMP is higher and the amount of Li_3PO_4 is lower than before the M-PO_4 formation. Additionally, the amount of $MnTiO_3$ and $Li(Mn,Ti)_2O_4$ is lower than during the holding step. Nevertheless, no further reactions take place during the cooling step. The final composition after cooling to 30 °C is: 38 wt% $LiMnPO_4$, 30 wt% $MnTiO_3$, 18 wt% Li_3PO_4, 11 wt% $Li(Mn,Ti)_2O_4$ and 3 wt% Mn_3O_4 (**Fig. 4.11**).

The reaction products of the LMO-l + LATP sample are comparable to the LMO-s + LATP sample. LATP decomposes to Li_3PO_4, TiO_2 and $LiTiOPO_4$ and LMO-l decomposes to LMO-s and Mn_3O_4. These species are the educts of subsequent reactions to $LiMnPO_4$, $MnTiO_3$ and

Li(Mn,Ti)$_2$O$_4$. Al-containing phases cannot be detected. This indicates that Al is dissolved in the other crystal lattices or the Al-containing phases are below the resolution limit.

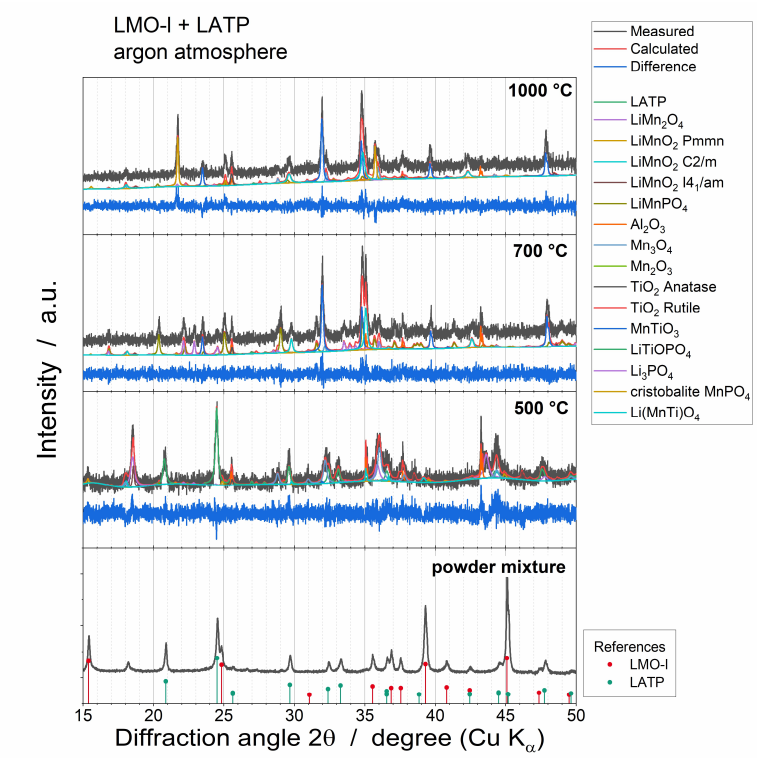

Fig. 4.10 Selected HT-XRD patterns and their Rietveld refinements of the LMO-l + LATP pellet sintered in argon atmosphere at 500 °C, 700 °C and 1000 °C. Additionally, the XRD pattern of the pristine LMO-l + LATP powder is presented. Published by and reprinted from Rumpel et al.[130] (published under CC-BY license in Royal Society of Chemistry: *Materials Advances* 2022).

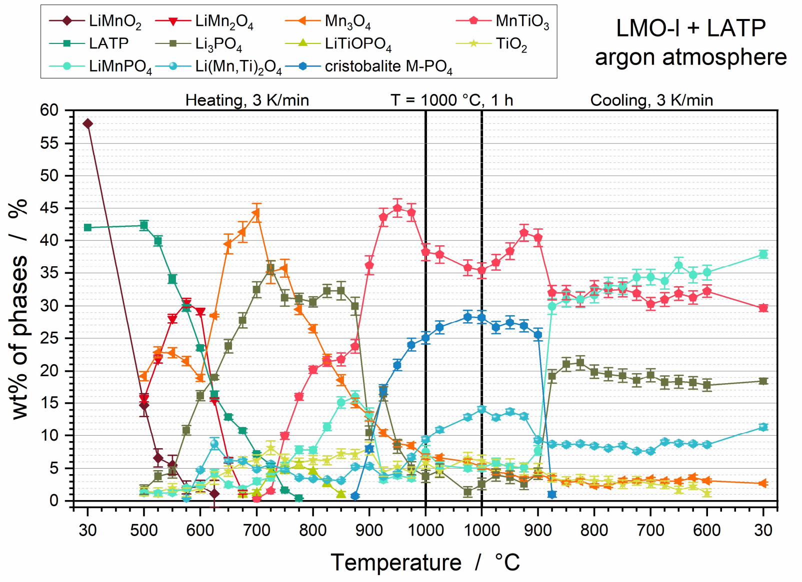

Fig. 4.11 Weight percentages wt% of crystalline phases obtained by Rietveld refinement of the LMO-l + LATP pellet as a function of the annealing temperature. Heating up to 1000 °C with 3 K/min, holding step at 1000 °C for 1 h, and afterward cooling with 3 K/min to 30 °C. Published by and reprinted from Rumpel et al.[130] (published under CC-BY license in Royal Society of Chemistry: *Materials Advances* 2022).

SEM Images and EDS Analyses

The SEM cross-section of the LMO-l + LATP pellet sintered at 800 °C for 2 h in argon atmosphere shows a porous microstructure caused by oxygen formation (**Fig. 4.12a**). Four different contrasts for the grains with grain sizes of ca. 0.1 µm to ca. 1 µm can be detected. The four different regions correspond to the five crystalline phases detected via HT-XRD. The light contrast grain at position 1 (**Fig. 4.12a**) represents the Mn_3O_4 since only Mn and O can be detected in the EDS analysis (**Fig. 4.12b**). Grains appearing with a second contrast (**Fig. 4.12a**, position 2) show grain sizes of a few 100 nm and belong to $MnTiO_3$ or $Li(Mn,Ti)_2O_4$. Since a quantitative analysis of the EDS data is not possible, since Li atoms are below the resolution limit, a clear separation of $MnTiO_3$ and $Li(Mn,Ti)_2O_4$ is not possible. Nevertheless, traces of Al can be detected at position 2, which indicates that Al is dissolved in these crystal lattices. Moreover, $LiMnPO_4$ (Pos 3) and Li_3PO_4 (Pos 4) can be detected.

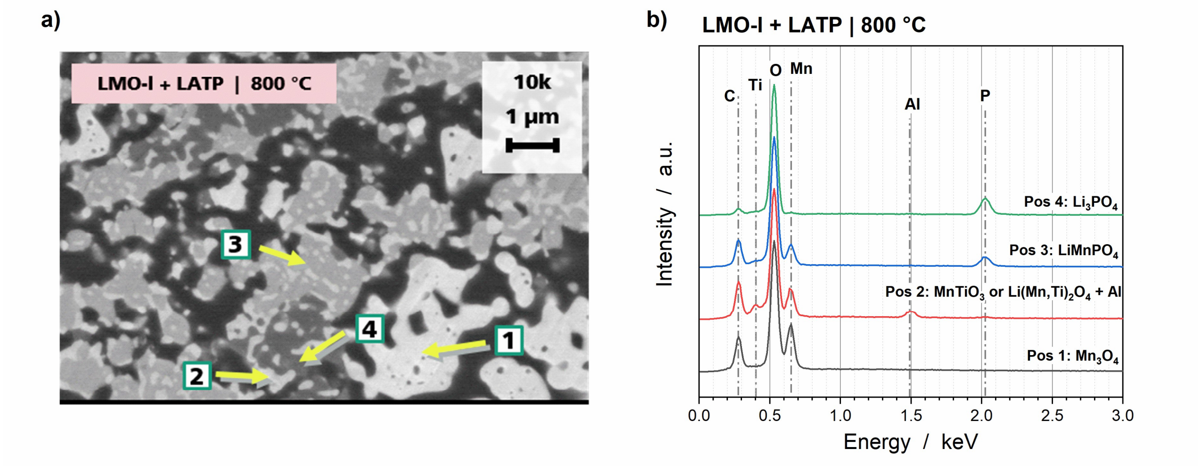

Fig. 4.12 a) SEM cross-section and **b)** EDS analyses of a LMO-l + LATP pellet sintered for 2 h at 800 °C in argon atmosphere. Published by and reprinted from Rumpel et al.[130] (published under CC-BY license in Royal Society of Chemistry: *Materials Advances* 2022).

Correlation and Summary

The findings obtained from the HT-XRD (**Fig. 4.11**) and DSC-TG incl. MS (**Fig. 4.9**) measurements of the LMO-l and LATP powder mixture are summarized in **Table 4.2**. The mixture of LMO-l and LATP is thermally not stable in an argon atmosphere. LATP starts to decompose into Li_3PO_4 and TiO_2 at 525 °C as well as $LiTiOPO_4$ at 675 °C (**Fig. 4.11**). In contrast, high amounts of LMO-l are already decomposed to LMO-s and Mn_3O_4 at 500 °C. The oxidation states of Mn are 3+ in LMO-l, 3+ and 4+ in LMO-s and 2+ and 3+ in Mn_3O_4. Consequently, this decomposition is a disproportionation reaction of LMO-l, thus same parts of Mn^{3+} are oxidized and reduced. Consequently, exothermic or endothermic peaks and oxygen loss cannot be detected below 620 °C in the DSC curves. The first endothermic peak at 662 °C (**Fig. 4.9**, P1) goes along with the highest oxygen gassing and a strong increase in the Mn_3O_4 amount up to 700 °C (44 wt%, **Fig. 4.11**), which is accompanied by the disappearance of LMO-l (650 °C) and LMO-s (700 °C). Consequently, a steady reduction of Mn takes place by forming Mn_3O_4. In addition, the reaction of Li_3PO_4, TiO_2 and $LiTiOPO_4$ with Mn_3O_4 to $LiMnPO_4$ and $MnTiO_3$ results in a further reduction of Mn, since the oxidation state of Mn is 2+ in $LiMnPO_4$ and $MnTiO_3$. Both species significantly start to increase at 700 °C, which goes along with the decrease of Mn_3O_4 and Li_3PO_4 as well as the vanishing of $LiTiOPO_4$. This temperature range can be related to the endothermic peaks P2 at 707 °C and P3 at 816 °C (**Fig. 4.9**), which are accompanied by an oxygen loss, which supports the Mn reduction. Mn and Ti in $Li(Mn,Ti)_2O_4$ have oxidation states of 3+ and 4+, respectively. The first increase of $Li(Mn,Ti)_2O_4$ to 5 wt% at 575 °C goes along with the decrease of LMO-s so that a reduction of Mn^{4+} to Mn^{3+} can be suggested, which might also correspond with the oxygen loss at the first endothermic peak in addition to the Mn_3O_4 formation (**Fig. 4.9**, P1). The subsequent formation of $Li(Mn,Ti)_2O_4$ starts at 875 °C. It is accompanied by an increase of $MnTiO_3$ and the formation of the cristobalite $MnPO_4$ as well as significant drops in the amounts of $LiMnPO_4$ and Li_3PO_4. This reaction can be related to the endothermic peak at 915 °C (**Fig. 4.9**, P4). During the cooling step, $MnPO_4$ disappears at 875 °C and $LiMnPO_4$ is formed in a higher amount than before the $MnPO_4$ formation. In parallel, the amount of Li_3PO_4 is reduced. Additionally, low reductions of the $MnTiO_3$ and $Li(Mn,Ti)_2O_4$ amounts compared to the amounts in the holding step can be detected. During the subsequent cooling, these amounts remain constant and the final composition is: 38 wt% $LiMnPO_4$, 30 wt% $MnTiO_3$, 18 wt% Li_3PO_4, 11 wt% $Li(Mn,Ti)_2O_4$ and 3 wt% Mn_3O_4. EDS analysis of the SEM cross-section confirms this composition (**Fig. 4.12**). Additionally, Al can be detected in the $MnTiO_3$ and $Li(Mn,Ti)_2O_4$ grains, which indicates that Al is dissolved in their crystal lattices. Due to the oxygen gassing, the microstructure is porous.

Table 4.2 Summary of the results and findings of the analyses of the thermal stability of LMO-l and LATP. DSC Peak positions: 662 °C (P1), 707 °C (P2), 816 °C (P3) and 915 °C (P4).

Published by and reprinted from Rumpel et al.[130] (published under CC-BY license in Royal Society of Chemistry: *Materials Advances* 2022).

Detected Phases	Valence of Transition Metals	Temperature Range and Trend	Possible Educts	Possible corre-spond-ding DSC Peaks	Expected Oxygen Formation and Mass Loss	Final Composition
$LiMnO_2$ (LMO-l)	Mn^{3+}	Decrease already < 500 °C Disappearance at 650 °C	--	--	--	--
$Li_{1.3}Al_{0.3}Ti_{1.7}(PO_4)_3$ (LATP)	Al^{3+} and Ti^{4+}	Decrease starts at 525 °C Disappearance at 800 °C	--	--	--	--
$LiMn_2O_4$ (LMO-s)	Mn^{3+} and Mn^{4+}	Detectable between 500 °C and 675 °C	LMO-l	--	No	--
Mn_3O_4	Mn^{2+} and Mn^{3+}	Formation already < 500 °C Strong increase up to 700 °C, afterwards steady decrease to 1000 °C, during cooling constant	LMO-l and LMO-s	P1	Yes	3 wt%
Li_3PO_4	--	Strong increase to 700 °C Strong decrease between 875 °C heating and 875 °C cooling, than increase	LATP	--	No	18 wt%
TiO_2	Ti^{4+}	Detectable during heating and cooling	LATP	--	No	--
$LiTiOPO_4$	Ti^{4+}	Detectable between 675 °C and 850 °C	LATP	--	No	--
$LiMnPO_4$	Mn^{2+}	Formation at 500 °C Increase between 675 °C and 875 °C Decrease between 875 °C heating and 875 °C cooling, than increase	Mn_3O_4 and $LiTiOPO_4$, LATP and during cooling: M-PO_4	P3	Yes	38 wt%
$MnTiO_3$	Mn^{2+} and Ti^{4+} + Al^{3+} (dissolved)	Formation at 700 °C Strong increase to 950 °C	Mn_3O_4 and $LiTiOPO_4$, TiO_2	P2 and P3	Yes	30 wt%
$Li(Mn,Ti)_2O_4$	Mn^{3+} and Ti^{4+} + Al^{3+} (dissolved)	Formation at 575 °C Strong increase to 1000 °C	Mn_3O_4, LMO-s and LATP, TiO_2, $LiTiOPO_4$	P1 and P3	Yes (at P1)	11 wt%
Cristobalite Phase M-PO_4	n/a	Detectable between 875 °C heating and 875 °C cooling	Mn_3O_4, $MnTiO_3$, $LiMnPO_4$ and Li_3PO_4	P4	No	--

4.6 Thermal Stability of LMP and LATP Powder Mixture

DSC-TG and MS Measurements

The TG curve (**Fig. 4.13**) of the 1:1 vol% LMP + LATP powder mixture shows a steady mass loss of 1.2 wt% up to 1000 °C. CO_2 signals could be detected via MS between 200 °C and 400 °C as well as above 800 °C. No oxygen loss can be detected. The pure LATP and pure LMP samples show mass losses of 0.1 wt% and 1.8 wt% (**Fig. 4.4b**), respectively, so that the CO_2 mass loss relates to the residues of the LMP synthesis or carbonate formation (i.e. Li_2CO_3) during storage, which is well known from the literature.[134,135] The DSC curve shows an exothermic peak at 777 °C (**Fig. 4.13**, P1) and an endothermic peak at 872 °C (**Fig. 4.13**, P2), which cannot be reasonably correlated to the mass losses due to CO_2 formation. The endothermic peak at 872 °C can probably be related to the endothermic peak at 921 °C of pure LMP (**Fig. 4.4b**). The exothermic peak at 777 °C indicates that a new reaction between LMP and LATP takes place.

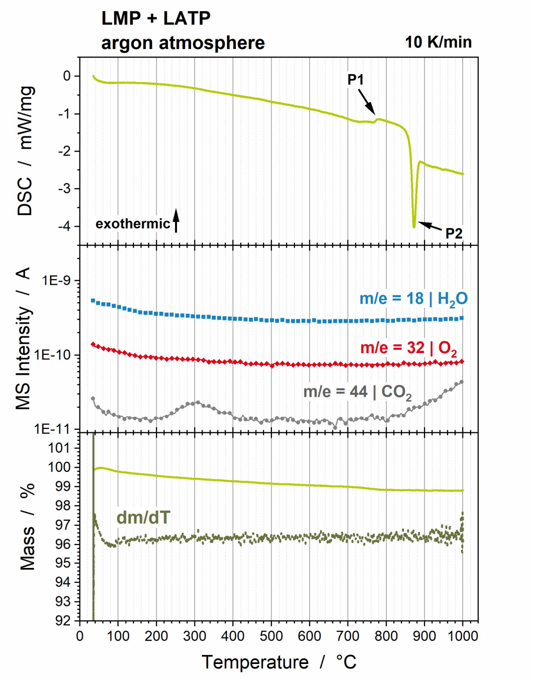

Fig. 4.13 Results of the DSC-TG and MS analyses of a 1:1 vol% LMP + LATP powder mixture measured in argon atmosphere with 10 K/min. Published by and reprinted from Rumpel et al.[130] (published under CC-BY license in Royal Society of Chemistry: *Materials Advances* 2022).

HT-XRD Measurements and Rietveld Refinements

The maximum temperature for the HT-XRD measurements is set to 800 °C since the form integrity test shows no deformation of the pellet up to 800 °C. The XRD patterns incl. Rietveld refinement still show crystalline phases of LATP and LMP at 800 °C (**Fig. 4.14**). At 700 °C, significant reflections of $LiTiOPO_4$ can be detected at 27.04°, 27.42° and 27.95° (ICSD 153522). The calculated weight percentages of all HT-XRD patterns are demonstrated in **Fig. 4.15**. The initial values of LATP and LMP are 41 wt% and 59 wt%, respectively. At 680 °C the formation of $LiTiOPO_4$ takes place. Its amount increases to 7 wt% during the holding step at 800 °C, which is accompanied by slight decreases of 5 wt% for LATP and 2 wt% for LMP. The final composition after cooling is: 36 wt% LATP, 57 wt% LMP and 7 wt% $LiTiOPO_4$.

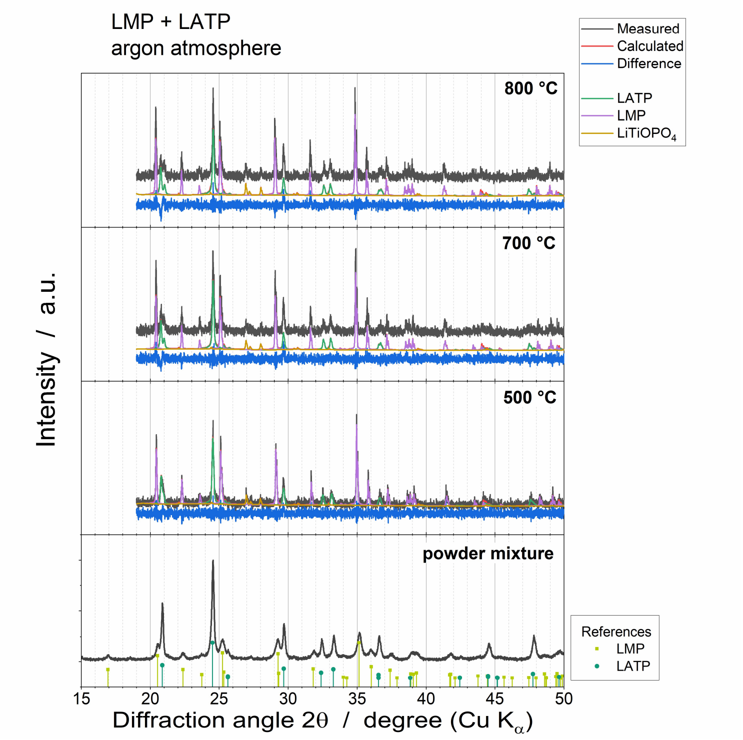

Fig. 4.14 Selected HT-XRD patterns and their Rietveld refinements of the LMP + LATP pellet sintered in argon atmosphere at 500 °C, 700 °C and 800 °C. Additionally, the XRD pattern of the pristine LMP + LATP powder is presented. Published by and reprinted from Rumpel et al.[130] (published under CC-BY license in Royal Society of Chemistry: *Materials Advances* 2022).

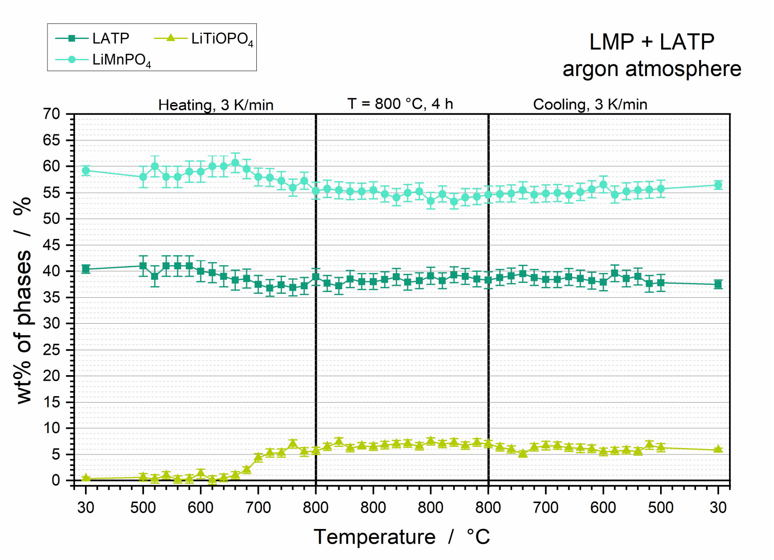

Fig. 4.15 Weight percentages wt% of crystalline phases obtained by Rietveld refinement of the LMP + LATP pellet as a function of the annealing temperature. Heating up to 800 °C with 3 K/min, holding step at 800 °C for 4 h, and afterward cooling with 3 K/min to 30 °C. Published by and reprinted from Rumpel et al.[130] (published under CC-BY license in Royal Society of Chemistry: *Materials Advances* 2022).

SEM Images and EDS Analyses

The SEM cross-section of the LMP + LATP pellet sintered at 800 °C for 2 h in an argon atmosphere shows a dense microstructure with a low degree of porosity. The grain sizes of pure LMP and pure LATP grains (**Fig. 4.16a**, Pos1 and Pos2) are between 0.2 µm and 2 µm. The EDS analyses reveal that the light contrast regions correspond to LMP and the dark contrast regions correspond to LATP (**Fig. 4.16b**). A low amount of a third contrast (**Fig. 4.16a,** Pos3) can be detected, which exclusively shows signals of the elements Ti, O and P in the EDS analysis (**Fig. 4.16b**), which corresponds to LiTiOPO$_4$. Further areas cannot be detected.

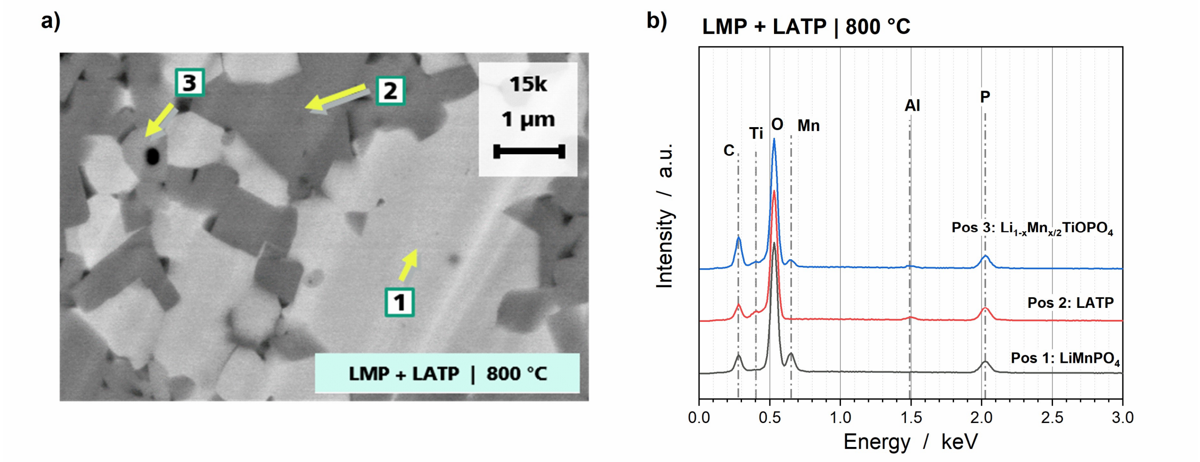

Fig. 4.16 a) SEM cross-section and **b)** EDS analyses of a LMP + LATP pellet sintered for 2 h at 800 °C in argon atmosphere. Published by and reprinted from Rumpel et al.[130] (published under CC-BY license in Royal Society of Chemistry: *Materials Advances* 2022).

Correlation and Summary

The powder mixture of LMP and LATP is to a high degree thermally stable up to 800 °C in argon atmosphere. A summary of the results of the HT-XRD (**Fig. 4.15**) and DSC-TG incl. MS (**Fig. 4.13**) measurements can be found in **Table 4.3**. The LMP and LATP amounts decrease at 680 °C by 2 wt% and 5 wt%, respectively, which is accompanied by the formation of 7 wt% LiTiOPO$_4$ (**Fig. 4.15**). The final composition after cooling is: 57 wt% LMP, 36 wt% LATP and 7 wt% LiTiOPO$_4$. The formation of LiTiOPO$_4$ can be related to the exothermic peak at 777 °C detected via DSC (**Fig. 4.13**, P1). The thermal stability is limited by the intrinsic decomposition of LMP, which can be detected as an endothermic peak at 921 °C for pure LMP (**Fig. 4.4b**) and 872 °C in combination with LATP (**Fig. 4.13**, P2), since LATP particles can function as reaction seeds and accelerate the decomposition process. The microstructure has a low degree of pores and the EDS analyses confirm the three crystalline phases detected in the HT-XRD measurements.

The decreases in LMP and LATP indicate that both components participate in the formation of LiTiOPO$_4$. Therefore, two points need to be discussed: i) the remaining Mn must react to another species but no evidence of a further crystalline phase could be found in the XRD diffractograms; ii) $LiTiOPO_4$ formation requires an additional oxygen atom, since the O/P ratios are 5 for $LiTiOPO_4$ and 4 for LMP and LATP.

Since no further crystalline Mn-containing phases can be detected, the substitution of two Li^+ ions or one Ti^{4+} ion by Mn in the $LiTiOPO_4$ lattice is thinkable. The possibility of the substitution of two Li^+ ions by Mn^{2+} has been reported for the materials $LiMnPO_4$ and $LiMnVO_4$.[138,139] With reference to these publications, the chemical formula of the oxy-phosphate would be $Li_{1-x}Mn_{x/2}TiOPO_4$. The substitution of Ti^{4+} by Mn^{4+} requires the oxidation of Mn^{2+} of LMP and would result in the formula $LiMn_{1-x}Ti_xOPO_4$. Since no increase in the total mass can be detected in the TG measurement, oxidation of the Mn^{2+} by O_2 impurities in the argon atmosphere can be excluded. The quantitative analysis of the amounts of substances leads to the formation of 0.105 mmol oxy-phosphate, which is equal to 7 wt% (17.5 mg) of the 250 mg pellet. The decrease of 2 wt% LMP and 5 wt% LATP equates to 0.032 mmol Mn and 0.055 mmol Ti, which is in total 0.087 mmol. Consequently, the formation of 0.105 mmol $Li_{1-x}Mn_{x/2}TiOPO_4$ cannot solely be explained by the decrease of the crystalline LMP and LATP, further sources for Mn and Ti need to be considered. A comparable consideration has to be done for the additional oxygen atom in $Li_{1-x}Mn_{x/2}TiOPO_4$ since additional 1.7 mg O^{2-} (equates to 0.7 wt% of the 250 mg pellet) are required for the formation of 0.105 mmol of the oxy-phosphate. However, the TG curve (**Fig. 4.13**) shows no increase in mass but a mass loss of 1.2 wt% up to 1000 °C due to CO_2 formation. CO_2 gassing can be caused by the decomposition of carbon-containing residues from the sol-gel synthesis, such as Li_2CO_3 or $MnCO_3$, which additionally can be formed during storage.[134,135] Simplified formulations of these reactions can be:

$$Li_2CO_3 \rightarrow 2 \cdot Li^+ + O^{2-} + CO_2 \uparrow \; or \; MnCO_3 \rightarrow Mn^{2+} + O^{2-} + CO_2 \uparrow$$

The decomposition of these carbonates would additionally supply O^{2-} for the oxy-phosphate formation. Consequently, the existence of Li_2CO_3 and $MnCO_3$ and their decomposition would most likely explain the origin of the additional Mn and O. However, this hypothesis must be tested and verified in further studies. In addition, the synthesis route and storage of the starting materials should be optimized in order to achieve higher purity and clear the material from remaining carbonates. Probably, a further enhancement of the thermal stability can be achieved without an oxygen source for the reaction to $Li_{1-x}Mn_{x/2}TiOPO_4$, so that its formation can probably be completely inhibited.

Table 4.3 Summary of the results and findings of the analyses of the thermal stability of LMP and LATP. DSC Peak positions: 777 °C (P1) and 872 °C (P2).

Published by and reprinted from Rumpel et al.[130] (published under CC-BY license in Royal Society of Chemistry: *Materials Advances* 2022).

Detected Phases	Valence of Transition Metals	Temperature Range and Trend	Possible Educts	Possible corresponding DSC Peaks	Expected Oxygen Formation and Mass Loss	Final Composition
$LiMnPO_4$ (LMP)	Mn^{2+}	Decrease of 2 wt% at 680 °C, afterwards constant	--	--	--	57 wt%
$Li_{1.3}Al_{0.3}Ti_{1.7}(PO_4)_3$ (LATP)	Al^{3+} and Ti^{4+}	Decrease of 5 wt% at 680 °C, afterwards constant	--	--	--	36 wt%
$Li_{1-x}Mn_{x/2}TiOPO_4$	Mn^{2+} and Ti^{4+}	Increase to 7 wt% at 680 °C, afterwards constant	LATP, LMP and probably Carbonates	P1	No	7 wt%

4.7 Comparison of the Powder Mixtures

The investigation of the thermal stabilities of the active materials LMO-s, LMO-l or LMP in combination with LATP showed that only the LMP and LATP powder mixture has sufficient thermal stability. LMO-s and LMO-l decomposed already < 500 °C in combination with LATP in an argon atmosphere.

The basis of the thermodynamical consideration of the powder mixtures is the diffusion of the elements along the concentration gradients between the two components in order to obtain equilibrium conditions for the chemical potentials. If diffusion between two components is not possible, either mixed phase formation takes place or the material combination remains thermally stable. A deeper understanding and better description of the interdiffusion can be obtained by taking the Hume-Rothery rules for substitutional solid solutions into account (**Chapter 2.4**): valence factor, size factor, chemical affinity and lattice structure.[90] Considering Mn and Ti or Al in the active materials and LATP, respectively, interdiffusion leads to the substitution of Mn in the active material lattice by Ti or Al in parallel to the substitution of Ti or Al in the LATP lattice by Mn. The valence of the substitution element must be the same as the valence of the substituted element in the host material to maintain electroneutrality. The oxidation states of Al and Ti in LATP are 3+ and 4+, respectively. Since the oxidation states of Mn are 3+ and 4+ in LMO-s, 3+ in LMO-l and 2+ in LMP, in some cases reduction or oxidation of Mn must take place for interdiffusion. Furthermore, the ionic radii should not differ by more than 15 %. The ionic radii are 58 pm for Mn^{3+}, 53 pm for Mn^{4+}, 61 pm for Ti^{4+} and 54 pm for Al^{3+}.[140] Thus, the difference of Mn^{3+} and Al^{3+} is 7 % and of Mn^{4+} and Ti^{4+} is 13 %, so that a substitution is in general possible. Moreover, chemical affinity describes the capability of different chemical species to form a new compound or a mixed phase, which may limit the interdiffusion. Finally, the more similar the two lattice structures are, the greater the capability of interdiffusion. Since the spinel structure of LMO-s, the layered structure of LMO-l and the olivine structure of LMP significantly differ from the NASICON structure type of LATP, a high dissimilarity is given, which is not favorable for interdiffusion. The first evaluation of these rules leads to the conclusion that interdiffusion is unlikely since the oxidation or reduction of Mn is necessary and the structure types significantly differ. This could be confirmed by the experimental results obtained from HT-XRD, DSC-TG incl. MS and SEM/EDS.

The active materials LMO-s and LMO-l show decompositions below 500 °C and they vanish at 650 °C in combination with LATP (**Fig. 4.7** and **Fig. 4.11**). LATP starts to decompose at higher temperatures but it disappears in both samples at 800 °C. The decomposition products of both powder mixtures are also comparable. LATP decomposes to Li_3PO_4, TiO_2 and $LiTiOPO_4$. LMO-s decomposes to Mn_3O_4 and Mn_2O_3, which goes along with the reduction of the Mn transition metal from Mn^{3+} and Mn^{4+} in LMO-s to Mn^{3+} in Mn_2O_3 as well as Mn^{2+} and Mn^{3+} in Mn_3O_4. LMO-l (Mn^{3+}) decomposes to Mn_3O_4 (Mn^{2+} and Mn^{3+}). These reduction processes are accompanied by oxygen gassing (**Fig. 4.5** and **Fig. 4.9**), which makes the decomposition thermodynamically more favorable due to a significant increase in entropy. Since the decomposition processes of LMO-l and LMO-s are similar, the subsequent reactions of the decomposition products of LMO-l or LMO-s and LATP lead to the same reaction products at higher temperatures: mainly $LiMnPO_4$, $MnTiO_3$ and $Li(Mn,Ti)_2O_4$ (**Table 4.4**). In addition, it means a subsequent decrease of the oxidation state of Mn to 2+, which is also accompanied by oxygen formation. This causes mass losses of 5.2 % (LMO-l + LATP) and 7.7 % (LMO-s + LATP) at 1000 °C (**Fig. 4.5** and **Fig. 4.9**). Additionally, the gas formation results in a porous microstructure after the sintering process (**Fig. 4.8a** and **Fig. 4.12a**).

Consequently, the heat treatment of LMO-l and LMO-s in combination with LATP results in the complete decomposition of the starting powders and the formation of mixed phases accompanied by the reduction of Mn and the oxidation of oxygen.

In contrast to LMO-l and LMO-s, LMP shows high thermal stability in combination with LATP. Interdiffusion processes cannot be detected in the SEM/EDS analyses and only one additional mixed phase ($Li_{1-x}Mn_{x/2}TiOPO_4$) can be determined. However, the oxy-phosphate formation is probably related to residues of the sol-gel synthesis or carbonate formation during storage, since CO_2 gassing can be detected in the MS (**Fig. 4.13** max. mass loss 1.2 %) and an additional oxide source is necessary for the oxy-phosphate formation. The quantitative analyses of the HT-XRD and TG measurements additionally indicate that another Mn source is needed, which can be $MnCO_3$ left from synthesis. A further result of the quantitative analyses is that Mn might substitute two Li^+ ions in the crystal lattice of $LiTiOPO_4$ so that the formulation $Li_{1-x}Mn_{x/2}TiOPO_4$ is most likely. High thermal stability without significant gassing during the sintering process results in a dense microstructure (**Fig. 4.16a**).

In conclusion, LMO-l and LMO-s in combination with LATP are not feasible for bulk-cathodes for ASSBs because of the complete decomposition and a porous microstructure. In contrast, the LMP + LATP powder mixture shows high thermal stability and a dense microstructure with firmly bonded grain-to-grain contacts necessary for a fast Li-ion transfer. On that basis, LMP and LATP were chosen for subsequent tests of the thermal stability in combination with an electrically conductive component.

Table 4.4 Comparison of remaining components after cooling of the 1:1 vol% powder mixtures of various active materials and LATP.

	LATP	**$Li_{1-x}Mn_{x/2}TiOPO_4$**	**Li_3PO_4**	**Mn_3O_4**	**$LiMnPO_4$**	**$MnTiO_3$**	**$Li(Mn,Ti)_2O_4$**	**O_2 loss**
LMO-s + LATP	--	--	8 wt%	17 wt%	47 wt%	28 wt%	--	7.7 wt%
LMO-l + LATP	--	--	18 wt%	3 wt%	38 wt%	30 wt%	11 wt%	5.2 wt%
LMP + LATP	36 wt%	7 wt%	--	--	57 wt%	--	--	--

4.8 Thermal Stability of LMP and LATP Powder Mixture with Ag

Since the LMP + LATP powder mixture showed the most thermally stable characteristics, Ag was added. Ag was chosen since it has a lower tendency for alloy formation in comparison with other metals (i.e. Au)[141] and the noble metal is naturally resistant to oxidation. A 1:1:1 vol% powder mixture of LMP, LATP and Ag was prepared and its thermal stability was investigated via DSC-TG incl. MS, HT-XRD and Rietveld refinement as well as SEM/EDS. The particle sizes of the purchased Ag powder were between 48 nm and 78 nm (Nanografi®[142]).

DSC-TG and MS Measurements

The DSC-TG curves incl. MS data of the powder mixture LMP + LATP + Ag and the pure Ag powder are given in **Fig. 4.17a** and **Fig. 4.17b**, respectively. Both DSC curves show an endothermic peak at 969 °C (**Fig. 4.17a and b**, P2), which is in accordance with the melting point of 962 °C of the nanoparticulate Ag powder reported in the datasheet.[142] The powder mixture has an additional endothermic peak at 879 °C (**Fig. 4.17a**, P1), which can be correlated to the intrinsic decomposition of LMP, since it is in good accordance with the endothermic peak at 872 °C of the LMP + LATP powder mixture (**Fig. 4.13**, P2). An exothermic peak related to the $LiTiOPO_4$ formation due to the reaction of LMP and LATP at about 777 °C (**Fig. 4.13**, P1) cannot be detected.

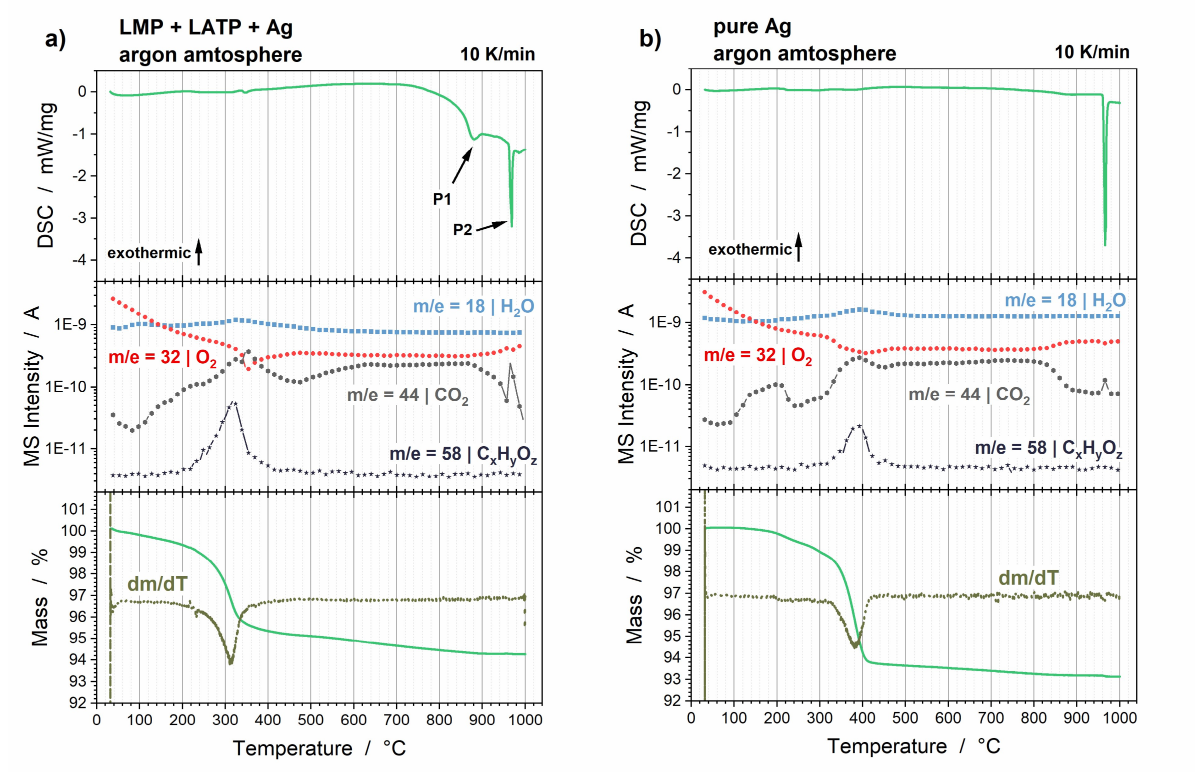

Fig. 4.17 Results of the DSC-TG and MS analyses of **a)** 1:1:1 vol% LMP + LATP + Ag powder mixture and **b)** pure Ag powder measured in argon atmosphere with 10 K/min. Published by and reprinted from Rumpel et al.[130] (published under CC-BY license in Royal Society of Chemistry: *Materials Advances* 2022).

The TG curve of the powder mixture (**Fig. 4.17a**) shows a significant mass loss of 4.7 % between 200 °C and 400 °C, which is accompanied by intensive CO_2 gassing and several $C_xH_yO_z$ formations with mass-to-charge ratios in the range of m/e = 40 to m/e = 87. In **Fig. 4.17a**, the signal of m/e = 58 is representative of the signals of the further ratios. That correlates to the combustion of the carbon coatings of the Ag nanoparticles, which is needed to inhibit the agglomeration of the nanoparticles after the manufacturing process so that long time storage of the nano-sized particles is possible. The mass loss of the pure Ag particles is in total 6.3 % at 1000 °C. Thus, the powder mixture shows a lower total mass loss of 5.7 % at 1000 °C.

HT-XRD Measurements and Rietveld Refinements

The HT-XRD measurements were performed with a maximum temperature of 800 °C. The XRD patterns incl. Rietveld refinement of the 1:1:1 vol% powder mixture of LMP, LATP and Ag before and after sintering at 800 °C for 4 h are demonstrated in **Fig. 4.18**. After sintering, no additional crystalline phases except the expected $LiTiOPO_4$ can be detected.

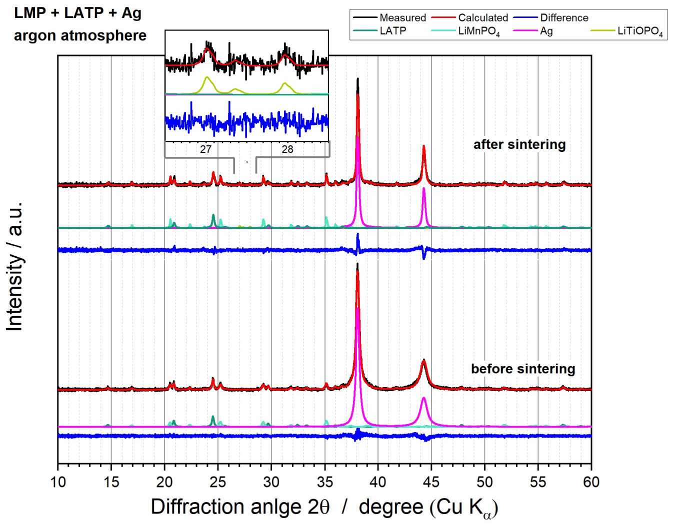

Fig. 4.18 HT-XRD patterns and their Rietveld refinements of the LMP + LATP + Ag pellet measured at RT before and after sintering in argon atmosphere at 800 °C for 4 h with a heating and cooling rate of 3 K/min. Published by and reprinted from Rumpel et al.[130] (published under CC-BY license in Royal Society of Chemistry: *Materials Advances* 2022).

The deduced weight percentages of all XRD patterns are shown in **Fig. 4.19**. Similar to the LMP + LATP sample, the increase of $LiTiOPO_4$ starts at 680 °C. However, the total weight fractions cannot be reliably used for quantitative analysis. Between 760 °C and 800 °C, the Ag amount significantly drops from 68 wt% to 43 wt%. This is most likely caused by Ag evaporation and a change in the Ag absorption factor.

Solid Ag has a saturation vapor pressure of 6.62 E-5 Pa at 800 °C, which corresponds to an evaporation rate of ca. 3 mg/(cm²·h).[143–145] That results in a theoretical evaporation of ca. 12 mg/cm² of Ag during the holding step at 800 °C for 4 h. However, this estimation must be considered carefully, as no information about the effective surface area of the nanosized particles is given and can be obtained in this study. Additionally, the surface area decreases due to particle growth during the annealing step (**Fig. 4.20a**), which complicates a more accurate calculation. However, the high evaporation rate at 800 °C indicates that the Ag evaporation is significant and might be a reason for the reduction of the Ag amount.

A further impact on the phase fraction analysis might have the change in the absorption factor A_{hkl} for Ag due to particle growth, which is a known error source for Rietveld refinement.[117,119]

The absorption factor A can be defined as a function of the particle size *d*:[119]

$$A_{hkl} = \frac{I}{I_0} = exp(-\mu \cdot d)$$

where I_0 is the initial intensity and I is the intensity of the radiation, which is not absorbed by the material and detected from the detector. The phase-specific absorption coefficient μ of Ag for Cu K_α radiation is 2289 cm^{-1}.[146] A decrease in the absorption factor means an increase in absorption of the radiation by the Ag particles. If the absorption by one phase (i.e. Ag) significantly increases, its detected scattered radiation decreases, thus the intensities in the diffractogram decrease. Additionally, it has an impact on the amount of scattering in the further phases (i.e. LMP, LATP). Consequently, the change in the absorption factor leads to wrong crystalline statistics and an error-prone quantification of the weight fractions. Applying the above equation, the absorption factor A_{hkl} is above 0.9 for Ag particle sizes below 1 µm, such as the starting Ag powder. After sintering at 800 °C, the SEM image reveals particle sizes of ca. 2 µm - 6 µm (**Fig. 4.20a**), which result in absorption factors between 0.6 (2 µm) and 0.2 (6 µm). Thus, the X-ray absorption by the Ag particles significantly increases with particle growth during the heat treatment so that the maximum intensities differ with temperature and a quantitative Rietveld refinement cannot be reliably done.

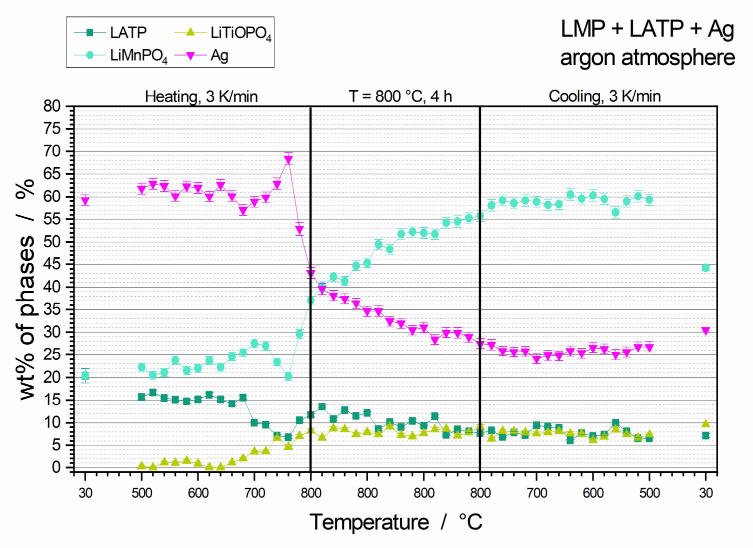

Fig. 4.19 Weight percentages wt% of crystalline phases obtained by Rietveld refinement of the LMP + LATP + Ag pellet as a function of the annealing temperature. Heating up to 800 °C with 3 K/min, holding step at 800 °C for 4 h, and afterward cooling with 3 K/min to 30 °C. Published by and reprinted from Rumpel et al.[130] (published under CC-BY license in Royal Society of Chemistry: *Materials Advances* 2022).

Although a quantitative analysis is not possible, the XRD diffractograms exhibit good thermal stability of the LMP + LATP + Ag powder mixture. The expected $LiTiOPO_4$ phase can be detected, but no additional phases are formed by adding Ag.

SEM Images and EDS Analyses

The SEM cross-section shows an almost dense microstructure with grain size in a range of 2 µm and 8 µm for LMP, LATP and Ag (**Fig. 4.20a**). The EDS analyses of the three different contrasts/positions show no interdiffusion (**Fig. 4.20b**). The first position belongs to $LiMnPO_4$ (**Fig. 4.20a,** Pos1), position 2 is related to LATP and the light contrast is Ag (**Fig. 4.20a**, Pos3). The EDS profiles of LATP, LMP and Ag only show the elements corresponding to their starting powders so that interdiffusion can be neglected (**Fig. 4.20b**).

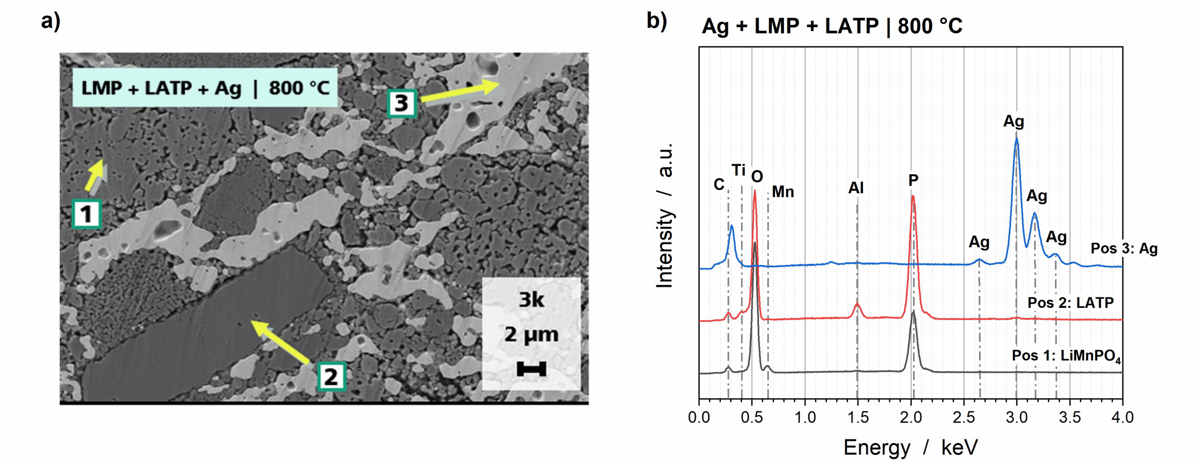

Fig. 4.20 a) SEM cross-section and **b)** EDS analyses of a LMP + LATP + Ag pellet sintered for 2 h at 800 °C in argon atmosphere. EDS energies for Ag are in accordance with literature.[147] Published by and reprinted from Rumpel et al.[130] (published under CC-BY license in Royal Society of Chemistry: *Materials Advances* 2022).

Correlation and Summary

The addition of Ag to the LMP + LATP powder mixture has no significant impact on the thermal stability in argon atmosphere. As expected from the LMP + LATP investigations, an oxyphosphate phase is formed at 680 °C, which is most likely $Li_{1-x}Mn_{x/2}TiOPO_4$ (**Fig. 4.19**). A quantitative analysis cannot be reliably done, since the adsorption factor of Ag decreases with particle growth during the sintering process. Nevertheless, no further crystalline phases could be detected. Interdiffusion processes between the grains of the components can be excluded (**Fig. 4.20b**). The nano-sized (48 nm - 78 nm) Ag particles are protected against agglomeration by a carbon surface coating, which causes gassing of CO_2 and heavy $C_xH_yO_z$ species (**Fig. 4.17**). This need to be considered for further efforts toward an ASSB bulk cathode. The SEM image (**Fig. 4.20a**) shows an almost dense microstructure, however, it appears slightly more porous than the LATP + LMP pellet (**Fig. 4.16a**).

In conclusion, the powder mixture of LMP, LATP and Ag can be a good starting point for electrochemical investigation and subsequent optimization of ASSB bulk cathodes.

4.9 Summary and Conclusion of the Investigation into Thermal Stabilities

The analyses of the thermal stabilities of the Mn-based active materials LMO-s, LMO-l and LMP in combination with the ceramic solid-state electrolyte LATP show that the 1:1 vol% powder mixture of LMP and LATP remains thermally stable after sintering at 800 °C in an argon atmosphere. Only low amounts of an additional $Li_{1-x}Mn_{x/2}TiOPO_4$ phase could be detected as of 680 °C. A quantitative analysis of the amounts of substances suggests that the formation of the additional phase is most likely intensified by the combustion of residues from the sol-gel synthesis or storage, such as Li_2CO_3 or $MnCO_3$. They function as additional Mn and O sources needed for the oxy-phosphate formation. That leads to the assumption that further optimization of the synthesis and storage of the starting materials might completely inhibit the oxy-phosphate formation. Nonetheless, the amount of the $Li_{1-x}Mn_{x/2}TiOPO_4$ phases is just 7 wt% and LATP and LMP remain at 36 wt% and 57 wt%, respectively (**Fig. 4.15**).

In contrast, LMO-s and LMO-l completely decompose up to 650 °C in combination with LATP (**Fig. 4.7** and **Fig. 4.11**). Their behaviors are very similar since the decompositions go along with the reduction of the Mn transition metal. LMO-s (Mn^{3+} and Mn^{4+}) decomposes to Mn_2O_3 (Mn^{3+}) and Mn_3O_4 (Mn^{2+} and Mn^{3+}). LMO-l (Mn^{3+}) decomposes to Mn_3O_4 (Mn^{2+} and Mn^{3+}). LATP vanishes at 800 °C and decomposes to Li_3PO_4, TiO_2 and $LiTiOPO_4$. These products of the intrinsical decompositions are the educts for further reactions to $LiMnPO_4$, $Li(Mn,Ti)_2O_4$ or $MnTiO_3$. In the case of $MnTiO_3$ and $LiMnPO_4$, a subsequent reduction to Mn^{2+} takes place.

The reduction of Mn goes along with the oxidation of O^{2-} and, consequently, O_2 gassing. The mass losses due to oxygen gassing of the LMO-s + LATP and LMO-l + LATP powder mixtures are 7.7 wt% and 5.2 wt%, respectively (**Fig. 4.5** and **Fig. 4.9**). In contrast, LMP + LATP shows a mass loss of 1.2 wt%, which can be completely correlated with CO_2 formation, since no oxygen signal could be detected via MS (**Fig. 4.13**). The low gassing of the LMP + LATP sample results in a dense microstructure with grain sizes for LMP and LATP between 0.2 µm and 2 µm (**Fig. 4.16a**). The high gassing of the LMO-s + LATP and LMO-l + LATP samples results in very porous microstructures with grain sizes of the various mixed phases below 1 µm (**Fig. 4.8** and **Fig. 4.12**).

The reduction of the Mn transition metal and the parallel oxygen gassing are the main driving forces for the mixed phase formation. Consequently, LMP remains thermally stable, since the oxidation state of Mn is 2+ and no subsequent reduction is possible. Interdiffusion processes between LMP and LATP could not be detected.

The addition of Ag particles to the LMP and LATP powder mixture does not change the thermal stability (**Fig. 4.18**). Except for the expected oxy-phosphate, no further mixed phases could be detected. The microstructure of the pellet sintered at 800 °C appears slightly more porous than the LATP + LMP pellet (**Fig. 4.20a**) since combustion of the carbon coating of the Ag nanoparticles leads to CO_2 and $C_xH_yO_z$ (m/e > 40) gassing (**Fig. 4.17**).

However, the combination of LMP, LATP and Ag can be a starting point for further investigations of bulk cathodes for ASSBs. Further optimization of the composition and the sintering process should be validated by electrochemical measurements. A perfect ratio of active material, solid-state electrolyte and electrical conductor regarding tortuosity and percolation need to be found to achieve high energy densities and a good electrochemical performance.

5 Impact of the Sintering Additive Li_3PO_4 on the Sintering Behavior, Microstructure and Electrical Properties of LATP

One possible approach to inhibit interdiffusion processes and reduce the formation of mixed phases is to reduce the processing temperature. Additionally, the production cost and the CO_2 emission due to manufacturing might be reduced. However, firmly-bonded contacts between the active material and electrolyte material as well as between the electrolyte particles are necessary for good charge transfer or ionic conductivity. Thus, sintering is unavoidable and the sintering temperature needs to be reduced. For that purpose, sintering additives can be used to accelerate the sintering and densification processes. For instance, additives with a lower melting temperature than the sintering temperature of the host material cause liquid phase sintering. The liquid phase of the melted additive enhances particle rearrangement, mass transport and diffusion, which influence densification, grain growth, the nature of grain boundaries, etc. (**Chapter 2.3**). Consequently, the microstructure of the host material changes, so that changes in the mechanical and electrical properties, like ionic conductivity of ceramic electrolytes, are expected. A deeper understanding of the interaction of these processes is the basis of an efficient process design and optimization of the total ionic conductivity.

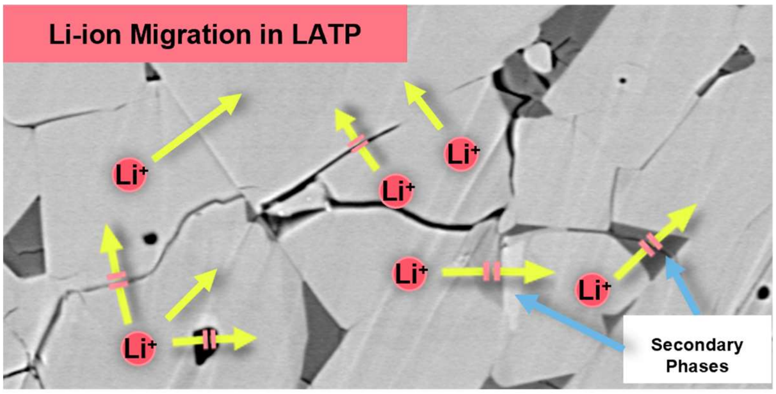

Fig. 5.1 Li-ion migration through LATP microstructure can be hindered by cracks, pores and secondary phases, which depend on the sintering behavior of LATP.

On this account, the correlation between the sintering behavior, microstructure and electrical properties of LATP in the presence of lithium phosphate (Li_3PO_4) has been investigated. The melting point of Li_3PO_4 is 837 °C[142] and lower than the sintering temperature of LATP (> 900 °C[73,148]), thus liquid phase sintering is expected. Pressed pellets of the powder mixtures were sintered at various temperatures. The sintering process had been investigated via thermal-optical measuring devices (TOM) at the Center for High Temperature Materials and Design HTL, Bayreuth, with the assistance of Jens Baber. Porosity measurements based on the Archimedes principle were done at HTL. The changes in microstructure could be examined by SEM images. Electrical properties have been determined via electrical impedance spectroscopy (EIS). The powder synthesis, pellet preparation and impedance measurement had been done by Lavinia Appold within her master thesis: “Thermooptische und elektrische Untersuchungen des

Einflusses von Li_3PO_4 auf das Sintern des keramischen Festkörperelektrolyten LATP und die Auswirkungen auf dessen elektrische Eigenschaften" (2021). The author developed the experimental plan and managed the collaboration with the HTL. Data analyses, discussions and interpretation had taken place under my supervision.

The study has been published in the Journal *Materials Advances* of the Royal Society of Chemistry:

M. Rumpel, L. Appold, J. Baber, W. Stracke, A. Flegler, and G. Sextl, "Impact of the sintering additive Li_3PO_4 on the sintering behaviour, microstructure and electrical properties of a ceramic LATP electrolyte," Mater. Adv. 3 (22), 8157–8167 (2022).[149]

5.1 Introduction and Status Quo

In 1989 and 1990, Aono et al.[150–152] published comprehensive studies on $Li_{1+x}M_xTi_{2-x}(PO_4)_3$ (M = Al, Sc, Y, La) systems. In 1991, Aono et al.[70] added the first time Li_3PO_4 and Li_3BO_3 to $LiTi_2(PO_4)_3$ (LTP) and observed an increase in pellet density and ionic conductivity sintered at 800 °C and 900 °C. In the following years, research focused on the understanding and optimization of further $Li_{1+x}M_xTi_{2-x}(PO_4)_3$ systems in terms of synthesis and preparation, especially the substitution of titanium with germanium or aluminum.[64,65,153,154] Furthermore, finite element studies and simulations based on the brick layer model had been used for a better understanding of the theoretical background of ionic diffusion in microstructural ceramics.[99–108] The brick layer model defines the grain boundaries as a separate phase with grain boundary thickness and area as well as a probably different permittivity than the grain interior (**Chapter 2.5**).[97] The ionic conductivity can be perpendicular or parallel to the grain boundary and varies from the bulk conductivity. Bouchet et al.[99] calculated that a decrease in grain size from 500 nm to 5 nm with constant grain boundary thickness can decrease the overall grain boundary resistance due to a higher amount of diffusion pathways parallel to the grain boundaries. Indris et al.[109] validated this calculation by comparing the ionic conductivities in nanocrystalline and microcrystalline $Li_2O:B_2O_3$ composites. In the nanocrystalline composites, a higher amount of the non-conductive B_2O_3 does not cause a decrease in ionic conductivity due to faster ion diffusion along the grain boundaries. Further studies could confirm the correlation between grain size and ionic conductivity by varying the synthesis and sintering conditions.[73,155,156] Hupfer et al.[73] demonstrated higher conductivities for LATP sintered at 1100 °C for 10 min instead of 8 h. The authors could relate it to smaller grain size, fewer cracks and grain lattice orientation. The grain lattice orientations of two neighboring grains affect the grain boundary orientation and energy. High-angle boundaries have a higher grain boundary energy than low-angle boundaries due to their higher degree of misalignment.[86] Ma et al.[98] could identify both types in $Li_{3x}La_{2/3-x}TiO_3$ (LLTO) ionic conductors and assumed a lithium depletion in the grain boundary, which might affect the ionic conductivity and the activation energy for the Li-ion hopping from one grain to another. Consequently, density, grain size and the nature of grain boundary affect the ionic conductivity. It is well known, that sintering additives influence these parameters.[86–89]

First studies of sintering additives for ionic lithium conductors demonstrate an increase in ionic conductivity by adding a specific amount of sintering additive.[70,157–163] Kobayashi et al.[160] added lithium nitrate ($LiNO_3$) to LTP and could increase the ionic conductivity. Chen et al.[157,158] enhanced the ionic conductivity by adding 10 wt.% sol or powder of $Li_7La_3Zr_2O_{12}$ (LLZO) to LLTO. Additionally, the authors observed an increase in the activation energy, which indicates a change in the grain boundary's nature. Comparable effects could be detected by Mei et al.[161,162], who added silica (SiO_2) to LLTO. The authors observed amorphous silica phases in the grain boundaries, which seem to remove the anisotropy of lithium diffusion in the grain's outer-shell, thus, more possibilities for ion transport. Sintering additives for LATP had been investigated by Hupfer et al.[159] and Waetzig et al.[163] Hupfer et al.[159] added $LiTiOPO_4$ to LATP and demonstrated an increase in ionic conductivity at sintering temperatures up to 925 °C. At higher sintering temperatures abnormal grain growth takes place so that the ionic conductivity decreases and is lower than in pure LATP. In 2020, Waetzig et al.[163] published the first study, which focused on lower sintering temperatures down to 740 °C. The authors compared the sintering additives Li_3PO_4, Li_3BO_3 and Li_2CO_3 and analyzed the electrical properties. Ionic conductivities could be achieved at 850 °C, which are comparable to pure LATP sintered at 1100 °C. However, a deeper interpretation of the microstructure and sintering behavior had not been done. For that reason, this chapter focuses on a more detailed look into the correlation between microstructure, sintering behavior and electrical properties by adding Li_3PO_4 to LATP.

5.2 Experimental Approach

This subchapter gives a short overview of the experimental plan (**Fig. 5.2**). Detailed information can be found in the experimental section (**Chapter 9.2**).

$Li_{1.3}Al_{0.3}Ti_{1.7}(PO_4)_3$ (LATP) powder was synthesized via a sol-gel process. After drying and crystallization at 800 °C for 5 h, the LATP powder was ball-milled. The primary particle size was 200 – 600 nm (**Fig. 4.3a**). Afterward, 3, 5 or 10 vol% Li_3PO_4 (SigmaAldrich®, CAS: 10377-52-3) was added and mixed via speed mixer for 10 min at 1000 rpm.

Pellets of pure LATP and the 5 vol% mixture were pressed with 2000 kN for the TOM investigations of thermal diffusivity and shrinkage. The green body pellet thickness was ca. 2 mm and the diameter 11 mm. These pellets were analyzed by TOM with a heating ramp of 5 K/min to the end temperature, which was held for 24 h. The sintering temperature varied between 600 °C and 950 °C in 50 °C steps. Afterward, the furnace cooled down at a rate of ca. 2 K/min. The sintered pellets were analyzed by water saturation based on the Archimedes principle to examine the porosity.

For the electrical characterization, 0.5 g of powder was used to press each pellet with 80 kN. The green body pellet thickness was ca. 1.4 mm and the diameter was 16 mm. The same sintering condition used for the TOM analysis was applied. The sintered pellets were sputtered with round gold electrodes with a diameter of 1 cm. Afterward, the pellets were dried in a vacuum (10^{-2} mbar) at 120 °C for 12 h and inserted in an argon-filled glovebox to assemble pouch bags in order to protect the pellets from humidity. Three pellets of each parameter set of Li_3PO_4 content and sintering temperature were measured via electrical impedance spectroscopy (EIS) at room temperature to examine reproducibility. One representative pellet was used for temperature-dependent EIS measurements between -20 °C and 60 °C in 10 °C steps. Afterward, the microstructure of this pellet was analyzed via SEM.

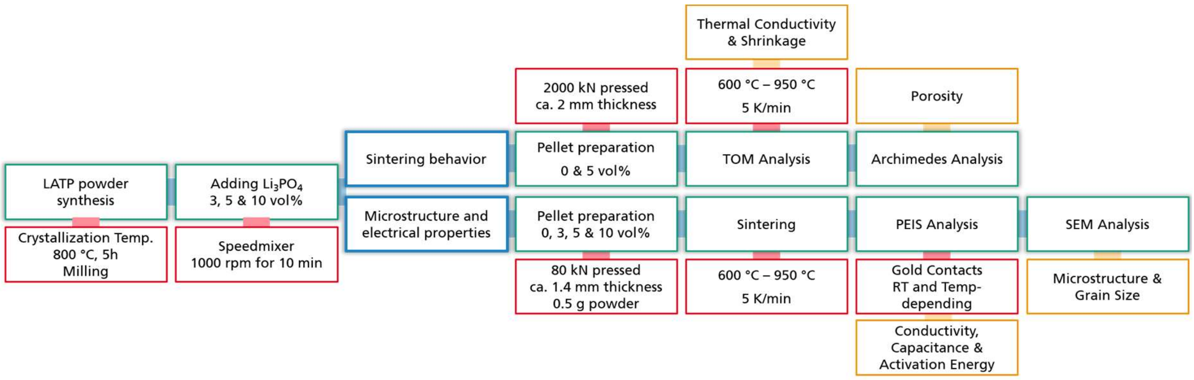

Fig. 5.2 Experimental plan of the investigation of Li_3PO_4 as sintering additive for LATP. Experimental steps (green), parameters (red) and measured properties (orange).

5.3 Investigations of Sintering Behavior and Microstructure

The sintering behaviors of pure LATP and LATP + 5 vol% Li_3PO_4 were investigated by XRD, TOM and water saturation (Archimedes principle). In this way, mixed phases can be detected. The start of sinter neck formation as well as the start and maximum of shrinkage can be determined by TOM. The porosity can be examined by means of water saturation. Additionally, SEM images give an insight into the microstructure and grain size. The sintering temperatures of the pellets were in the range of 600 °C to 950 °C and varied by 50 °C steps.

Crystalline Phases and Secondary Phases

XRD patterns of the pure LATP sample and all powder mixtures with Li_3PO_4 are shown in **Fig. 5.3**. Pellets were sintered at 900 °C for 24 h and afterward ground to powder for the measurements. The intensities were normalized to the intensity of the main reflection of LATP at 24.52°. All samples show crystalline LATP (ICSD 95979). However, $LiTiOPO_4$ can be detected at 27.04°, 27.42°, 27.85° and 27.95° (ICSD 153522). Additionally, $AlPO_4$ can be detected at 20.62° (ICSD 44880). An increase in the intensities of the $LiTiOPO_4$ and $AlPO_4$ reflections with a higher amount of Li_3PO_4 can be observed. This indicates a higher amount of $LiTiOPO_4$ and $AlPO_4$ in the sample with 10 vol% Li_3PO_4, which leads to the assumption that during the sintering process Li_3PO_4 reacts with LATP to $AlPO_4$ and $LiTiOPO_4$. Li_3PO_4 cannot be detected.

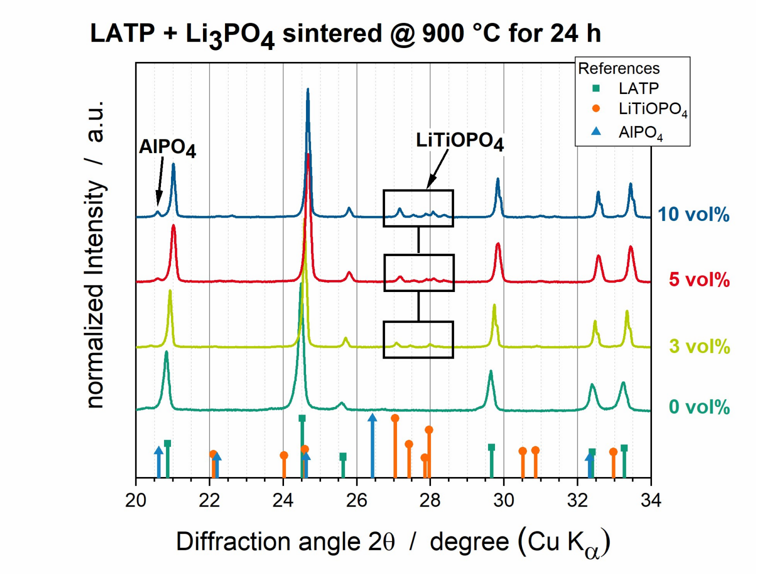

Fig. 5.3 XRD patterns of all powder mixtures sintered as pellets at 900 °C for 24 h. Pure LATP (dark green), LATP + 3 vol% Li_3PO_4 (light green), LATP + 5 vol% Li_3PO_4 (red) and LATP + 10 vol% Li_3PO_4 (blue). Published by and reprinted from Rumpel et al.[149] (published under CC-BY license in Royal Society of Chemistry: *Materials Advances* 2022).

EDS analyses confirm the formation of $LiTiOPO_4$ and $AlPO_4$ (**Fig. 5.4**). The SEM cross-section of the LATP + 5 vol% Li_3PO_4 sample annealed at 950 °C (**Fig. 5.4a**) shows four different contrasts of grains, which were analyzed via EDS (**Fig. 5.4b**). Position 1 can be correlated with

LATP since Al, Ti, O and P can be detected via EDS. Position 4 shows the signals for P and O, thus, Li_3PO_4. Position 2 and 3 can be correlated with $LiTiOPO_4$ and $AlPO_4$, respectively. These secondary phases are formed at the interface of LATP and Li_3PO_4.

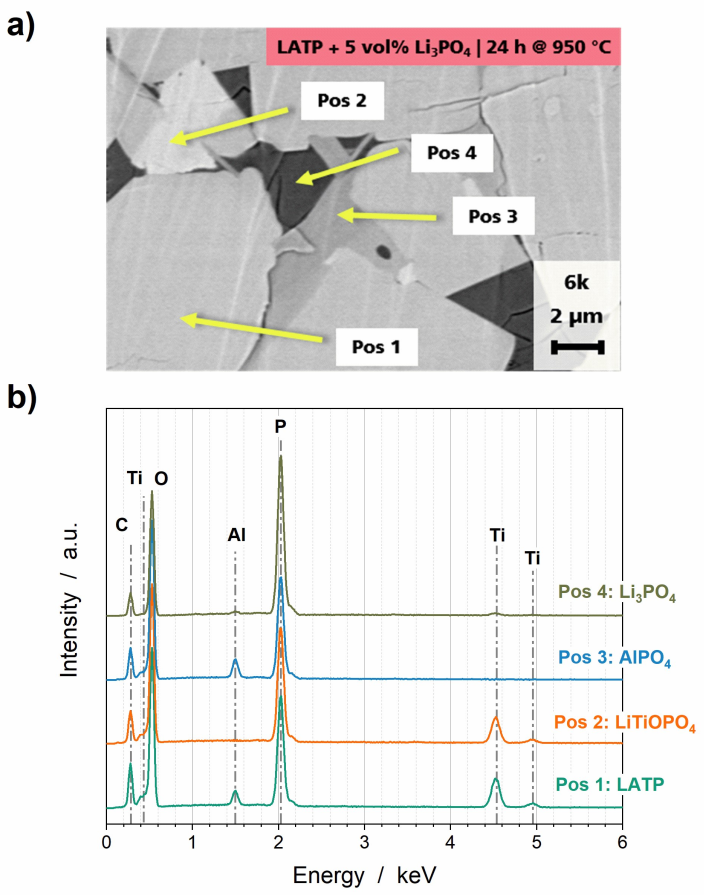

Fig. 5.4 a) SEM cross-section and **b)** corresponding EDS analyses of a LATP + 5 vol% Li3PO4 sample sintered at 950 °C for 24 h. Published by and reprinted from Rumpel et al.[149] (published under CC-BY license in Royal Society of Chemistry: *Materials Advances* 2022).

Thermal Diffusivity, Shrinkage and Porosity

TOM analyses of pure LATP pellets and the LATP + 5 vol% Li_3PO_4 pellets are shown in **Fig. 5.5a** and **Fig. 5.5b**. The thermal diffusivity in crystalline materials is a measure of the heat transport due to elastic vibrations of the lattice (phonon waves). Since LATP is the main component, the thermal diffusivities of all as-prepared pellets are ca. 0.24 mm²/s. On a macroscopic scale, the phonon vibrations are transferred from particle to particle or grain to grain. Thus, particle reorganization in the first sintering stage leads to a slight decrease in thermal diffusivity to ca. 0.20 mm²/s. In **Fig. 5.6**, the thermal diffusivities and relative densities of two representative samples sintered at 900 °C are plotted as a function of the temperature for the heating ramp and as a function of time for the holding step. An increase in thermal diffusivity can be detected between 600 °C and 650 °C for the pure LATP sample and between 550 °C and 600 °C for the LATP + 5 vol% Li_3PO_4 sample. This first increase correlates with the sinter neck formation.

The further increase can be correlated with the decrease in porosity. A more compact microstructure without pores and more grain-to-grain contacts has more possibilities to transport the heat or phonon waves through the material. Thus, it indicates that the LATP + 5 vol% Li_3PO_4 sample sintered at 900 °C shows a higher degree of pore elimination, since the thermal diffusivity gains to 0.47 mm^2/s at 800 °C compared to 0.31 mm^2/s at 900 °C for the pure LATP pellet. A further increase to 0.38 mm^2/s can be detected during the holding step of 24 h at 900 °C for the pure LATP sample. In contrast, the LATP + 5 vol% Li_3PO_4 sample shows a slight decrease to 0.45 mm^2/s, which can be considered constant. Consequently, most of the pore elimination in the pure LATP pellet takes place during the holding step at 900 °C and it is already completed at 800 °C for the LATP + 5 vol% Li_3PO_4 sample. An increase in thermal diffusivity of ca. 0.06 mm^2/s during the holding step can also be detected for the pure LATP samples sintered at 800 °C, 850 °C and 950 °C. The end values are 0.30 mm^2/s, 0.34 mm^2/s and 0.38 mm^2/s, respectively. The values of the LATP + 5 vol% Li_3PO_4 samples sintered at temperatures $\geq$ 800 °C reach 0.47 mm^2/s at 800 °C and stay constant during the holding step. The sample sintered at 750 °C shows an increase from 0.38 mm^2/s to 0.47 mm^2/s during the 24 h. The 600 °C, 650 °C or 700 °C sintered samples obtain values of 0.22 mm^2/s, 0.27 mm^2/s or 0.36 mm^2/s at the end of sintering.

Pore elimination runs parallel to densification and shrinkage of the pellet. For that reason, the plots of the relative thickness (**Fig. 5.5a** and **Fig. 5.5b**) show the exact opposite course than the thermal diffusivities. The pure LATP pellets undergo the most shrinkage of 1.6 %, 1.9 % and 3.1 % during the holding step at 850 °C, 900 °C and 950 °C, respectively. The sample sintered at 800 °C exhibits a total shrinkage of 0.8 %. Consequently, the start of the densification can be evaluated between 800 °C and 850 °C, which is also confirmed in **Fig. 5.6**. In contrary, the start of shrinkage of the LATP + 5 vol% Li_3PO_4 sample is between 650 °C and 700 °C (**Fig. 5.6**). The highest degree of densification is reached at 800 °C for all samples sintered at temperatures $\geq$ 800 °C. The shrinkage gains a value of ca. 13.7 %. During the holding step, the pellets sintered $\geq$ 850 °C show a slight increase in relative thickness again of 0.8 % (850 °C), 1.0 % (900 °C) and 1.3 % (950 °C) (**Fig. 5.5b**). This can be explained by leakage of the melted Li_3PO_4, which lifts the pellet from the ground and falsify the results. The sample sintered at 750 °C shows the most shrinkage of 4.7 % during the holding step but has a similar end value to the samples sintered at higher temperatures. Lower shrinkage can be determined for the pellets sintered at lower temperatures. The maximum shrinkages of these pellets are 1.1 % (650 °C) and 4.9 % (700 °C). The sample sintered at 600 °C shows no shrinkage.

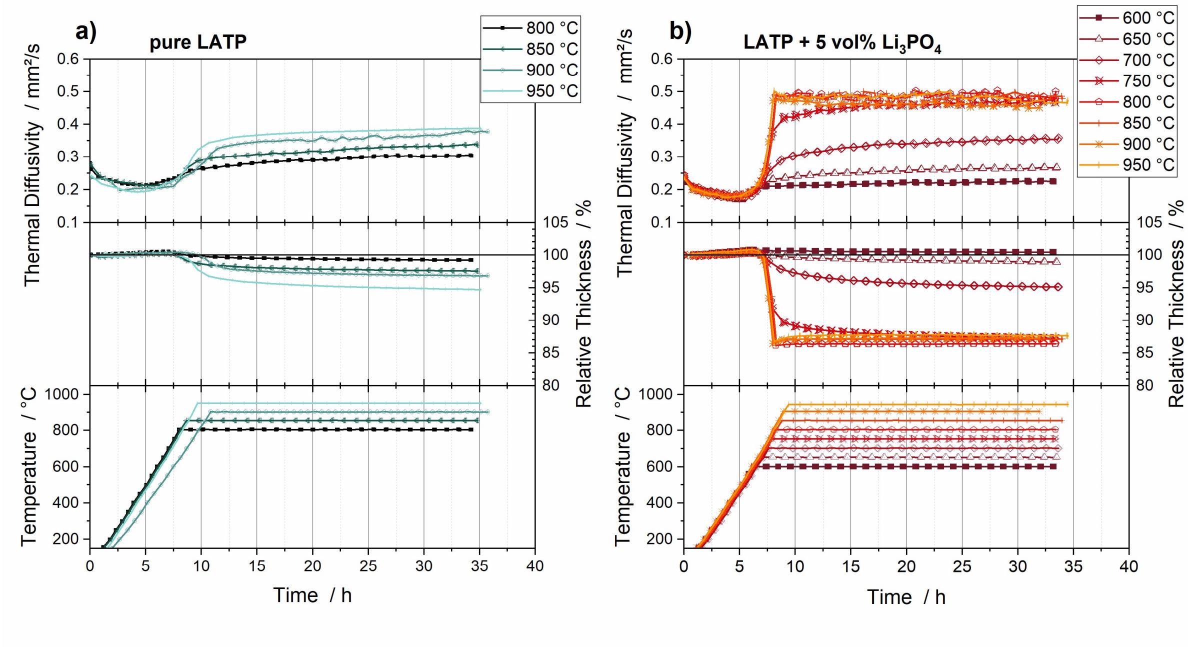

Fig. 5.5 Thermal diffusivities, relative densities and temperature profiles as a function of time of **a)** the pure LATP samples sintered between 800 °C and 950 °C and **b)** the LATP + 5 vol% Li_3PO_4 samples sintered between 600 °C and 950 °C. Published by and reprinted from Rumpel et al.[149] (published under CC-BY license in Royal Society of Chemistry: *Materials Advances* 2022).

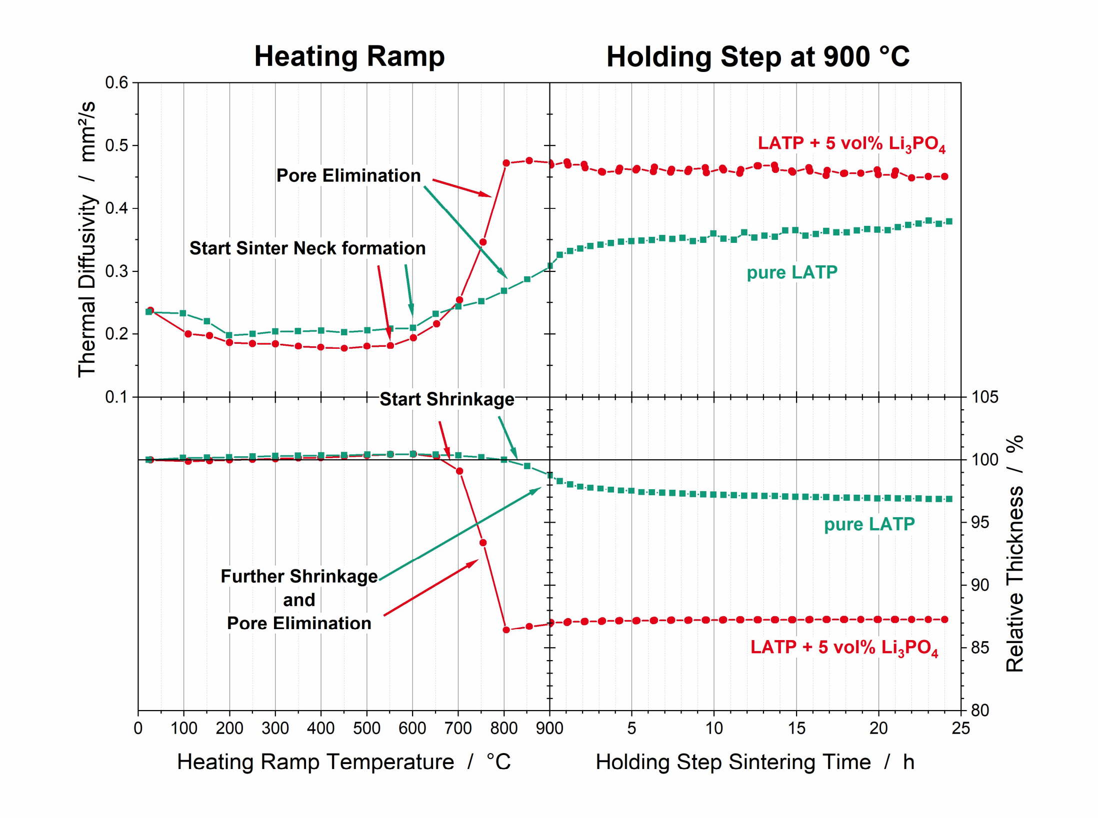

Fig. 5.6 Thermal diffusivities and relative densities of the pure LATP (green) and the LATP + 5 vol% Li_3PO_4 (red) pellets sintered at 900 °C. The heating ramp is plotted as a function of temperature and the following holding step as a function of time. The courses during the heating ramp are representative of the further pellets. Published by and reprinted from Rumpel et al.[149] (published under CC-BY license in Royal Society of Chemistry: *Materials Advances* 2022).

The values of the shrinkage at the end of sintering and the values of the porosities are demonstrated in **Fig. 5.7a** for the pure LATP and in **Fig. 5.7b** for the LATP + 5 vol% Li_3PO_4 samples. Since pore elimination decreases the porosity, the trend goes along with the shrinkage and the thermal diffusivity. The pure LATP pellets show a steady increase in shrinkage (5.3 % at 950 °C) and a steady decrease in porosity (39.0 % at 800 °C to 32.6 % at 950 °C) with the temperature. The LATP + 5 vol% Li_3PO_4 samples demonstrate a significant increase in shrinkage to 12.5 % up to 750 °C. The porosity decreases from 38.5 % at 600 °C to 7.3 % at 750 °C. At higher sintering temperatures the values are quite constant. A slight increase and decrease of the porosity (+ 2.3 %) and shrinkage (- 1.3 %), respectively, can be detected, which can be explained by a higher degree of leakage of Li_3PO_4 at higher temperatures. This is confirmed by a thin film of Li_3PO_4, which could be seen with the eye at the bottom of the pellet after the measurement.

In conclusion, Li_3PO_4 has a significant impact on the sintering behavior. Even at 700 °C, the porosity has a lower value (28.4 %) than the pure LATP sample sintered at 950 °C (32.6 %). The lowest porosity of 6.8 % can be detected for the LATP + 5 vol% Li_3PO_4 sample sintered at 800 °C. Additionally, the temperature of sinter neck formation is lowered by 50 °C and the temperature of the start of shrinkage and densification is reduced by 150 °C. The trend of shrinkage and porosity of the LATP + 5 vol% Li_3PO_4 samples can be correlated to the sintering stages well known from the literature (**Chapter 2.3**).[86–89] The intermediate stage starts between 650 °C and 700 °C. At 750 °C, the final stage begins (**Fig. 5.7b**). In contrast, the pure LATP samples seem still to be in the first or intermediate stage up to 950 °C, since no plateau of the porosity or shrinkage is reached. This is in accordance with the publications of Hupfer et al.[73] and Waetzig et al.[148]. They demonstrate a maximum shrinkage of pure LATP at a sintering temperature of 1100 °C.

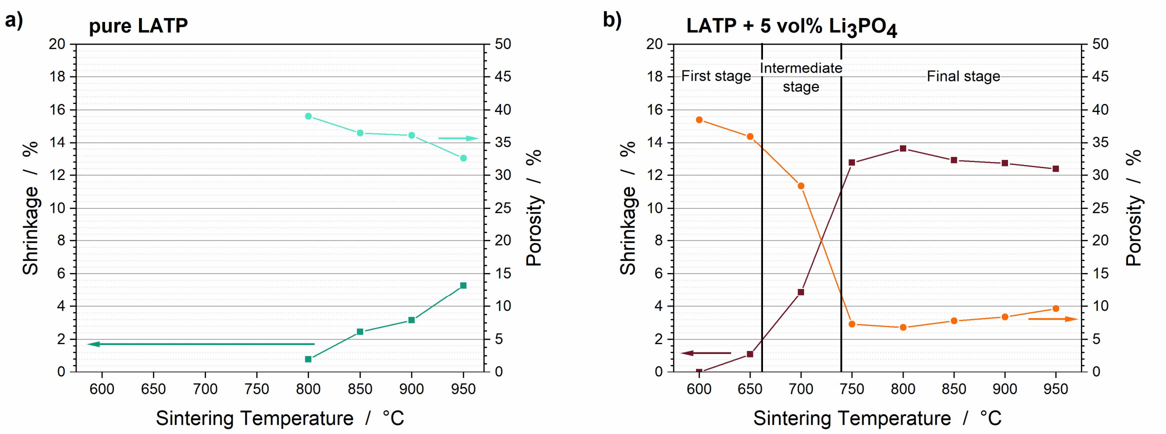

Fig. 5.7 Values of shrinkage at the end of sintering and the porosity as a function of sintering temperature of **a)** the pure LATP samples and **b)** LATP + 5 vol% Li_3PO_4 samples. Published by and reprinted from Rumpel et al.[149] (published under CC-BY license in Royal Society of Chemistry: *Materials Advances* 2022).

Microstructure and Grain Size

SEM cross-sections of pure LATP pellets sintered at 850 °C, 900 °C and 950 °C for 24 h are demonstrated in **Fig. 5.8 a-c**. The microstructure of the 850 °C sample shows open pore channels and sinter necks between the grains. At 900 °C and 950 °C, closed pores are present. Additionally, cracks can be observed at the grain boundaries. The grain sizes are 4 - 8 µm (850 °C), 10 - 50 µm (900 °C) and > 60 µm (950 °C). Consequently, the 850 °C sample shows all characteristics of the intermediate stage. 900 °C and 950 °C are dominated by grain growth and crack formation. However, pores are still visible so that it is more likely the transition from the intermediate stage to the final stage. Taking the TOM analysis and porosity measurements into account, it tends to be the intermediate stage.

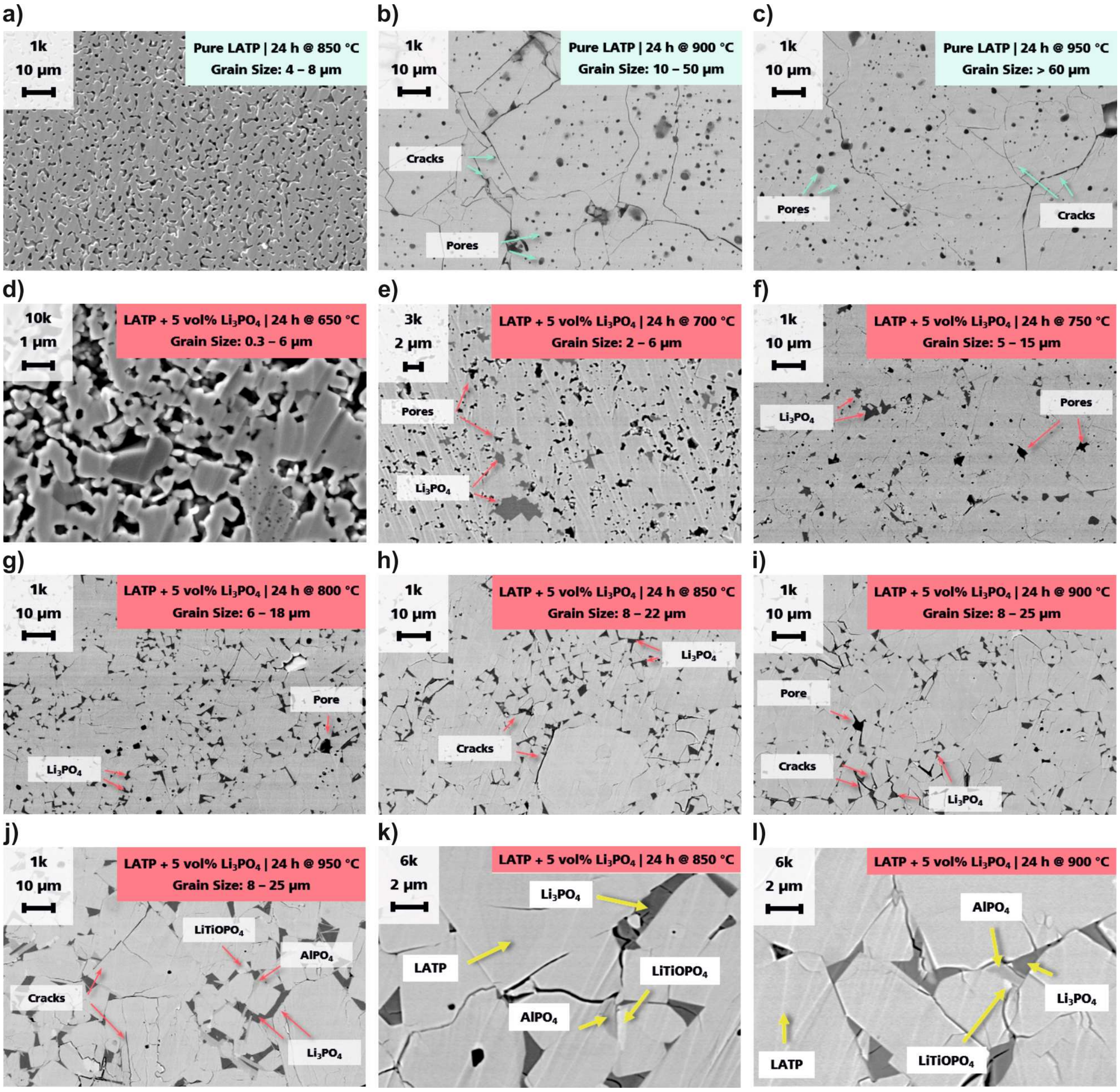

Fig. 5.8 SEM cross-sections of the pure LATP pellets sintered at **a)** 850 °C, **b)** 900 °C and **c)** 950 °C and LATP + 5 vol% Li_3PO_4 pellets sintered at **d)** 650 °C, **e)** 700 °C, **f)** 750 °C, **g)** 800 °C, **h)** and **k)** 850 °C, **i)** and **l)** 900 °C and **j)** 950 °C. The sintering time was 24 h. Accelerating voltage was 5 kV. A backscattered electron detector was used to obtain a higher contrast. Published by and reprinted from Rumpel et al.[149] (published under CC-BY license in Royal Society of Chemistry: *Materials Advances* 2022).

The cross-section of the LATP + 5 vol% Li_3PO_4 sample sintered at 650 °C is shown in **Fig. 5.8d**. The dark spots are Li_3PO_4, which is not dispersed. Large cracks and a high porosity can be detected. A higher magnification was used in **Fig. 5.9a**. It reveals sinter necks between grains of 300 nm, which is similar to the particle size of the initial powder (**Fig. 4.4a**). The grain size distribution is between 0.3 µm and 6 µm. That indicates the first stage of sintering. **Fig. 5.8e** and **Fig. 5.9b** demonstrate that at 700 °C the porosity is significantly reduced and Li_3PO_4 is better dispersed. Additionally, sinter necks are not detectable anymore and grain growth took place up to 2 - 6 µm. The 750 °C sintered pellet shows a further decrease of porosity and a further increase in grain growth up to grain sizes of 5 - 15 µm (**Fig. 5.8f** and **Fig. 5.9c**). At higher sintering temperatures, no further densification can be detected. Grain growth is the dominating process. The grain sizes increase to 6 - 18 µm (800 °C, (**Fig. 5.8g**), 8 - 22 µm (850 °C, **Fig. 5.8h**) and 8 - 25 µm (900 °C, **Fig. 5.8i**). At 950 °C (**Fig. 5.8j**) the grain size distribution is still between 8 µm and 25 µm, but with a higher amount of large grains and, therefore, a maximum of grain growth seem to be reached. Moreover, the Li_3PO_4 concentrate in the pores or triple points between the grains. Their size also increases with sintering temperature. Precipitations of $AlPO_4$ and $LiTiOPO_4$ are evident for the LATP + 5 vol% pellets annealed at 850 °C (**Fig. 5.8k**), 900 °C (**Fig. 5.8l**) and 950 °C (**Fig. 5.8j**). Their grain sizes also grow with sintering temperature to about 1 µm at 950 °C. First cracks appear at 850 °C and their amount seems to increase at 900 °C and 950 °C. The SEM images lead to the conclusion that the high porosity at 700 °C indicates the intermediate sintering stage. Afterward, the densification is finished and grain growth is the main process. Thus, at 750 °C starts the final stage. This is in perfect accordance with the TOM analysis (**Fig. 5.7b**).

Comparing the pure LATP samples and LATP + 5 vol% Li_3PO_4 samples, it can be concluded that the sintering additive Li_3PO_4 has a strong impact on the microstructure. Especially, the grain size is limited to 25 µm with Li_3PO_4. In contrast, the pure LATP sample sintered at 950 °C has grain sizes of > 60 µm. Additionally, pure LATP shows a higher amount of cracks and porosity. Furthermore, LATP + 5 vol% Li_3PO_4 reaches the final sintering stage at 750 °C, whereas it is uncertain if pure LATP already reached the final stage at 950 °C.

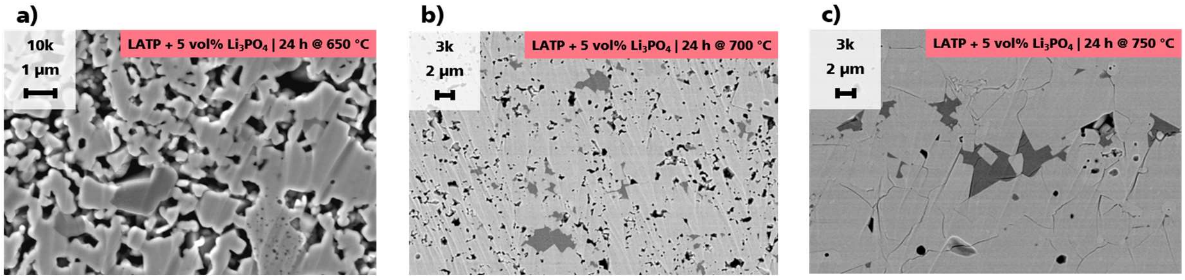

Fig. 5.9 SEM cross-sections with higher magnification of LATP + 5 vol% Li_3PO_4 samples sintered at **a)** 650 °C, **b)** 700 °C and **c)** 750 °C.

5.4 Investigation of Electrical Properties

Electrical impedance spectroscopy (EIS) was used to determine the bulk conductivities σ_b, grain boundary conductivities σ_{gb}, grain boundary capacitances C_{gb} and grain boundary activation energies $E_{a,gb}$ of pure LATP pellets and pellets of the powder mixtures of LATP with 3 vol%, 5 vol% and 10 vol% Li_3PO_4. The pure LATP pellets were sintered between 800 °C and 950 °C for 24 h. The LATP pellets with Li_3PO_4 were sintered between 600 °C and 950 °C for 24 h. However, the pure LATP pellets sintered at 800 °C and the powder mixtures sintered at 600 °C could not be measured due to their mechanical instability. Three pellets of each parameter set were measured via EIS at room temperature (25 °C). As a consequence of good reproducibility, one representative pellet was measured depending on the temperature in the range between -20 °C and 60 °C in 10 °C steps.

Data Analysis and Fitting

The fundamentals of EIS can be found in **Chapter 3.4**. A common presentation of the real and imaginary parts of the complex impedance is the Nyquist plot (**Fig. 5.10**). The equivalent circuit used for fitting is presented in **Fig. 5.10b**. The data show one semicircle, which corresponds to the grain boundary conduction process. The first intercept of the x-axis represents the bulk resistance and the second intercept represents the total resistance. **Fig. 5.10a** shows the Nyquist plots of the samples sintered at 900 °C. The total ohmic resistances are 3240 Ω ± 79 Ω (0 vol%, pure LATP), 1083 Ω ± 7 Ω (3 vol% Li_3PO_4), 1240 Ω ± 74 Ω (5 vol% Li_3PO_4) and 1659 Ω ± 57 Ω (10 vol% Li_3PO_4). Thus, the total resistance significantly decreases by adding Li_3PO_4. However, the thicknesses of the pellets need to be taken into account in order to obtain a more accurate result. Consequently, the analyses of the fitted and calculated conductivities by means of **Eq. 3.9** follow below.

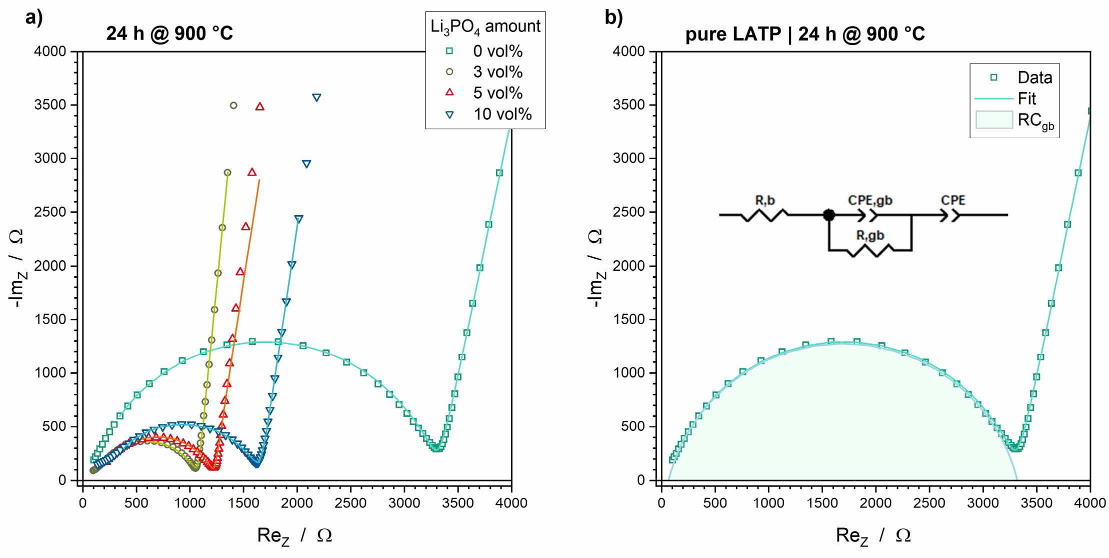

Fig. 5.10 Nyquist plots including fits of **a)** samples sintered at 900 °C for 24 h. **b)** Fit of EIS data of a pure LATP pellet sintered at 900 °C for 24 h using the given equivalent circuit. Published by and reprinted from Rumpel et al.[149] (published under CC-BY license in Royal Society of Chemistry: *Materials Advances* 2022).

Bulk Conductivity

The bulk conductivities, which represent the lithium migration within the grains, are demonstrated in **Fig. 5.11**. The pure LATP pellets sintered at 850 °C, 900 °C and 950 °C show conductivities of 1.69 E-3 S/cm ± 0.49 E-3 S/cm, 1.91 E-3 S/cm ± 0.65 E-3 S/cm and 1.52 E-3 S/cm ± 0.17 E-3 S/cm, respectively. These values are comparable within their error range and also comparable with the literature.[65,73,148] The pellets with Li_3PO_4 content sintered at 650 °C show values of 2.71 E-3 S/cm ± 1.20 E-3 S/cm (3 vol%), 4.16 E-3 S/cm ± 2.58 E-3 S/cm (5 vol%) and 5.29 E-3 S/cm ± 1.80 E-3 S/cm (10 vol%). The errors of 34 % to 62 % are very high. The errors decrease at 750 °C to 6 % (3 vol%), 8 % (5 vol%) and 7 % (10 vol%) with conductivities of 3.06 E-3 S/cm ± 0.18 E-3 S/cm (3 vol%), 2.74 E-3 S/cm ± 0.22 E-3 S/cm (5 vol%) and 3.18 E-3 S/cm ± 0.21 E-3 S/cm (10 vol%). The error margins at higher sintering temperatures are still high between 6 % and 15 %. Nevertheless, the samples with 3 vol% Li_3PO_4 show a steady decrease to 1.46 E-3 S/cm ± 0.08 E-3 S/cm at 950 °C. The conductivities of the 5 vol% and 10 vol% samples show a drop at 800 °C to 1.69 E-3 S/cm ± 0.26 E-3 S/cm and 1.48 E-3 S/cm ± 0.14 E-3 S/cm. A further reduction within the error margin to 1.23 E-3 S/cm ± 0.12 E-3 S/cm (5 vol%) and 1.19 E-3 S/cm ± 0.32 E-3 S/cm (10 vol%) at 950 °C can be determined.

The data of the LATP and Li_3PO_4 powder mixtures might suggest a steady change in the grain lattice of LATP or a significant change between 750 °C and 800 °C for the 5 vol% and 10 vol% samples. This could be explained by the formation of $LiTiOPO_4$ and $AlPO_4$ accompanied by removing Ti^{4+} and Al^{3+} from the LATP lattice. However, it is important to estimate the error sources, since the range of error is high. Especially at low sintering temperatures, porosity can have an impact on the data measured at high frequencies.[97,164] Additionally, the complex impedances at high frequencies of the contacts and cables need to be considered. Information about the accuracy of the bulk conductivities would be given by the capacitance of the bulk migration. The bulk capacitance is supposed to be in the range of pF and could be identified by analyzing the semicircle of the bulk conduction.[96,165] However, this semicircle cannot be detected with the experimental set-up used in this study. Breuer et al.[96] demonstrate a possibility to obtain the semicircle by using 4 mm thick pellets and reducing the EIS measurement temperature to -150 °C and -100 °C. Their bulk conductivity of 3.4 E-3 S/cm at 25 °C could be determined by extrapolating to room temperature.[96]

In conclusion, an explanation of the decrease of the bulk conductivity with sintering temperature and of the slightly higher conductivities of the LATP + 3 vol% Li_3PO_4 samples can be given by the formation of the secondary phases $LiTiOPO_4$ and $AlPO_4$. Furthermore, the values are in good accordance with the literature.[65,96,163] Nonetheless, further investigation at lower measurement temperatures should be done to achieve more reliable results and to verify the interpretation.

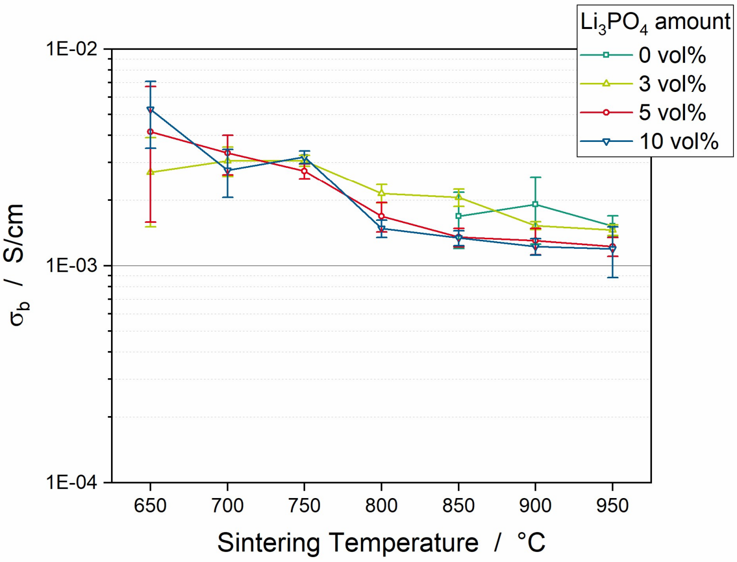

Fig. 5.11 Bulk conductivities σ_b of the samples sintered at various sintering temperatures. Published by and reprinted from Rumpel et al.[149] (published under CC-BY license in Royal Society of Chemistry: *Materials Advances* 2022).

Grain Boundary Conductivity

The limiting factor of Li-ion migration through a microstructural material is the diffusion through grain boundaries represented by the grain boundary conductivity. Contrary to the bulk conductivities, the excitation frequency of the Li-ion hopping at room temperature is between 100 Hz and 1 MHz so that a semicircle can be measured in this range (**Fig. 5.10**). This leads to accurate fit results. Additionally, the error range of all samples is lower than 5 %, except for the 750 °C sintered samples. The calculated grain boundary conductivities are plotted in **Fig. 5.12** as a function of the sintering temperature. The pure LATP pellets show grain boundary conductivities of 2.93 E-5 S/cm ± 0.80 E-5 S/cm (850 °C), 5.43 E-5 S/cm ± 0.25 E-5 S/cm (900 °C) and 6.03 E-5 S/cm ± 0.14 E-5 S/cm (950 °C). Considering the sintering temperature and duration, these values are in accordance with the literature.[73,96] Higher values of > 1E-4 S/cm are reported for higher sintering temperatures and shorter sintering duration.[65,73,148]

The LATP + Li_3PO_4 samples sintered at 650 °C have grain boundary conductivities of 7.28 E-5 S/cm ± 0.20 E-5 S/cm (3 vol%), 6.61 E-5 S/cm ± 0.09 E-5 S/cm (5 vol%) and 4.85 E-5 S/cm ± 0.30 E-5 S/cm (10 vol%). These values significantly increase at 700 °C to 2.46 E-4 S/cm ± 0.33 E-4 S/cm (3 vol%), 1.94 E-4 S/cm ± 0.07 E-4 S/cm (5 vol%) and 1.37 E-4 S/cm ± 0.06 E-4 S/cm (10 vol%). At 750 °C, high errors of > 14 % occur. This sintering temperature corresponds to the transition from the intermediate sintering stage to the final sintering stage implying an unsteady microstructure development with many influencing factors such as pores, grain size distribution or grain boundary orientations at this transition. The maximum grain boundary conductivities can be obtained at 800 °C for the 5 vol% and 10 vol% samples: 2.46 E-4 S/cm ± 0.33 E-4 S/cm (3 vol% at 700 °C), 2.08 E-4 S/cm ± 0.04 E-4 S/cm

(5 vol% at 800 °C) and 1.93 E-4 S/cm ± 0.03 E-4 S/cm (10 vol% at 800 °C). The grain boundary conductivity of the 3 vol% sample at 800 °C is 2.04 E-4 S/cm ± 0.02 E-4 S/cm, thus comparable to the values of the 5 vol% and 10 vol% samples. At higher sintering temperatures, a steady decrease in the grain boundary conductivity is observable for all Li_3PO_4-containing LATP pellets. The degree of reduction depends on the Li_3PO_4 amount so that a lower reduction for the LATP + 3 vol% Li3PO4 samples is observable. The grain boundary conductivities at 950 °C are 1.40 E-4 S/cm ± 0.08 E-4 S/cm (3 vol%), 0.86 E-4 S/cm ± 0.04 E-4 S/cm (5 vol%) and 0.76 E-4 S/cm ± 0.11 E-4 S/cm (10 vol%).

Nevertheless, using Li_3PO_4 as a sintering additive for LATP reduces the sintering temperature to 650 °C. The values show similar grain boundary conductivities to the pure LATP samples sintered at 950 °C. At 700 °C the conductivity is already enhanced by ca. 1.9 E-4 S/cm (3 vol%), ca. 1.3 E-4 S/cm (5 vol%) and ca. 0.8 E-4 S/cm (10 vol%) compared to the pure LATP sample sintered at 950 °C. The most stable values with high conductivity can be observed at 800 °C. The difference to the pure LATP samples sintered at 950 °C is approx. 1.4 E-4 S/cm. Since the grain boundary conductivity of the pure LATP samples is expected to increase to ≥ 1E-4 S/cm at sintering temperatures ≥ 1000 °C[65,73,148], the most reasonable approach is to compare the conductivities of Li_3PO_4-containing LATP sintered at 800 °C, which have the lowest error, with the literature values of pure LATP. That leads to the conclusive statement that the sintering temperature can be reduced by 200 °C with respect to the ionic conductivity.

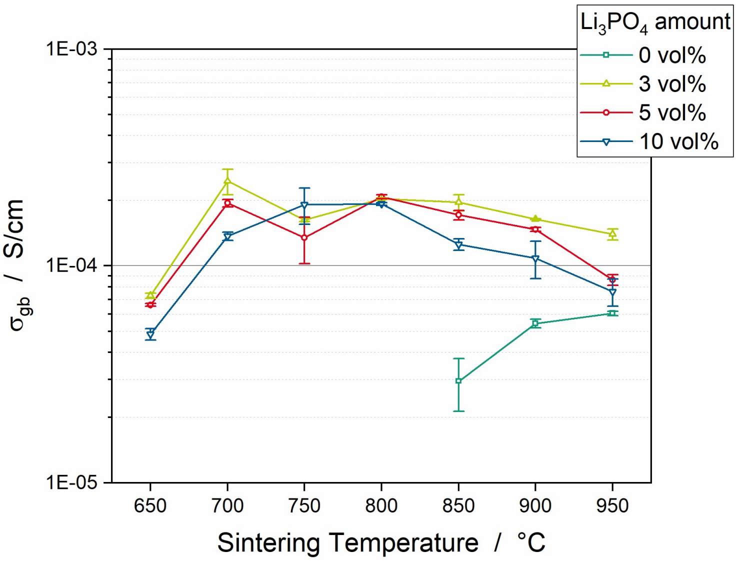

Fig. 5.12 Grain boundary conductivities σ_{gb} of the samples sintered at various sintering temperatures. Published by and reprinted from Rumpel et al.[149] (published under CC-BY license in Royal Society of Chemistry: *Materials Advances* 2022).

Grain Boundary Capacitance

In reference to the brick layer model (**Chapter 2.5**), the grain boundaries can be interpreted as capacitors with the plate area depending on the grain size, the plate distance represented by the grain boundary thickness and the particular permittivity being based on the grain boundary condition (**Eq. 3.10**). The expected value range for the grain boundary capacitance are given in literature with 1 E-11 F to 1 E-8 F.[165] The capacitances obtained from the fit results are demonstrated in **Fig. 5.13**. The capacitance of the pure LATP pellets increases from 0.74 E-8 F ± 0.13 E-8 F at 850 °C to 2.23 E-8 F ± 0.76 E-8 F at 950 °C. The values of the 3 vol%, 5 vol% and 10 vol% Li_3PO_4-containing LATP pellets are similar within the error margin for each sintering temperature. The grain boundary capacitances of 0.33 E-8 F ± 0.04 E-8 F (3 vol%), 0.26 E-8 F ± 0.02 E-8 F (5 vol%) and 0.20 E-8 F ± 0.03 E-8 F (10 vol%) gain between 650 °C and 750 °C to 1.88 E-8 F ± 0.09 E-8 F (3 vol%), 1.57 E-8 F ± 0.11 E-8 F (5 vol%) and 2.10 E-8 F ± 0.26 E-8 F (10 vol%). Afterward, a lower increase to 2.94 E-8 F ± 0.16 E-8 F (3 vol%), 5.09 E-8 F ± 0.27 E-8 F (5 vol%) and 3.61 E-8 F ± 1.14 E-8 F (5 vol%) at 900 °C can be observed. The capacitance stays constant at 950 °C. Consequently, two slopes can be determined. The first and steeper one corresponds to pore elimination which leads to densification and more grain boundaries. However, the grain growth is also enhanced in this temperature range, so that a clear separation of these two effects cannot be reliably done. The second slope exclusively depends on the grain growth which reaches a maximum at 900 °C so that the capacitance remains constant at 950 °C. The pure LATP samples sintered at 950 °C show a comparable value like the Li_3PO_4 containing samples but much larger grain sizes, which indicates that influences of a possibly different grain boundary permittivity due to the Li_3PO_4, $AlPO_4$ and $LiTiOPO_4$ cannot be excluded. The change in grain boundary thickness cannot be examined by the techniques used in this study. However, its influence on the capacitance seems to be low.

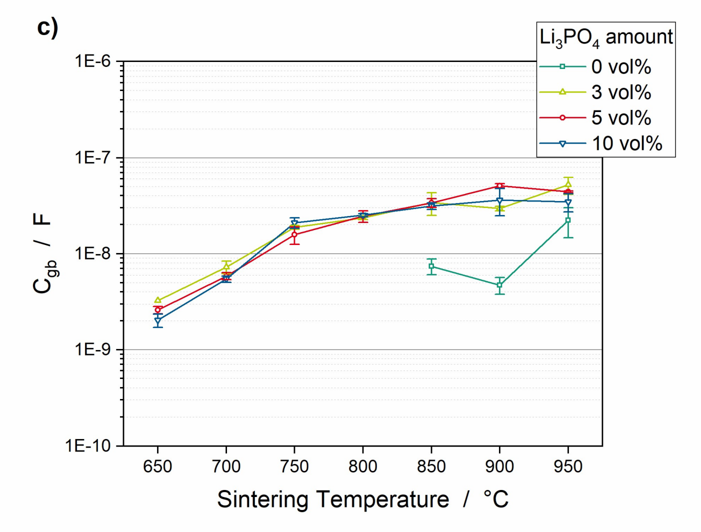

Fig. 5.13 Grain boundary capacitances C_{gb} of the samples sintered at various sintering temperatures. Published by and reprinted from Rumpel et al.[149] (published under CC-BY license in Royal Society of Chemistry: *Materials Advances* 2022).

Arrhenius Plots and Activation Energies

The activation energies of the Li-ion grain boundary migration $E_{a,gb}$ can be determined by analyzing the Arrhenius plots obtained via temperature-dependent EIS measurements. For that purpose, one representative pellet of each sintering temperature and Li_3PO_4 content was measured between -20 °C and 60 °C in 10 °C steps. The calculated conductivities can be plotted by means of the Arrhenius equation (**Eq. 3.12**) as demonstrated in **Fig. 5.14**. All samples show a linear trend; thus, they perfectly follow the expected Arrhenius behavior. The heights of the linear courses correlate to the grain boundary conductivities. The grain boundary activation energies $E_{a,gb}$ can be determined by analyzing the slope value obtained from the linear fit. The slope corresponds to $-E_{a,gb}/k_B$. Alternations of the slope are visible such as the intercept of the curves of the pure LATP samples sintered at 900 °C and 950 °C (**Fig. 5.14a**). The obtained $E_{a,gb}$ values of all samples are demonstrated in **Fig. 5.15**.

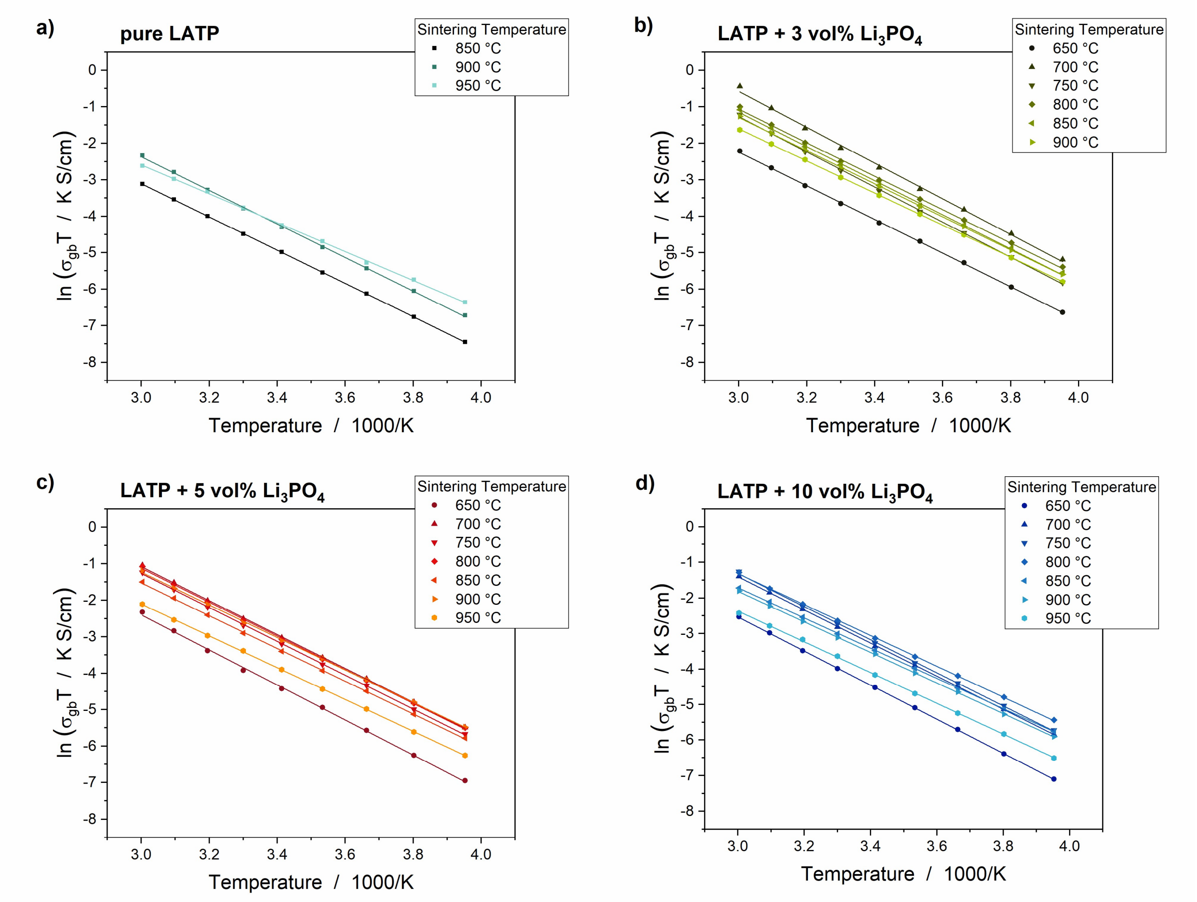

Fig. 5.14 Arrhenius plots obtained from the temperature-dependent EIS measurements of **a)** pure LATP, **b)** LATP + 3 vol% Li_3PO_4, **c)** LATP + 5 vol% Li_3PO_4 and **d)** LATP + 10 vol% Li_3PO_4. Solid lines represent the linear fits. Published by and reprinted from Rumpel et al.[149] (published under CC-BY license in Royal Society of Chemistry: *Materials Advances* 2022).

The activation energies of the pure LATP samples are 393 meV (850 °C), 397 meV (900 °C) and 341 meV (950 °C). Values between 310 meV and 360 meV are reported in the literature.[96,156] Consequently, the most sintered pure LATP pellet in this study is in accordance with the literature data. All Li_3PO_4-containing LATP samples show activation energies > 370 meV. The trend of the activation energies starts with a high value of 414 meV for the 5 vol% and 10 vol% samples and continues with a decrease to 376 meV (5 vol%) and 373 meV (10 vol%) at 950 °C. The activation energy of the 3 vol% sample is 398 meV at 650 °C. It significantly increases to 422 meV at 700 °C. Afterward, a decrease to 379 meV at 950 °C can be observed, which is comparable to the 5 vol% and 10 vol% samples. Since only one representative pellet was measured via temperature-dependent EIS, the 3 vol% samples sintered at 650 °C and 800 °C are most likely statistical outliers. The 3 vol% and 5 vol% samples demonstrate a steady decrease of $E_{a,gb}$ with sintering temperature. In contrast, the 10 vol% samples show a significant decrease of 35 meV between 750 °C (402 meV) and 850 °C (367 meV) followed by a slight increase to 950 °C (373 meV). Since the curves show a coherent course, a statistical error is implausible. Apparently, a higher Li_3PO_4 amount leads to lower activation energies. The largest difference in the activation energies is at 850 °C. The 3 vol%, 5 vol% and 10 vol% samples show values of 403 meV, 387 meV and 366 meV, respectively.

In conclusion, Li_3PO_4 has a significant impact on the grain boundary activation energies, which can be correlated with the grain boundary orientation or the grain boundary's nature in general. The energy barrier of Li-ion hopping between grains seems to be significantly increased compared to pure LATP. Interestingly, the amount of Li_3PO_4 and the trend of activation energies behave counter-intuitive: a higher Li_3PO_4 content results in lower activation energies. Thus, it is too simple to consider the formed $LiTiOPO_4$ or $AlPO_4$ as a blocking layer between the grains. Further impacts on the grain boundary energy need to be considered such as changes in the grain boundary angle and lattice changes in the outer region of the grains due to Ti^{4+} or Al^{3+} depletion because of the $LiTiOPO_4$ and $AlPO_4$ formation. Firstly, low-angle grain boundaries, which imply low grain boundary energies, are mostly formed in the final sintering stage. This might explain the overall decrease of activation energy with sintering temperature, in particular the decrease of the pure LATP sample sintered at 950 °C. Secondly, Ti^{4+} and Al^{3+} depletion additionally changes the structure of the grain boundaries and probably increases the grain boundary thickness. This could result in a separate phase so that the determined activation energy does not correspond to the barrier between grain and grain but between grain and grain boundary, which might be lower for thicker grain boundaries. This consideration would explain the lower activation energies for the 10 vol% samples compared with 3 vol% and 5 vol%, but higher than pure LATP. Nevertheless, all hypotheses considered here could not be tested or confirmed in this study. A closer look into the grain boundary regions need to be taken in further studies.

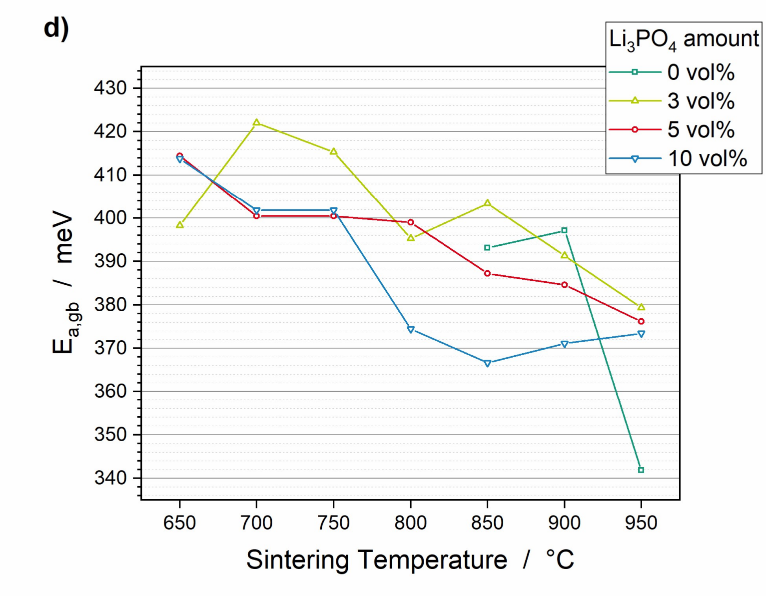

Fig. 5.15 Grain boundary activation energies $E_{a,gb}$ of the samples sintered at various sintering temperatures. Published by and reprinted from Rumpel et al.[149] (published under CC-BY license in Royal Society of Chemistry: *Materials Advances* 2022).

5.5 Correlation of Sintering Behavior, Microstructure and Electrical Properties

In the following, the sintering behavior as well as the changes in the microstructure of the LATP + 5 vol% Li_3PO_4 samples will be correlated with the electrical properties. The findings will be compared with the pure LATP pellets. Finally, a transfer of the gained knowledge to the LATP + 3 vol% Li_3PO_4 samples and LATP + 10 vol% Li_3PO_4 samples will be attempted, for which no information about the sintering behavior and microstructure is available.

In general, four effects with regard to the sintering process could be identified: i) formation of the secondary phases $LiTiOPO_4$ and $AlPO_4$; ii) pore elimination, densification and shrinkage; iii) grain growth and grain size distribution; iv) crack formation.

The impact of these effects on the microscopic properties such as grain lattice stoichiometry, grain boundary orientation and grain boundary nature as well as the impact on the macroscopic properties like the size of the percolation network or the number of possibilities of lithium migration will be discussed.

Indications of the changes in these properties can be deduced from the correlation of the four listed effects and the obtained electrical values of bulk conductivity, grain boundary conductivity, grain boundary capacitance and grain boundary activation energy. Since the most important characteristic value for ceramic ionic conductors is the overall ionic conductivity, the main focus will be on the development of the grain boundary conductivity.

$LiTiOPO_4$ and $AlPO_4$ formation

The XRD patterns (**Fig. 5.3**) reveal the formation of $LiTiOPO_4$ and $AlPO_4$ during the sintering of the Li_3PO_4-containing samples. The amount of the secondary phases also increases with a higher amount of Li_3PO_4. The formation of secondary phases during the sintering of pure LATP has also been reported in the literature.[72,73,153,166] It is explained by the decomposition of LATP induced by stoichiometric imbalances during sintering. However, the pure LATP sample is free from impurity phases, as shown in the XRD diffractogram (**Fig. 5.3**). Consequently, the addition of Li_3PO_4 induces the formation of the secondary phases by either reducing the decomposition temperature of LATP or by reacting with LATP to $AlPO_4$ and $LiTiOPO_4$. Both can result in changes in the stoichiometry of the LATP lattice by extracting Ti and Al. Since the precipitations of $LiTiOPO_4$ and $AlPO_4$ appear at the interface of Li_3PO_4 and LATP, it can be assumed that the changes in stoichiometry mainly take place in the outer region of the LATP grains, which might increase the misorientation at the grain boundaries. Indications of changes in the grain lattice stoichiometry and grain boundary nature can be deduced from the electrical data.

The bulk conductivity shows a steady decrease with sintering temperature and a slightly higher value for the pure LATP and LATP + 3 vol% Li_3PO_4 sample (**Fig. 5.11**). Furthermore, a significant drop in bulk conductivity can be observed between 750 °C and 800 °C for the 5 vol% and 10 vol% samples. These trends can be explained by either the decrease in the overall LATP amount due to decomposition or by a change in the grain lattice stoichiometry. As discussed before, the error margin is high so that more accurate measurements should be done to verify this assumption.

The grain boundary conductivities of the 3 vol%, 5 vol% and 10 vol% Li_3PO_4 samples demonstrate trends depending on the Li_3PO_4 amount (**Fig. 5.12**). An overall decrease between 800 °C and 950 °C can be observed, which is more significant with a higher Li_3PO_4 amount. This indicates additionally a higher amount of secondary phases, which interrupts the percolation network. Consequently, an enhanced reduction in grain boundary conductivity can be observed with a higher Li_3PO_4 amount.

A measure of the degree of misorientation is the grain boundary activation energy since misorientation increases the barrier for Li-ion transfer. However, the curves of the activation energies show the opposite effect. In general, the activation energies of the Li_3PO_4-containing samples are significantly higher than the values of the pure LATP pellet sintered at 950 °C. However, a higher amount of Li_3PO_4 leads to lower activation energies, thus a decrease of the barrier (**Fig. 5.15**). This contradicts the assumption regarding the grain boundary conductivity. A vague explanation might be the increase in grain boundary thickness so that it can be seen as a separate phase. The transfer of the Li-ion from the grain into the grain boundary has a low barrier, but the overall migration of lithium ions from grain to grain is inhibited. The hopping of Li-ions into the secondary phases or Li_3PO_4 is also conceivable. The lower barrier for the charge transfer is probably correlated with the grain sizes of $AlPO_4$, $LiTiOPO_4$ and Li_3PO_4, which are larger at high sintering temperatures and with higher Li_3PO_4 amounts so that an easier transfer of Li-ions is possible.

However, an increase in grain boundary thickness is supposed to be observable in the grain boundary capacitance, but indications could not be deduced from the data, since grain growth has a dominating impact. Nonetheless, the grain boundary capacitance is enhanced in comparison to the pure LATP samples (**Fig. 5.13**) despite the factor three larger grain size of pure LATP. That indicates a change in the grain boundary permittivity and it would support the hypothesis of a separate phase.

Recapitulating these results, the existence of a separate grain boundary phase seems to be likely. Two hypotheses can be established. Firstly, the Al^{3+} and Ti^{4+} depletion in the outer grain region causes a high degree of misorientation, which appear as a separate grain boundary phase. Secondly, the hopping of Li-ions into the secondary phases is taken place. These two ideas need to be tested and verified. For instance, atomic-resolution high-angle annular dark-field scanning transmission electron microscopy could be used to obtain images of grain boundaries in a resolution, which reveals the lattice planes and misorientation in the grain boundary region.[98]

Pore Elimination, Densification and Shrinkage

Pore elimination, densification and shrinkage take place simultaneously and finally result in a compact microstructure. Measures for the pore elimination and densification are the thermal diffusivity (**Fig. 5.5**) and the porosity (**Fig. 5.7**). Shrinkage is described by the reduction of the relative thickness (**Fig. 5.6**). All parameters show the same trend. Classification in the three sintering stages, known from the literature, could be done for the LATP + 5 vol% Li_3PO_4 sample. Particle reorganization and sinter neck formation take place in the first sintering stage, which is observed at 650 °C sintering temperature (**Fig. 5.9a**). The porosity of 36 % is still high. The intermediate stage could be determined as around 700 °C. It is characterized by pore elimination, thus a high reduction in porosity, which is completed in the final stage and grain growth becomes the dominating effect. The final stage starts at 750 °C (**Fig. 5.7b** and **Fig. 5.8f**). The porosities are 28 % at 700 °C and ca. 7 - 9 % in the final stage (**Fig. 5.7b**). This is in huge contrast to the pure LATP samples since the porosity is still 33 % at 950 °C (**Fig. 5.7a**). SEM images additionally show pores at 950 °C (**Fig. 5.8c**), which leads to the conclusion that the pure LATP is still in the intermediate stage at 950 °C. Consequently, the sintering temperature is significantly reduced by adding Li_3PO_4. The start of the sinter neck formation is reduced by 50 °C and the start of the shrinkage is reduced by 150 °C (**Fig. 5.6**).

The densification process has an impact on the grain boundary conductivity. The curves of the grain boundary conductivity and porosity of the LATP + 5 vol% Li_3PO_4 samples are compared in **Fig. 5.16**. The pellets sintered at 600 °C could not be measured via EIS due to their mechanical instability. The significant increase in the ionic conductivity between 650 °C and 700 °C can be correlated with pore elimination. However, the porosity of 28 % is still high, which indicates that another parameter influences the grain boundary conductivity. Additionally, the overall decrease in grain boundary conductivity above 800 °C cannot be explained by densification, since the porosity stays quite constant at sintering temperature ≥ 750 °C. Nevertheless, the conductivities in the final stage are > 1E-4 S/cm. The best value of 2.08 E-4 S/cm ± 0.04 E-4 S/cm is obtained at 800 °C, which also shows the lowest porosity of 6.8 %. The high error of 24 % at the beginning of the final stage (750 °C) is also noteworthy. Indications of an unsteady pore elimination cannot be proved and cannot be excluded.

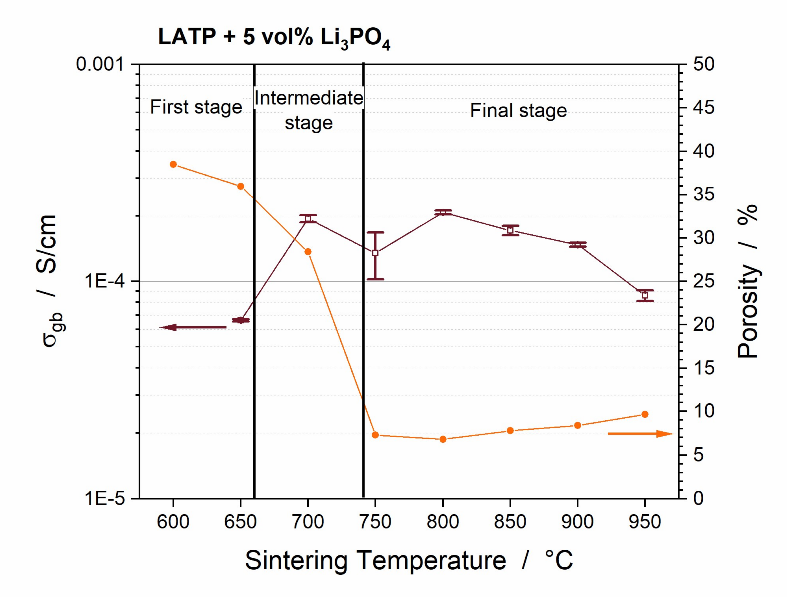

Fig. 5.16 Comparison of grain boundary conductivity σ_{gb} and porosity of the LATP + 5 vol% Li_3PO_4 samples.

The grain boundary conductivity of 6.03 E-5 S/cm ± 0.14 E-5 S/cm of pure LATP sintered at 950 °C is comparable with the conductivity of 6.61 E-5 S/cm ± 0.09 E-5 S/cm of the LATP + 5 vol% Li_3PO_4 pellets sintered at 650 °C (**Fig. 5.12**). Their porosities are 33 % and 36 % (**Fig. 5.7**), respectively. This confirms the impact of the densification process on the grain boundary conductivity. Since the densification process is not finished at 950 °C, higher values of > 1E-4 S/cm are expected at sintering temperatures > 950 °C. This is reported in literature and correlates with higher densification.[65,73,148] Finally, the grain boundary conductivities of the 3 vol% and 10 vol% samples show the same trend like the 5 vol% samples (**Fig. 5.12**). Thus, a similar densification process of these samples is expected.

In contrast to the grain boundary conductivity, the bulk conductivity and activation energy seem not to be affected by the densification process. The only effect of porosity on the bulk conductivity is the significant increase in the error range of the Li_3PO_4-containing LATP samples sintered at 650 °C and 700 °C (**Fig. 5.11**). The capacitance shows an increased slope up to the sintering temperature of 750 °C (**Fig. 5.13**). This is in accordance with the pore elimination so that it can be assumed as an influencing factor since the densification creates more grain boundaries.

The densification process due to pore elimination and shrinkage results in a compact microstructure with an increased number of grain-to-grain contacts, which increases the percolation network for Li-ion migration as well as the possibility of Li-ion hopping from grain to grain. Thus, it has a high impact on the grain boundary conductivity, particularly, in the intermediate sintering stage.

Grain Growth and Grain Size Distribution

Grain growth takes place immediately after the sinter neck formation; hence, it can be observed during all sintering stages. As a result, the grain sizes increase with the sintering temperature. In the final sintering stage, Ostwald ripening is the dominating grain growth process, in which large grains grow by assimilating small grains. This results in a microstructure of large grains surrounded by smaller grains. This kind of microstructure can be observed in the final sintering stage of the LATP + 5 vol% Li_3PO_4 samples at sintering temperatures ≥ 750 °C (**Fig. 5.8 f-j**). In general, the grain sizes increase from 0.3 - 6 µm at 650 °C to 8 - 25 µm at 950 °C (**Fig. 5.8 d-j**). The grain size distribution is significantly broadened at the beginning of the final sintering stage (**Fig. 5.17**). Since the lower and upper limit of the grain sizes at 900 °C is also 8 µm and 25 µm, it can be concluded that a maximum in grain growth is reached. In contrast, the pure LATP sample demonstrates a rapid increase with sintering temperature to grain sizes > 60 µm at 950 °C (**Fig. 5.8c**).

Considering a highly efficient percolation network for ion migration, the grain size distribution might have an important impact. Small grain sizes with a narrow distribution might increase the overall grain-to-grain contacts, thus the probability of Li-ion hopping from grain to grain. Furthermore, the lattice orientation within the grains needs to be considered. The Li-ion diffusion within the LATP NASICON structure occurs along the a, b and c axes of the rhombohedral lattice in 3D tunnels.[64] The lattice planes corresponding to the tunnels must match with the lattice planes of the neighboring grain to ensure an efficient ion hopping through the grain boundary. The probability of matching lattice planes is increased with a smaller grain size, since a higher amount of contact areas, which differ in their contact angle, is present.

Keeping the benefits of small grain sizes in mind, the overall decrease of the grain boundary conductivity as well as the high conductivity of the LATP + 5 vol% Li_3PO_4 samples sintered at 700 °C can be explained. In **Fig. 5.17**, the grain boundary conductivity is compared with the lower and upper limits of the grain sizes obtained from the SEM images (**Fig. 5.8**). The overall decrease between 800 °C and 950 °C correlates with the grain growth. A further impact of crack formation needs to be considered, which will be discussed in the next section. Finally, the sample sintered at 700 °C shows a high conductivity of 1.94 E-4 S/cm ± 0.07 E-4 S/cm despite a high porosity of 28 %, as discussed previously. However, the grain size distribution is very narrow and the grain sizes are about 2 - 6 µm. In contrast, the sample sintered at 800 °C shows a grain size distribution of about 6 - 18 µm with a porosity of 6.8 % and a just slightly higher grain boundary conductivity of 2.08 E-4 S/cm ± 0.04 E-4 S/cm. That suggests that the percolation network formed at 700 °C is comparable with the percolation network formed at 800 °C despite the significant differences in porosity. This can be explained by the decrease of the number of different contact areas by grain growth so that the probability of contact areas with mismatching lattice planes might increase.[73]

That indicates that the most significant impact on an efficient percolating network has the grain size distribution so that for the further development of ceramic ion conductors a minimal grain size should be aimed at.

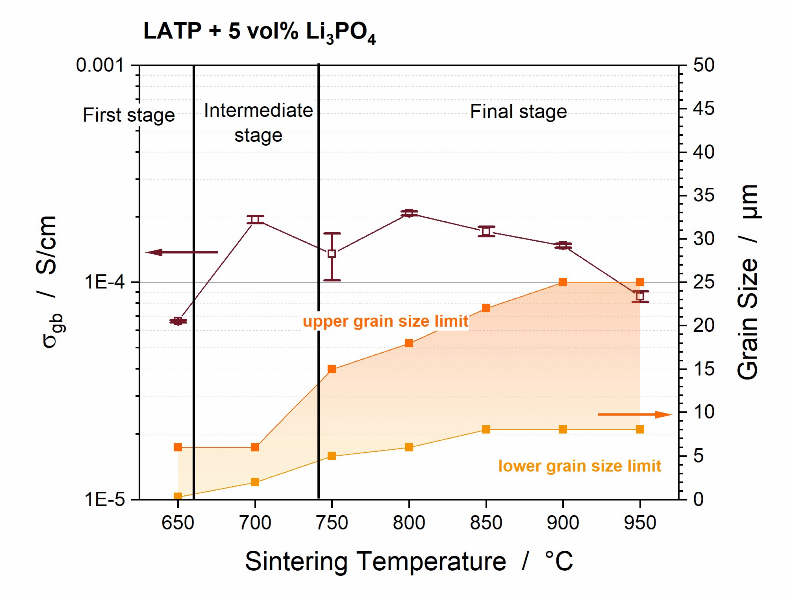

Fig. 5.17 Comparison of grain boundary conductivity σ_{gb} and grain size of the LATP + 5 vol% Li_3PO_4 samples.

Large grain sizes could additionally explain the low conductivities of the pure LATP pellets. Transferring the findings to the 3 vol% and 5 vol% samples, it indicates that an overall decrease in grain boundary conductivity correlates with grain growth. Since the overall decrease in conductivity of the 3 vol% samples is lower and higher for the 10 vol% samples, the assumption made above can be verified by analyzing their microstructure. Nonetheless, it indicates that the grain size distribution is affected by the Li_3PO_4 amount.

A further parameter, which is highly affected by the grain size, is the grain boundary capacitance. As discussed before, the capacitance is in direct correlation with the grain size (**Eq. 3.10**). In fact, the two slopes between 650 °C and 750 °C and between 750 °C and 900 °C demonstrated in the capacitance curve (**Fig. 5.13**) are in perfect accordance with the trend of the grain size. The most significant increase in grain size takes place between 650 °C and 750 °C, thus an increased slope can be determined in the capacitance curve.

Finally, the grain boundary activation energy shows a continuous decrease, which could be correlated with the grain size (**Fig. 5.15**). However, the activation energy has no theoretical foundation which would justify a correlation to the grain size. This also applies to the bulk conductivity (**Fig. 5.11**).

In the end, small grain sizes and a narrow distribution have a significantly positive impact on the percolating network for ion migration so that the ionic conductivity is high even with high porosity. The alternations and the overall decrease of the grain boundary conductivities could be explained. However, the significant decrease at 950 °C needs further consideration.

Crack Formation

Cracks in the microstructure can appear during the cooling process after sintering due to the reduction of internal stress. The crack formation could be detected at sintering temperatures ≥ 850 °C for the LATP + 5 vol% Li_3PO_4 samples (**Fig. 5.8 h-j**) and at sintering temperatures ≥ 900 °C for the pure LATP samples (**Fig. 5.8 b-c**). Since cracks result in empty spaces between grains, the grain boundary conductivities are supposed to be decreased. An impact on bulk conductivity, grain boundary capacitance and grain boundary activation energy is not expected and could not be detected.

The crack formation can be an explanation for the low ionic conductivities of the pure LATP pellets. Additionally, it explains the significant decrease of the grain boundary conductivity of the LATP + 5 vol% Li_3PO_4 pellets sintered at 950 °C (**Fig. 5.12**), which could not finally be clarified by porosity and grain size. This indicates that 3 vol% samples at 950 °C are supposed to have a less crack amount since the ionic conductivity is higher than for the 5 vol% and 10 vol% samples.

5.6 Summary and Conclusion of the Investigation into Sintering Additives

The sintering process of LATP could be significantly accelerated by adding Li_3PO_4 as a sintering additive. The obtained liquid phase sintering results in a reduction of the temperatures of sinter neck formation by 50 °C and the start of shrinkage by 150 °C (**Fig. 5.6**). This additionally causes good grain boundary conductivities at lower sintering temperatures. It could be shown, that the pellets sintered at 800 °C have the highest grain boundary conductivities of 2.08 E-4 S/cm ± 0.04 E-4 S/cm (5 vol%) with the lowest error (**Fig. 5.12**). A reliable comparison is between the conductivities of these pellets and the expected grain boundary conductivities of > 1E-4 S/cm of pure LATP pellets sintered at 1000 °C reported in the literature.[65,73,148] The pure LATP pellets sintered at 950 °C in this study obtain grain boundary conductivities of 6.03 E-5 S/cm ± 0.14 E-5 S/cm (**Fig. 5.12**), which is also in good accordance with the literature.[73,96]

The analyses of the sintering behavior and the microstructure via XRD, thermal-optical measurements devices (TOM), water saturation by Archimedes principle and SEM lead to the identification of four main effects, which influence the electrical properties obtained via EIS: i) formation of the secondary phases $LiTiOPO_4$ and $AlPO_4$; ii) pore elimination, densification and shrinkage; iii) grain growth and grain size distribution; iv) crack formation.

As a result of these analyses, the LATP + 5 vol% Li_3PO_4 samples could be classified in the three sintering stages, known from the literature. The start of the final stage could be determined at 750 °C (**Fig. 5.7b**). The pure LATP samples are still in the intermediate sintering stage or the transition from the intermediate to the final stage at 950 °C (**Fig. 5.7a**). This is in good accordance with the literature, where the maximum shrinkage is reported between 950 °C and 1100 °C.[73,148] Consequently, the maximum grain boundary conductivity of pure LATP is not reached in this study.

The $LiTiOPO_4$ and $AlPO_4$ formations (**Fig. 5.3** and **Fig. 5.4**) suggest a depletion of Ti^{4+} and Al^{3+} in the LATP lattice, which is supposed to cause a high degree of misorientation, hence, a separate phase at the grain boundaries. Indications could be found in the decreases of bulk conductivities (**Fig. 5.11**) and grain boundary activation energies (**Fig. 5.15**). Li-ion transfer into the secondary phases and Li_3PO_4 is also conceivable. However, these hypotheses need to be verified in further studies.

On a macroscopic level, secondary phases, densification, grain size distribution and crack formation significantly affect the grain boundary conductivity, which is the most important characteristic value and limiting factor of an ionic conductive ceramic. A rapid increase in conductivity between the first sintering stage and final sintering stage (650 °C to 750 °C) could be observed, which corresponds to the decrease of porosity and the increase of grain-to-grain contacts due to pore elimination. Secondly, an overall decrease in the ionic conductivity during the final sintering stage (800 °C to 950 °C) was detected. This is in accordance with the grain growth via Ostwald ripening, which causes large grains by assimilating small grains and a significant change in microstructure. Larger grains result in less grain-to-grain contacts, thus, a decrease in possibilities of Li-ion hopping between two grains. Additionally, the interruption of the percolation network by secondary phases, Li_3PO_4 and cracks results in a further decrease of the grain boundary conductivity up to 950 °C (**Fig. 5.12**).

The error margin at 750 °C is high so that an unsteady microstructure development seems to be likely at the transition of the intermediate to final sintering stage (**Fig. 5.12**). The second effect is the high ionic conductivity at a sintering temperature of 700 °C. The material is in the intermediate sintering stage and has a high porosity of 26 % (**Fig. 5.7b**). However, the grain boundary conductivity is 1.94 E-4 S/cm ± 0.07 E-4 S/cm, so slightly lower than the sample sintered at 800 °C. This confirms the importance of the grain size and a narrow grain size distribution since the grain size is 2 - 6 µm (700 °C, **Fig. 5.8e**), which is significantly lower than 6 - 18 µm (800 °C, **Fig. 5.8g**). That results in an efficient percolating network despite a high porosity.

Consequently, a small grain size (< 6 µm) and high densification (< 10 % porosity) should be aimed for further optimization. Nevertheless, a reduction of the sintering temperature of 200 °C with high ionic conductivities could successfully be achieved. The impact of macroscopic effects such as densification, grain size distribution and crack formation on the electrical properties like grain boundary capacitance, conductivity and activation energies could be clarified. For that purpose, the microstructure of the LATP + 3 vol% samples should be analyzed, since these samples demonstrate the most constant and best ionic conductivities. Furthermore, the sintering process could be optimized by optimization of the heating ramp and by reduction of the sintering duration. Moreover, two hypotheses for the impact of the $LiTiOPO_4$ and $AlPO_4$ secondary phases on the microscopic properties like grain lattice stoichiometry and grain boundary nature were set up, which need to be verified. For instance, atomic-resolution high-angle annular dark-field scanning transmission electron microscopy could be applied to obtain information about the grain boundary orientation and to reveal the expected separate grain boundary phas

6 TF-SSB | Engineering Current Collector/Cathode Interface

Thin-film solid-state batteries (TF-SSBs) can be used as a model system to investigate the influences of interdiffusion processes and mixed phase formation between cathode active material and solid-state electrolyte (SSE) on the electrochemical performance of the battery cell. Since the film thicknesses of the active material and SSE are < 1 µm, the diffusion path ways for electrons and Li-ions are short, which reduces significantly the internal resistance. Furthermore, by simplifying the cell geometry in comparison to bulk cathodes, parameters like active area and layer thicknesses of cathode and SSE films can be controlled more accurately than the parameters tortuosity, percolation, microstructure or porosity for particulate bulk-cathodes. Thus, these parameters can be neglected and by that the cell system can be simplified, which enables electrochemical investigations of solely the impact of interdiffusion and mixed phase formation on the cell performance. After deposition of the cathode active material on the substrate current collector, the subsequent SSE deposition on the cathode active material film uncouples the SSE from the electrically conductive component so that further considerations about their thermal stability are not necessary. However, the crystallization of the cathode material on the substrate current collector requires high-temperature processes above 600 °C. Consequently, the thermal stability of the active material in combination with the current collector must be given and it has to withstand temperatures ≥ 650 °C,[78,167,168] which are required to obtain the high Li-ion conductive crystalline phases of the SSEs, such as LATP or LLZO, after the subsequent SSE deposition.

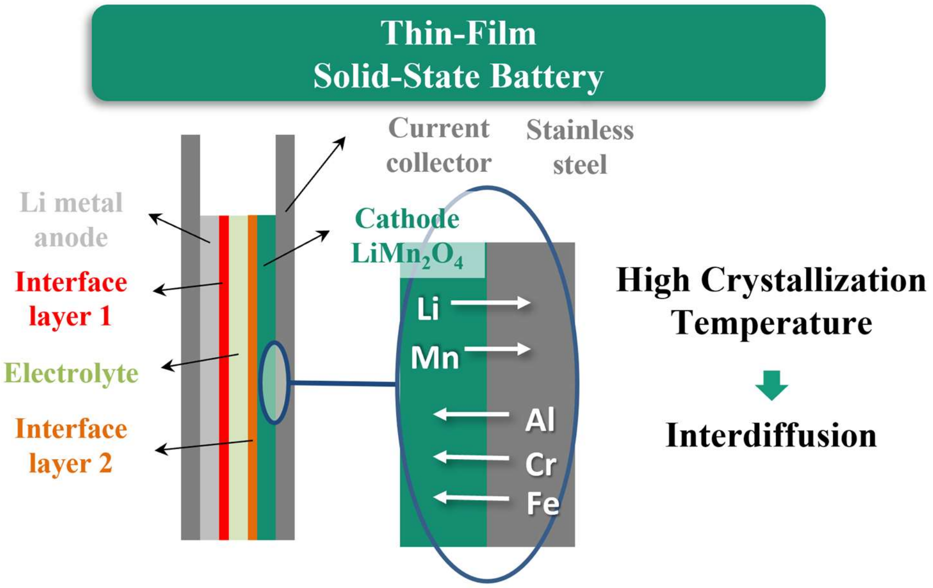

Fig. 6.1 Interdiffusion processes between StSt current collector and LMO thin-film can occur during the high-temperature manufacturing process of TF-SSBs.

As a first step towards TF-SSBs, the thermal stability of $LiMn_2O_4$ (LMO) cathode thin-films on a heat-resistant stainless-steel (StSt) current collector has been investigated. Interdiffusion processes and mixed phase formation could be correlated with changes in the electrochemical performance. Additionally, the three conductive interlayers ITO, Pt and Au were tested as interdiffusion barriers between LMO and StSt. Interdiffusion processes could be revealed by time-of-flight secondary ion mass spectrometry (ToF-SIMS), which was performed at the Swiss Federal Laboratories of Material Science and Technology (EMPA, Schweiz) in cooperation with the group of Yaroslav Romanyuk. Layer quality and thickness could be examined by SEM. GIXRD measurements reveal changes in the lattice parameters of the LMO spinel and XPS measurements show changes in the oxidation states of Mn at the LMO surface. The results of the structural analyses could be correlated with the electrochemical results obtained via galvanostatic cycling (GCPL) and electrochemical impedance spectroscopy (EIS). Some of these results are summarized in the master thesis of Michael Machhaus; “Electrochemical investigation on $LiMn_2O_4$ thin films on a stainless-steel substrate for all solid-state batteries” (2020). Further optimization of the interdiffusion barrier had been done within the project work of Johannes Friedrich Nowarra: “Elektrochemische Untersuchung des Einflusses von Indiumzinnoxid Schutzschichten auf LMO Kathoden für Festkörperbatterien” (2022). The author developed the experimental plan and managed the collaboration with EMPA. Data analyses, discussions and interpretation had taken place under my supervision.

The study has been published in the Journal *Materials Advances* of the Royal Society of Chemistry:

M. Rumpel, M. Machhaus, J. Sastre, S. Ziegler, X. Chen, A. Flegler, Y. E. Romanyuk, and G. A. Giffin, “How interdiffusion affects the electrochemical performance of $LiMn_2O_4$ thin films on stainless steel,” Mater. Adv. 2 (7), 2289–2298 (2021).[169]

6.1 Introduction and Status Quo

First principal studies on TF-SSBs show the benefits of SSEs in battery systems and elucidate the potential of ASSBs. Li et al.[52] could demonstrate a TF-SSB, based on a $LiMn_{1.5}Ni_{0.5}O_4$ (LMNO) cathode film, a glassy LIPON SSE film and a Li-metal anode, with a capacity retention of 90.6 % after 10,000 cycles and a coulombic efficiency of almost 100 %. A comparable liquid electrolyte cell showed an irreversible capacity loss of 30 % after ca. 6,000 cycles due to a lower coulombic efficiency and side reactions. However, the specific capacity of the $LiMn_{1.5}Ni_{0.5}O_4$ cathode in the TF-SSB was determined to be about 83 % of the theoretical capacity of 148 mAh/g.[52] Since the LIPON electrolyte is an amorphous, glassy electrolyte, which does not need a high-temperature crystallization step after sputter deposition, it can be assumed that the lack of utilization of the LMNO cathode is caused by side effects during crystallization at 700 °C for 1 h of the cathode film on the substrate. Li et al.[52] used Pt on Al as substrate. Further studies with Pt[170,171], Au[172,173], StSt[174] or metal alloy[175] substrates show a similar effect of low utilization.

Komaba et al.[174] could show that the electrochemical performance of LMO thin films on StSt substrate depends on the annealing temperature. The authors identified the interdiffusion of Cr and Fe atoms into the LMO layer. Gellert et al.[173] used Au interlayers between LMNO and StSt substrates and they found oxide formation at the LMNO and Au interface including iron oxides and chromium oxide from the StSt substrate. Kim et al.[171] could slightly increase the cell performance of LMNO cathodes on a Pt|StSt substrate by introducing an ITO interlayer between Pt and StSt. These studies have demonstrated the importance of the choice of substrate and crystallization temperature in terms of cell performance. However, since various active materials and annealing conditions were used in several studies, an accurate comparison of the different interlayer materials is difficult to realize.

On this account, this section focuses on a comprehensive and structured comparison of the interlayers Pt, Au and ITO between LMO thin films and StSt substrates and their capability of functioning as interdiffusion barriers for StSt elements depending on the crystallization temperature of the LMO thin films. On basis of the work of Röder et al.[176], who successfully realized LMO thin films on FTO glass substrates via a sol-gel synthesis at the Fraunhofer ISC, these LMO thin films are transferred to flexible StSt substrates, which additionally enables roll-to-roll manufacturing. By analyzing the structural properties of LMO via GIXRD, XPS and ToF-SIMS as a function of the crystallization temperature and interlayer material, a correlation with the electrochemical performance can be given. A better understanding of the interdiffusion processes and their impact on electrochemistry elucidate the lack of utilization of the cathode materials, which has been reported in the literature, and it can be shown that an optimized ITO interlayer enables a better electrochemical performance even at elevated temperatures.

6.2 Experimental Approach

This subchapter gives a short overview of the experimental plan (**Fig. 6.2**). Detailed information can be found in the experimental section (**Chapter 9.3**).

The base substrate was a heat-resistant ferritic chrome steel with 20 wt% Cr and 5 wt% Al and a thickness of 30 µm (1.4767, X8CrAl 20-5, H + S Präzesionsfolien GmbH). It was cut into 5 x 5 cm² samples. Au and Pt were sputtered on top of the StSt substrate. ITO interlayers were deposited by dip-coating of a sol solution. The deposition parameters were particularly chosen to obtain 100 nm thick interlayers.

LMO was deposited on the various substrates via dip-coating of a sol solution. The coated layers were immediately dried at 180 °C for 30 min. Afterward, the LMO layers were rapidly annealed at 600 °C for 1 h or at 700 °C for 1 h.

These samples were analyzed via SEM, ToF-SIMS, GIXRD and XPS, of which more information can be found in the experimental section (**Chapter 9.3**).

Before cell assembly, the backside of the coated StSt was polished to remove the oxide layer formed during annealing. Cathodes were cut into round (16 mm diameter, 2.01 cm²) pieces and dried in vacuum (10^{-2} mbar). Pouch cells were assembled in an argon-filled glovebox with Li-metal anodes and an EC:DMC (1:1 vol%) with 1 M $LiPF_6$ electrolyte (LP30, BASF).

Galvanostatic cycling with limited potential (GCPL) was performed at 25 °C with a current density of 30 µA/cm² between 4.4 V vs. Li/Li^+ and 3.2 V vs. Li/Li^+. After the constant current charge step, a constant voltage step at 4.4 V with the end criteria of 5 min or a current density limit of 0.5 µA/cm² was executed. After 24 cycles, the cells were charged to 4.4 V and held for 3 h or until a current density limit of 0.75 µA/cm² was reached to obtain quasi-stable conditions for the electrochemical impedance spectroscopy (EIS), which was carried out at 4.4 V in the frequency range between 1 MHz and 1 mHz with an amplitude of 5 mV. Two cells of each sample type were tested.

Rate capability tests were carried out in triplicates with the same test protocol as described above, except the current densities were varied between 200 µA/cm² and 10 µA/cm².

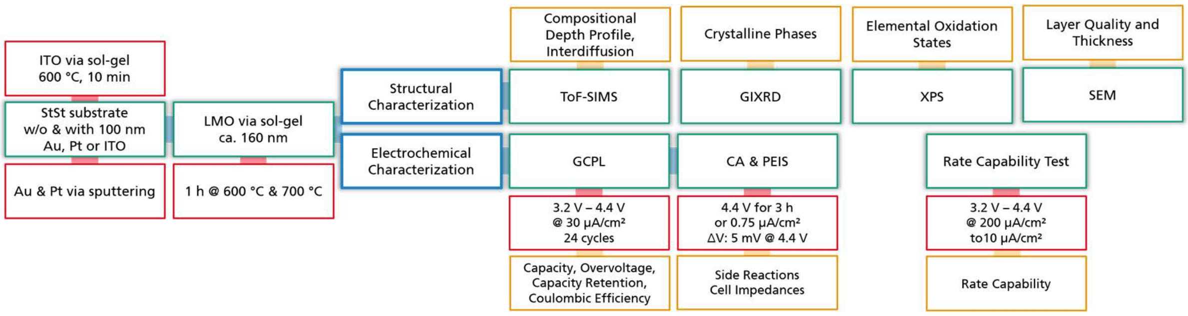

Fig. 6.2 Experimental plan of the investigation into the cathode / current collector interface. Experimental steps (green), parameters (red) and measured properties (orange).

6.3 Structural Investigation of the Interdiffusion Barriers Pt, Au and ITO

Pt, Au and ITO were tested as interdiffusion barriers between LMO and the StSt substrate and were compared with the LMO @ StSt samples without interlayer. Since the degree of interdiffusion depends on the annealing temperature, 600 °C and 700 °C were chosen as crystallization temperatures of the amorphous LMO films obtained from sol-gel dip-coating. SEM images reveal the changes in morphology, ToF-SIMS depth profiles give information about the interdiffusion processes, GIXRD shows changes in the lattice parameters and crystalline phases and the oxidation states of Mn and Fe can be measured via XPS. The obtained structural properties could be correlated with the electrochemical properties obtained by means of GCPL and EIS measurements. The designations of the samples in this chapter are summarized in **Table 6.1**.

Table 6.1 Designation of the samples.

600 °C crystallization temperature	*700 °C crystallization temperature*
LS600 | LMO @ StSt	LS700 | LMO @ StSt
LIS600 | LMO @ ITO @ StSt	LIS700 | LMO @ ITO @ StSt
LPS600 | LMO @ Pt @ StSt	LPS700 | LMO @ Pt @ StSt
LAS600 | LMO @ Au @ StSt	LAS700 | LMO @ Au @ StSt

Morphology of the LMO Thin Films and Interlayers

The interlayers Pt, Au and ITO show comparable layer thicknesses of ca. 100 nm (**Fig. 6.3**). The LMO layer thickness does not depend on the substrate material and is ca. 160 nm for all samples. Cracks between the layers are not observable so that a good electrical contact can be ensured. An additional region of dark contrast is observable between LMO and StSt (**Fig. 6.3a**). This dark contrast can also be detected between ITO and StSt (**Fig. 6.3b**) as well as between Pt and StSt (**Fig. 6.3c**). The sample with an Au interlayer shows the dark contrast between LMO and Au (**Fig. 6.3d**). Such a dark contrast area indicates the formation of an oxide layer during annealing, which will be confirmed and discussed in the ToF-SIMS section.

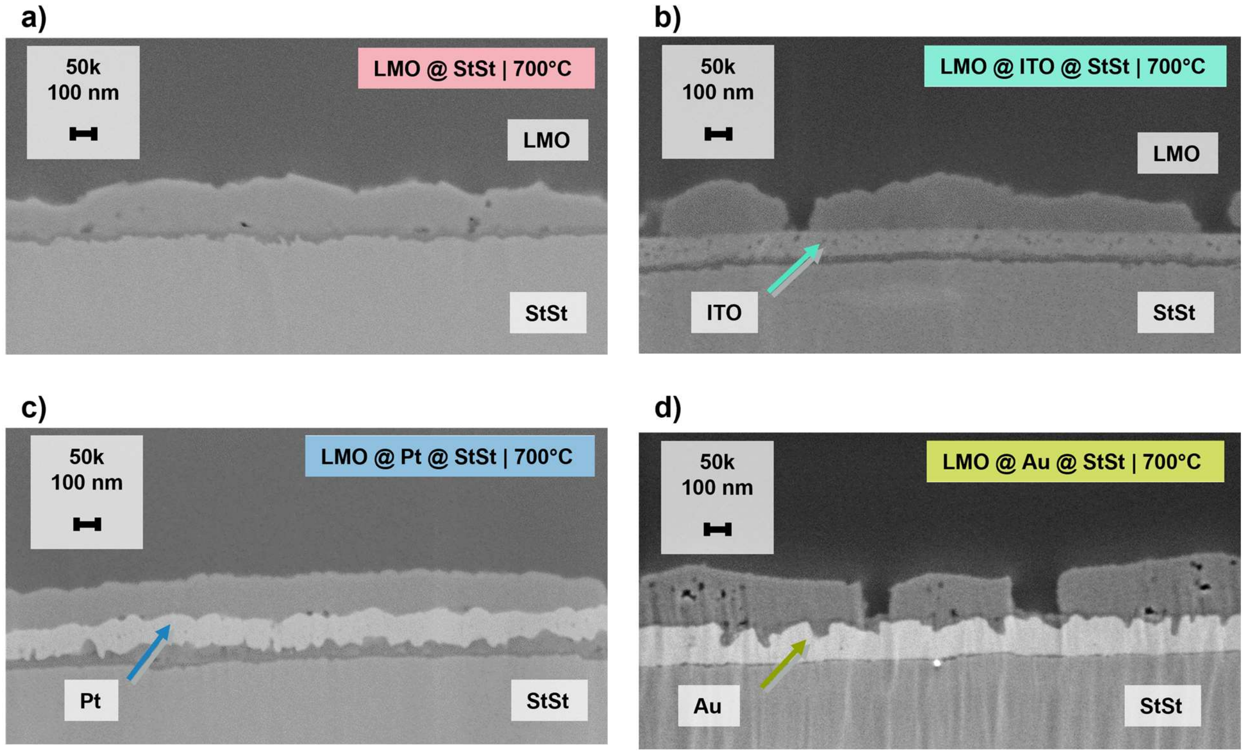

Fig. 6.3 SEM cross-sections of **a)** LMO @ StSt (LS700), **b)** LMO @ ITO (LIS700), **c)** LMO @ Pt (LPS700) and **d)** LMO @ Au (LAS700) annealed at 700 °C for 1 h. LMO layer thicknesses are approx. 160 nm. Layer thicknesses of Pt, Au and ITO are approx. 100 nm. Published by and reprinted from Rumpel et al.[169] (published under CC-BY license in Royal Society of Chemistry: *Materials Advances* 2021).

The top view SEM images of the LMO films on the various substrates reveal cracks and crystallite growth with temperature (**Fig. 6.4**).

Cracks can be detected for all LMO layers. Their origin can be explained by the pyrolysis of the carbon residues from the sol-gel formulation during the crystallization step. After drying the dip-coated LMO film at 180 °C, an amorphous LMO layer, which contains carbon residues, remains. During crystallization at 600 °C or 700 °C, these residues react to CO_2 and this plus the crystallization itself causes a decrease in the volume, which supports the crack formation.

The sizes of the LMO crystallites increase with elevated temperatures. However, the samples also show differences in crystallite size and shape depending on the substrate. For instance, the LS600 sample (**Fig. 6.4a)** appears with larger crystallites and is different in shape compared to the LIS600 sample (**Fig. 6.4b)**. This can also be detected in fewer amounts for the LPS600 (**Fig. 6.4c**) and LAS600 (**Fig. 6.4g**) samples. At this point, it cannot be differentiated whether this effect is caused by differences in the crystallite growth rate or by interdiffusion processes and changes in the crystalline phase. Nevertheless, the increase in crystallite size at 700 °C reduces the electrochemically active area, which should be considered in the analysis of the electrochemical results.

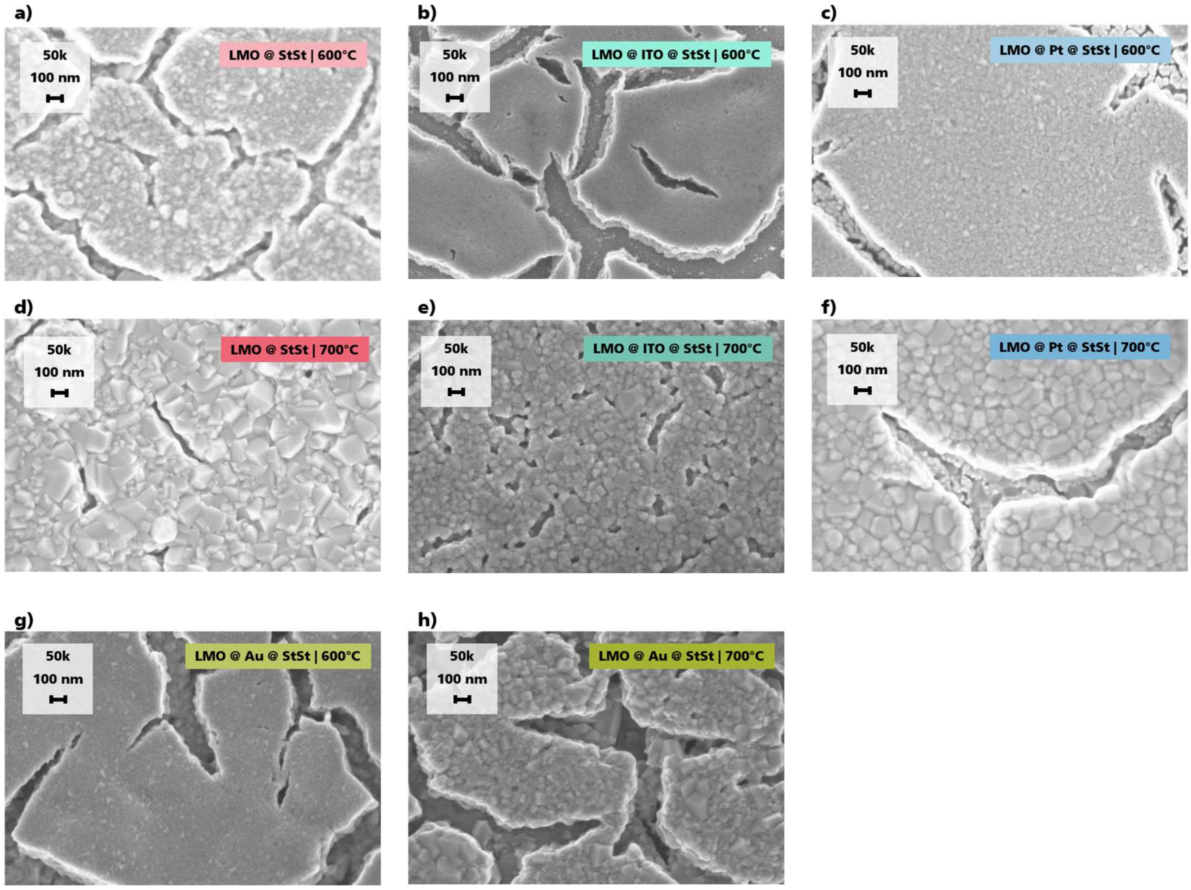

Fig. 6.4 Top view SEM images of the LMO layers annealed at 600 °C on **a)** StSt, **b)** ITO, **c)** Pt and **g)** Au as well as annealed at 700 °C on **d)** StSt, **e)** ITO, **f)** Pt and **h)** Au. Published by and reprinted from Rumpel et al.[169] (published under CC-BY license in Royal Society of Chemistry: *Materials Advances* 2021).

Interdiffusion Processes

The compositional depth profiles obtained via ToF-SIMS measurements are shown in **Fig. 6.5**. The sputter time, which is a measure of the depth of the sample, is normalized to one for the interface between LMO and the interlayer, which is defined as the intercept of the MnO^- signal and the interlayer element signal. This normalization is useful for comparison since the sputter yields differ for Au, Pt, ITO and StSt. The detected mass-to-charge ratios (m/z) will be described by Li^- (m/z = 7 u), MnO^- (m/z = 71 u), AlO^- (m/z = 43 u), CrO^- (m/z = 68 u), InO^- (m/z = 131 u), Pt^- (m/z = 195 u), PtO^- (m/z = 211 u), Au^- (m/z = 197 u) and AuO^- (m/z = 213 u). FeO^- cannot be reliably analyzed because it has the same m/z value as $MnOH^-$ (m/z = 72 u).

The compositional depth profile of the LS600 sample shows an overlap of the Li^- and MnO^- signals from LMO with the AlO^- and CrO^- signals from the StSt substrate (**Fig. 6.5a**). The overlap of the signals increases with temperature and the signal´s overlap becomes broader at 700 °C (LS700, **Fig. 6.5b**). This implies the interdiffusion of substrate elements into the LMO layer as well as Li and Mn into the substrate, which is enhanced with temperature. Additionally, the signal of Li^- is significantly decreasing at the surface, which suggests a Li depletion at the surface. This Li depletion can be detected for all samples. However, the lowest degree can be seen for the samples with an ITO interlayer (LIS600 and LIS700, **Fig. 6.5 c-d**). Moreover, the ITO samples demonstrate, in general, a clear separation between the LMO, ITO and StSt substrate signals. The ITO interlayer appears to block completely the interdiffusion of the substrate elements represented by the AlO^- and CrO^- signals. Additionally, the Li depletion and Mn interdiffusion are significantly reduced compared with the other samples. Thus, ITO shows excellent blocking characteristics, although the Li depletion seems to be slightly increased at 700 °C.

The Pt interlayer shows also blocking characteristics compared with the samples without an interlayer, but in contrast to the ITO interlayer, interdiffusion processes still take place. The LPS600 and LPS700 samples show the inhibition of Cr and Al interdiffusion, however, Pt appears to diffuse into the LMO layer (LPS600, **Fig. 6.5e**). At 700 °C, Pt can be detected in the whole LMO layer and a high degree of Li depletion and Mn interdiffusion can be detected (LPS700, **Fig. 6.5f)**.

The Au interlayer does not block the diffusion of substrate and LMO elements. Even at 600 °C, an overlap of all elemental signals in the interlayer region can be detected (LAS600, **Fig. 6.5g**). This overlap becomes broader at 700 °C (LAS700, **Fig. 6.5h**). Consequently, Cr and Al diffuse through the Au interlayer into the LMO layer as well as Li and Mn diffuse into the substrate. An Au signal cannot be detected in the LMO layer at 600 °C or 700 °C.

As discussed before, the SEM images (**Fig. 6.3**) showed indications of oxide layer formation, which can be confirmed by the ToF-SIMS depth profiles. These oxide layers are represented in the compositional depth profiles by the peaks of the CrO^- and AlO^- signals. These peaks can be detected at LMO/StSt (**Fig. 6.5 a-b**), ITO/StSt (**Fig. 6.5 c-d**) and Pt/StSt (**Fig. 6.5 e-f**) interfaces. Since the Au interlayer cannot block the Cr and Al interdiffusion, the oxide layer can be detected at the LMO/Au interface (**Fig. 6.5 g-h**). This oxide layer is highlighted by the gap between the maxima of the AuO^- signal representing the oxide layer at ca. 1.5 normalized sputter time and the pure Au^- signal representing the Au interlayer at ca. 3.5 normalized sputter time for the LAS600 sample (**Fig. 6.5g**). The AlO^- and CrO^- signal have their maxima at ca. 2.0 normalized sputter time.

In conclusion, the compositional depth profiles reveal interdiffusion processes of Li and Mn into the substrate and of Cr and Al into the LMO layer. This leads to Li depletion at the LMO surface. The best blocking characteristics could be found for the ITO interlayer even at elevated temperatures. Li depletion is significantly reduced and no substrate elements can be detected in the LMO layer. Pt can block the substrate element interdiffusion but Pt diffuses into the LMO layer. Au does not block Li and Mn as well as substrate element interdiffusion.

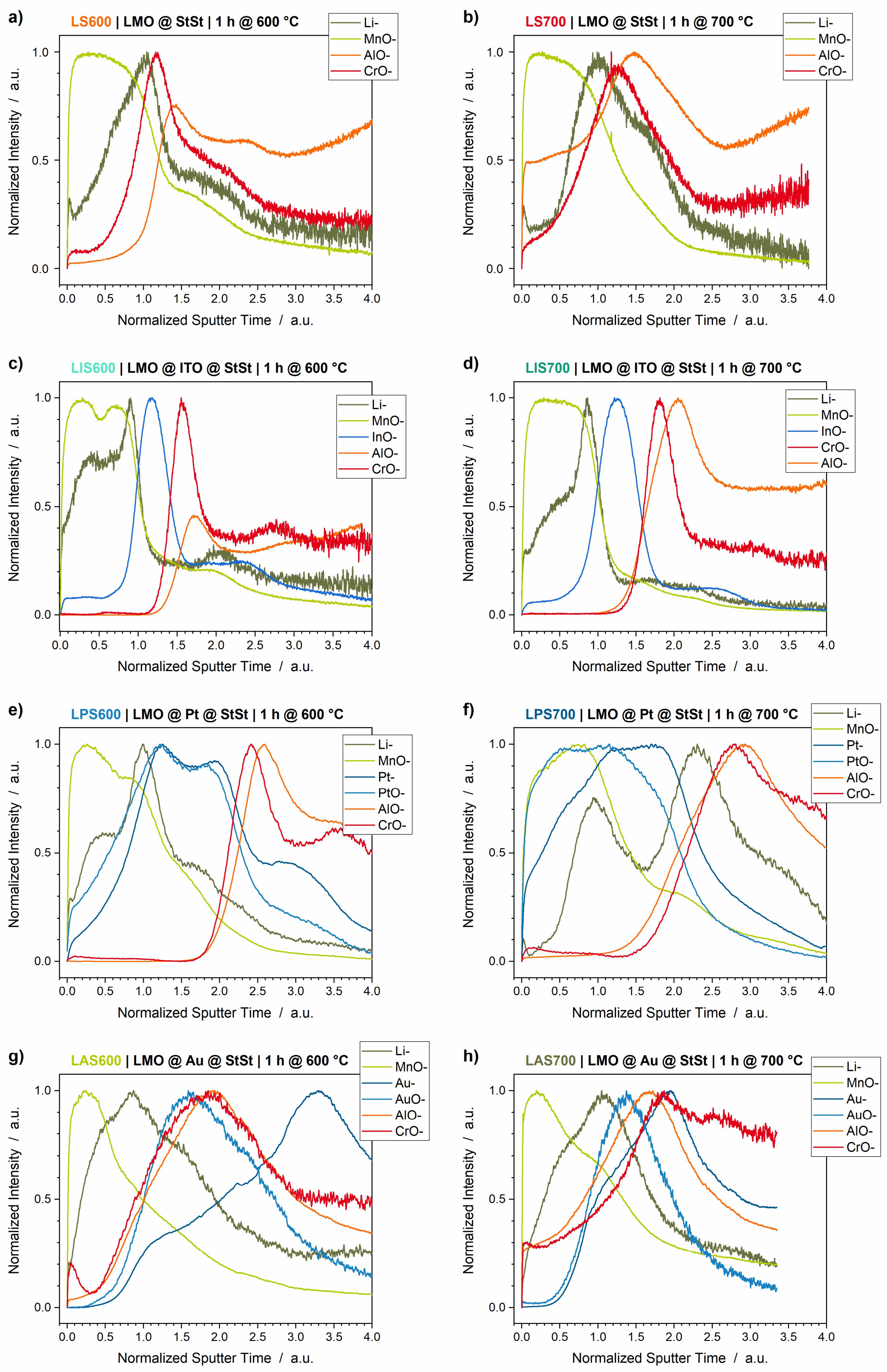

Fig. 6.5 ToF-SIMS depth profiles of 600 °C annealed samples: **a)** LMO @ StSt, **c)** LMO @ ITO, **e)** LMO @ Pt and **g)** LMO @ Au; as well as 700 °C annealed samples: **b)** LMO @ StSt, **d)** LMO @ ITO, **f)** LMO @ Pt and **h)** LMO @ Au. Sputter time is normalized to 1 for the interface between LMO and interlayer. LMO elements (Li^- and MnO^-) in green, StSt elements (AlO^- and CrO^-) in red and interlayer elements (InO^-, Pt^-, PtO^-, Au^- and AuO^-) in blue. Published by and reprinted from Rumpel et al.[169] (published under CC-BY license in Royal Society of Chemistry: *Materials Advances* 2021).

Crystalline Phases

The GIXRD diffractograms of all samples show crystalline LMO with the main reflections at ca. 18.72°, ca. 36.28° or ca. 44.12° (LMO, ICSD 94340). One reflection of the StSt substrate can be detected at ca. 44.35° for all samples (Fe, ICSD 64795) (**Fig. 6.6a**). Using the ITO interlayer results in reflections at ca. 21.50°, ca. 30.59° or ca. 35.46° representing ITO (In_2O_3 ICSD 41265) (**Fig. 6.6a**). LPS600 and LPS700 show reflections of Pt at ca. 39.84° and ca. 46.33° (Pt, ICSD 649493) (**Fig. 6.6b**). Additional crystalline phases due to mixed phase formation are not detectable for the samples with ITO and Pt interlayers or without interlayers (**Fig. 6.6 a-b**). In contrast, the samples with Au interlayers demonstrate reflections belonging to the crystalline phases AuLi ($2\theta = 28.9°$ and 41.0°, ICSD 58523), $AuLi_3$ ($2\theta = 28.1°$, ICSD 58524), Au_2Mn ($2\theta = 28.1°$, 37.8° and 41.3°, ICSD 657181) and $AlAu_2$ ($2\theta = 20.0°$, 38.1° and 43.3°, ICSD 606020) (**Fig. 6.6b**). These several Au alloys with Mn, Li or Al confirm the interdiffusion processes, which have been detected by ToF-SIMS. Additionally, MnO_2 ($2\theta = 38.7°$, ICSD 20228) and MnO ($2\theta = 34.8°$ and 40.2°, ICSD 18006) phases can be detected, which confirms the oxide layer formation at the LMO/Au interface.

A deeper insight into the interdiffusion processes can be given by the analyses of the positions of the 111 reflections of the LMO phases (**Fig. 6.6c**). The 2θ position is reported in the literature with 18.714° (LMO, ICSD 94340) and is in good accordance with the 2θ position of the LIS600 sample of 18.720° so that this value can be set as a benchmark. Depending on an increasing annealing temperature and on the interlayer material, shifts in the range of 0.053° (LIS700, **Fig. 6.6c**) up to 0.1848° (LS700, **Fig. 6.6c**) to lower 2θ values can be detected. These shifts can be caused by changes in the lattice parameters. Considering further spinel phases including Mn and the substrate elements Fe and Cr, such as Mn_3O_4, Fe_3O_4, $FeMn_2O_4$, $MnFe_2O_4$ or $CrMn_2O_4$, with reported 111 reflections at 18.022° (ICSD 31094), 18.467° (ICSD 77592), 18.040° (ICSD 28666), 18.237° (ICSD 56121) and 18.097° (ICSD 74707), respectively, it can be deduced that the interdiffusion of substrate elements causes substitution of Li and Mn in the spinel lattice, which leads to a shift to lower 2θ values of the 111 reflection of the LMO phase.

Li and Mn depletion and the interdiffusion of interlayer elements and substrate elements into the LMO layer detected by ToF-SIMS (**Fig. 6.5**) can be correlated with the findings of the GIXRD measurements. The possible substitutions of Li and Mn might result in further spinel species represented by the formulas AB_2O_4 (A or B = Mn, Fe, Cr, Al, Pt) or $LiMnXO_4$ (X = Fe, Cr, Al, Pt). A deeper consideration will be given in the discussion section.

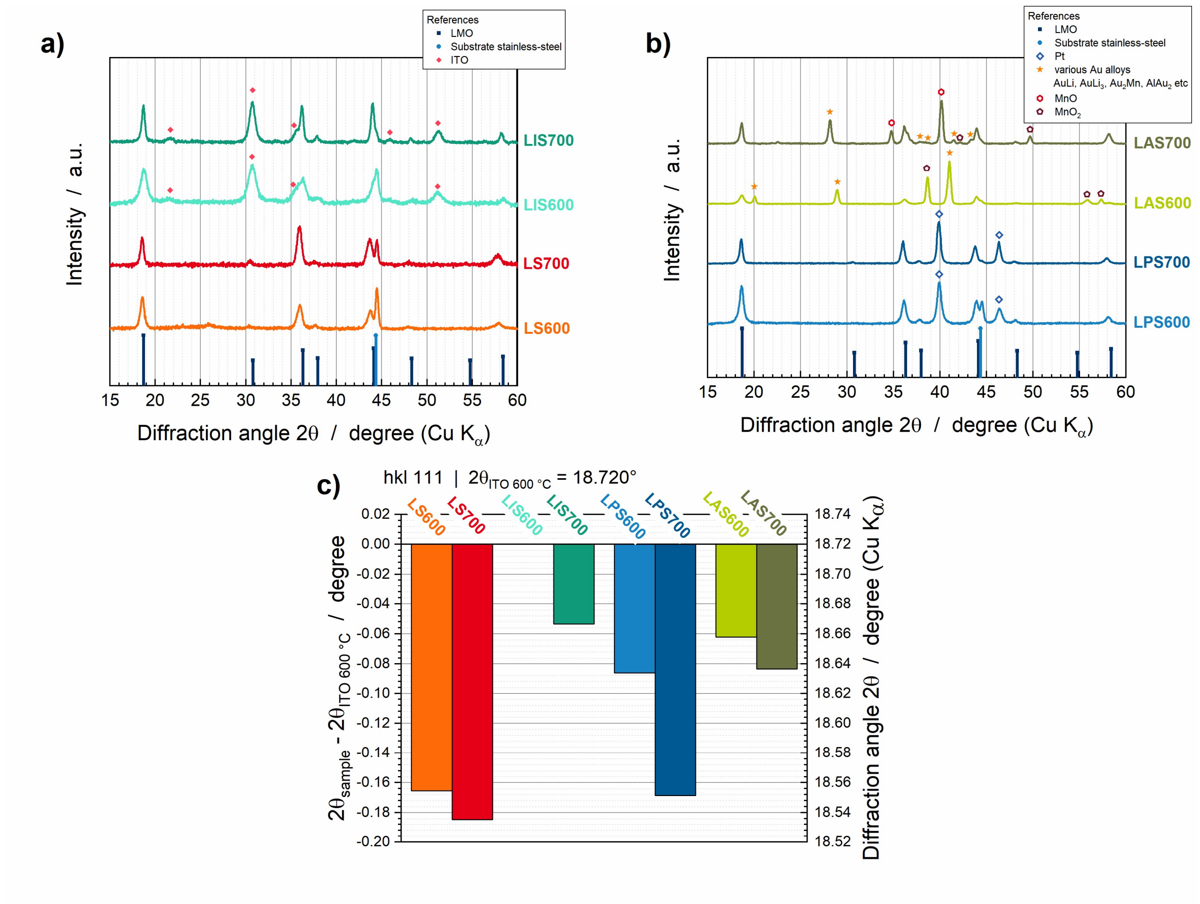

Fig. 6.6 a) GIXRD patterns of LMO on top of StSt (red) and ITO (cyan) and **b)** GIXRD patterns of LMO on top of Pt (blue) and Au (green). **c)** Analysis of the shifts of the reflection positions of all samples: LIS600 is set as a benchmark. Published by and reprinted from Rumpel et al.[169] (published under CC-BY license in Royal Society of Chemistry: *Materials Advances* 2021).

Changes in Oxidation States

The Li depletion at the surface may result in Li^+ substitution in the spinel lattice, which may lead to various AB_2O_4 spinel phases (A or B = Mn, Fe, Cr, Al, Pt). The oxidation states of Mn in LMO are 3+ and 4+ and the general oxidation states in the AB_2O_4 spinel phases are 2+ for A and 3+ for B.[177] Thus, the Li depletion can lead to the reduction of the Mn^{3+} and Mn^{4+} to Mn^{2+}. Indications of the Mn reduction can be detected via XPS (**Fig. 6.7**). Before interpretation of the XPS data, it is important to keep in mind, that the XPS method is surface sensitive. Consequently, it can give information about a few nanometers of the sample surface and does not allow an interpretation of the bulk layer.

The data analyses of the Mn $p_{3/2}$ peak reveal Mn^{2+} at the surface of LS600, LS700, LIS600 and LIS700, which indicates the presence of MnB_2O_4 species (B = Mn, Fe, Cr, Al, Pt). Without interlayer, the amount of Mn^{2+} is 18 % at 600 °C (LS600, **Fig. 6.7a**) and increases with temperature to 24 % (LS700, **Fig. 6.7a**). Additionally, the decrease of the Mn^{4+} to 37 % (LS600) and 35 % (LS700) from the theoretically expected 50 % suggests that the formation of the MnB_2O_4 (B = Mn, Fe, Cr, Al, Pt) at the surface is benefited. Lower percentages of Mn^{2+} of 11 % (LIS600) and 17 % (LIS700) can be detected for the samples with ITO interlayer

(**Fig. 6.7a**). The formation of Mn^{2+} of the LIS700 goes exclusively along with the reduction of Mn^{4+} to 32 %, which also indicates the formation of MnB_2O_4 (B = Mn, Fe, Cr, Al, Pt) due to Li depletion at the surface.

The analyses of the Fe $2p_{1/2}$ and Fe $2p_{3/2}$ peaks show that Fe signals with high intensities can be detected for the samples without interlayer (LS600 and LS700, **Fig. 6.7b**). The LIS600 sample demonstrates the good blocking characteristics of ITO since no Fe can be detected at the surface (**Fig. 6.7b**). At 700 °C, the LIS700 sample shows very low amounts of Fe at the surface (**Fig. 6.7b**). Since the Fe signal of the ToF-SIMS measurement could not be analyzed, these XPS data give a further inside in the Fe interdiffusion. Thus, Cr and Al interdiffusion seem to be blocked by a 100 nm ITO interlayer (**Fig. 6.5 c-d**), however, the ITO interlayer lets pass low amounts of Fe.

The interdiffusion of Fe and the formation of further MnB_2O_4 species (B = Mn, Fe, Cr, Al, Pt) could be confirmed by XPS. The change in the oxidation states and formation of electrochemical inactive MnB_2O_4 at the surface might affect the electrochemical performance.

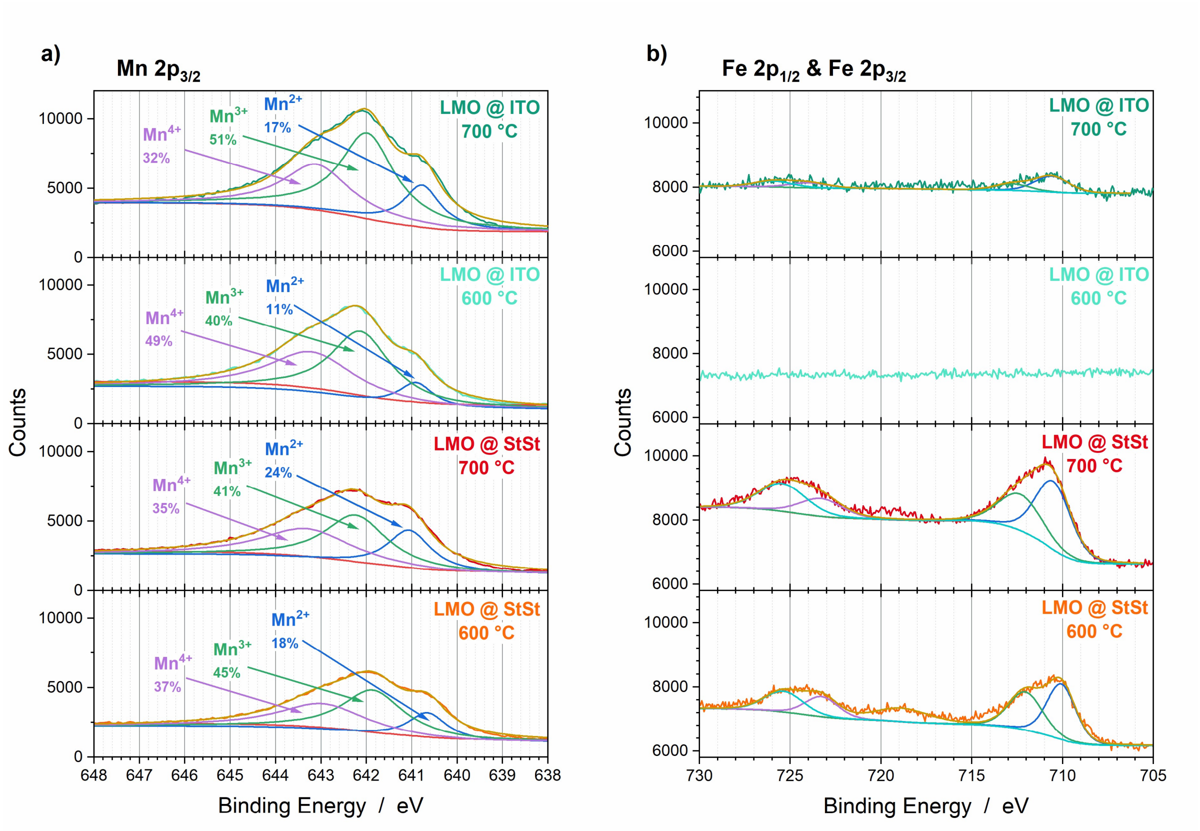

Fig. 6.7 XPS data of LMO @ StSt and LMO @ ITO samples annealed at 600 °C and 700 °C. **a)** Mn $2p_{3/2}$ region and **b)** Fe $2p_{1/2}$ and Fe $2p_{3/2}$ region. Published by and reprinted from Rumpel et al.[169] (published under CC-BY license in Royal Society of Chemistry: *Materials Advances* 2021).

6.4 Electrochemical Investigation of the Interdiffusion Barriers Pt, Au and ITO

Galvanostatic Cycling with Potential Limits (GCPL)

The voltage profiles obtained via galvanostatic cycling at 30 µA/cm² are shown in **Fig. 6.8**.

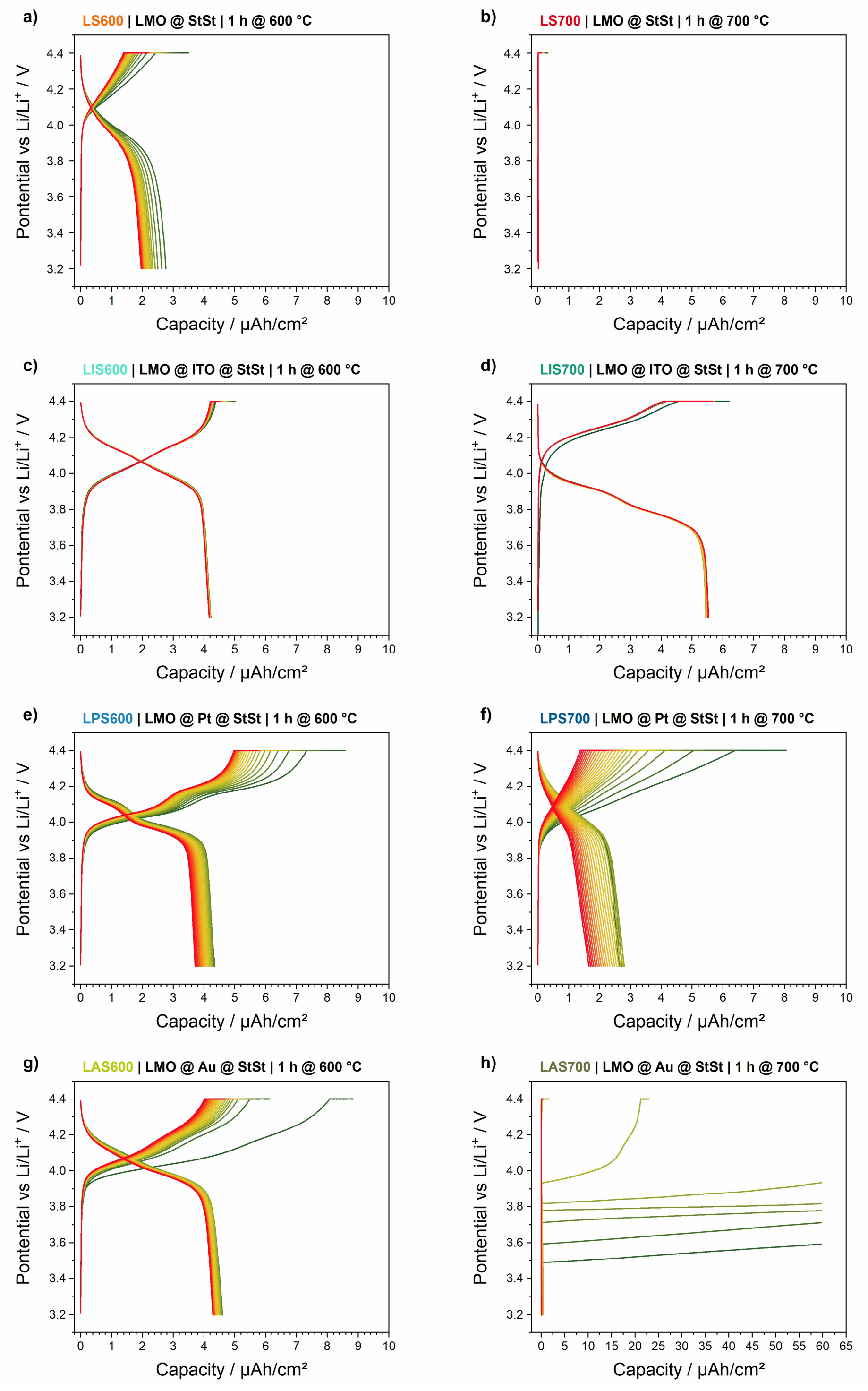

Fig. 6.8 Voltage profiles of 600 °C annealed samples: **a)** LMO @ StSt, **c)** LMO @ ITO, **e)** LMO @ Pt and **g)** LMO @ Au; as well as 700 °C annealed samples: **b)** LMO @ StSt, **d)** LMO @ ITO, **f)** LMO @ Pt and **h)** LMO @ Au. The color gradient starts with green for cycle 1 and ends with red for cycle 24. Current density: 30 µA/cm². Potential limits: 3.2 V and 4.4 V vs. Li/Li$^+$. Published by and reprinted from Rumpel et al.[169] (published under CC-BY license in Royal Society of Chemistry: *Materials Advances* 2021).

At first sight, the voltage profiles (**Fig. 6.8**) differ significantly in terms of discharge and charge capacities, coulombic efficiency, overvoltage and redox plateaus of the Li insertion and extraction (**Chapter 2.1**: Cathode Active Materials). The samples annealed at 600 °C show an electrochemical response and two redox plateaus can be seen for all samples with interlayers, which is in accordance with the literature.[13,23] LS600 shows just one redox plateau. The samples annealed at 700 °C show that LS700 and LAS700 polarize and no capacity can be obtained from the cells. LIS700 and LPS700 demonstrate two redox plateaus, however, their curves differ from LIS600 and LPS600. The samples with Pt interlayers have higher charge capacities than discharge capacities. In the following, the obtained quantitative values of discharge capacity, cycle stability, coulombic efficiency, rate capability, capacity retention and overvoltage are discussed in detail and are summarized in **Table 6.2**.

The comparison of the discharge curves of cycle 24 (**Fig. 6.9a**) shows the influence of interlayer and annealing temperature on the discharge capacities. LS600 has the lowest discharge capacity of 1.99 µAh/cm² ± 0.03 µAh/cm² of the samples annealed at 600 °C. The incorporation of the interlayers Pt, Au and ITO result in an increase of the discharge capacity to 3.57 µAh/cm² ± 0.15 µAh/cm² (LPS600), 4.45 µAh/cm² ± 0.16 µAh/cm² (LAS600) and 4.22 µAh/cm² ± 0.07 µAh/cm² (LIS600). The samples LS700 and LAS700, which were annealed at 700 °C, show no capacity and the LPS700 sample shows a decrease in discharge capacity to 1.19 µAh/cm² ± 0.46 µAh/cm². In contrast, LIS700 demonstrates an increase in discharge capacity by ca. 0.84 µAh/cm² to 5.06 µAh/cm² ± 0.46 µAh/cm². The discharge capacities of the LS600, LAS600, LIS600 and LIS700 samples show a stable trend with cycling number (**Fig. 6.9b**) and have capacity retentions of > 97 % after 24 cycles (**Table 6.2**). The samples with Pt interlayers, in contrast, demonstrate a reduction of the discharge capacities with cycle number, which results in capacity retentions of ca. 86 % for LPS600 and ca. 46 % for LPS700.

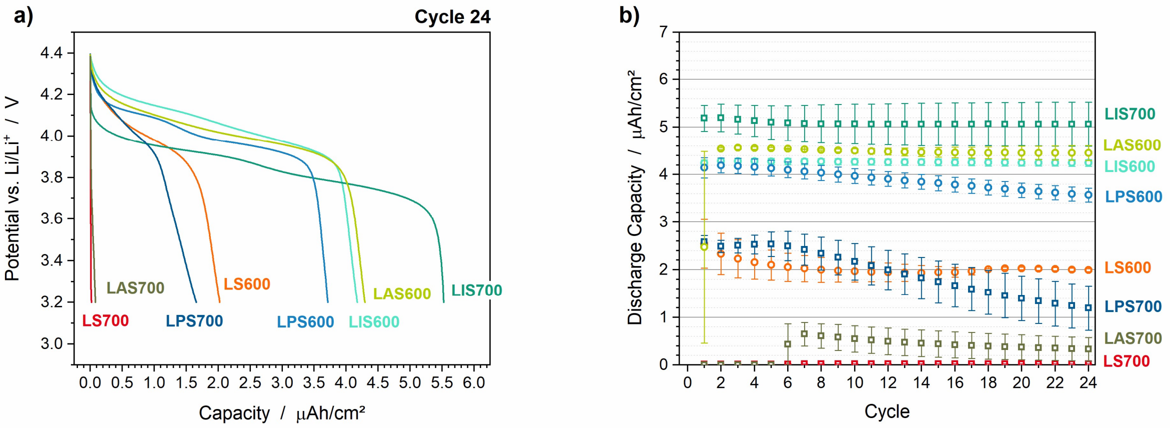

Fig. 6.9 GCPL results of the LMO@StSt (red), LMO@Pt (blue), LMO@Au (green) and LMO@ITO (cyan) samples. **a)** Voltage profile of cycle 24 at 30 µA/cm² and **b)** discharge capacities as a function of cycles at 30 µA/cm². Published by and reprinted from Rumpel et al.[169] (published under CC-BY license in Royal Society of Chemistry: *Materials Advances* 2021).

A decrease in capacity retention is an indication that side reactions take place, which negatively impacts the cell performance. A further indication of that can be deduced from the coulombic efficiency (**Fig. 6.10a**). The coulombic efficiency is the quotient of discharge capacity and charge capacity (**Eq. 3.13**); thus, it is a measure of how much more capacity is required during the charge step, which suggests an irreversible side reaction during charging. The low coulombic efficiencies of the LPS600 (67.1 % ± 2.5 %) and LPS700 (67.0 % ± 11.0 %) indicate such an irreversible side reaction. In contrast, the coulombic efficiencies of the other samples are > 90 % and the ITO samples show 92.5 % ± 0.4 % for LIS600 and 97.3 % ± 0.3 %, which are the best performances (**Table 6.2**).

The influence of an irreversible side reaction for the Pt samples can also be observed in the results of the rate capability tests (**Fig. 6.10b**). These tests give information about the internal loss mechanisms, which are caused by polarization processes and ohmic resistance (**Chapter 2.1**). In general, these effects depend on the current density and have less impact at smaller current densities. By varying the current density and analyzing the differences in discharge capacity, the impact of these loss mechanisms can be quantified and qualitatively compared between the samples. Small differences mean a low effect of the loss mechanisms. In this study, the rate capability is defined as the difference in the discharge capacity at 30 µA/cm² (Cycle 73) and 100 µA/cm² (Cycle 19).

Analyzing the rate capability of the Pt samples, it appears that they cannot be reasonable interpreted, because the discharge capacities decrease by 9 % and 16 % for the LPS600 and LPS700 between cycle 19 (100 µA/cm²) and cycle 73 (30 µA/cm²). This indicates again the presence of an irreversible side reaction. This capacity fade is unique for the Pt cells since the rate capabilities of the other samples have the expected positive values (**Table 6.2**), thus, an increase in discharge capacity with lower currents. The LIS600 shows the lowest difference in discharge capacity of 6 %. At 700 °C, the difference increases to 19 % for the ITO sample. LS600 and LAS600 show differences of 38 % and 15 %, respectively. Comparing the samples annealed at 600 °C, the ITO interlayer demonstrates once again the best performance.

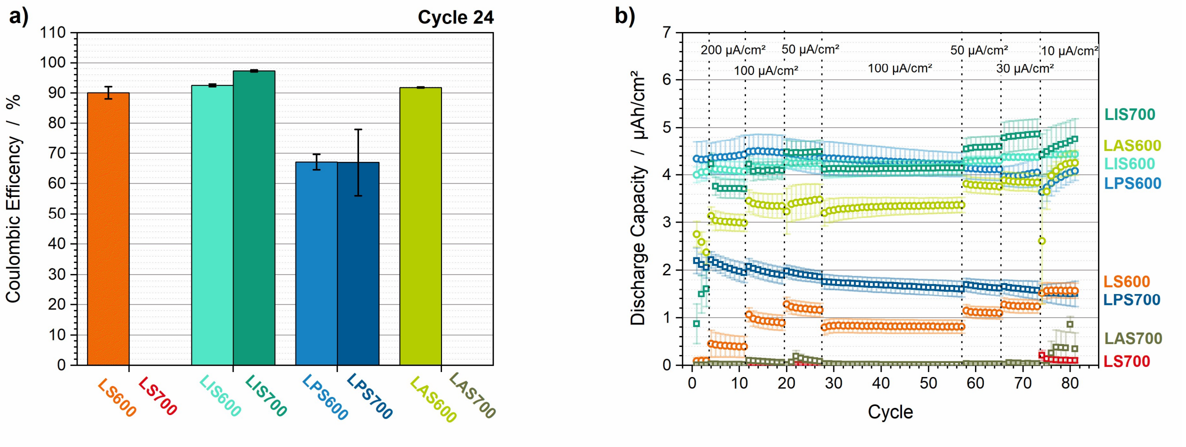

Fig. 6.10 GCPL results of the LMO@StSt (red), LMO@Pt (blue), LMO@Au (green) and LMO@ITO (cyan) samples. **a)** Coulombic efficiencies of cycle 24 and **b)** discharge capacities during the rate capability test. Published by and reprinted from Rumpel et al.[169] (published under CC-BY license in Royal Society of Chemistry: *Materials Advances* 2021).

Polarization processes affect also the overvoltages, which are defined here as the difference between the first redox peak for charge and discharge (**Fig. 6.11**). The overvoltage is related to the overpotential described by the Butler-Volmer-Equation (**Eq. 2.10**) so that it is in particular a measure for the charge transfer polarization. The results for the 600 °C annealed samples represent the same trend as the rate capability. LIS600 has the lowest overvoltage of 12 mV ± 2 mV (**Table 6.2**) and the value are higher for LAS600 (79 mV ± 3 mV) and LS600 (139 mV ± 30 mV). The LIS700 samples show a significant increase in the overvoltage to 574 mV ± 143 mV with a high error, which additionally results in an incomplete charge during the constant current step. That indicates a higher barrier for the charge transfer at 700 °C.

The two-step redox process is reported in the literature at an average potential of ca. 4.0 V vs Li/Li^+ and it is separated by ca. 150 mV. The second redox peak is also reported with a higher peak height than the first redox peak. The nature of these two redox potentials is explained by the change in the diffusion activation energy of the Li-ion by reaching a composition of $Li_{0.5}Mn_2O_4$. At $Li_xMn_2O_4$ $(0.5 < x < 1)$, the Li-ions are extracted from the 8a tetrahedral site of the spinel structure, which is represented by the first redox peak at ca. 3.95 V vs. Li/Li^+. At a composition $Li_xMn_2O_4$ $(0.2 < x < 0.5)$, the Li-ions are ordered at one half of the 8a tetrahedral sites and the diffusion to another 8a side is along an energetically unfavorable neighboring 16c octahedral site. This increases the diffusion activation energy and results in a second redox peak at higher potentials. Additionally, the diffusion activation energies depend on the atomic neighbors of the Li-ion on the 8a-16c-8a pathway.[13,23]

On the basis of this reported knowledge, the ratio between the redox peaks can be analyzed. The LIS600 sample shows a higher peak height for the second redox peak as expected and reported in the literature.[13,23] In contrast, the second redox peaks of the LAS600 and LPS600 samples have a lower maximum and peak area than the first redox peak. The second redox peak of the LS600 sample cannot be detected. That indicates that the neighboring elements of the Li-ions change due to the substitution of Mn elements, which impacts the diffusion activation energy. This might be a further indication of interdiffusion processes.

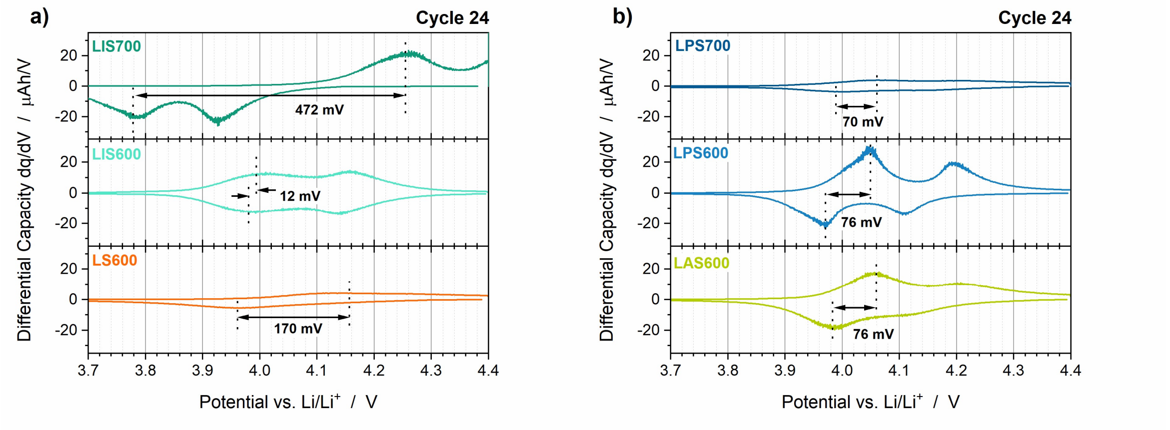

Fig. 6.11 GCPL results of the LMO@StSt (red), LMO@Pt (blue), LMO@Au (green) and LMO@ITO (cyan) samples. **a)** and **b)** Differential capacity plots of cycle 24 (representative cells). Published by and reprinted from Rumpel et al.[169] (published under CC-BY license in Royal Society of Chemistry: *Materials Advances* 2021).

In conclusion, the ITO samples show the best electrochemical performance of all cells. In contrast to the other interlayer samples, the discharge capacity even increases at 700 °C. The trends of the samples seem to correlate with the degree of interdiffusion. The correlation between the structural findings and the electrochemical performance will be discussed in the next subchapter.

Table 6.2 Electrochemical results obtained from galvanostatic cycling. Published by and reprinted from Rumpel et al.[169] (published under CC-BY license in Royal Society of Chemistry: *Materials Advances* 2021).

Sample	**Discharge Capacity Cycle 24 (μAh/cm^2)**	**Coulombic Efficiency Cycle 24 (%)**	**Overvoltage Cycle 24 (mV)**	**Capacity Retention after 24 cycles (%)**	**Rate Capability* (%)**
600 °C crystallization temperature					
LS600 (LMO @ StSt)	1.99 ± 0.03	90.1 ± 2.0	139 ± 30	97.3 ± 16.1	38
LIS600 (LMO @ ITO)	4.22 ± 0.07	92.5 ± 0.4	14 ± 2	99.3 ± 0.2	6
LPS600 (LMO @ Pt)	3.57 ± 0.15	67.1 ± 2.5	66 ± 9	86.4 ± 0.1	n.a.**
LAS600 (LMO @ Au)	4.45 ± 0.16	91.8 ± 0.2	79 ± 3	97.9 ± 4.0	15
700 °C crystallization temperature					
LS700 (LMO @ StSt)			No Capacity		
LIS700 (LMO @ ITO)	5.06 ± 0.46	97.3 ± 0.3	574 ± 143	99.1 ± 2.3	19
LPS700 (LMO @ Pt)	1.19 ± 0.46	67.0 ± 11.0	76 ± 9	45.8 ± 13.6	n.a.**
LAS700 (LMO @ Au)			No Capacity		

* Ratio of Discharge Capacity 30 μA/cm^2: 100 μA/cm^2. ** n.a.: negative values due to side reaction, not reasonable to analyse.

Electrochemical Impedance Spectroscopy

EIS measurements were performed after the GCPL measurements. In between, a constant voltage step at 4.4 V vs. Li/Li$^+$ was executed for 3 h or until a current density limit of 0.75 μA/cm^2 was reached in order to obtain quasi-stable conditions for the EIS measurements.

The current decay during the constant voltage step is demonstrated in **Fig. 6.12**. All samples, except the Pt samples, reach the current density limit in less than 2 h. Their curves seem to be more capacitive in nature, which is related to the finalization of the formation of the electrochemical double-layer. In contrast, the Pt samples show faradic currents with current density values of 6.0 µA/cm² (LPS600, **Fig. 6.12**) and 4.6 µA/cm² (LPS700, **Fig. 6.12**) throughout the entire CV step. These faradaic currents suggest once again the presence of an electrochemical side reaction with a cumulative charge of ca. 18 µAh/cm² (LPS600) and ca. 14 µAh/cm² (LPS700) after 3 h at 4.4 V. Since these values are about three times higher than the measured LMO capacities, it is most likely that a reaction of the Pt interlayer is the origin of the additional irreversible reaction, which will be discussed in the discussion section.

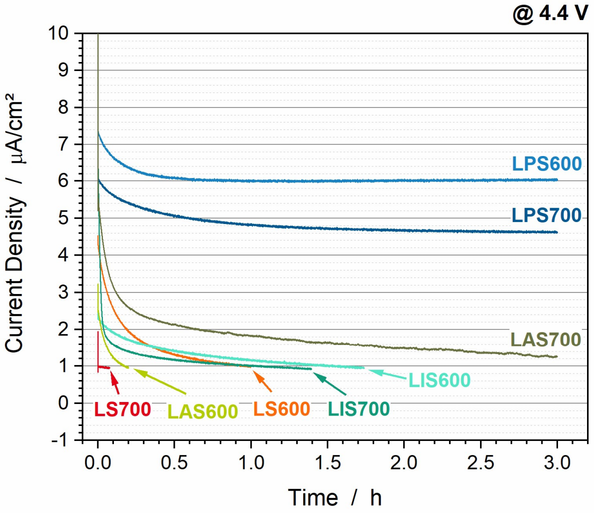

Fig. 6.12 Current decay during the CV step @ 4.4 V vs. Li/Li$^+$ for 3 h. Published by and reprinted from Rumpel et al.[169] (published under CC-BY license in Royal Society of Chemistry: *Materials Advances* 2021).

The EIS measurements were performed at 4.4 V vs. Li/Li$^+$ directly after the constant voltage step. A comparison of the obtained Nyquist plots is shown in **Fig. 6.13**.

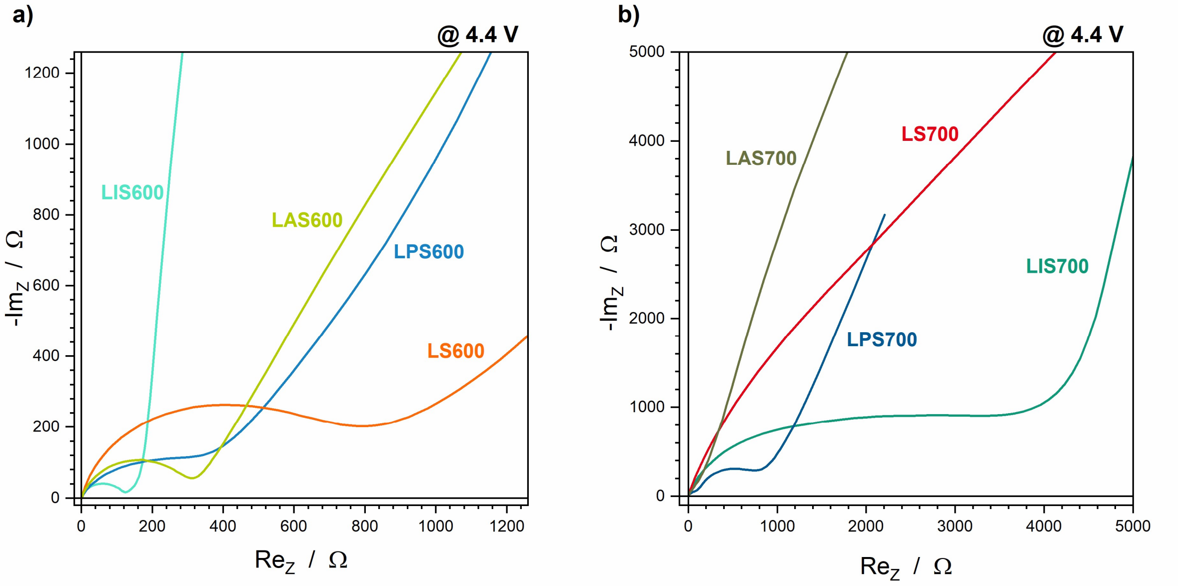

Fig. 6.13 Comparison of Nyquist plots of the samples annealed at **a)** 600 °C and **b)** 700 °C. Published by and reprinted from Rumpel et al.[169] (published under CC-BY license in Royal Society of Chemistry: *Materials Advances* 2021).

The samples annealed at 600 °C show a lower total resistance for the samples with interlayers. The LS600 sample has a total resistance of ca. 800 Ω. The total resistance is reduced to ca. 120 Ω, ca. 320 Ω and ca. 290 Ω by the incorporation of the ITO, Pt and Au interlayers, respectively (**Fig. 6.13a**). At elevated temperatures (**Fig. 6.13b**), the EIS data of the LS700 and LAS700 samples cannot be reasonably analyzed, since their charge transfer resistances are very high, which is also reflected in the GCPL measurements by their polarization behavior (**Fig. 6.9a**). The LIS700 sample shows a significant increase of the total resistance by ca. 3400 Ω compared with the LIS600 sample. The Pt sample shows also an increase to ca. 900 Ω at 700 °C.

A more detailed analysis of the Nyquist plots reveals two semicircles, which correspond to an insulating layer (**Fig. 6.14**, RC_{In}) and the charge transfer (**Fig. 6.14**, RC_{CT}) (**Chapter 3.4**). This interpretation is well reported in the literature and the EIS data can be fitted with the equivalent circuit demonstrated in **Fig. 6.14i**.[178] It consists of an ohmic resistance R_{Ω} representing the internal resistance of the cell, the two RC elements RC_{In} and RC_{CT} for the insulating layer and the charge transfer as well as the Warburg impedance W, which describes the slope at low frequencies and it represents the diffusion mechanisms in the electrolyte. The obtained fit values are summarized in **Table 6.3**.

The formation of the oxide layer detected by SEM (**Fig. 6.3**) and ToF-SIMS (**Fig. 6.5**) was expected to affect the ohmic resistances R_{Ω}. However, R_{Ω} is similar for all samples (**Table 6.3**), so that it has a comparatively little impact on the electrochemical performance.

The insulating layer resistance R_{In} and the charge transfer resistance R_{CT} show a more significant correlation with the interlayer material and the annealing temperature. Comparing the 600 °C annealed samples, R_{In} and R_{CT} have the lowest values of 21.3 Ω and 94.7 Ω for the ITO sample LIS600 (**Fig. 6.14b**). The LPS600 and LAS600 samples have comparable trends with values for R_{In} and R_{CT} of ca. 33 Ω and ca. 270 Ω (**Fig. 6.14c and Fig. 6.14g**). Without an interlayer, the resistances have significantly higher values of 377.6 Ω (R_{In}, LS600) and 424.6 Ω (R_{CT}, LS600) (**Fig. 6.14a**). The trends of R_{In} and R_{CT} for the 600 °C annealed samples correlate with the trends of Li depletion and interdiffusion of substrate and interlayer elements, respectively, which will be discussed in the next section. At 700 °C, the LIS700 sample shows a significant increase in R_{In} and R_{CT} to 1397.0 Ω and 2129.2 Ω, respectively (**Fig. 6.14e**). This is most likely caused by the decrease of the effective electrochemically active area due to crystallite growth (**Fig. 6.4**). However, R_{In} is a fifth of the total resistance for LIS600 and about a half for LIS700. The difference in ratio cannot be solely explained by the change in surface morphology. It indicates that an insulating layer due to Li depletion is formed stronger at elevated temperatures. The LPS700 samples show also an increase in R_{In} to 88.6 Ω and R_{CT} to 806.1 Ω (**Fig. 6.14f**) compared with the LPS600 sample, but the values are significantly lower than for LIS700 so that it is very unlikely that the measured electrochemical reaction is the Li insertion/extraction of LMO. This can be explained by the side reaction of Pt shown before, which is measured here. The Nyquist plots over the entire frequency range of the LS700 and LAS700 samples are demonstrated in **Fig. 6.14d and Fig. 6.14h**. The total resistances are above 80,000 **Ω**, which is in accordance with the voltage profiles, which show solely polarization, thus, no redox plateaus (**Fig. 6.9a**).

The benefits of an ITO interlayer are also shown by the EIS measurements. Indications of a formation of an insulating layer due to Li depletion and further confirmation of an irreversible side reaction for the Pt samples can be observed. A detailed correlation between the electrochemical findings and structural changes is done in the following section.

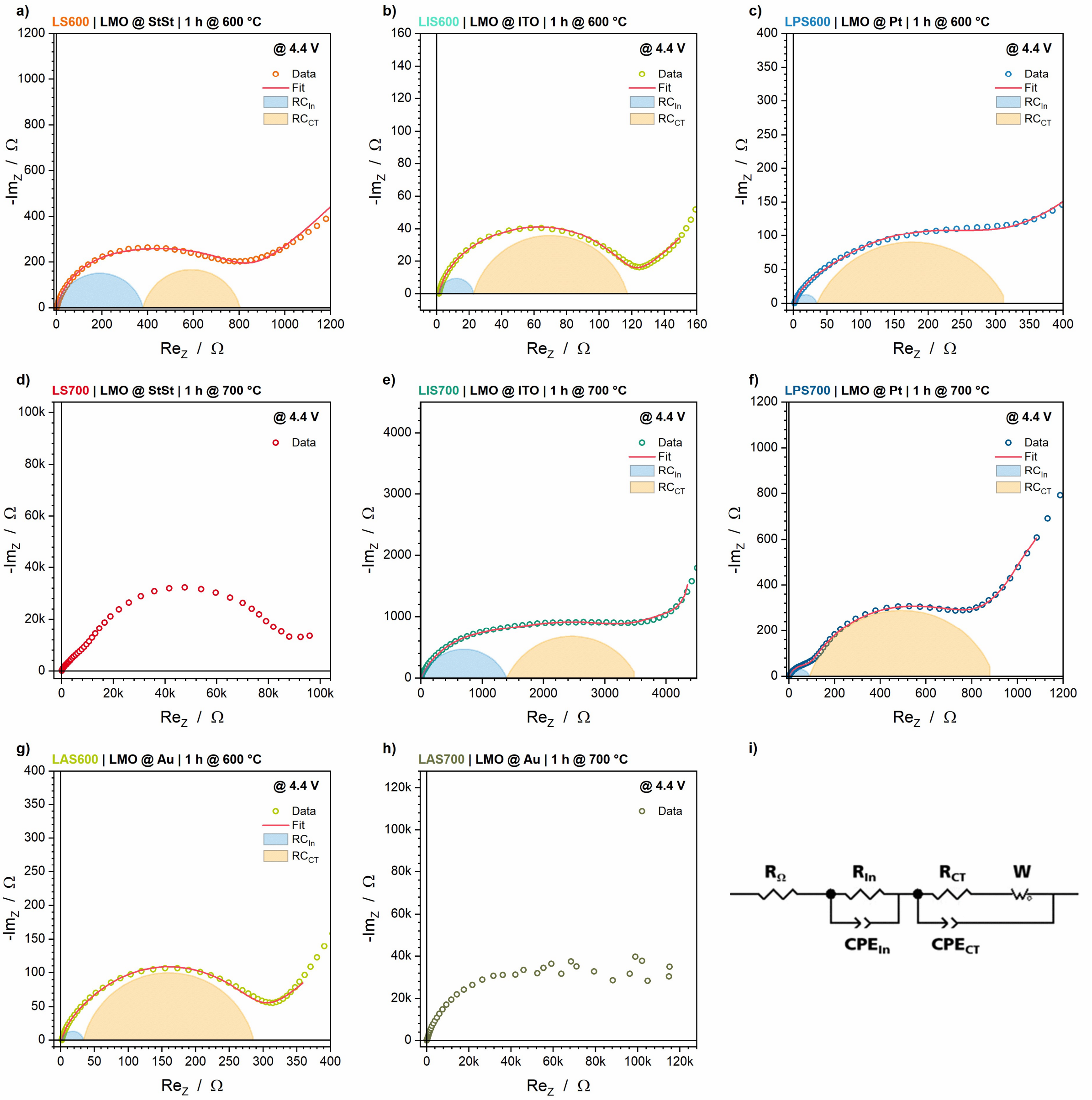

Fig. 6.14 Nyquist plots of the EIS data incl. fits using the equivalent circuit: **a)** LS600, **b)** LIS600, **c)** LPS600, **d)** LS700, **e)** LIS700, **f)** LPS700, **g)** LAS600, **f)** LAS700 and **i)** the used equivalent circuit. Published by and reprinted from Rumpel et al.[169] (published under CC-BY license in Royal Society of Chemistry: *Materials Advances* 2021).

Table 6.3 The ohmic resistance R_Ω, insulating layer resistance R_{In} and charge transfer resistance R_{CT} obtained by fitting the EIS data with the equivalent circuit shown in **Fig. 6.14**. Published by and reprinted from Rumpel et al.[169] (published under CC-BY license in Royal Society of Chemistry: *Materials Advances* 2021).

Sample	R_Ω (Ω)	R_{In} (Ω)	R_{CT} (Ω)
600 °C crystallization temperature			
LS600 (LMO @ StSt)	1.6	377.6	424.6
LIS600 (LMO @ ITO)	1.4	21.3	94.7
LPS600 (LMO @ Pt)	1.4	33.3	282.6
LAS600 (LMO @ Au)	1.6	32.3	252.1
700 °C crystallization temperature			
LS700 (LMO @ StSt)		No Capacity	
LIS700 (LMO @ ITO)	1.4	1397.0	2129.2
LPS700 (LMO @ Pt)	1.8	88.6	806.1
LAS700 (LMO @ Au)		No Capacity	

6.5 Discussion and Correlation of Structural and Electrochemical Results

The structural and electrochemical investigations of the capability of the interlayers ITO, Pt and Au between LMO and StSt to block interdiffusion processes have revealed four main phenomena: i) interdiffusion processes cause Li depletion at the surface as well as substitution of LMO elements in the spinel lattice by substrate or interlayer elements; ii) changes in morphology and crystallinity of LMO at elevated temperatures; iii) samples with Pt interlayer show irreversible side reactions; iv) oxide layer formation. These phenomena will be discussed in the following.

Impact of Interdiffusion Processes on Electrochemical Performance

The ToF-SIMS measurements (**Fig. 6.5**) and XPS spectra (**Fig. 6.7**) show that Cr, Al, Fe and the interlayer element Pt tend to diffuse into the LMO layer as well as Li and Mn diffuse into the StSt layer. This results in the substitution of Li and Mn with Fe, Cr, Al and Pt in the spinel LMO lattice. The substitution of Mn leads to spinels with the formula $LiMnXO_4$ (X = Fe, Cr, Al, Pt) and the depletion of Li at the surface leads to AB_2O_4 (A or B = Mn, Fe, Cr, Al, Pt) spinel species. The interdiffusion processes can be explained by the Hume-Rothery-Rules (**Chapter 2.4**) considering valence factor, size factor, chemical affinity and lattice structure.[90] In terms of valence and size, the requirements of ions in the spinel structure AB_2O_4 are well reported in literature.[177,179] The oxidation states are 2+ for A and 3+ for B. The oxidation states for $LiMnXO_4$ are 3+ and 4+ for Mn and X. The ion radii have to be between 0.55 Å and 0.80 Å.[177,179] The ion radii of the substrate and interlayer elements, which were observed to diffuse into the LMO layer, fill this criterion. Their ion radii are 0.78 Å for Fe^{2+}, 0.65 Å for Fe^{3+}, 0.59 Å for Fe^{4+}, 0.54 Å for Al^{3+}, 0.80 Å for Cr^{2+}, 0.62 Å for Cr^{3+}, 0.55 Å for Cr^{4+} and 0.60 Å for Pt^{4+}.[140] In contrast, Au^{3+} has an ion radius of 0.85 Å so that Au cannot substitute Mn or Li in the spinel lattice, thus, it cannot be detected in the LMO layer. In^{3+} and Sn^{4+} of the ITO interlayer have ion radii of 0.80 Å and 0.69 Å, respectively, whereby they are in general able to substitute Li and Mn.[140] However, since the ionic bonding of the ceramic ITO interlayer is significantly stronger than the metallic bonding of Pt, Au and StSt, the remove of In and Sn from the ITO lattice is impeded. Additionally, the substitution of In and Sn in the ITO lattice or the formation of new phases is necessary to maintain electroneutrality. Since In and Sn cannot be detected in the LMO layer and StSt substrate (**Fig. 6.5**) as well as no mixed phases can be detected (**Fig. 6.6**), it is reasonable to assume, that the annealing temperature of 700 °C is insufficient to activate the diffusion of In and Sn into the LMO layer as well as into the substrate, which explains the good blocking characteristics of the ITO interlayer.

The existence of $LiMnXO_4$ (X = Fe, Cr, Al, Pt) and AB_2O_4 (A or B = Mn, Fe, Cr, Al, Pt) can be confirmed by the shift of the 111 LMO reflection detected via XRD (**Fig. 6.6**) and the Mn^{2+} species at the surface detected via XPS (**Fig. 6.7**). The degree of their formation is related to the degree of interdiffusion. Without interlayers, a higher degree of interdiffusion can be detected than with the interlayer Pt, Au and ITO. ITO shows the lowest degree of interdiffusion followed by Pt and Au (**Fig. 6.5**).

The amounts of the new spinel compositions have a significant impact on the electrochemical performance. Since these spinels are electrochemical inactive, the discharge capacities are reduced with a high degree of interdiffusion. The discharge capacity of the StSt sample annealed at 600 °C (**Fig. 6.9**, LIS600) is about half lower than the samples with interlayer annealed at 600 °C. At 700 °C, no capacity can be detected. Pt and Au have insufficient blocking characteristics at 700 °C, which results in a reduction of the discharge capacities. In contrast, the ITO samples annealed at 700 °C exhibits the highest discharge capacity of all samples (**Fig. 6.9**).

In terms of coulombic efficiency, capacity retention and rate capability the ITO samples show the best performance (**Fig. 6.10**). The StSt and Au samples do not show a noteworthy behavior. However, the Pt samples show a unique capacity fade and lower coulombic efficiency, which will be discussed later.

An impact of interdiffusion on the redox plateaus and overvoltage can be observed (**Fig. 6.11**). The change in the ratio of the first and second redox peaks in the differential capacity plots can be explained by the $LiMnXO_4$ (X = Fe, Cr, Al, Pt) spinels. The diffusion activation energies of the Li ions along the 8a-16c-8a pathways can be increased by the change of their atomic neighbors in the spinel lattice due to substitution. The ITO samples show the expected higher maximum of the second redox peak compared with the first peak, which is reported in literature.[13,23] Due to interdiffusion, the peak area and the height of the second redox peak are decreased for the other samples. The second redox peak is not observable for the LS600 sample.

An increase in the overvoltage can also be correlated with the degree of interdiffusion. The overvoltage depends on the charge transfer and concentration polarizations. Consequently, an increase in overvoltage suggests a higher charge transfer barrier for the Li-ion insertion/extraction. This is in accordance with the impedances for the charge transfer R_{CT}. The LIS600 sample has the lowest R_{CT} (**Fig. 6.14**) and overvoltage (**Fig. 6.11**). Without interlayers, these values significantly increase. Additionally, the Li depletion at the surface (**Fig. 6.5**) results in the formation of AB_2O_4 (A or B = Mn, Fe, Cr, Al, Pt) spinel, which functions as an insulating layer for the Li insertion/extraction. Thus, higher degrees of interdiffusion and Li depletion result in a thicker insulating layer at the surface and a higher R_{In}. The LIS600 sample has the lowest R_{In} value followed by LPS600, LAS600 and finally the LS600 sample (**Table 6.3**).

The ITO sample annealed at 700 °C exhibits a significant increase in R_{In} and R_{CT} as well as the overvoltage so that this cannot be solely explained by the interdiffusion processes and will be discussed in the next section. However, the XPS data show low amounts of Fe at the surface of the LIS700 sample (**Fig. 6.7**) so that interdiffusion cannot be neglected. Additionally, the XRD data show a slight shift of the 111 LMO reflection (**Fig. 6.6**) and the ToF-SIMS depth profiles reveal a higher Li depletion at the surface for the LIS700 compared with LIS600 (**Fig. 6.5**). Partly substitution of Mn^{4+} with Fe^{4+} might explain the increase in overvoltage and R_{CT}. The higher degree of Li depletion causes a higher ratio of R_{In} of the total impedance for the LIS700 than for LIS600 (**Table 6.3**). However, the discharge capacity of LIS700 is 20 % higher than the discharge capacity of the LIS600 sample (**Table 6.2**).

The best blocking characteristics are shown by the ITO interlayer, which results in the best electrochemical performance for the LIS600 and LIS700. The high increase in R_{In} and R_{CT} and the higher discharge capacity will be discussed in the following.

Changes in Morphology and Crystallinity of LMO

The SEM images (**Fig. 6.4**) show an increase in the crystallite growth with elevated temperature. This results in a lower electrochemically active area for the LIS700 sample, which might explain the significant increase in the total impedance of the LIS700 sample compared with the LIS600 sample. A lower active area means fewer possibilities for the Li insertion/extraction redox reaction, which increases the total impedance.

The increase of the discharge capacity for the ITO sample at 700 °C suggests a higher crystallinity of the LMO layer at 700 °C. It can be assumed, that the LMO layer is not completely crystallized at 600 °C. However, indications cannot be found in the XRD measurements.

Irreversible Side Reaction of the Pt samples

The analyses of the rate capability and coulombic efficiency (**Fig. 6.10**) as well as the current decay during the constant voltage step at 4.4 V for 3 h (**Fig. 6.12**) exhibit that an irreversible side reaction takes place during the charge of the Pt samples. Since the cumulative charges are ca. 18 µAh/cm² and ca. 14 µAh/cm² for LPS600 and LPS700, respectively, this charge is not related to the LMO layer, which shows a maximum capacity of ca. 5 µAh/cm² for the LIS700 sample, which can be assumed as maximum (**Fig. 6.9**). Considering the cracks in the LMO layer, the Pt interlayer is in direct contact with the liquid electrolyte, so that an electrochemical dissolution of Pt can be assumed. The redox reaction $Pt \rightarrow Pt^{2+} + 2e^-$ has a standard redox potential of 1.20 V vs. SHE (standard hydrogen electrode), which corresponds to 4.24 V vs.

Li/Li^+.[11] However, in the application in a TF-SSB in combination with a dense cathode layer and SSE the risk of Pt dissolution would likely be small, but still present.

Oxide Layer Formation

The SEM images (**Fig. 6.3**) and ToF-SIMS depth profiles (**Fig. 6.5**) reveal the formation of an oxide layer at the LMO/StSt, Pt/StSt, ITO/StSt and LMO/Au interface. It was expected that it influences the electrochemical performance by increasing the internal resistance of the cell since the oxide layer is not electrically conductive. The ohmic resistances R_Ω are similar for all samples (**Table 6.3**) so that the impact of the oxide layer is negligible at annealing temperatures of 700 °C.

6.6 Optimization of the ITO Interlayer

The ITO interlayer showed the best blocking characteristics for interdiffusion between LMO thin-films and StSt substrates for annealing temperatures of 600 °C and 700 °C. However, a low degree of interdiffusion could be detected at 700 °C using an ITO interlayer with 100 nm thickness. This interdiffusion is responsible for high overvoltages of the redox reactions and the formation of an insulating layer at the surface, which is unfavorable for the application in TF-SSBs. Consequently, further optimization is required. For that purpose, the electrochemical performance of LMO|ITO|StSt cathodes was tested as a function of the ITO interlayer thickness in the expectation that thicker blocking interlayers would impede the interdiffusion. Furthermore, an annealing temperature of 800 °C was applied and an ITO layer thickness of 50 nm was tested in order to determine the limits of the material system. The layer thicknesses were varied by multiple dip-coating of the ITO layer up to four layers (see experimental section: **Chapter 9.3**). The settings of the dip-coating were chosen to obtain an interlayer thickness of 50 nm. After each ITO interlayer deposition, the layer was crystallized at 600 °C for 10 min.

An additional optimization had been done due to the change in the substrate thickness. StSt substrates of 30 µm thickness were used so far since a later application in roll-to-roll processes was planned, which requires flexible and thin substrates. **Fig. 6.15a** shows a LMO|ITO|StSt sample (5 x 5 cm^2) on a 30 µm thick StSt substrate after heat treatment at 700 °C for 1 h. Kinks and deformations are visible, which are expected to enhance at annealing temperatures of 800 °C. This is additionally unfavorable for the subsequent deposition of SSEs materials, because of the most probable crack formation through the whole multilayer system. Therefore, StSt substrates of 100 µm thickness were used for the following studies. The benefits are evident in **Fig. 6.15b**, which shows a LMO/ITO/StSt sample on 100 µm thick StSt after annealing at 700 °C for 1 h. The stiffer substrate shows no deformation. The LMO layer also appears to be more homogenous.

The samples were evaluated by GCPL performing the rate capability tests and analyzing the voltage profiles, cycle trends of the discharge capacities and the overvoltages.

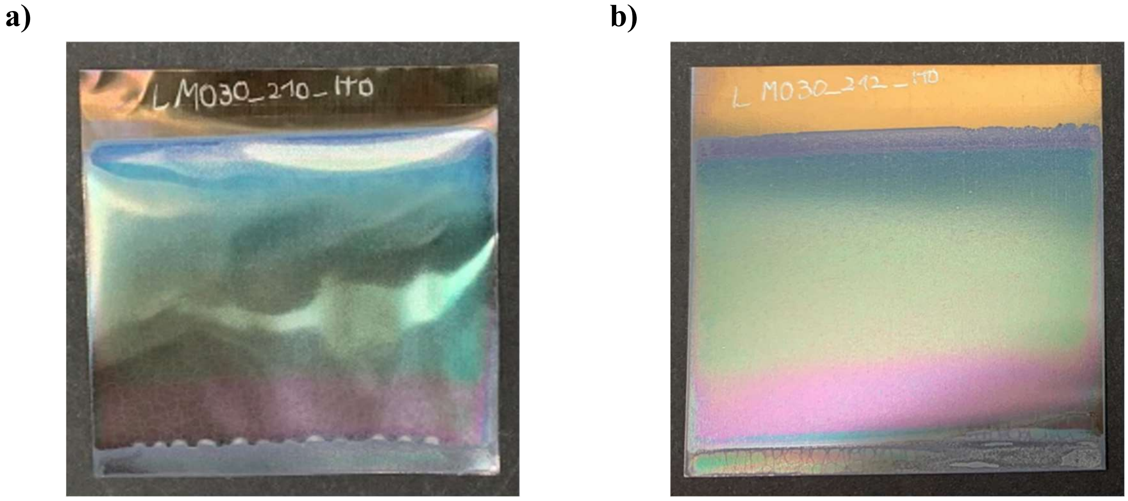

Fig. 6.15 Photographs of 5 x 5 cm² LMO/ITO/StSt samples annealed at 700 °C for 1 h on **a)** a 30 µm StSt foil and **b)** a 100 µm StSt foil.

ITO Layer Thickness and LMO Morphology

The layer thicknesses of the ITO interlayers were determined by means of SEM cross-sections of the samples annealed at 700 °C (**Fig. 6.16**). The thickness of the LMO layer is about 160 nm. The thicknesses of the single layer and the double layer are about 50 nm and about 100 nm, respectively. The 3x ITO interlayer and 4x ITO interlayer have layer thicknesses of ca. 190 nm and ca. 250 nm. This not linear trend can be explained by the visible pores between the interlayers, whose influence on the electrochemical results needs to be discussed later.

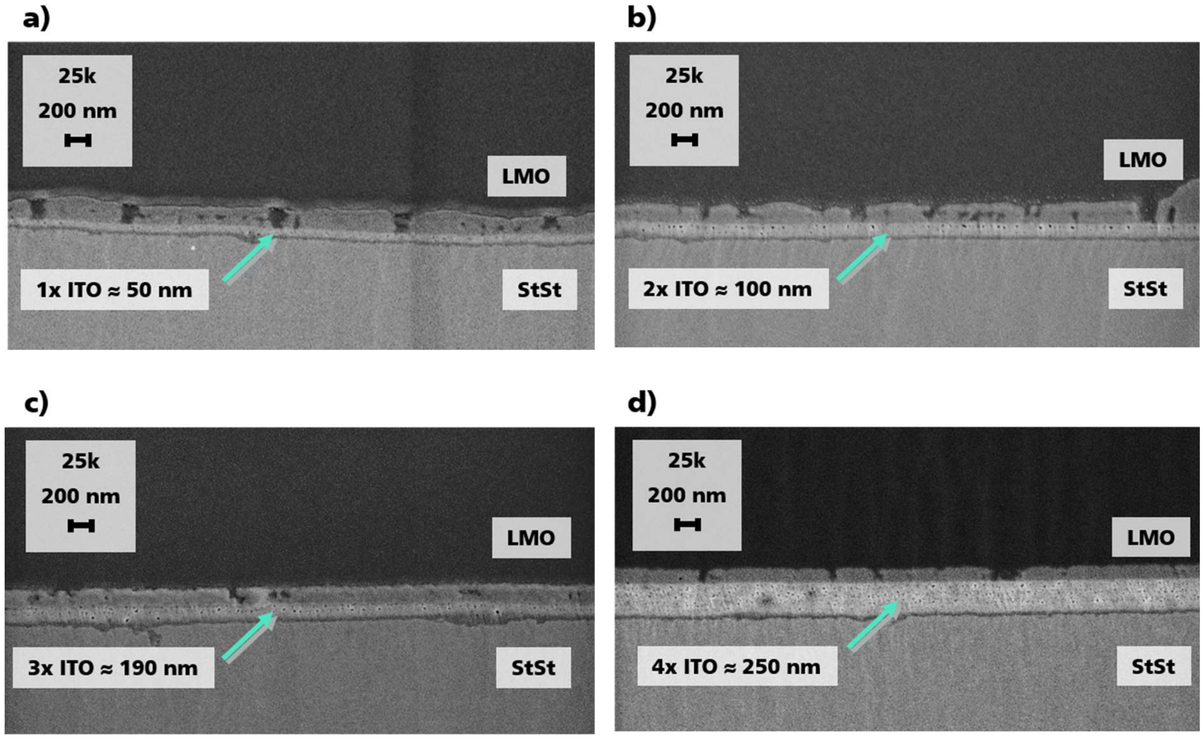

Fig. 6.16 SEM cross-sections of LMO @ ITO @ StSt samples with various ITO interlayer thicknesses annealed at 700 °C for 1 h. a) 1x ITO, b) 2x ITO, c) 3x ITO and d) 4x ITO interlayer.

The top view SEM images of the 4x ITO interlayer samples annealed at 600 °C, 700 °C and 800 °C show an increase in crystallite size with annealing temperature (**Fig. 6.17**). At 600 °C and 700 °C, the crystallite sizes are below 50 nm. At 800 °C it increases up to 200 nm.

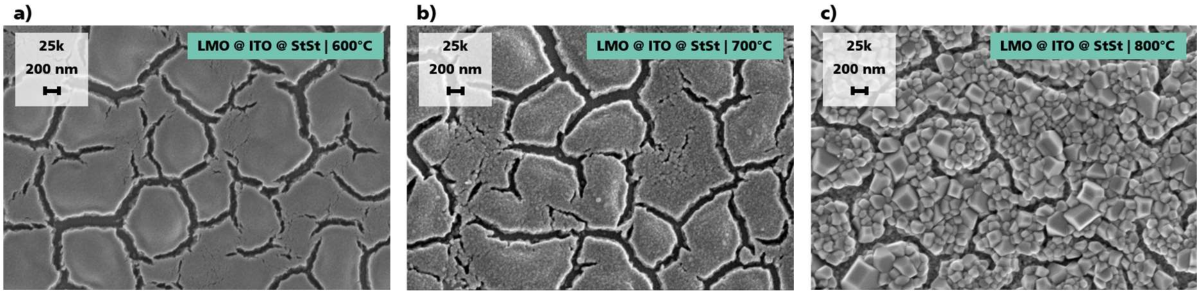

Fig. 6.17 Top view SEM images of the LMO/ITO/StSt samples with 4x ITO interlayer annealed at a) 600 °C for 1 h, b) 700 °C for 1 h and c) 800 °C for 1 h.

Electrochemical Performance

The voltage profiles of cycle 73 at 30 µA/cm^2 for all annealing temperatures and ITO layer thicknesses are compared in **Fig. 6.18**. The current density of 30 µA/cm^2 was chosen in order to compare the results easily with the previous results of the samples with 30 µm StSt substrates.

The voltage profiles of the samples annealed at 600 °C show similar trends (**Fig. 6.18a**) for all ITO layer thicknesses. They are also comparable with the voltage profiles of the LIS600 sample, which were prepared with a 30 µm StSt foil (**Fig. 6.8c**). The discharge capacities are about 4.6 µAh/cm^2, which is slightly higher by ca. 0.4 µAh/cm^2 than the LIS600 sample. This suggests a slight improvement in the layer quality by using a thicker StSt substrate of 100 µm. However, the ITO layer thickness seems to not affect the voltage profiles at 600 °C.

Using a thicker substrate leads to better electrochemical results when the samples are annealed at 700 °C. The LIS700 sample on 30 µm StSt showed a significant polarization so that the cell could not be completely charged during the constant current step (**Fig. 6.8d**). However, the samples prepared on a 100 µm StSt substrate show no significant polarization and both redox plateaus can be detected during the constant current charge step, which is a significant improvement of the electrochemical performance (**Fig. 6.18b**). The discharge capacities seem to depend on the layer thickness of ITO (**Fig. 6.18d**). They slightly increase with the thickness of the ITO interlayer, which results in discharge capacities of 5.40 µAh/cm^2 ± 0.03 µAh/cm^2 (1x ITO), 5.42 µAh/cm^2 ± 0.06 µAh/cm^2 (2x ITO), 5.61 µAh/cm^2 ± 0.04 µAh/cm^2 (3x ITO) and 5.87 µAh/cm^2 ± 0.21 µAh/cm^2 (4x ITO). These values are slightly higher than the discharge capacity of 5.06 µAh/cm^2 ± 0.46 µAh/cm^2 of LIS700 on the 30 µm StSt substrate (**Table 6.2**). These results show that the pores between the ITO interlayers (**Fig. 6.16**) have no significant effect on the electrochemical performance and can be neglected.

The samples annealed at 800 °C show polarization and no capacities for the sample with 1x ITO and 2x ITO interlayers (**Fig. 6.18c**). Thicker interlayers result in discharge capacities of 1.78 µAh/cm^2 ± 0.39 µAh/cm^2 (3x ITO) and 3.80 µAh/cm^2 ± 0.40 µAh/cm^2 (4x ITO)

(**Fig. 6.18d**). The polarization effect is also evident in the voltage profiles. It indicates that a thicker interlayer of > 100 nm can inhibit interdiffusion at 800 °C, but not completely block the element diffusion.

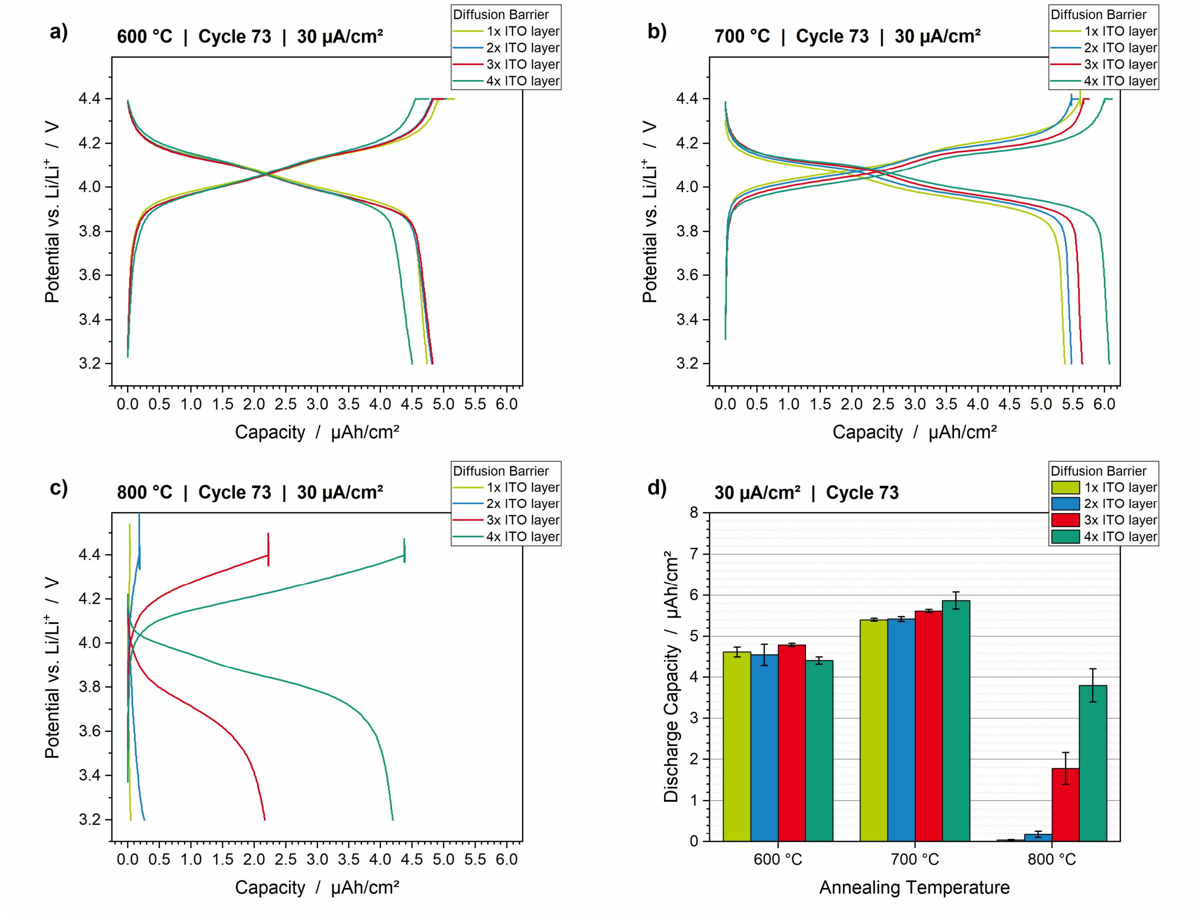

Fig. 6.18 Voltage profiles of cycle 73 at 30 µA/cm² of samples with various interlayers and annealing temperatures: a) 600 °C for 1 h, b) 700 °C for 1 h, c) 800 °C for 1 h and d) the corresponding discharge capacities.

In the previous section, the correlation of the overvoltage with the degree of interdiffusion and the substitution of Li and Mn with substrate elements was discussed. A higher degree of interdiffusion leads to higher overvoltages and the ratio between the first and second redox peaks could be correlated with the degree of interdiffusion. These findings will be used in the following to estimate the impact of interdiffusion processes.

The differential capacity plots of the samples annealed at 600 °C show no significant differences between the samples with different ITO interlayer thicknesses (**Fig. 6.19a**). The overvoltages are for all samples in the range from 22 mV to 29 mV, which can be considered similar. Thus, the interlayer thickness does not influence the electrochemical performance so that even with a 50 nm thick ITO interlayer (1x ITO) the blocking of element interdiffusion is guaranteed at 600 °C annealing temperature.

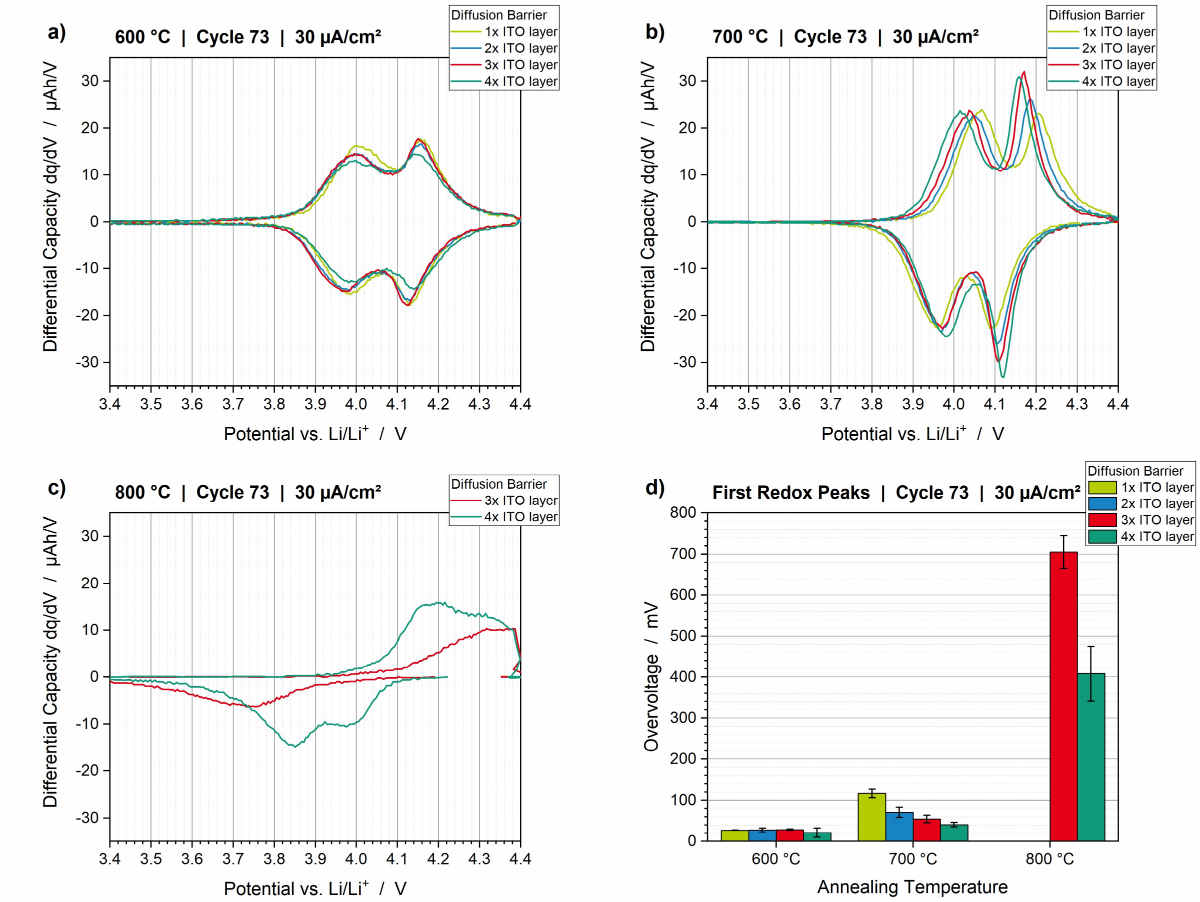

Fig. 6.19 Differential capacity plots of cycle 73 at 30 µA/cm² of samples with various interlayers and annealing temperatures: a) 600 °C for 1 h, b) 700 °C for 1 h, c) 800 °C for 1 h and d) the corresponding overvoltages.

The advantages of the 100 µm StSt substrate in contrast to the 30 µm StSt substrate are also evident in the differential capacity plots of the samples annealed at 700 °C (**Fig. 6.19b**). The overvoltages of the first redox peak are in the range of ca. 41 mV and ca. 117 mV (**Fig. 6.19d**), which is significantly lower than the overvoltage of 574 mV ± 143 mV for the LIS700 sample (**Table 6.2**). Additionally, a dependency of the layer thickness and the overvoltage can be assumed, since the overvoltage decreases with thicker ITO interlayers. Their values are 117 mV ± 11 mV (1x ITO), 71 mV ± 12 mV (2x ITO), 55 mV ± 9 mV (3x ITO) and 41 mV ± 5 mV (4x ITO) (**Fig. 6.19d**). That indicates that the interdiffusion can be further inhibited due to thicker interlayers, which is also reflected in the analysis of the ratio between the first and second redox peaks. The peak height and peak area increase for the samples with thicker interlayers (**Fig. 6.19b**). The samples with 1x ITO and 2x ITO interlayer show quite similar peak heights for the first and second redox peaks. The samples with 3x ITO and 4x ITO interlayers show an increase in the peak height of the second redox peak while the first redox peak stays constant. This indicates that the interdiffusion processes can be inhibited more successfully with an ITO interlayer of ≥ 190 nm, which results in a slightly enhanced electrochemical performance.

In contrast, the differential plots of the samples annealed at 800 °C show all indications of interdiffusion (**Fig. 6.19c**). The overvoltages are very high: 705 mV ± 40 mV (3x ITO) and 408 mV ± 67 mV (4x ITO) (**Fig. 6.19d**). The peak height of the second redox peak is also lower than the peak height of the first redox peak, which suggests substitution of Mn in the spinel lattice by substrate elements. However, the decrease of the overvoltage with ITO interlayer thickness suggests that the interdiffusion processes can be inhibited by ITO interlayers even at an annealing temperature of 800 °C, although a layer thickness of ca. 250 nm is not sufficient for good electrochemical performance.

The trends of the discharge capacities with cycle number are demonstrated in **Fig. 6.20**. In accordance with the previous chapter, the rate capabilities are analyzed by determining the differences between the discharge capacities at 100 µA/cm² (Cycle 19) and 30 µA/cm² (Cycle 73).

All 600 °C and 700 °C annealed samples show very constant trends (**Fig. 6.20 a-b**). The rate capabilities are below 4 %, which is once again a significant improvement for the 700 °C annealed samples by using the 100 µm thick StSt substrates, as the rate capability of the LIS700 sample was about 19 % (**Table 6.2**). Even the comparison of cycle 19 (100 µA/cm²) with cycle 81 (10 µA/cm²) results in differences below 6 %.

The rate capabilities of the 800 °C annealed samples cannot be reliably analyzed, since the discharge capacity has an unexpectedly low value at 30 µA/cm², which is comparable with the discharge capacity at 100 µA/cm² (**Fig. 6.20c**) and lower than the values of the 50 µA/cm² cycles. Considering the voltage profiles at 30 µA/cm² (**Fig. 6.18c**), it is evident that voltage spikes during the constant voltage step at 4.4 V vs. Li/Li$^+$ result in an uncompleted charge of all 800 °C samples. It cannot be distinguished if the origin of the voltage spikes is material specific or a technical problem, such as contact losses. They occur in all samples annealed at 800 °C and only at 30 µA/cm². Nevertheless, the voltage profiles at 10 µA/cm² and 50 µA/cm² show no voltage spikes and a usual charging behavior during the constant voltage step, which leads to higher discharge capacities. Considering the discharge capacities at 10 µA/cm², 4.44 µAh/cm² ± 0.17 µAh/cm² and 5.36 µAh/cm² ± 0.21 µAh/cm² can be obtained for the 3x ITO and 4x ITO interlayer samples annealed at 800 °C (**Fig. 6.20d**), respectively. The differences to cycle 19 (100 µA/cm²) are 59 % (3x ITO) and 27 % (4x ITO), which reflect the results of the analyses of the overvoltages (**Fig. 6.19c**).

However, the discharge capacity of the 4x ITO interlayer sample annealed at 800 °C is in the range of the values of the 700 °C annealed samples and higher than the values of the 600 °C annealed samples (**Fig. 6.20d**). This suggests once again an uncompleted crystallization of the samples annealed at 600 °C for 1 h. Additionally, it shows that good discharge capacities can be obtained even with a low degree of interdiffusion. However, the increase of the polarization effects makes the 800 °C annealed samples unusable for application in TF-SSBs.

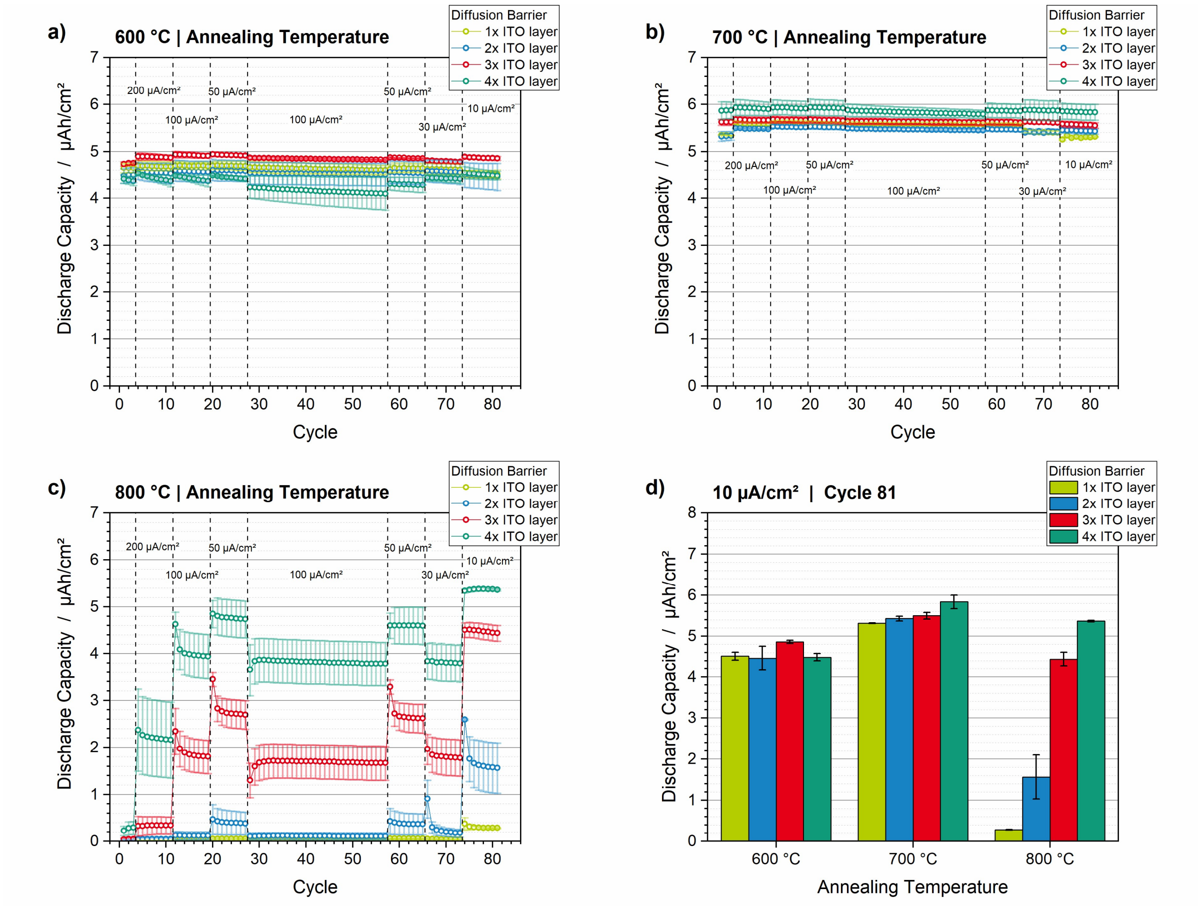

Fig. 6.20 Discharge capacities of the rate capability tests as a function of the cycle number of samples with various interlayers and annealing temperatures: a) 600 °C for 1 h, b) 700 °C for 1 h, c) 800 °C for 1 h and d) comparison of the discharge capacities of cycle 81 at 10 µA/cm².

In conclusion, the change of the substrate from a 30 µm thick StSt to a 100 µm StSt substrate improves the cell performance, particularly, at 700 °C. This can be explained by the stiffness of the thicker substrate, which results in no deformation during the heat treatment. The kinks and deformation of the 30 µm substrate might result in cracks through the multiple layer system, thus, cracks in the ITO diffusion barrier. That might bring LMO and StSt in contact, which enables interdiffusion between LMO and StSt. Additionally, a thicker ITO diffusion barrier leads to a better electrochemical performance of the LMO cathodes annealed at 700 °C. Consequently, a low degree of interdiffusion takes place at 700 °C but can be further inhibited by thicker ITO interlayers. The comparison of the samples annealed at various temperatures reveals that the LMO might be incompletely crystallized at 600 °C since the discharge capacity has lower values than for the samples annealed at 700 °C. At 700 °C the LMO cathodes show the best performance. At 800 °C, the interdiffusion cannot be sufficiently inhibited even with ITO diffusion barriers of ca. 250 nm.

6.7 Summary and Conclusion of the Investigation into the Current Collector/Cathode Interface

Considering a subsequent layer deposition and crystallization of SSE thin films on top of cathode thin films on a current collector substrate for the manufacturing of TF-SSBs, the thermal stability between the cathode and current collector substrate must be guaranteed for temperatures above 650 °C. This study reveals the interdiffusion processes and changes in the spinel structure of LMO during crystallization on heat-resistant StSt at 600 °C and 700 °C. Li depletion at the surface and Mn diffusion into the substrate are compensated by the substitution of Mn and Li in the spinel structure by Fe, Cr and Al elements of the substrate (**Fig. 6.5**), which leads to spinels according to the formula $LiMnXO_4$ (X = Al, Cr, Fe) and AB_2O_4 (A or B = Mn, Al, Cr, Fe) (**Fig. 6.6** and **Fig. 6.7**). This explains the low electrochemical utilization of the LMO thin-films up to malfunction after annealing at 700 °C (**Fig. 6.9**).

The incorporation of the interdiffusion barriers Pt, Au and ITO could improve the cell performance due to the inhibition of the interdiffusion processes at 600 °C. However, only the ITO interlayer could maintain good electrochemical performance after annealing at 700 °C (**Fig. 6.9**). Au could not inhibit the interdiffusion at 700 °C and Pt diffuses into the LMO layer and substitutes Mn in the spinel lattice (**Fig. 6.5**), which results in a low utilization (**Fig. 6.9**). Additionally, Pt electrochemically dissolves into the liquid electrolyte at potential above 4.24 V vs. Li/Li^+ (**Fig. 6.12**).

It could be shown that the degree of interdiffusion has a significant impact on the discharge capacities, impedances and overvoltages. The formation of electrochemically inactive AB_2O_4 (A or B = Mn, Al, Cr, Fe, Pt) due to Li depletion causes a low utilization and the formation of an insulating layer at the surface, which increases the charge transfer resistance. The latter is also reflected in the overvoltages, which increase with a higher degree of interdiffusion (**Fig. 6.11**). It could also be shown that the ratio between the first and second redox peak can be a measure for interdiffusion since the diffusion activation energy of Li on the 8a-16c-8a pathways in the $LiMnXO_4$ (X = Al, Cr, Fe, Pt) spinel is increased due to a change of the neighboring elements, which lowers the peak height and area of the second redox peak.

Since the ITO interlayer showed the best blocking characteristics, further optimization and the determination of the limits of the material combination had been done. It could be shown that the change of the substrate thickness from 30 µm to 100 µm improves the cell performance at 700 °C, as no deformations of the substrate take place and so no kinks and cracks are formed (**Fig. 6.18**). It is evident that the degree of interdiffusion significantly decreases by using the thicker StSt substrate (**Fig. 6.19**). That can be explained by cracks in the ITO interlayer due to the deformation of the substrate, so that contacts between LMO and StSt are thinkable, through which interdiffusion is possible. In conclusion, the LMO layers on the 100 µm StSt substrate with ITO interdiffusion barrier showed a significantly lower degree of interdiffusion at 700 °C and better cell performance in terms of overvoltages and polarization effects (**Fig. 6.19**).

Furthermore, it could be shown that thicker ITO interdiffusion barriers of ≥ 190 nm slightly increase the cell performance in terms of discharge capacity and overvoltage after annealing at 700 °C (**Fig. 6.20** and **Fig. 6.19**). Comparing the 700 °C with the 600 °C samples, a lower discharge capacity after annealing at 600 °C is obtained, which can be explained by a lower degree of crystallization. At 800 °C, the interdiffusion processes are so dominant that even ITO interdiffusion barriers of 250 nm cannot block the interdiffusion sufficiently.

In conclusion, using an ITO interlayer on a 100 µm thick StSt substrate for LMO crystallization at 700 °C is a good and reliable basis for further SSE deposition and crystallization in order to investigate the thermal stability and its impact on the electrochemical performance of TF-SSBs.

7 TF-SSB | Engineering Cathode/SSE Interface

After solving the issue of interdiffusion between the current collector and cathode active material by incorporation of an ITO interlayer, the next step towards a TF-SSB is the implementation of the SSE. Ceramic SSEs require crystallization temperatures of ≥ 650 °C in order to obtain its high Li-ion conductive crystalline phase.[78,167,168] Consequently, interdiffusion processes between the LMO cathode and the SSE are expected so that an interdiffusion barrier between the cathode and SSE might be necessary, which inhibits the element diffusion but should be able to let pass Li-ions. For that purpose, TiO_2 and $Li_4Ti_5O_{12}$ (LTO) were tested as interlayers. LTO has a higher Li diffusion coefficient (ca. 1 E-12 cm^2/s)[180–183] than TiO_2 (ca. 1 E-16 cm^2/s)[184,185], which is expected to impact the cell performance. The first step is the characterization of these interlayers on top of LMO in a liquid electrolyte cell. By that, the capability of these interlayers to inhibit Mn dissolution and electrolyte decomposition can be tested, which are the most important loss mechanisms of the LMO active material during long-term cycling (**Chapter 2.1**: Cathode Active Materials). Secondly, the general functionality of these interlayers is evaluated in a TF-SSB cell by using LIPON as SSE. LIPON is an amorphous SSE so that heat treatment after sputter deposition is not required, whereby interdiffusion processes can be avoided. Finally, the target system of Ga-LLZO as SSE on top of LMO with and without interlayers is tested. The ionic conductivity of Ga-LLZO is by a factor of 100 higher than the ionic conductivity of LIPON.[46,56] However, Ga-LLZO requires a crystallization temperature of ≥ 650 °C to obtain the high conductive crystalline phase, so that interdiffusion processes can take place, which significantly decreases the cell performance. This has been reported, for instance, for the combination of LCO and Ga-LLZO but has not been tested with a LMO cathode so far.[186]

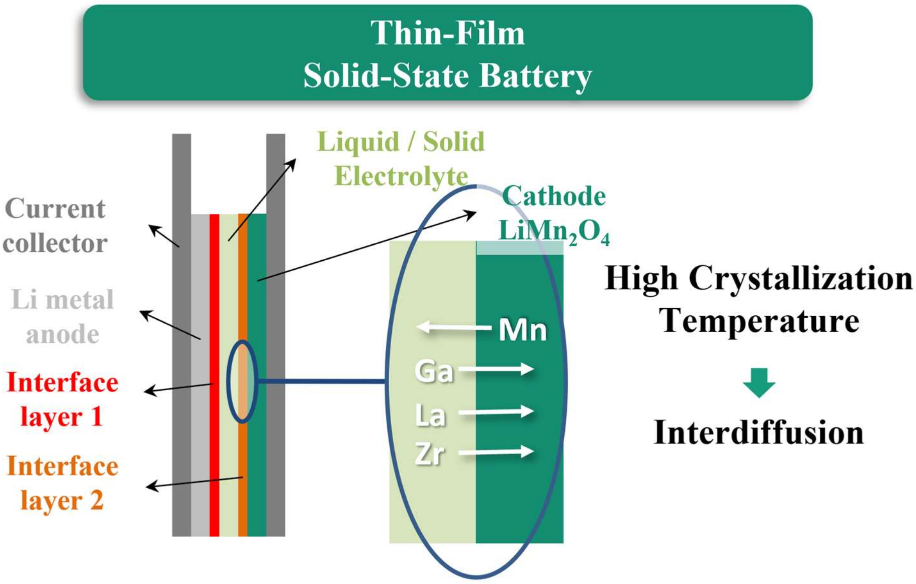

Fig. 7.1 Interdiffusion processes between Ga-LLZO SSE and LMO thin-film cathode can occur during the high-temperature manufacturing process of TF-SSBs.

This study is supposed to evaluate the general functionality of LLZO|LMO TF-SSBs. Furthermore, the interdiffusion processes depending on the interlayers TiO_2 and LTO and their impact on the electrochemical performance are examined. The cathode active material LMO as well as the interlayers TiO_2 and LTO were deposited by sol-gel-based dip-coating at the Fraunhofer ISC. LIPON and Ga-LLZO were sputtered, processed and analyzed via ToF-SIMS and GIXRD at the Swiss Federal Laboratories of Material Science and Technology (EMPA, Switzerland) in cooperation with the group of Yaroslav E. Romanyuk. Electrochemical testing has been done at the Fraunhofer ISC within the master thesis of Simon Ziegler: “Engineering the cathode-electrolyte interface for stable thin-film solid-state batteries” (2021). The author developed the experimental plan and managed the collaboration with EMPA. Data analyses, discussions and interpretation had taken place under my supervision.

7.1 Introduction and Status Quo

Many studies have been done to investigate metal oxide coatings on top of LMO in liquid electrolyte cells since these coatings are a promising approach to inhibit Mn dissolution and electrolyte decomposition at high voltages.[25–27,187–190] These side effects result in a significant capacity fade, thus, poor long-term cycling stability. The disproportionation of Mn^{3+} (LMO lattice) to Mn^{2+} (dissolves in the electrolyte) and Mn^{4+} (remains in lattice) at the LMO surface results in a blocking layer at the surface, which increases the charge transfer resistance and polarization effects.[13,191] The instability is enhanced by the Jahn-Teller distortion and the tendency of losing oxygen at the end of charge.[13] A further drawback is the decomposition of the electrolyte during charge at high voltages. For instance, ethylene carbonate (EC) and the subsequent reaction to ethylene glycol form a cathode solid interphase (CEI) by polymerization to polyethylene glycol.[38,192] This is triggered by hydroxide or carbonate residues or traces of humidity and hydrofluoric acid (HF) formed by the $LiPF_6$ electrolyte salt.[38,39,134,135,191–200] The formation of the CEI also causes higher charge transfer resistances and polarization effects, which significantly reduces the lifetime of the battery cell.

To overcome these drawbacks, several coatings on LMO were tested, such as TiO_2 [201–204], LTO [205–209], Al_2O_3 [202,210–212], ZrO_2 [203], $LiNbO_3$[213], etc. Particularly, TiO_2 and LTO have shown an improvement in the long-term cycling behavior of LMO cathodes depending on layer thickness and layer homogeneity.

Recently, researchers started using these coatings as interlayers in ceramic ASSBs as probable interdiffusion barriers.[186,214–219] Sastre et al.[186] demonstrated an improvement in performance for LLZO|LCO TF-SSB cells by incorporation of a Nb_2O_5 interlayer. The authors could show, that the Nb_2O_5 interlayer suppresses the formation of a secondary $La_2Zr_2O_7$ phase and Co diffusion into LLZO during the crystallization process of the LLZO layer at 700 °C. As a result, the Nb_2O_5 containing TF-SSB cells showed a three times higher discharge capacity than without interlayer. One study about the combination of LLZO and amorphous LMO has been done by Delluva et al.[220], who showed a significant capacity fade with cycle number. The author could identify electrochemical side reactions at the LMO/LLZO interface during cycling.

In contrast, the combination of LMO and the amorphous LIPON SSE shows a stable cycling performance.[52,60] Li et al.[52] set a benchmark for spinel Li|LIPON|LMNO TF-SSB cells with a capacity retention of 90.6 % after 10,000 cycles. The authors mentioned that a major improvement could be achieved by depositing every single layer via PVD techniques and passing the sample from one chamber to the next in an inert gas atmosphere without exposure to air. Cathode thin films based on sol-gel synthesis have not been tested in TF-SSBs so far.

Considering the recent research, this study investigates the incorporation of sol-gel-based cathode LMO thin-films in LIPON and LLZO TF-SSB cells as well as the functionality of TiO_2 and LTO interlayers as interdiffusion barriers during LLZO crystallization.

7.2 Experimental Approach

This subchapter gives a short overview of the experimental plan (**Fig. 7.2**). Detailed information can be found in the experimental section (**Chapter 9.4**).

Double-layers of LMO were deposited via dip-coating of a sol solution on 100 nm ITO on top of the 100 µm thick StSt substrate, as described in the previous chapter. After each LMO deposition, the sample was dried at 300 °C for 30 min and finally rapidly crystallized at 600 °C or 700 °C for 1 h.

TiO_2 and LTO were dip-coated on top of the LMO double-layers from a sol solution. Two layer thicknesses were adjusted by using two different withdrawal velocities of 50 mm/min and 200 mm/min. The coatings were crystallized at 600 °C for 10 min.

The LIPON SSE was deposited via co-sputtering of Li_3PO_4 and Li_2O with a N_2 gas flow. The sputtering time was set to gain ca. 1 µm thick LIPON layer. Afterward, 2 µm Li and 200 nm Cu were deposited via thermal evaporation to obtain full cells. A sputter mask was used to obtain circular cells with a diameter of 1 mm, resulting in an active cell area of 0.00785 cm², which were electrochemically tested at EMPA in a glovebox with argon atmosphere.

The Ga-LLZO SSE was deposited following the procedure described by Sastre et al.[78,186] $Li_{6.25}Ga_{0.25}La_3Zr_2O_{12}$ and Li_2O targets were used for co-sputtering in an Ar:O_2 gas flow. Afterward, the Ga-LLZO was crystallized at 650 °C for 1 h in a controlled O_2 atmosphere.

These samples were analyzed via SEM, ToF-SIMS and GIXRD, of which more information can be found in the experimental section (**Chapter 9.4**).

The samples with and without Ga-LLZO were cut in 1 x 1 cm² for electrochemical testing in pouch cells by using Li-metal anodes and an EC:DMC (1:1 vol%) with 1 M $LiPF_6$ electrolyte (LP30, BASF).

Rate capability tests were performed at 25 °C with current densities between 10 µA/cm² and 400 µA/cm² in a potential range of 4.4 V vs. Li/Li^+ and 3.1 V vs. Li/Li^+ without constant voltage step at 4.4 V. Long term cycling were performed with 100 µA/cm² (600 °C samples) and 10 µA/cm² (700 °C samples) for 1,000 cycles. The Ga-LLZO samples were tested between 2.0 V vs. Li/Li^+ and 4.4 V vs. Li/Li^+ with a current density of 1 µA/cm² for ca. 400 cycles.

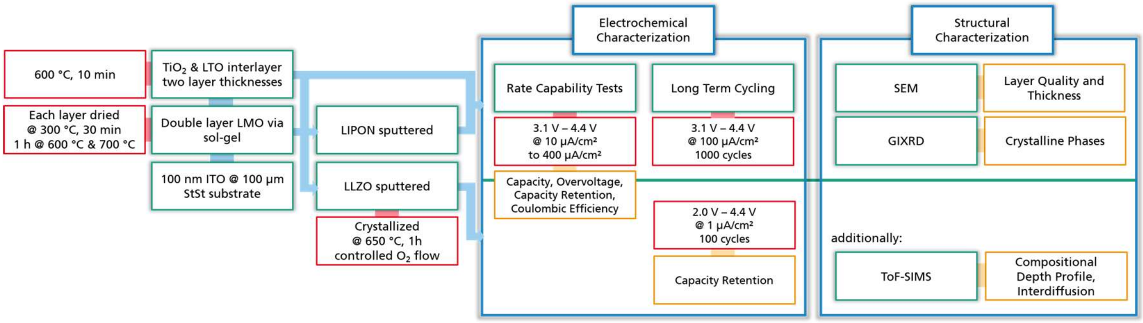

Fig. 7.2 Experimental plan of the investigation into the SSE / cathode interface. Experimental steps (green), parameters (red) and measured properties (orange).

7.3 Functionality of TiO_2 and LTO Coatings on LMO in Liquid Electrolyte Cells

Firstly, the TiO_2 and LTO coatings on top of the LMO double-layer were analyzed in liquid electrolyte cells in order to have a reference for the TF-SSB cells with LIPON and Ga-LLZO electrolytes. In addition, the protection characteristics against Mn dissolution and electrolyte decomposition can be tested. For that purpose, the coatings were characterized via SEM and GIXRD to gain information about layer quality and crystalline phases. GCPL measurements were performed between 4.4 V vs. Li/Li^+ and 3.1 V vs. Li/Li^+. The rate capability test with current densities in the range of 10 µA/cm² and 400 µA/cm² are supposed to give information on probable blocking of the charge transfer by the coatings as a function of coatings thickness and crystallization temperature of LMO (600 °C and 700 °C). Finally, long-term cycling tests with 1,000 cycles were performed to evaluate the capacity fading due to Mn dissolution and electrolyte decomposition in dependency on the coating and crystallization temperature of LMO.

Table 7.1 Designation of the samples.

600 °C LMO crystallization temperature	*700 °C LMO crystallization temperature*
LMO$_{600}$ | 2xLMO @ ITO|StSt	LMO$_{700}$ | 2xLMO @ ITO|StSt
LTO$_{<10nm}$LMO$_{600}$ | < 10 nm LTO @ 2xLMO @ ITO|StSt	LTO$_{<10nm}$LMO$_{700}$ | < 10 nm LTO @ 2xLMO @ ITO|StSt
LTO$_{\approx 20nm}$LMO$_{600}$ | ≈ 20 nm TiO_2 @ 2xLMO @ ITO|StSt	LTO$_{\approx 20nm}$LMO$_{700}$ | ≈ 20 nm TiO_2 @ 2xLMO @ ITO|StSt
TiO$_{<10nm}$LMO$_{600}$ | < 10 nm TiO_2 @ 2xLMO @ ITO|StSt	TiO$_{<10nm}$LMO$_{700}$ | < 10 nm TiO_2 @ 2xLMO @ ITO|StSt
TiO$_{\approx 20nm}$LMO$_{600}$ | ≈ 20 nm TiO_2 @ 2xLMO @ ITO|StSt	TiO$_{\approx 20nm}$LMO$_{700}$ | ≈ 20 nm TiO_2 @ 2xLMO @ ITO|StSt

Morphology of TiO_2 and LTO coatings

SEM top view images were taken from LMO single layers annealed at 600 °C on FTO glass substrate (**Fig. 7.3**). The LTO and TiO_2 coatings obtained from dip-coating with 50 mm/min withdrawal velocity (**Fig. 7.3 b-c**) show a homogeneous film on top of LMO, which thicknesses can be roughly estimated as < 10 nm. TEM images with a higher resolution might be helpful to validate the layer thicknesses more accurately. In addition, the thicknesses of the LTO and TiO_2 coatings obtained with 200 mm/min are also hard to evaluate (**Fig. 7.3 d-e**). However, it is evident that thicker layers can be achieved with 200 mm/min since the cracks of the LMO layer are filled with the coating material. The island-like structure of the LMO layer is still visible. The coating thicknesses of the LTO and TiO_2 can be estimated to be ca. 20 nm. The LTO coating appears denser than the TiO_2 coating, which seems to have a particulate morphology. This particle-like texture may suggest a porous microstructure of the coating, which also should be validated by means of TEM in further studies.

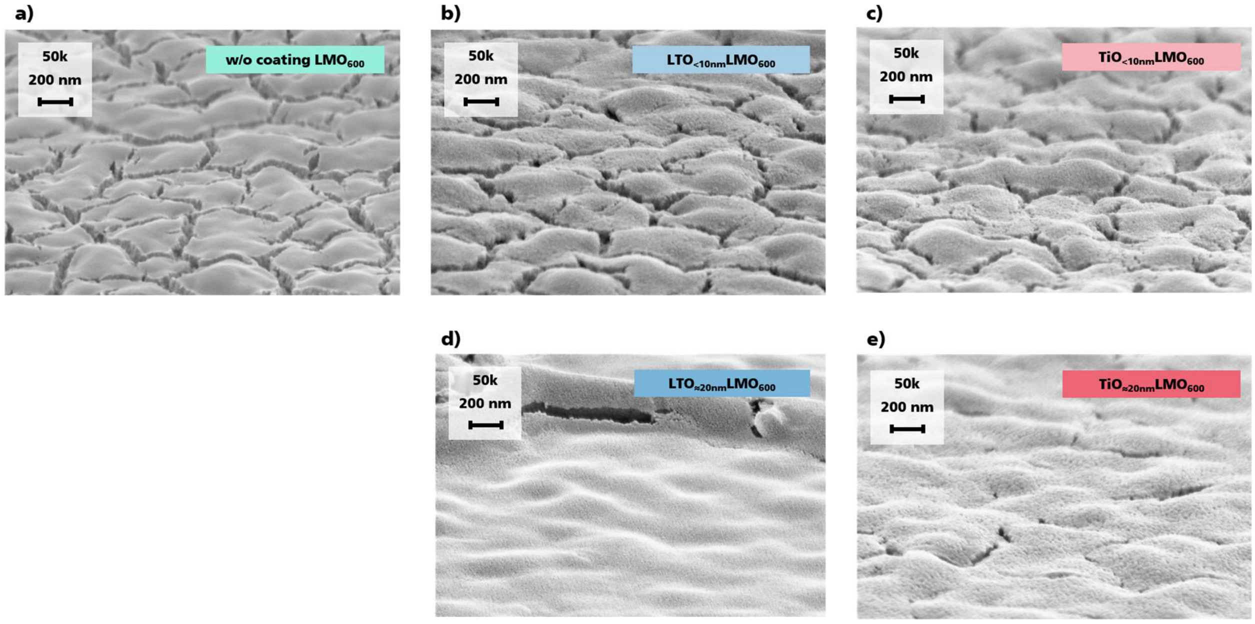

Fig. 7.3 SEM top view images of LMO single layers annealed at 600 °C: **a)** without coating, **b)** and **c)** LTO and TiO_2 coatings deposited with 50 mm/min withdrawal velocity, **d)** and **e)** LTO and TiO_2 coatings deposited with 200 mm/min withdrawal velocity.

Crystallinity of TiO_2 and LTO coatings

The GIXRD diffractograms of the LMO double-layers on top of ITO|StSt show the crystalline LMO main reflections at ca. 18.72°, ca. 36.28° or ca. 44.12° (LMO, ICSD 94340) (**Fig. 7.4**). As described in the previous chapter, the samples annealed at 700 °C show a higher LMO crystallinity (**Fig. 7.4b**) than the samples annealed at 600 °C (**Fig. 7.4a**). ITO is not detected because of the thicker LMO layer. The samples with TiO_2 coatings show one reflection related to anatase-structured TiO_2 at ca. 25.33° (Anatase TiO_2, ICSD 202243). The LTO reflections are expected at ca. 18.37°, ca. 35.59° or ca. 43.25° (ICSD 82954). Although the LTO reflections are difficult to differentiate from the LMO reflections since both materials crystallize in the spinel structure, the difference at higher 2θ degrees is sufficient to differentiate but LTO reflections cannot be detected. A shift of the reflections to lower 2θ values is also not observable. This indicates either that the LTO coating is amorphous or the coating is too thin to be detectable via the GIXRD technique. Further characterization tools like high-resolution TEM or XPS should be used in further studies in order to get a more detailed picture of the coating's nature.

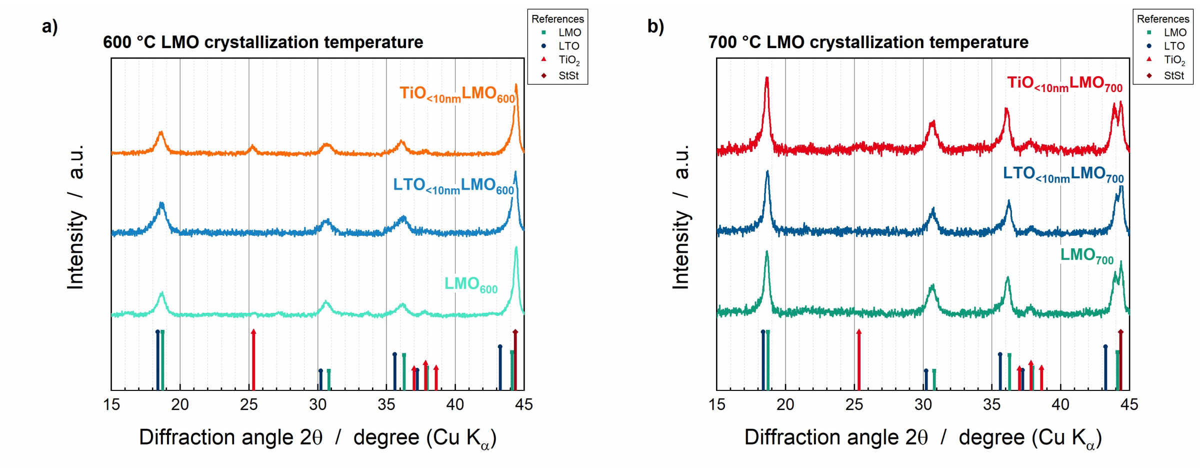

Fig. 7.4 GIXRD diffractograms of double-layer LMO samples on ITO|StSt without coating (green), with TiO2 coating (red) and with LTO coating (blue). **a)** LMO layers annealed at 600 °C and **b)** LMO layers annealed at 700 °C.

Electrochemical Characterization: Rate Capability Tests

Rate capability tests were performed in liquid electrolyte cells (LP30, EC:DMC 1:1 vol%, 1 M $LiPF_6$) at current densities in the range of 10 µA/cm² and 400 µA/cm². The voltage profiles at 10 µA/cm² (cycle 35) and 100 µA/cm² (cycle 20) are shown in **Fig. 7.5 a-d** and the trends of the discharge capacities over cycle number and as a function of the current density are shown in **Fig. 7.5 e-f**. The results of the electrochemical analyses are summarized in **Table 7.2**.

The comparison of the voltage profiles obtained with 10 µA/cm² (**Fig. 7.5 a-b**) and with 100 µA/cm² (**Fig. 7.5 c-d**) reveals similarities as well as dependencies of the discharge capacity, rate capability and overvoltages as a function of the coating and coating thickness as well as crystallization temperature of LMO.

Considering the voltage profiles at 10 µA/cm², it appears that the discharge capacity of the LMO_{700} sample (13.78 µAh/cm², **Fig. 7.5b**) is slightly higher than the discharge capacity of the LMO_{600} sample (11.50 µAh/cm², **Fig. 7.5a**). This is in accordance with the single-layer samples described in the previous chapter and can be correlated with a higher crystallinity of the LMO_{700} sample due to a higher crystallization temperature (**Fig. 7.4**). The discharge capacities are slightly reduced by using a coating. The $TiO_{<10nm}LMO_{600}$ and $TiO_{\approx 20nm}LMO_{600}$ samples show discharge capacities of 10.77 µAh/cm² and 10.43 µAh/cm². The $LTO_{<10nm}LMO_{600}$ and $LTO_{\approx 20nm}LMO_{600}$ show slightly more reduced discharge capacities of 9.80 µAh/cm² and 9.81 µAh/cm², respectively (**Fig. 7.5a**). The samples with TiO_2 and LTO coatings on LMO_{700} show discharge capacities of 13.01 µAh/cm² ($TiO_{<10nm}LMO_{700}$), 13.58 µAh/cm² ($TiO_{\approx 20nm}LMO_{700}$), 12.73 µAh/cm² ($LTO_{<10nm}LMO_{700}$) and 12.21 µAh/cm² ($LTO_{\approx 20nm}LMO_{700}$) (**Fig. 7.5b**). Consequently, the LTO coatings show slightly lower discharge capacities than the TiO_2 coatings.

The coulombic efficiencies at cycle 35 (10 µA/cm²) are in the range of 96 % and 98 % for all samples (**Table 7.2**), whereas the values at cycle 20 with 100 µA/cm² are all above 99 %. This leads to the conclusion that side effects such as electrolyte decomposition are beneficial at lower current densities.

First indications of the formation of the CEI are given by analyzing the rate capabilities, which is defined here as the difference of the discharge capacity at 10 µA/cm² (cycle 35) and 100 µA/cm² (cycle 20). Considering the LMO_{600} samples with and without coating, the difference in discharge capacity is very low and independent of the coatings (≤ 3 %, **Table 7.2**). In contrast, the LMO_{700} samples show a very poor rate capability for the pure LMO_{700} sample (difference of 58 %) and the thin TiO_2 coating ($TiO_{<10nm}LMO_{700}$, difference of 61 %). Both samples with LTO coating and the thicker TiO_2 coating show rate capabilities of 18 % ($LTO_{<10nm}LMO_{700}$), 12 % ($LTO_{\approx 20nm}LMO_{700}$) and 22 % ($TiO_{\approx 20nm}LMO_{700}$). These rate capabilities are also reflected in the voltage profiles at 100 µA/cm² (**Fig. 7.5d**). The LMO_{700} sample and $TiO_{<10nm}LMO_{700}$ sample show significant polarization effects, which goes along with a high overvoltage of 661 mV and 684 mV, respectively. The LTO samples and thicker TiO_2 sample on LMO_{700} have overvoltages of about 380 mV (**Table 7.2**). These differences in rate capability and overvoltage can be explained by the CEI formation and Mn dissolution in the first 20 cycles. The samples without coating and thin TiO_2 coating show no protection against the electrolyte decomposition or Mn dissolution, which results in a thicker CEI or blocking layer at the surface of the LMO so that the charge transfer is inhibited and the concentration polarization (formation of the electrochemical double-layer) is enhanced. In contrast, the LTO coatings and thicker TiO_2 coating show better protection characteristics, which results in less electrolyte decomposition and a thinner CEI, thus, lower overvoltages and better rate capabilities.

Interestingly, the LMO_{600} samples with and without coatings show very good rate capabilities (≤ 3 %, **Table 7.2**) and lower overvoltages at 100 µA/cm² (≤ 150 mV, **Table 7.2**). This indicates that a further effect impacts the polarization processes, which is correlated with the crystallization temperature of the LMO double-layer. The lower overvoltages and better rate capabilities of LMO single layers annealed at 600 °C have already been observed in the previous chapter and could be related to a smaller crystallite size, which increases the ionic and electrical conductivity, and a higher electrochemical active surface area, which increases the charge transfer probability, in comparison to the samples annealed at 700 °C. In addition to the ionic diffusion through larger LMO crystallites, the increase in layer thickness by using a LMO double-layer seems to increase the internal ionic and electrical resistances of the LMO layer crystallized at 700 °C so significantly that it has a major impact on the rate capability and overvoltage. The lower polarization effects of the double-layer LMO_{600} samples suggest that this sample has a higher ionic and electrical conductivity due to lower crystallinity and probable amorphous phases. However, this assumption needs to be tested in further studies.

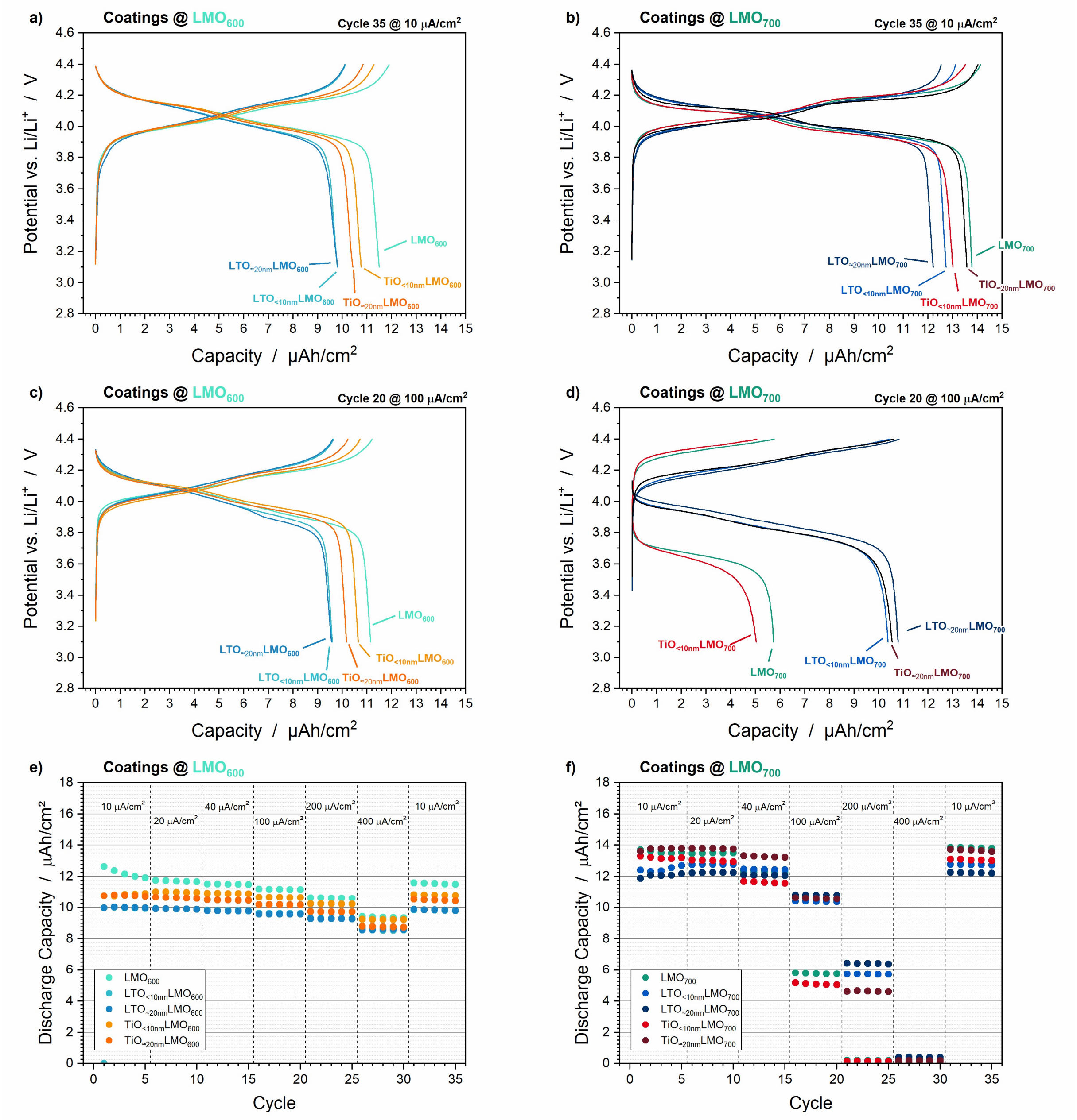

Fig. 7.5 Electrochemical data obtained from rate capability tests of liquid electrolyte cells (LP 30, EC:DMC 1:1 vol%, 1 M $LiPF_6$). Voltage profiles of all samples with and without LTO and TiO_2 coatings on top of LMO_{600} at **a)** 10 µA/cm² (cycle 35) and **c)** 100 µA/cm² (cycle 20) as well as on top of LMO_{700} at **b)** 10 µA/cm² (cycle 35) and **d)** 100 µA/cm² (cycle 20). Discharge capacities during rate capability tests for **e)** coatings on LMO_{600} and **f)** coatings on LMO_{700}.

Table 7.2 Electrochemical results obtained from rate capability tests of liquid electrolyte cells. LMO_{600} and LMO_{700} samples without and with LTO and TiO_2 coatings.

Sample	Discharge Capacity Cycle 35 @ 10 µA/cm^2 (µAh/cm^2)	Coulombic Efficiency Cycle 35 (%)	Overvoltage Cycle 35 @ 10 µA/cm^2 (mV)	Discharge Capacity Cycle 20 @ 100 µA/cm^2 (µAh/cm^2)	Overvoltage Cycle 20 @ 100 µA/cm^2 (mV)	Rate Capability* (%)
600 °C crystallization temperature						
LMO_{600}	11.50	96.7	14	11.15	154	3
$LTO_{<10nm}LMO_{600}$	9.80	96.7	12	9.60	133	1
$LTO_{\approx 20nm}LMO_{600}$	9.81	97.2	16	9.56	163	2
$TiO_{<10nm}LMO_{600}$	10.77	95.5	9	10.65	71	2
$TiO_{\approx 20nm}LMO_{600}$	10.43	99.2	11	10.18	81	3
700 °C crystallization temperature						
LMO_{700}	13.78	97.6	90	5.74	661	58
$LTO_{<10nm}LMO_{700}$	12.73	97.0	48	10.38	396	18
$LTO_{\approx 20nm}LMO_{700}$	12.21	97.5	47	10.79	358	12
$TiO_{<10nm}LMO_{700}$	13.01	96.3	96	5.03	684	61
$TiO_{\approx 20nm}LMO_{700}$	13.58	96.8	57	10.55	388	22

* Ratio of Discharge Capacity 10 µA/cm^2 : 100 µA/cm^2.

Electrochemical Characterization: Long-Term Cycling Test

Long-term cycling tests over 1,000 cycles were performed on the LMO_{600} and LMO_{700} samples without and with the thinnest TiO_2 and LTO coatings. LMO_{600} samples were tested at 100 µA/cm^2 since these samples showed a good rate capability. The LMO_{700} samples were tested at 10 µA/cm^2. The results of the data analyses are summarized in **Table 7.3**.

The voltage profiles of the LMO_{600} (**Fig. 7.6a**) and $TiO_{<10nm}LMO_{600}$ (**Fig. 7.6e**) samples show capacity losses over 1,000 cycles of 59 % (LMO_{600}: 11.13 µAh/cm^2 (initial) to 4.51 µAh/cm^2 (cycle 1,000)) and $TiO_{<10nm}LMO_{600}$: 64 % (11.14 µAh/cm^2 (initial) to 4.11 µAh/cm^2 (cycle 1,000)). This capacity fade goes along with a significant increase in the polarization effects, observable in the voltage profiles of cycle 1,000. This can be correlated with an increase in the charge transfer polarization and concentration polarization due to a CEI formation or Mn dissolution. In contrast, the $LTO_{<10nm}LMO_{600}$ sample shows a stable cycling behavior (**Fig. 7.6c**). The discharge capacity decreases just by 11 % from 9.72 µAh/cm^2 (initial) to 8.63 µAh/cm^2 (cycle 1,000) over 1,000 cycles. A significant impact of enhanced polarization effects cannot be observed.

Better cycling stabilities are shown for the LMO_{700} samples. The discharge capacities decrease by 18 %, 2 % and 26 % for the LMO_{700} (**Fig. 7.6b**), $LTO_{<10nm}LMO_{700}$ (**Fig. 7.6d**) and $TiO_{<10nm}LMO_{700}$ (**Fig. 7.6f**), respectively. Consequently, the LTO coating shows also on top of LMO_{700} the best cycling characteristics including no significant increase in polarization effects after 1,000 cycles. In contrast, the TiO_2 coating does not have any additional protection characteristics at all and is slightly worse than the pure LMO samples.

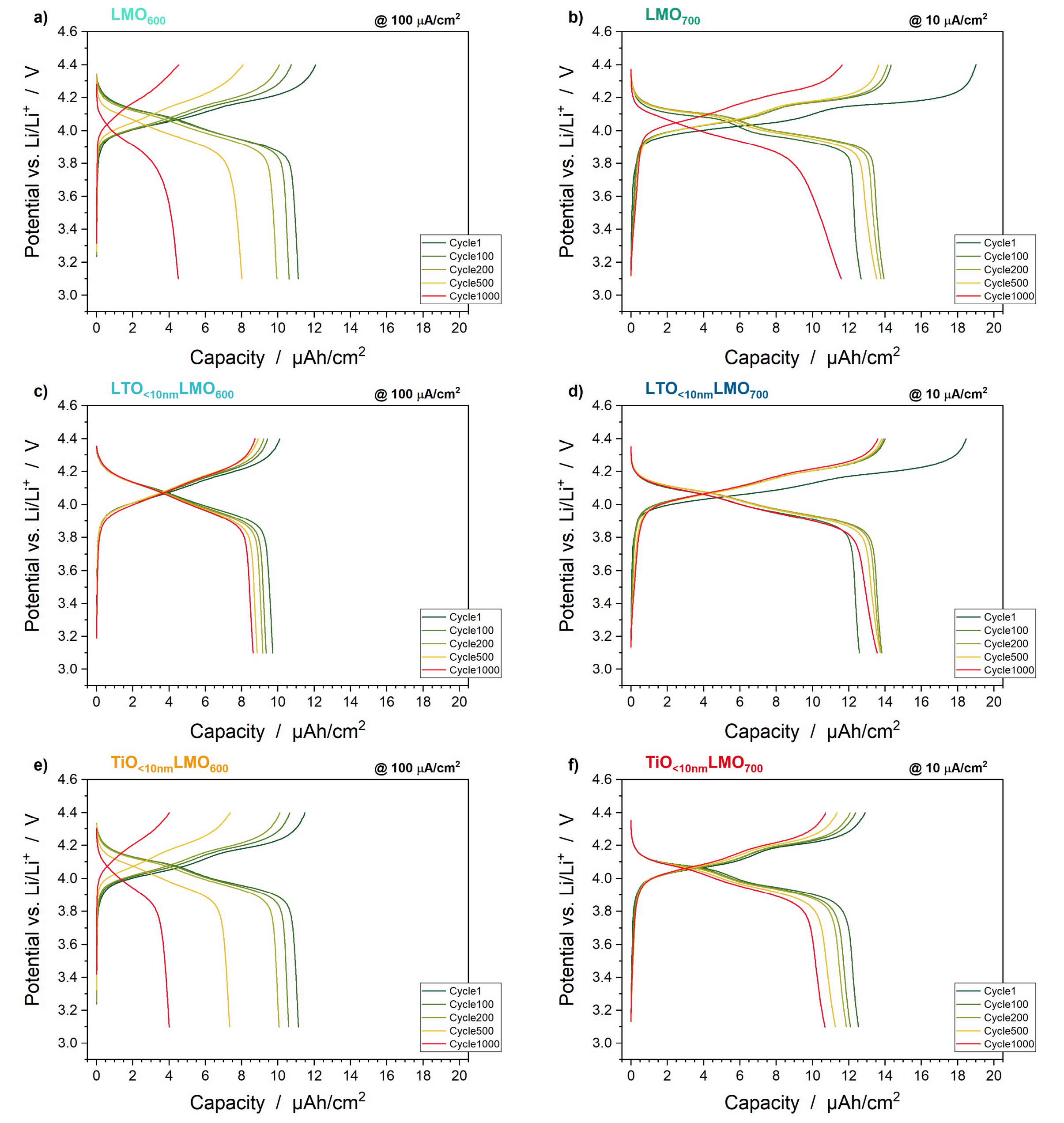

Fig. 7.6 Voltages profiles of long-term cycling tests in liquid electrolyte cells over 1,000 cycles. LMO_{600} samples tested at 100 µA/cm² **a)** without coating, **c)** with < 10 nm LTO coating and **e)** with < 10 nm TiO_2 coating. LMO_{700} samples tested at 10 µA/cm² **b)** without coating, **d)** with < 10 nm LTO coating and **f)** with < 10 nm TiO_2 coating.

The benefits of the LTO coatings become more evident by illustrating the discharge capacities as a function of the cycle number (**Fig. 7.7 a-b**). It is a common way to determine the cycle life as the cycle number, at which 80 % of the initial discharge capacity is reached. These cycles are 364, 330 and 758 for LMO_{600}, $TiO_{<10nm}LMO_{600}$ and $TiO_{<10nm}LMO_{700}$, respectively (**Table 7.3**). The LTO-coated samples $LTO_{<10nm}LMO_{600}$ and $LTO_{<10nm}LMO_{700}$ as well as the LMO_{700} samples show capacity retentions of 89 %, 98 % and 82 % after 1,000 cycles, respectively (**Table 7.3**).

As described in the section about the rate capability tests, the coulombic efficiencies are correlated with the current densities. It appears that higher current densities lead to a faster charge process and an increase in polarization so that the potential limit is reached faster. Consequently, the LMO_{600} samples with and without coatings reach coulombic efficiencies of about 99 % already after ca. 100 cycles (**Fig. 7.7c**) since current densities of 100 µA/cm² were used. The cycling tests of the LMO_{700} samples were performed with 10 µA/cm², which results in different trends for the coulombic efficiencies (**Fig. 7.7d**). The LMO_{700} and $TiO_{<10nm}LMO_{700}$ samples have very poor coulombic efficiencies < 99 % until cycle 400, which indicates electrolyte decomposition during the charge process. The $LTO_{<10nm}LMO_{700}$ sample reaches 99 % of coulombic efficiency at ca. cycle 100, which confirms the good protection characteristics of the LTO coating observed in the previous measurements.

Even though the analyses of the coulombic efficiencies of the LMO_{600} indicate less CEI formation than for the LMO_{700} samples, the cycling stabilities are worse than for the LMO_{700} samples. That indicates that Mn dissolution might be the dominating loss mechanism for the LMO_{600} samples. Since Mn dissolution is the disproportionation of Mn^{3+} (LMO lattice) to Mn^{2+} (dissolves in the electrolyte) and Mn^{4+} (remains in lattice), no charge is required for this reaction and it does not affect the coulombic efficiency. This leads to the conclusion, that the lower crystallinity and the existence of probable amorphous LMO phases of the LMO_{600} samples benefit the Mn dissolution. Post-mortem analyses via GIXRD or XPS should be done to validate this hypothesis in further studies.

The existence of a higher degree of carbonate or hydroxide residues from the sol-gel synthesis can be a further explanation for the significant capacity fade of the LMO_{600} samples. Sicklinger et al.[197] could demonstrate a comparable capacity fade of NMC active material, to which carbonates and hydroxide were deliberately added. The authors could show that the purification of these NMC materials by calcination at > 500 °C in argon flow significantly enhances the cycling stability. Transferring these findings to the LMO samples, it can be assumed that the LMO_{600} samples annealed in air atmosphere at 600 °C have a higher degree of carbonates and hydroxides than the LMO_{700} samples annealed at 700 °C, thus, poor cycling stability.

Nevertheless, the LTO coatings seem to enhance the cycling stability of the LMO samples independent of the annealing temperature.

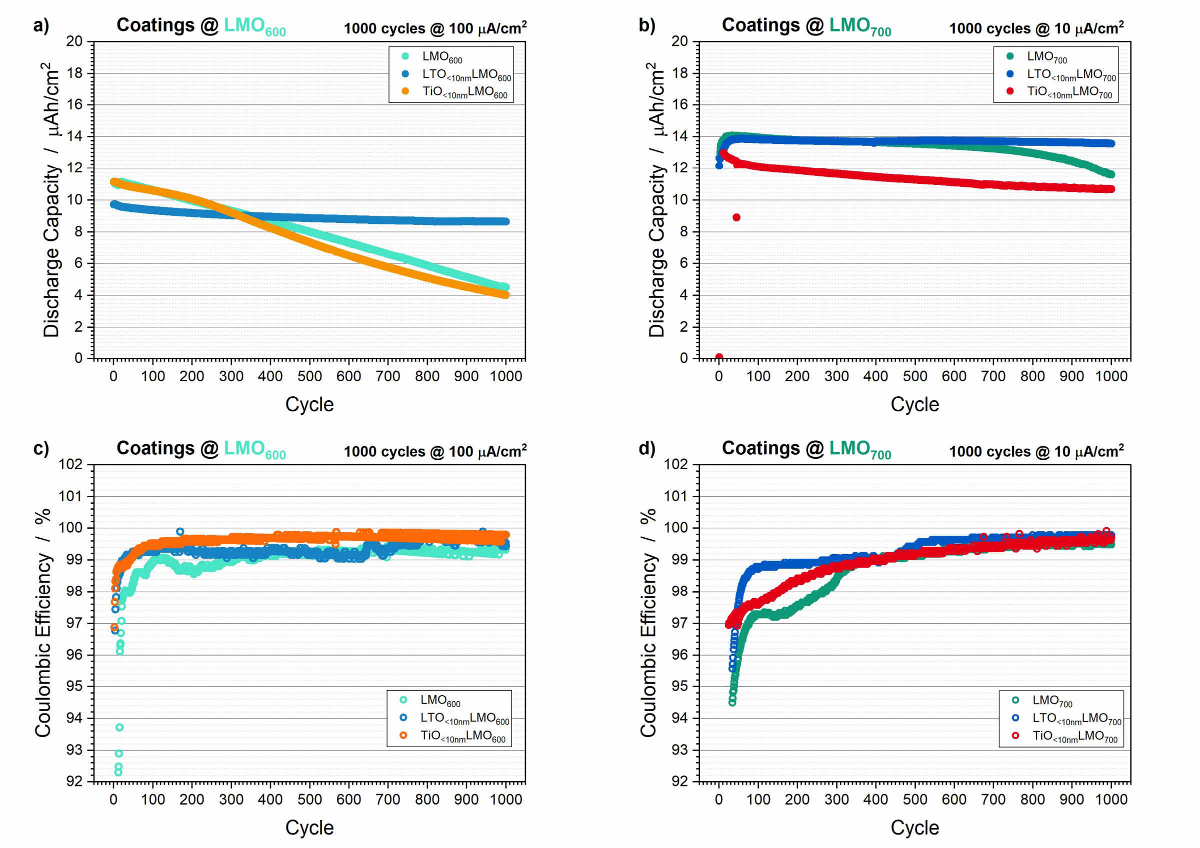

Fig. 7.7 Discharge capacities as a function of cycle number for the **a)** LMO_{600} samples and **b)** LMO_{700} samples tested in liquid electrolyte cells over 1,000 cycles. Corresponding coulombic efficiencies as a function of cycle number for the **c)** LMO_{600} samples and **d)** LMO_{700} samples.

Table 7.3 Electrochemical results obtained from long-term cycling tests in liquid electrolyte cells. LMO_{600} and LMO_{700} samples without and with LTO and TiO_2 coatings.

Sample	**Initial Discharge Capacity (µAh/cm²)**	**Discharge Capacity after 1000 cycles (µAh/cm²)**	**Initial Coulombic Efficiency (%)**	**Coulombic Efficiency after 1000 cycles (%)**	**Cycle number at 80 % Discharge Capacity**	**Capacity retention after 1000 cycles**
600 °C crystallization temperature @ 100 µA/cm²						
LMO_{600}	11.13	4.51	92.2	99.5	364	41 %
$LTO_{<10nm}LMO_{600}$	9.72	8.63	97.1	99.7	--	89 %
$TiO_{<10nm}LMO_{600}$	11.14	4.01	98.16	99.8	330	36 %
700 °C crystallization temperature @ 10 µA/cm²						
LMO_{700}	14.06	11.57	94.6	99.5	--	82 %
$LTO_{<10nm}LMO_{700}$	13.81	13.56	95.7	99.8	--	98 %
$TiO_{<10nm}LMO_{700}$	13.12	9.76	97.1	99.7	758	74 %

Conclusion and Summary

The investigation of the LTO and TiO_2 coatings on top of LMO in liquid electrolyte cells shows that LTO has excellent protection characteristics against electrolyte decomposition and Mn dissolution. Even though the initial discharge capacities are slightly lower for the LTO-coated samples (**Table 7.2**), the long-term cycling tests show high capacity retentions of 89 % ($LTO_{<10nm}LMO_{600}$, **Fig. 7.7a**) and 98 % ($LTO_{<10nm}LMO_{700}$, **Fig. 7.7b**). Additionally, the LTO-coated LMO_{700} samples show good rate capabilities in comparison with the pure LMO_{700} and $TiO_{<10nm}LMO_{700}$ samples (**Fig. 7.7b**). The thin TiO_2 coatings seem to have no additional protection characteristics compared with the pure LMO thin films (**Fig. 7.6 e-f**). This can be explained by its particulate morphology (**Fig. 7.3 c and e**), which suggests a porous structure, which can be infiltrated with the liquid electrolyte so that it gets in direct contact with the LMO surface, thus, electrolyte decomposition and Mn dissolution takes place.

The degree of electrolyte decomposition and Mn dissolution seem to be related to the crystallization temperature of the LMO layer independent of the coating since the LMO_{700} samples have a significantly better rate capability than the LMO_{600} samples (**Fig. 7.5 e-f**). Two possible explanations can be given: i) the Mn dissolution is benefited by the lower crystallinity and existence of amorphous phases of the LMO_{600} sample; ii) the lower crystallization temperature and uncompleted LMO crystallization leads to a higher amount of carbonate and hydroxide residues from the sol-gel solution, which enhances the electrolyte decomposition.[197] However, these hypotheses need to be tested and validated in further studies.

Finally, the increase in the LMO layer thickness causes poorer rate capabilities compared with the single LMO layers of the previous chapter (**Fig. 6.10b**). Particularly, the LMO_{700} samples show a major effect on the layer thickness (**Fig. 7.5f**). The thicker layers increase the ohmic resistances for electron and Li-ion diffusion (**Eq. 2.14**), which also affects the polarization processes so that a lower utilization at higher current densities is obtained. Considering the subsequent deposition of SSEs materials with lower ionic conductivities than liquid electrolytes, the layer thicknesses of the LMO layers need to be taken into account as an additional electrical and ionic resistance.

7.4 Functionality of TiO_2 and LTO Interlayers in LIPON|Interlayer|LMO Full Cells

The general functionality of the TiO_2 and LTO interlayers incorporated in TF-SSBs was tested by using LIPON as SSE. LIPON is an amorphous SSE, which does not require additional heat treatment after deposition so that interdiffusion processes can be neglected. Consequently, it is suitable to investigate the influence of probable blocking behavior of the TiO_2 and LTO interlayers for Li-ion diffusion through these interlayers as a function of the interlayer thickness. LTO (ca. 1 E-12 cm²/s)[180–183] and TiO_2 (ca. 1 E-16 cm²/s)[184,185] differ in their Li-ion diffusion coefficient by factor 10,000. In order to investigate the impact of the interlayer material and thickness, ca. 1 µm of LIPON was sputtered on top of the LMO_{600} and LMO_{700} samples with and without interlayers. Afterward, Li and Cu were deposited to obtain full cells (**Fig. 7.8**), which were tested via the same rate capability tests and long-term cycling tests as in the previous section.

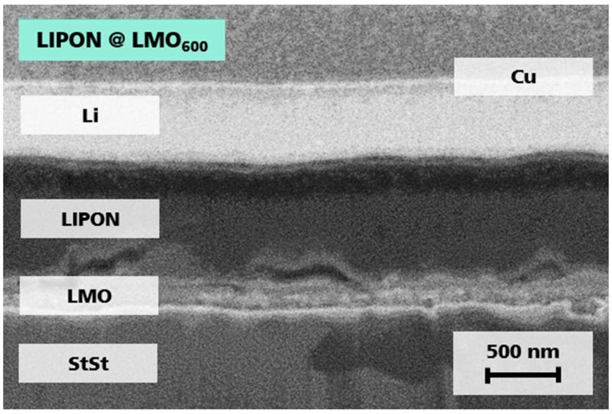

Fig. 7.8 SEM cross-section of a LIPON @ LMO_{600} full cell with Li anode and Cu current collector.

Electrochemical Characterization: Rate Capability Tests

The voltage profiles of cycle 35 (10 µA/cm², **Fig. 7.9 a-b**) and cycle 20 (100 µA/cm², **Fig. 7.9 c-d**), as well as the plots of the discharge capacities over cycle number (Fig. 7.9 e-f), reveal major effects of the coating material and thickness as well as the crystallization temperature of the LMO layers on the electrochemical performance. The results of the electrochemical characterization are summarized in **Table 7.4**.

Analyzing the voltage profiles obtained at 10 µA/cm², the pure LMO_{600} sample appears to have a discharge capacity of 15.13 µAh/cm², whereas the $LTO_{<10nm}LMO_{600}$ and $LTO_{\approx 20nm}LMO_{600}$ samples have discharge capacities of 11.45 µAh/cm² and 12.75 µAh/cm², respectively (**Fig. 7.9a**). The TiO_2 interlayers show a strong impact of the interlayer thickness on the electrochemical performance. The sample with a thinner TiO_2 interlayer shows a discharge capacity of 13.96 µAh/cm², which is slightly higher than for the samples with LTO interlayers. In contrast, no capacity can be obtained by using the thicker TiO_2 layer, so that it can be concluded that ca. 20 nm of TiO_2 blocks Li-ion diffusion through the interlayer.

Considering the LMO_{700} samples with and without an interlayer, the increased ohmic resistance of the LMO layer, which was already observed in liquid electrolyte cells, in combination with the low conductive LIPON SSE results in a complete malfunction for all tested current densities (**Fig. 7.9b**). Lower current densities are required to overcome the high ionic and electrical resistances of both the LMO_{700} active material and the LIPON SSE.

The analyses of the rate capabilities of the LMO_{600} samples show that the pure LMO_{600} and the $LTO_{<10nm}LMO_{600}$ samples demonstrate the lowest differences in discharge capacity between 10 µA/cm² (cycle 35, **Fig. 7.9a**) and 100 µA/cm² (cycle 20, **Fig. 7.9c**). The differences between both are about 20 % (**Table 7.4**), whereas the $LTO_{\approx 20nm}LMO_{600}$ sample with thicker LTO interlayer has a rate capability of 53 % and an overvoltage of 338 mV at 100 µA/cm² (cycle 20, **Fig. 7.9c**). The $TiO_{<10nm}LMO_{600}$ sample shows also a poor rate capability of 42 %. However, its overvoltage at 100 µA/cm² (cycle 20) is 100 mV and comparable with the LMO_{600} and $LTO_{<10nm}LMO_{600}$ samples at 100 µA/cm² (**Table 7.4**). In general, the pure LMO_{600} sample and the LMO_{600} samples with the thin TiO_2 and LTO interlayers demonstrate very low overvoltages at 10 µA/cm² (cycle 35) of about 15 mV to 18 mV, which is slightly higher than the reference values obtained from the liquid electrolyte cells (9 mV to 14 mV, **Table 7.2**). This indicates that thin interlayers have no significant impact on the cell performance of the LIPON full cells by acting as a blocking layer for Li-ion diffusion.

However, the consideration of the coulombic efficiencies suggests that side reactions take place. The values of about 90 % for all samples (cycle 35 at 10 µA/cm², **Table 7.4**) are 6 % to 8 % lower than the coulombic efficiencies of the samples tested in liquid electrolyte cells (**Table 7.2**). Low coulombic efficiencies mean that more charge is required during the charge process than during the discharge process. Moreover, the LIPON full cells show 2 µAh/cm² to 4 µAh/cm² higher discharge capacities than the liquid electrolyte cells. This indicates also an additional reaction during the discharge process. Consequently, a partly reversible side reaction or several different side reactions take place between the LMO_{600} samples and the LIPON SSE during the charge and discharge processes, which are independent of the interlayer material. This can also explain the unexpected good rate capabilities and low overvoltages of the LIPON full cells since the side reactions superpose the LMO extraction/insertion reaction, which causes lower polarization effects than expected by the Li-ion charge transfer into or out of LMO.

Since the LMO_{700} samples show just polarization effects and no indications for side reactions, it can be assumed, that the side reactions are related to the crystallization temperature of the LMO layer. As discussed in the previous subchapter, lower LMO crystallinity and the probable existence of carbonates and hydroxides might have an impact on the long-term cycling stability of the LMO_{600} samples with and without interlayer in liquid electrolyte cells, so that it can be assumed that especially the carbonate and hydroxide residues from the sol-gel synthesis also affect the electrochemical processes of the LIPON full cells. Consequently, an impact on the long-term cycling stability is expected, which will be analyzed in the next section.

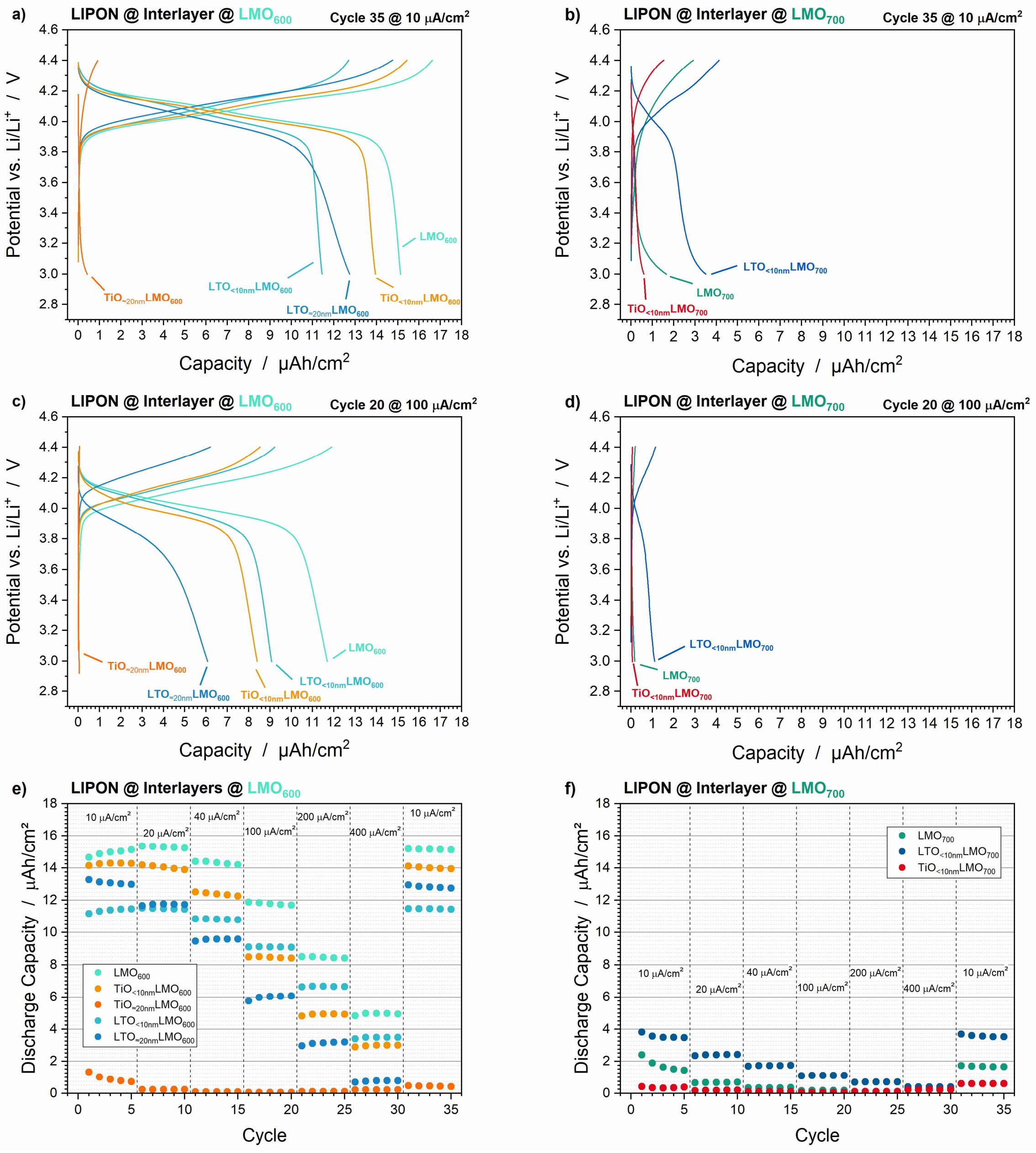

Fig. 7.9 Electrochemical data obtained from rate capability tests of LIPON full cells. Voltage profiles of all samples with and without LTO and TiO_2 interlayers between LIPON and LMO_{600} at **a)** 10 µA/cm² (cycle 35) and **c)** 100 µA/cm² (cycle 20) as well as between LIPON and LMO_{700} at **b)** 10 µA/cm² (cycle 35) and **d)** 100 µA/cm² (cycle 20). Discharge capacities during rate capability tests of samples with and without **e)** interlayers between LIPON and LMO_{600} and **f)** interlayers between LIPON and LMO_{700}.

Table 7.4 Electrochemical results obtained from rate capability tests of LIPON full cells. LMO_{600} and LMO_{700} samples without and with LTO and TiO_2 interlayers.

Sample	Discharge Capacity Cycle 35 @ 10 µA/cm^2 (µAh/cm^2)	Coulombic Efficiency Cycle 35 (%)	Overvoltage Cycle 35 @ 10 µA/cm^2 (mV)	Discharge Capacity Cycle 20 @ 100 µA/cm^2 (µAh/cm^2)	Overvoltage Cycle 20 @ 100 µA/cm^2 (mV)	Rate Capability* (%)
600 °C crystallization temperature						
LMO_{600}	15.13	91.1	15	11.69	73	23
$LTO_{<10nm}LMO_{600}$	11.45	90.2	17	9.08	102	21
$LTO_{\approx 20nm}LMO_{600}$	12.75	86.4	42	6.08	338	53
$TiO_{<10nm}LMO_{600}$	13.96	90.5	18	8.41	100	42
$TiO_{\approx 20nm}LMO_{600}$	n.a.	n.a.	n.a.	n.a.	n.a.	n.a.
700 °C crystallization temperature	No capacity was obtained for all samples					

* Ratio of Discharge Capacity 10 µA/cm^2 : 100 µA/cm^2.

Electrochemical Characterization: Long-Term Cycling Test

Since the LMO_{700} samples show just polarization effects in combination with LIPON, solely the LMO_{600} samples without and with the thinnest LTO and TiO_2 interlayers were tested on their long-term cycling stability over 1,000 cycles at a current density of 100 µA/cm^2.

The initial discharge capacities are 15.15 µAh/cm^2 for LMO_{600} (**Fig. 7.10a**), 8.49 µAh/cm^2 for $LTO_{<10nm}LMO_{600}$ (**Fig. 7.10b**) and 12.07 µAh/cm^2 for $TiO_{<10nm}LMO_{600}$ (**Fig. 7.10c**). Over 1,000 cycles all samples experience significant capacity losses of 47 % to 8.03 µAh/cm^2 (LMO_{600}, **Fig. 7.10a**), 53 % to 4.00 µAh/cm^2 ($LTO_{<10nm}LMO_{600}$, **Fig. 7.10b**) and 70 % to 3.68 µAh/cm^2 ($TiO_{<10nm}LMO_{600}$, **Fig. 7.10c**). The capacity fades go along with an increase in the polarization effects, which become evident in the 1,000th cycles' voltage profiles. That indicates the formation of a blocking layer between the cathode and SSE comparable with the CEI in liquid electrolyte cells, thus, the reaction of the LIPON SSE with the cathode material.

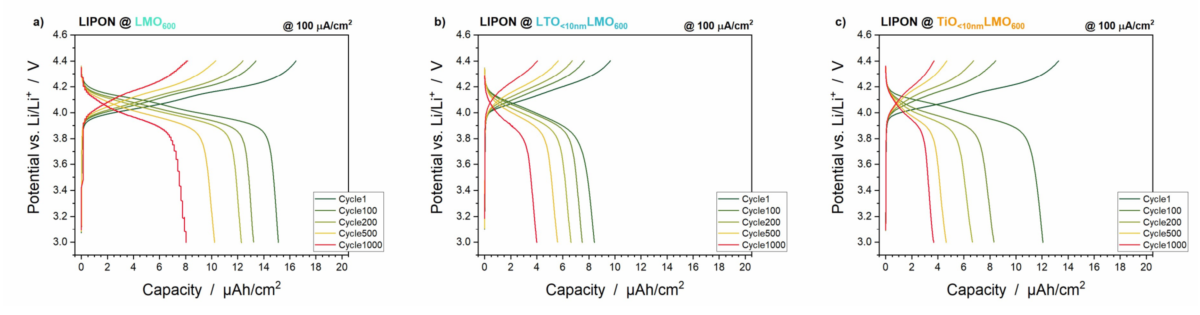

Fig. 7.10 Voltages profiles of long-term cycling tests in LIPON full cells over 1,000 cycles. LMO_{600} samples tested at 100 µA/cm^2 **a)** without interlayer, **b)** with < 10 nm LTO interlayer and **c)** with < 10 nm TiO_2 interlayer.

The discharge capacities over cycle number are plotted in **Fig. 7.11a**. The cycle numbers, at which 80 % of the initial discharge capacities are reached, are 213 for LMO_{600}, 175 for $LTO_{<10nm}LMO_{600}$ and 54 for $TiO_{<10nm}LMO_{600}$ and their capacity retentions after 1,000 cycles are 53 %, 47 % and 30 %, respectively (**Table 7.5**).

The continuous decrease in discharge capacity for all samples due to reactions between the cathode and SSE is also reflected in the coulombic efficiencies. Their values stay below 99 % in the first 500 cycles (**Fig. 7.11b**). The initial as well as the last cycles' coulombic efficiencies (**Table 7.5**) are lower than the values of the liquid electrolyte cells (**Table 7.3**). That suggests a steady side reaction over 1,000 cycles.

Conclusively, all LMO_{600} samples in combination with the LIPON SSE show very poor cycling stabilities independent of the interlayer material. Even the LTO interlayer, which shows a very good cycling stability in liquid electrolyte cells, exhibits a poor electrochemical performance. Every analysis indicates a side reaction between LIPON and the cathode.

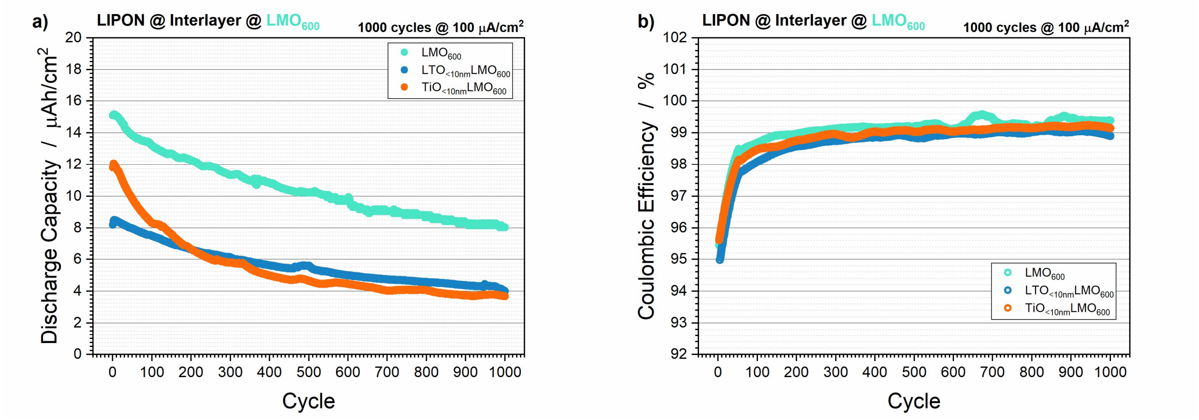

Fig. 7.11 a) Discharge capacities as a function of cycle number of the long-term cycling tests of the LIPON|Interlayer|LMO_{600} full cells and **b)** corresponding coulombic efficiencies as a function of the cycle number.

Table 7.5 Electrochemical results obtained from long-term cycling of LIPON full cells. LMO_{600} samples without and with LTO and TiO_2 interlayers.

Sample	**Initial Discharge Capacity (µAh/cm²)**	**Discharge Capacity after 1000 cycles (µAh/cm²)**	**Initial Coulombic Efficiency (%)**	**Coulombic Efficiency after 1000 cycles (%)**	**Cycle number at 80 % Discharge Capacity**	**Capacity retention after 1000 cycles**
600 °C crystallization temperature @ 100 µA/cm²						
LMO_{600}	15.15	8.03	93.5	99.4	213	53 %
$LTO_{<10nm}LMO_{600}$	8.49	4.00	93.2	98.9	175	47 %
$TiO_{<10nm}LMO_{600}$	12.07	3.68	93.4	99.2	54	30 %

Conclusion and Summary

The general functionality of the LTO and TiO_2 interlayers on top of LMO was meant to be validated in LIPON TF-SSB full cells. Dependencies of interlayer thickness and material with the rate capability of the full cells could be determined. The sample with a thin LTO interlayer of < 10 nm and the pure LMO_{600} sample showed good rate capabilities (**Fig. 7.9 e-f**). The sample with a thin TiO_2 interlayer demonstrated a worse rate capability, which was comparable to the sample with a thicker LTO interlayer of ca. 20 nm. The sample with a 20 nm TiO_2 interlayer solely showed significant polarization effects so that no capacity could be obtained (**Fig. 7.9a**). Consequently, the LTO interlayer shows less blocking behavior for Li-ion diffusion from LIPON to the LMO active material than TiO_2, which can be explained by the higher Li-ion diffusion coefficient of LTO.

These findings are related to the LMO samples, which were crystallized at 600 °C. The LMO samples annealed at 700 °C showed already indications for a higher resistance for Li-ion diffusion or a higher electrical resistance by testing them in liquid electrolyte cells (**Fig. 7.5f**). These high resistances in combination with the low conductive LIPON SSE result in a malfunction of all LIPON full cells due to the major impact of polarization effects (**Fig. 7.9f**). In further studies, GCPL tests should be performed at much lower current densities of ≤ 1 µA/cm². Alternatively, an increase of the testing temperature to ≥ 40 °C is also thinkable.

By comparing the LMO_{600} LIPON full cells with the liquid electrolyte reference cells, many indications for side reactions between LIPON and the cathode with or without interlayer could be found. The observations of higher capacities, lower coulombic efficiencies or poor cycling stabilities were unexpected and are not in accordance with the literature, where cycle lives of > 2,000 cycles or more than 10,000 cycles are reported.[52,60] The biggest difference to the literature is the preparation of the LMO cathode. Li et al.[52], for instance, used PVD techniques to prepare the cathode and LIPON SSE. Additionally, the authors transferred the sample between the deposition chambers in inert gas atmosphere in order to avoid exposure to air. As a result, highly impurity-free full cells can be assembled. In this study, the basis is a sol-gel synthesis in organic solvent and the samples were crystallized in air atmosphere. By that, it is most likely that carbonates and hydroxide got formed during crystallization or remain from the synthesis. Indications for that could already be found by analyzing the long-term cycling tests of the liquid electrolyte reference cells, where the LMO_{600} samples showed worse cycling stabilities than the LMO_{700} samples. These residues tend to outgas during charging due to the formation of CO_2, H_2O or O_2.[193,194,197–199] In combination with the LIPON SSE, these reactions can also take place and further reactions to NO_x or Li_3PO_4 are thinkable. However, these assumptions need to be validated in further studies. Post-mortem analyses as well as monitoring the outgassing during cycling are possible ways to investigate the side reactions. To avoid side reactions, heat treatment above 500 °C in inert gas is a reported possibility to purify the active material from carbonates and hydroxides.[197] This should be implemented before depositing the LIPON SSE.

7.5 TiO_2 and LTO as Interdiffusion Barriers in Ga-LLZO|Interlayer|LMO Cells

The target system is a TF-SSB based on the Ga-LLZO SSE and the LMO cathode. Because of the Ga-LLZO crystallization temperature of 650 °C, interdiffusion processes between LMO and Ga-LLZO are expected so that TiO_2 and LTO interlayers were tested as interdiffusion barriers. Since the thinnest interlayers showed the best results in the LIPON full cells, these were tested and the results of the investigations of the formation of impurity phases (GIXRD), interdiffusion (ToF-SIMS) and electrochemical performance are demonstrated in the following. Ga-LLZO was sputtered on the LMO_{600} and LMO_{700} samples with and without LTO and TiO_2 coatings and afterward crystallized at 650 °C. The electrochemical performance was tested by using a liquid electrolyte (LP30, EC:DMC 1:1 vol%, 1 M $LiPF_6$) against a Li-metal anode.

Crystalline Phases

The GIXRD diffractograms (**Fig. 7.12a**) of the samples with Ga-LLZO directly crystallized on LMO_{600} and LMO_{700} exhibit the main reflections of LMO at ca. 18.72° (LMO, ICSD 94340). Further LMO reflections are not evident or overlap with reflections of further phases. Weak Ga-LLZO reflections can be observed for the LMO_{600} sample at ca. 16.72°, ca. 25.65°, ca. 30.77°, ca. 33.80°, ca. 37.93° and ca. 42.91° (LLZO, ICSD 182312). However, an additional $La_2Zr_2O_7$ reflection at ca. 28.61° (ICSD 51573) as well as Mn_2O_3 reflections at ca. 23.12° and ca. 32.92° (ICSD 159865) can be detected. In contrast, the LMO_{700} sample shows no indications for the Ga-LLZO phase as well as the $La_2Zr_2O_7$ impurity phase. This indicates that the Ga-LLZO remains amorphous after crystallization. However, the Mn_2O_3 reflections are increased for the LMO_{700} samples and show higher intensities than the LMO main reflection, which suggests a significant decomposition of LMO.

Ga-LLZO crystallized on top of the $LTO_{<10nm}LMO_{600}$ and $LTO_{<10nm}LMO_{700}$ samples shows clear reflections at ca. 16.72°, ca. 25.65°, ca. 30.77°, ca. 33.80°, ca. 37.93° and ca. 42.91° with high intensities (**Fig. 7.12b**). LMO is detectable at ca. 18.72°. The impurity phase $La_2Zr_2O_7$ is also detectable for the $LTO_{<10nm}LMO_{600}$, but it is not observable for the $LTO_{<10nm}LMO_{700}$ sample. Mn_2O_3 as an impurity phase can also be detected for the LTO interlayer samples. However, its normalized intensities are lower in relation to the LMO and Ga-LLZO reflections, which indicates a lower amount of Mn_2O_3 in comparison with the samples without interlayer (**Fig. 7.12a**).

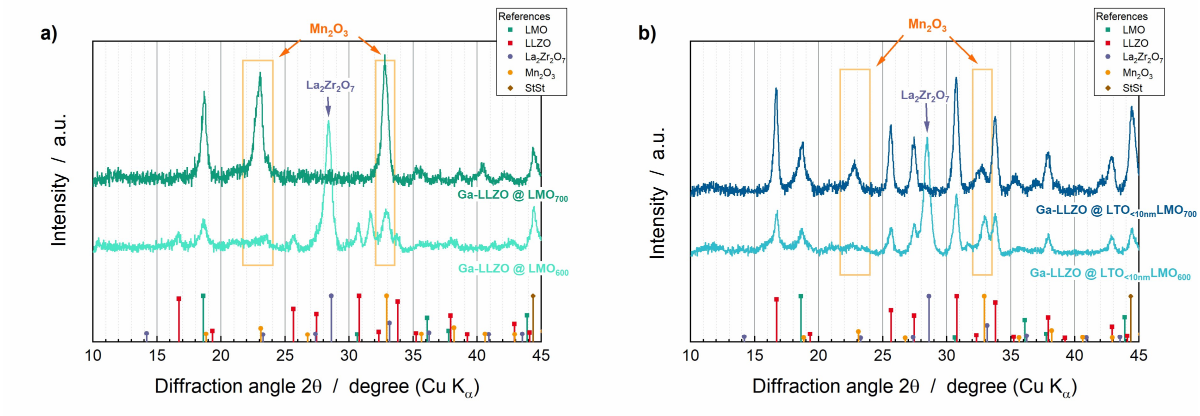

Fig. 7.12 GIXRD diffractograms of Ga-LLZO crystallized at 650 °C on top of **a)** pure LMO and **b)** LTO coated LMO.

The impurity phase $La_2Zr_2O_7$ is the dominant reflection for the LMO$_{600}$ and LTO$_{<10nm}$LMO$_{600}$ samples. Ga-LLZO on top of LTO$_{<10nm}$LMO$_{700}$ exhibits no $La_2Zr_2O_7$ impurity phases and crystalline Ga-LLZO, so the crystallinity of the LMO has an impact on the Ga-LLZO crystallization. The LTO interlayer clearly enhances the Ga-LLZO crystallization, since no Ga-LLZO phases can be detected on the pure LMO$_{700}$ sample. Consequently, TiO$_{<10nm}$LMO$_{700}$ was additionally used for Ga-LLZO deposition and crystallization. Its GIXRD diffractogram is comparable with the diffractogram of the LTO$_{<10nm}$LMO$_{700}$ sample (**Fig. 7.13**). Both samples show crystalline Ga-LLZO. Additionally, the Mn_2O_3 formation is inhibited with interlayer compared with the pure LMO$_{700}$ sample (**Fig. 7.13**).

Since the $La_2Zr_2O_7$ formation is inhibited by using the LMO$_{700}$ cathodes without and with interlayers, these samples were selected for further structural and electrochemical investigations.

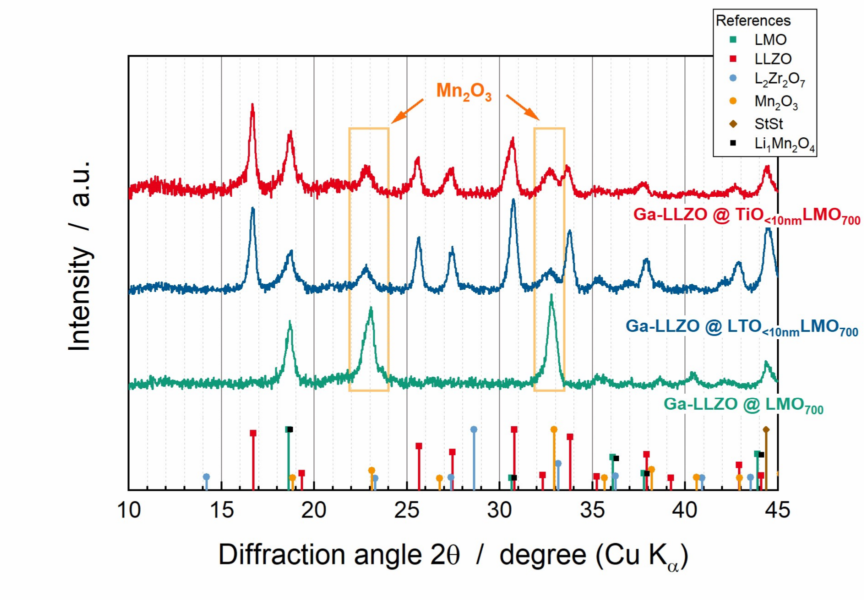

Fig. 7.13 GIXRD diffractograms of Ga-LLZO crystallized at 650 °C on top of LMO$_{700}$ with and without LTO and TiO_2 interlayer.

Cross-Sections

The SEM cross-sections of the samples with Ga-LLZO sputtered and crystallized on top of LMO$_{700}$ with and without interlayers are shown in **Fig. 7.14**. The LMO layer is about 300 nm for all samples and the Ga-LLZO layers have thicknesses of ca. 350 nm. The TiO_2 and LTO interlayer seem to be under the resolution limit and cannot be made visible by SEM. Further investigation by means of transmission electron spectroscopy (TEM) is thinkable to obtain further insights into the interlayer region. The Ga-LLZO and LMO layers appear to be dense and homogenous for the LTO$_{<10nm}$LMO$_{700}$ (**Fig. 7.14b**) and TiO$_{<10nm}$LMO$_{700}$ (**Fig. 7.14c**) samples. Dark contrast in the Ga-LLZO layer can be seen for the TiO$_{<10nm}$LMO$_{700}$, which indicates impurity phases. Additional measurements such as TEM/EDS are required to achieve further information like elemental distribution or the atomic resolution of the interface region.

In contrast to the samples with interlayers, the LMO$_{700}$ sample exhibits cracks and a non-uniform Ga-LLZO layer (**Fig. 7.14a**). The detected Mn_2O_3 phases (**Fig. 7.13**) cannot be distinguished from the Ga-LLZO and the LMO layer by means of SEM. Further examination by means of TEM/EDS could be done in further studies.

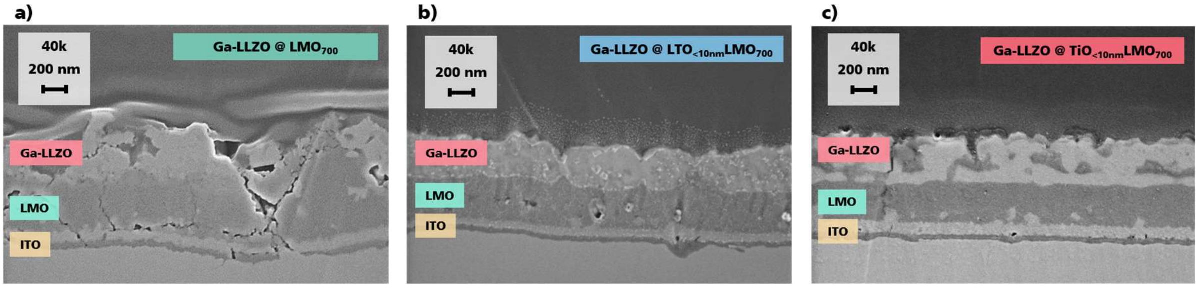

Fig. 7.14 SEM cross-sections of Ga-LLZO|LMO thin-film stacks **a)** without interlayer, **b)** with LTO (< 10 nm) interlayer and **c)** with TiO2 (< 10 nm) interlayer.

Interdiffusion Processes

The compositional depth profiles obtained via ToF-SIMS are shown in **Fig. 7.15**. Because of the different sputter yields of the single layers as well as the different thicknesses of the layer stacks, the sputter time is normalized to the peak maximum of the InO^- signal in order to obtain reasonable comparisons. The detected mass-to-charge ratios (m/z) will be described by GaO^- (m/z = 85 u), ZrO^- (m/z = 106 u), LaO^- (m/z = 155 u), TiO^- (m/z = 64 u), Li^- (m/z = 7 u), MnO^- (m/z = 71 u) and InO^- (m/z = 131 u).

The compositional depth profile of the Ga-LLZO @ LMO$_{700}$ sample shows the presence of Ga in the LMO layer as well as Mn in the Ga-LLZO layer (**Fig. 7.15a**). The signals of ZrO^- and LaO^- do not overlap with the LMO region so that an interdiffusion of Zr and La can be excluded. The oxidation states of Ga, La and Zr in Ga-LLZO are 3+, 3+ and 4+, respectively. The oxidation states of Mn in LMO are 3+ and 4+. Consequently, Ga might substitute Mn in the LMO lattice and Mn can substitute Ga in the Ga-LLZO, even though the GIXRD measurement indicates an amorphous Ga-LLZO. Furthermore, the presence of Mn_2O_3 (**Fig. 7.13**) gives a second explanation. Mn can diffuse into the Ga-LLZO layer during annealing but forms Mn_2O_3 in addition to the Ga-LLZO crystallization. The hypothesis is supported by the steadily decreasing trend of the MnO^- signal. If Mn_2O_3 is formed at the interface of LMO and Ga-LLZO, a peak in the signal will appear. This cannot be observed so that a distribution of Mn_2O_3 in the Ga-LLZO layer is most likely.

The implementation of the interlayers LTO and TiO_2 results in an inhibition of the Ga interdiffusion (**Fig. 7.15 b-c**) since no GaO^- signal can be observed in the LMO region. However, Mn still diffuses into the Ga-LLZO layer. This might cause the substitution of Ga or the formation of Mn_2O_3 in the Ga-LLZO layer, which was probably suggested by the dark contrast seen in the SEM cross-section of $TiO_{<10nm}LMO_{700}$ (**Fig. 7.8c**). It is also possible that both happen in parallel since peaks for the MnO^- and GaO^- signals at the surface (0 to 0.2 normalized sputter time, **Fig. 7.15 b-c**) are evident and the GaO^- signal decreases with sputter depth (0.2 to 0.4 normalized sputter time). The accumulation of Mn at the surface might suggest Mn_2O_3 formation. The accumulation of Ga might be explained by the depletion of Li at the surface, sine the existence of Ga_xO_y species cannot be confirmed by the GIXRD measurements (**Fig. 7.13**). The Li^- signal shows the opposite trend as the GaO^- signal. For a proper explanation, the stoichiometry of Ga-LLZO ($Li_{6.25}Ga_{0.25}La_3Zr_2O_{12}$) and LLZO ($Li_7La_3Zr_2O_{12}$) must be considered. As reported by Sastre et al.[78], the substitution of three Li^+ atoms by one Ga^{3+} atom stabilizes the high-temperature cubic phase at room temperature and provides more vacancies for Li-ion migration. Transferring this knowledge to the detected ToF-SIMS data, it can be deduced, that a stoichiometric gradient through the Ga-LLZO layer is present. At the surface, the $Li_{6.25}Ga_{0.25}La_3Zr_2O_{12}$ phase with a higher amount of Ga dominates, whereas the stoichiometry approaches $Li_7La_3Zr_2O_{12}$ with layer depth. By that, the compositional depth profiles suggest an inhomogeneous stoichiometry through the Ga-LLZO layer and the existence of Mn_2O_3 phases within the Ga-LLZO layer, although TiO_2 and LTO were used as interdiffusion barriers.

The consideration of the interlayer regions of the $LTO_{<10nm}LMO_{700}$ (**Fig. 7.15b**) and $TiO_{<10nm}LMO_{700}$ (**Fig. 7.15c**) samples reveals that the signals of both interlayer materials show a sharp peak for the TiO^- signal and clearly separate the Ga-LLZO from the LMO. Elements of the Ga-LLZO layer cannot be detected in the interlayer region. On the other hand, Mn diffusion cannot be blocked, so that the MnO^- signal overlaps with the TiO^- signals of both samples. Ti does not seem to diffuse into the Ga-LLZO layer but shows a shoulder in the signal into the LMO region so that the peak appears slightly asymmetric. It indicates a low degree of Ti interdiffusion into the LMO layer or the fusing of the interlayer material and LMO. However, this effect can also be explained by the measurement inaccuracy of the ToF-SIMS due to the different sputter yields of the single layers. Although Mn can substitute the Ti in the spinel LTO or anatase TiO_2, the Ti interdiffusion into LMO in consideration of the electroneutrality of the crystal lattice is not mandatory, since the crystallization takes place in a controlled oxygen atmosphere, which provides O^{2-} for the charge equalization.

In conclusion, the interlayer materials TiO_2 and LTO are able to block the Ga interdiffusion into the LMO layer but cannot block Mn diffusion. This results in either the substitution of Ga by Mn in the Ga-LLZO lattice or the formation of Mn_2O_3 within the Ga-LLZO layer. Zr and La do not diffuse into LMO even without interlayer. Additionally, the diffusion of Ti into Ga-LLZO can be excluded. The diffusion of Ti into LMO is unlikely but cannot be completely excluded.

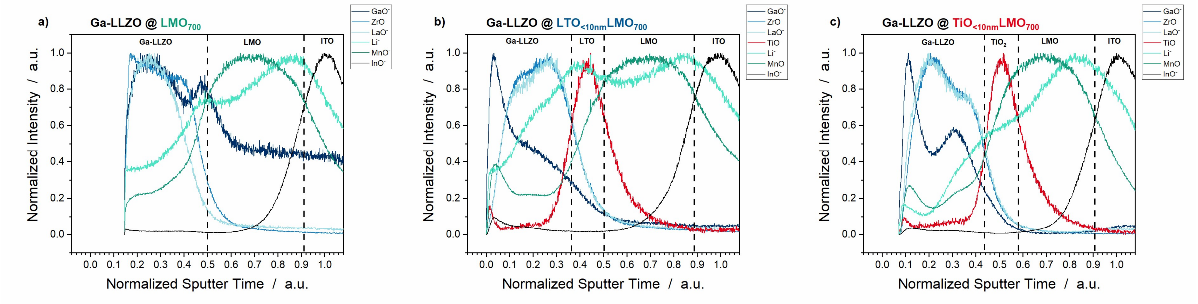

Fig. 7.15 ToF-SIMS depth profiles of Ga-LLZO|LMO thin-film stacks **a)** without interlayer, **b)** with LTO (< 10 nm) interlayer and **c)** TiO_2 (< 10 nm) interlayer.
Sputter time is normalized to 1 for the ITO peak maximum. Ga-LLZO elements (GaO^-, LaO^- and ZrO^-) in blue, LMO elements (Li^- and MnO^-) in green, ITO elements (InO^-) in black and interlayer elements (TiO^-) in red.

Electrochemical Characterization: 1. Formation Cycles at 5 µA/cm²

The electrochemical characterization was performed via galvanostatic cycling with potential limits (GCPL) in the potential range of 4.4 V vs. Li/Li^+ and 2.0 V vs. Li/Li^+ since the first tests between 4.4 V vs. Li/Li^+ and 3.1 V vs. Li/Li^+ resulted in the polarization of the cells after the first cycle (**Fig. 7.16a**). The test procedure was divided into two parts. The first part was thought of as a formation step for probable SEI formation at the anode and CEI formation between Ga-LLZO and LMO at the cathode. A current density of 5 µA/cm² was used for 5 cycles in the first part. After each charge step, a constant voltage step at 4.4 V vs. Li/Li^+ with the end criteria of 3 h or a current density limit of 0.02 µA/cm² was added (**Fig. 7.16b**). The second part was subsequently executed with 1 µA/cm² and without constant voltage step after the charge step (**Fig. 7.19** and **Fig. 7.20**). The second part was performed for ca. 400 cycles and was interrupted for ca. 2 days by a maintenance of the Maccor 4000 battery cycler.

Fig. 7.16b shows the voltage profiles of the initial cycles at 5 µA/cm². All samples demonstrate massive initial charge capacities of 221.33 µAh/cm² (LMO_{700}), 299.46 µAh/cm² ($LTO_{<10nm}LMO_{700}$) and 312.82 µAh/cm² ($TiO_{<10nm}LMO_{700}$), of which most is converted at ca. 3.00 V vs. Li/Li^+. The initial discharge capacities are 36.51 µAh/cm² for LMO_{700}, 24.78 µAh/cm² for $LTO_{<10nm}LMO_{700}$ and 40.10 µAh/cm² for $TiO_{<10nm}LMO_{700}$.

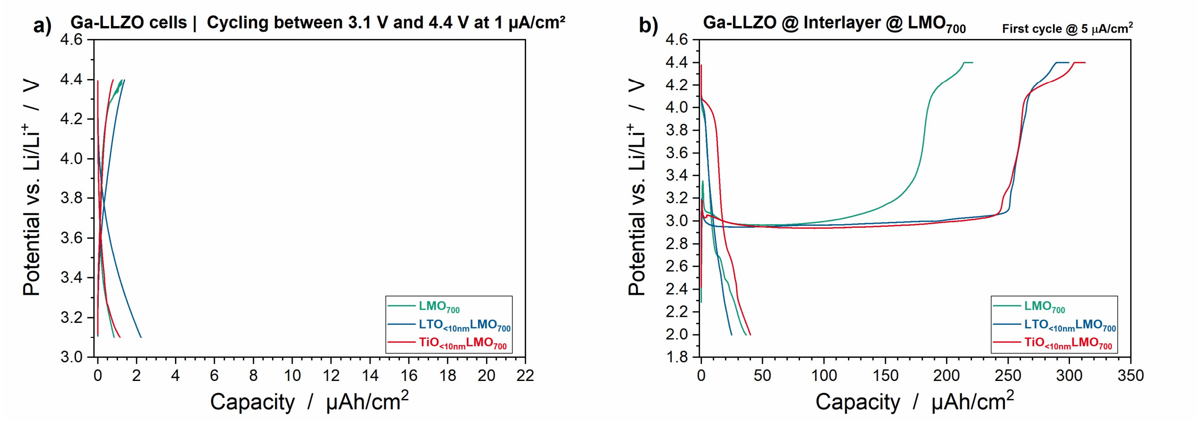

Fig. 7.16 Voltage profiles Ga-LLZO|LMO cells: **a)** second cycle of cells cycled between 3.1 V and 4.4 V; **b)** initial cycles of cells cycled between 2.0 V and 4.4 V.

The differential capacity plot of the first discharge curve of the LMO_{700} sample (**Fig. 7.17d**) reveals redox plateaus at ca. 3.96 V, 3.92 V, 2.92 V, 2.68 V, 2.48 V, 2.35 V and probably at ca. 2.00 V. The second charge voltage curve shows redox potentials at ca. 3.06 V, 3.52 V and 4.27 V. About 7.38 µAh/cm² are consumed during the 3 h constant voltage step at 4.4 V (**Fig. 7.17a**). These plateaus are flattened with cycle number, which goes along with reductions of the discharge capacity to 12.66 µAh/cm² and charge capacity to 19.88 µAh/cm² in the 5th cycle. Consequently, the redox peak areas decrease with cycle number (**Fig. 7.17d**) but are still present. In the 5th charge step, the peak positions are at ca. 3.01 V and 3.74 V. The significant redox peak at 4.27 V (first cycle) has become a shoulder going over into the constant voltage step at 4.4 V (**Fig. 7.17d**), during which 7.02 µAh/cm² are consumed in 3 h (**Fig. 7.17a**). In the 5th discharge step, the two redox peaks at high potentials are more distinguishable, as they shift to 3.92 V and 3.70 V. In the lower potential region, the various peaks of the first cycle seem to merge to a broad redox peak between 3.0 V and 2.13 V (**Fig. 7.17d**), which appear as one slope in the voltage profile (**Fig. 7.17a**). However, with a closer look, the redox peaks can still be distinguished at ca. 2.81 V, 2.57 V, 2.40 V, 2.33 V and 2.20 V.

A similar trend can be observed for the $TiO_{<10nm}LMO_{700}$ sample (**Fig. 7.17c**). In the initial discharge step, the differential capacity plot (**Fig. 7.17f**) shows peaks at ca. 4.05 V, 3.07 V, 2.70 V, 2.46 V, 2.24 V and 2.10 V. In accordance with the LMO_{700} sample, the peak areas decrease with cycle number. Besides the redox peak at 3.71 V, the redox peaks at lower potentials form a broad peak between 3.20 V and 2.18 V in the 5th cycle. Weak maxima are still observable at 3.09 V, 2.88 V, 2.40 V and 2.18 V. The discharge capacity reduces from 40.10 µAh/cm² (initial discharge) to 12.42 µAh/cm² (5th cycle). The second charge curve shows redox peaks at ca. 3.08 V, 3.56 V and 4.29 V, which are similar to the LMO_{700} sample. Additionally, a high capacity of 9.00 µAh/cm² is converted during the constant voltage step at 4.4 V (**Fig. 7.17c**). Until the 5th cycle, the peak areas decrease significantly but are still visible at 3.04 V and 3.71 V (**Fig. 7.17f**). The most dominant redox peak at 4.29 V disappears. However, the charge capacity in the constant voltage step of the 5th charge step is 6.84 µAh/cm².

The $LTO_{<10nm}LMO_{700}$ sample exhibits the lowest discharge capacity of 24.78 µAh/cm² in the initial cycle (**Fig. 7.17b**). Consequently, the redox peaks are less pronounced in the differential capacity plot (**Fig. 7.17e**). Peaks can be detected at ca. 4.03 V, 3.55 V, 3.11 V, 2.95 V, 2.69 V, 2.57 V, 2.44 V, 2.22 V and probably at ca. 2.00 V. In the 5th discharge step, the discharge capacity is reduced to 11.02 µAh/cm² (**Fig. 7.17b**). The redox peak at ca. 4.03 V is vanished in the 5th cycle. Besides the redox peak at 3.52 V, a broad redox peak between 3.47 V and 2.09 V with weak maxima at 3.09 V, 2.70 V, 2.38 V and 2.15 V is observable in the differential capacity plot (**Fig. 7.17e**). Furthermore, the charge capacity of 25.70 µAh/cm² in the second charge step is lower than for LMO_{700} (40.80 µAh/cm²) or $TiO_{<10nm}LMO_{700}$ (42.20 µAh/cm²) samples. This is also evident in the differential capacity plots with redox peaks of lower peak area at 3.10 V, 3.69 V and 4.29 V. However, a high amount of charge of 6.46 µAh/cm² is converted during the constant voltage step at 4.4 V within 3 h. In the 5th charge step the redox peak at 4.29 V is vanished. The other two redox peaks merge to a broad peak between ca. 2.40 V and 4.4 V with two maxima at 3.20 V and 3.56 V. The charge capacity of 6.20 µAh/cm² in the constant voltage step at 4.4 V is still high.

In conclusion, the high initial charge capacities of all samples indicate significant side reactions at the Ga-LLZO|LMO interface even with LTO or TiO_2 interlayers. Additionally, high discharge capacities can be measured. The capacities decrease in the subsequent cycles, which indicates irreversible side reactions. However, the high amount of various redox potentials in the charge as well as the discharge steps suggest a very complex system, which cannot be decoded in this study. Nevertheless, the redox peaks decrease with cycle number and go over in broad peak areas. The $LTO_{<10nm}LMO_{700}$ sample shows the lowest impact of side reactions. A further discussion can be found in the discussion part below.

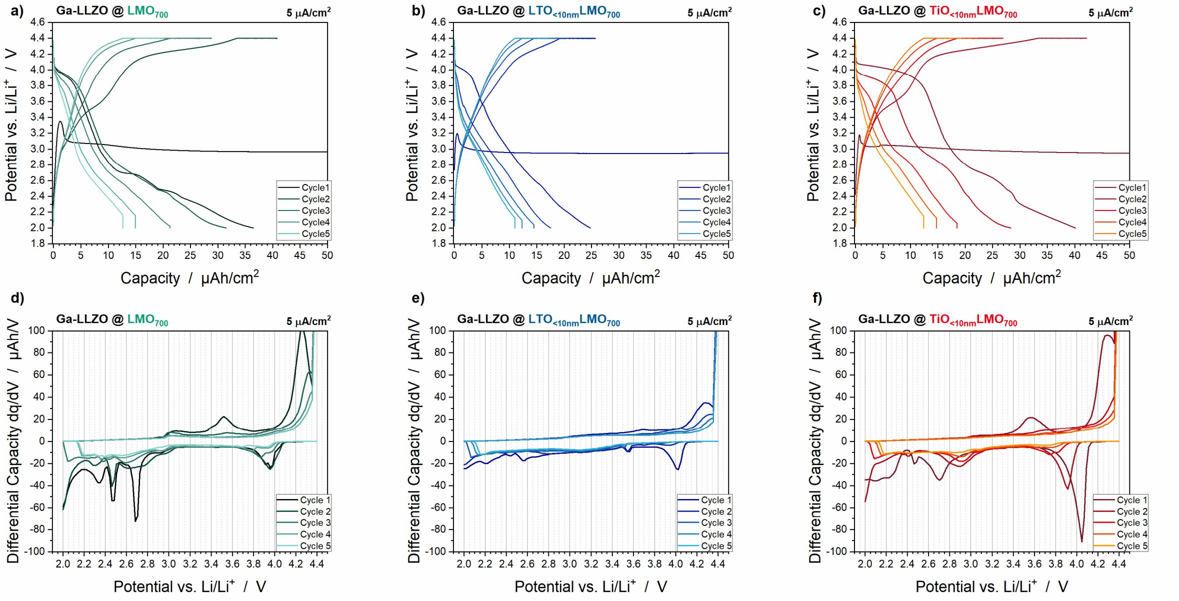

Fig. 7.17 Voltage profiles and corresponding differential capacity plots of the initial five cycles at 5 µA/cm² of the Ga-LLZO|LMO cells **a)** and **d)** without interlayer, **b)** and **e)** with LTO interlayer as well as **c)** and **f)** with TiO_2 interlayer.

Electrochemical Characterization: 2. Cycling Test at 1 µA/cm²

After the formation cycles with 5 µA/cm², galvanostatic cycling at 1 µA/cm² in the potential range of 4.4 V vs. Li/Li$^+$ and 2.0 V vs. Li/Li$^+$ was executed. In addition, the constant voltage step at 4.4 V was abandoned. The measurement had to be stopped for two days after ca. 200 cycles for the maintenance of the battery cycler. The initial cycle for the cycling at 1 µA/cm² is cycle 6.

The discharge capacities of all samples are plotted as a function of the cycle number in **Fig. 7.18a**. The corresponding coulombic efficiencies are shown in **Fig. 7.18b**.

Even with a lower current density of 1 µA/cm², the discharge capacities of all samples continue decreasing. The discharge capacities in cycle 6 are 14.86 µAh/cm² for LMO_{700}, 17.13 µAh/cm² for $LTO_{<10nm}LMO_{700}$ and 15.76 µAh/cm² for $TiO_{<10nm}LMO_{700}$ (**Fig. 7.18a**) with the corresponding coulombic efficiencies of 79.6 %, 86.9 % and 88.8 %, respectively (**Fig. 7.18b**). All samples show a steady decrease in discharge capacity to 7.23 µAh/cm² (LMO_{700}), 8.08 µAh/cm² ($LTO_{<10nm}LMO_{700}$) and 7.51 µAh/cm² ($TiO_{<10nm}LMO_{700}$) until the two days' rest after cycle 208, 209 and 204, respectively. The trends of the coulombic efficiencies differ for the samples. The LMO_{700} sample shows a minimum between cycle 14 and cycle 100, at which the first time 98.0 % is reached. The coulombic efficiency keeps quite constant until cycle 208 (98.3 %). The $LTO_{<10nm}LMO_{700}$ sample reaches a coulombic efficiency of 98.0 % at cycle 35 but it decreases again to 96.6 % in cycle 209. The $TiO_{<10nm}LMO_{700}$ shows for the first time a coulombic efficiency of 98.0 % in cycle 43 and a subsequent increase to 98.5 % in cycle 204.

The cells were stopped at ca. 3.7 V during charge and rest for two days because of a battery cycler maintenance. After the rest, the cells start again with higher discharge capacities than before the rest (**Fig. 7.18a**). The initial discharge capacities are 13.33 µAh/cm² (LMO_{700}, cycle 209), 13.76 µAh/cm² ($LTO_{<10nm}LMO_{700}$, cycle 210) and 13.10 µAh/cm² ($TiO_{<10nm}LMO_{700}$, cycle 205). The trends of the discharge capacities in the subsequent cycles demonstrate a positive effect due to the interlayers. The $LTO_{<10nm}LMO_{700}$ sample shows a lower decrease to 8.87 µAh/cm² (cycle 380) than the $TiO_{<10nm}LMO_{700}$ sample, which decreases to 7.74 µAh/cm² in cycle 393. The LMO_{700} sample exhibits the most significant reduction of the discharge capacity to 6.34 µAh/cm² (cycle 422). The coulombic efficiencies decline after the restart (**Fig. 7.18b**). However, with cycle number, the coulombic efficiencies stabilize and reach values of 98.3 % for LMO_{700}, 97.7 % for $LTO_{<10nm}LMO_{700}$ and 99.0 % for $TiO_{<10nm}LMO_{700}$ in the last cycle of each sample.

The steady decrease of the discharge capacities and the different cycling behavior after rest indicate side reactions during cycling as well as during the rest step. Nonetheless, after the two days rest step, the LTO interlayer sample shows the best performance followed by the TiO_2 interlayer sample.

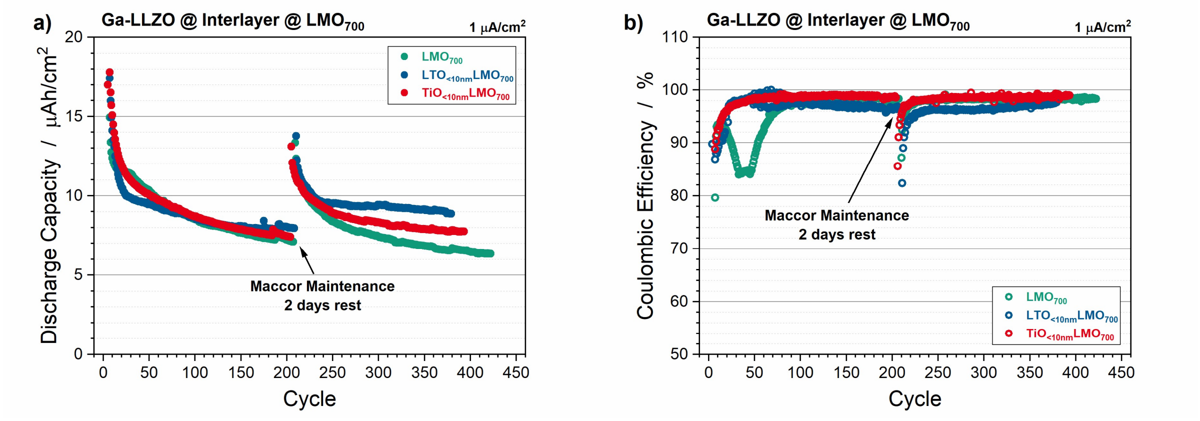

Fig. 7.18 GCPL results of the Ga-LLZO|LMO cells with and without interlayer cycled with 1 µA/cm^2 between 2.0 V and 4.4 V: **a)** Discharge capacities as a function of cycle number and **b)** the corresponding coulombic efficiencies.

The side reactions become more evident in the voltage profiles (**Fig. 7.19 a-c**) and differential capacity plots (**Fig. 7.19 d-f**). As a result of the lower current density of 1 µA/cm^2, more redox peaks can be distinguished in the initial cycle of the second part (cycle 6). For instance, the LMO_{700} charge curve of cycle 6 shows four redox peaks at ca. 2.79 V, 3.05 V, 3.92 V and 4.27 V as well as a broad shoulder between 2.00 V and 2.62 V (**Fig. 7.19d**). These redox peaks decrease with cycle number until a broad peak between 2.94 V and 3.98 V in cycle 100 can be observed, which might be interpreted as two redox peaks. Additionally, a broad peak between 2.00 V and 2.94 V can be assumed (**Fig. 7.19d**, cycle 100), as 1.40 µAh/cm^2 is converted in this potential range (**Fig. 7.19a**). The middle range up to 3.98 V consumes 5.00 µAh/cm^2 and above 4.00 V subsequent 2.23 µAh/cm^2 of charge is converted (**Fig. 7.19a**, cycle 100), which is represented by an increase in the differential capacity plot between 4.00 V and 4.40 V (**Fig. 7.19d**, cycle 100). These courses appear to be stabilized in the following cycles up to cycle 200 except for a further slight decrease in charge capacity. In accordance with the charge potential profiles, the discharge profiles also show a stabilization of the trends with cycle number. In the 6th cycle, a redox peak at 4.04 V and a broad redox region between 3.67 V and 2.00 V with slight maxima at 3.54 V, 3.14 V, 2.84 V, 2.64 V, 2.48 V, 2.20 V and 2.03 V can be observed (**Fig. 7.19d**). In cycle 100, these redox peaks merge and form two broad redox peaks between ca. 4.20 V and 2.91 V as well as between ca. 2.86 V and 2.00 V. The first redox region consumes 3.00 µAh/cm^2 and the second 5.46 µAh/cm^2 (**Fig. 7.19a**, cycle 100). The shape of the first redox region between 4.20 V and 3.91 V indicates two redox peaks. This course remains constant until cycle 200 (**Fig. 7.19d**), just the peak areas decrease because of the reduction of the discharge capacity.

A comparable trend can be observed for the $TiO_{<10nm}LMO_{700}$ sample (**Fig. 7.19c**). In the initial charge step (cycle 6), similar redox peaks can be observed slightly shifted to ca. 2.77 V, 3.25 V, 3.69 V, 4.14 V and 4.27 V followed by a further increase to 4.4 V (**Fig. 7.19f**). Additionally, a broad shoulder between 2.00 V and 2.55 V is detected. In cycle 100, three redox regions are left, which are also similar to the LMO_{700} sample: 2.00 V to 2.79 V consuming 1.18 µAh/cm^2, 2.79 V to 4.00 V consuming 5.08 µAh/cm^2 and 4.00 V to 4.40 V consuming 1.52 µAh/cm^2

(**Fig. 7.19c**). The middle region can also be interpreted as two redox peaks. The trend remains the same in the subsequent cycles. The initial discharge curve (cycle 6) shows many redox potentials and redox reactions over the whole potential range with weak maxima at ca. 3.85 V, 3.52 V, 3.14 V, 2.99 V, 2.70 V, 2.53 V, 2.15 V and 2.00 V (**Fig. 7.19f**). In accordance with the LMO_{700} sample, most of these redox peaks disappear with cycle number so that two broad redox peaks between 4.00 V and 2.90 V as well as between 2.90 V and 2.00 V can be observed in cycle 100. In the first range, 2.85 µAh/cm^2 and in the second range 4.84 µAh/cm^2 are converted (**Fig. 7.19c**). Consequently, the TiO_2 interlayer does not result in an enhancement of the electrochemical performance or shows a change in the electrochemical reactions.

The $LTO_{<10nm}LMO_{700}$ sample exhibits an additional redox reaction but in general the same trend as LMO_{700} and $TiO_{<10nm}LMO_{700}$ (**Fig. 7.19b**). The initial charge curve (**Fig. 7.19e**) shows a broad redox region between 2.00 V and 2.48 V followed by redox peaks at 2.72 V, 3.36 V, 3.96 V, 4.14 V and a further increase up to 4.4 V. In cycle 100, a broad peak between 2.00 V and 2.59 V (0.53 µAh/cm^2) is visible followed by an additional peak at 2.87 V (1.03 µAh/cm^2). A broad peak between 2.92 V and 4.00 V (5.39 µAh/cm^2) is observable, which can be interpreted as two peaks and is comparable with the LMO_{700} and $TiO_{<10nm}LMO_{700}$ samples. An additional peak can be detected at 4.18 V (1.13 µAh/cm^2). In the following, 0.62 µAh/cm^2 is consumed between 4.27 V and 4.40 V. This trend can be observed in the subsequent cycles. The initial discharge curve (cycle 6) shows redox reactions over the whole potential range with maxima at 3.85 V, 3.59 V, 3.05 V, 2.81 V, 2.53 V, 2.16 V and 2.00 V (**Fig. 7.19e**). In cycle 100, two redox regions can be seen between 4.00 V and 2.86 V (3.05 µAh/cm^2) and between 2.86 V and 2.00 V (5.46 µAh/cm^2). This trend can also be observed in the subsequent cycles.

Consequently, the Ga-LLZO samples with and without interlayer show many irreversible redox reactions during charge and discharge in the first 100 cycles. Afterward, two redox regions are left between 2.00 V and ca. 2.90 V as well as between ca. 2.90 V and 4.00 V in both the discharge and charge steps. Charge is additionally converted above 4.00 V in the charge step. The $LTO_{<10nm}LMO_{700}$ sample shows additional peaks during charge at 2.87 V and 4.18 V. The voltage profiles suggest that the main electrochemical processes are most unlikely related to the LMO redox reaction at 3.95 V and 4.10 V. Since all samples show the same trend, an impact of the interlayer material on the electrochemical reactions cannot be deduced. Further interpretation is given in the discussion section below.

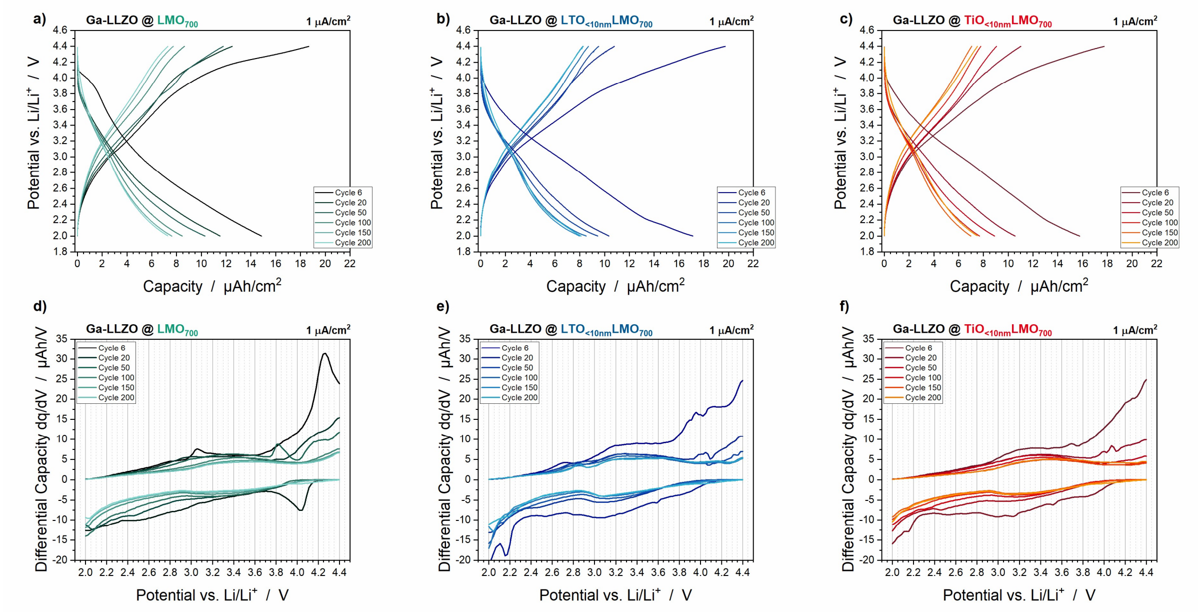

Fig. 7.19 Voltage profiles and corresponding differential capacity plots of the cycles 6 - 200 at 1 µA/cm² of the Ga-LLZO|LMO cells **a)** and **d)** without interlayer, **b) and e)** with LTO interlayer as well as **c)** and **f)** with TiO_2 interlayer.

The galvanostatic cycling had to be stopped for maintenance of the battery cycler for two days. This was done in cycle 208 for LMO_{700}, in cycle 209 for $LTO_{<10nm}LMO_{700}$ and in cycle 204 for $TiO_{<10nm}LMO_{700}$ at ca. 3.7 V during charge. The restart of the galvanostatic cycling was executed with a charge step. As discussed before, the discharge capacities have higher values after restart (**Fig. 7.18a**) and the coulombic efficiencies drop (**Fig. 7.18**b). The voltage profiles of the last cycles before the rest and the first cycles after the restart are shown in **Fig. 7.20 a-c**. The open circuit voltage of all samples drops to ca. 1.20 V, which indicates self-discharge during the rest step. The first charge curves exhibit charge capacities of 41.66 µAh/cm² for LMO_{700}, 37.30 µAh/cm² for $LTO_{<10nm}LMO_{700}$ and 39.79 µAh/cm² for $TiO_{<10nm}LMO_{700}$. The same four redox plateaus can be observed for all samples at ca. 2.70 V, ca. 3.21 V, ca. 3.60 V and ca. 4.27 V. The first discharge curves after the rest step show that the redox plateaus rapidly stabilize. The curves show higher discharge capacities than before the rest step but the same redox potentials for the electrochemical reactions. These redox plateaus do not change until the last cycles (**Fig. 7.20 d-f**).

The LMO_{700} sample shows the most significant decrease in discharge capacity to 6.34 µAh/cm² in cycle 422 (**Fig. 7.20d**). However, the redox potentials are constant and just decrease in the peak area. In cycle 350, two broad peaks between 2.00 V and 2.99 V (1.07 µAh/cm²) as well as 2.99 V and 4.04 V (3.99 µAh/cm²) can be observed during charge (**Fig. 7.20g**). This is similar to the potential ranges detected in cycle 100 (**Fig. 7.19d**). Additionally, the ratios of the converted charge of these reactions are comparable. Above 4.04 V subsequent 1.89 µAh/cm² are consumed (**Fig. 7.20d**). The discharge curve in cycle 350 is also similar to the discharge curve in cycle 100. A charge of 2.29 µAh/cm² is converted between 4.18 V and 2.90 V. The second redox range is between 2.90 V and 2.00 V with 4.55 µAh/cm².

The $TiO_{<10nm}LMO_{700}$ sample exhibits a reduction in discharge capacity to 7.74 µAh/cm² in cycle 393 (**Fig. 7.20f**). The redox potentials of the charge and discharge profiles in cycle 350 (**Fig. 7.20i**) are also similar to the profiles in cycle 100 (**Fig. 7.19f**). During charge of cycle 350, two broad peaks between 2.00 V and 2.90 V (0.91 µAh/cm²) as well as 2.90 V and 4.4 V (7.11 µAh/cm²) can be observed (**Fig. 7.20i**). In the discharge of cycle 350, two redox regions between 4.22 V and 2.92 V (2.92 µAh/cm²) as well as 2.90 V and 2.00 V (5.00 µAh/cm²) can be seen (**Fig. 7.20i**). In contrast to cycle 100, an additional peak beneath 2.28 V appears, during which 2.19 µAh/cm² of the 5.00 µAh/cm² is converted. This redox peak was also present in cycle 6 but vanished with cycle number most likely due to a shift of the redox potential beneath 2.00 V due to a higher overpotential for this reaction. Thus, the overpotential might be reduced by processes during the rest step.

The lowest reduction in discharge capacity can be observed for the $LTO_{<10nm}LMO_{700}$ sample (**Fig. 7.20e**). In the last cycle (cycle 380), a discharge capacity of 8.87 µAh/cm² can be obtained. In addition, the differential capacity plots show the lowest changes with cycle number (**Fig. 7.20h**). The charge curve of cycle 350 exhibits a broad peak between 2.00 V and 2.60 V (0.54 µAh/cm²) followed by a sharp peak at 2.86 V (1.25 µAh/cm²). Afterward, a broad peak between 3.03 V and 4.00 V (5.41 µAh/cm²) as well as a peak at 4.18 V (1.52 µAh/cm²) can be observed. Additional 0.69 µAh/cm² are converted above 4.29 V (**Fig. 7.20e**). In the discharge curve of cycle 350, two broad redox regions between 4.22 V and 2.86 V (3.33 µAh/cm²) and 2.86 V and 2.00 V (5.75 µAh/cm²) can be seen (**Fig. 7.20h**). The lower potential region includes a sharp peak at 2.28 V, which consumes 2.61 µAh/cm² of the 5.75 µAh/cm². These voltage profiles are similar to the voltage profiles of cycle 100 (**Fig. 7.19**b**Fig. 7.20**). They solely differ in the shape of the redox peak at 2.86 V during charge, which is more pronounced in cycle 350, as well as the additional peak at 2.28 V during discharge of cycle 350 (**Fig. 7.20h**). The latter was also detected for the $TiO_{<10nm}LMO_{700}$ sample (**Fig. 7.20i**) after the two days rest step. It can be explained by a decrease in the overpotential of this reaction in both cases.

In conclusion, self-discharge seems to appear during the rest of the two days, as the open circuit voltage drop to ca. 1.20 V for all samples (**Fig. 7.20 a-c**). The first charge curves have capacities of about 38 µAh/cm² and exhibit four redox plateaus for all samples. In the following cycles, the voltage profiles stabilize rapidly and just show a decrease of the peak areas in the differential capacity plots depending on the reduction of the capacities with cycle number (**Fig. 7.20 g-i**). The $LTO_{<10nm}LMO_{700}$ sample shows the lowest reduction of the discharge capacity followed by the $TiO_{<10nm}LMO_{700}$ sample and finally the LMO_{700} sample (**Fig. 7.20 d-f**). The peak positions after the two days' rest are similar to the peak positions before the rest. Only the additional peak at ca. 2.28 V for $LTO_{<10nm}LMO_{700}$ and beneath 2.28 V for $TiO_{<10nm}LMO_{700}$ differ from the voltage profiles before the rest step. This is most likely due to a reduction of the overpotential of this redox reaction after the rest step.

In comparison with the LMO_{700} samples with and without interlayer tested in liquid electrolyte and LIPON full cells, the voltage profiles of the Ga-LLZO cells show a completely different picture. The redox reactions obtained in the Ga-LLZO cells cannot be related to the LMO redox reactions at 3.95 V and 4.10 V vs. Li/Li$^+$, so the electrochemical reactions of the Ga-LLZO SSE are most likely, which will be discussed in the next section.

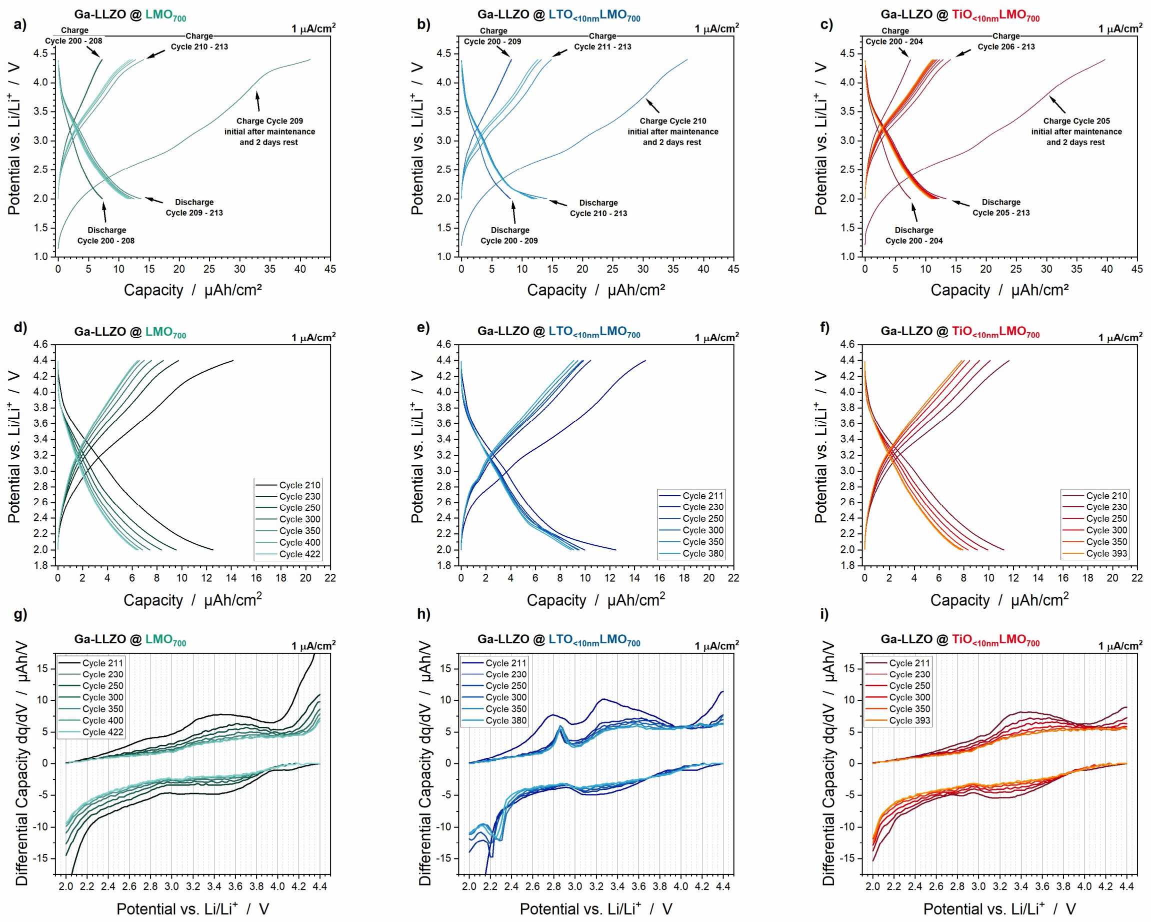

Fig. 7.20 Voltage profiles of the last cycles before and the first cycles after the maintenance and two days' rest of Ga-LLZO|LMO cells **a)** without interlayer, **b)** with LTO interlayer and **c)** with TiO_2 interlayer.
Voltage profiles and corresponding differential capacity plots of the cycles 210 until last cycle at 1 µA/cm² of the Ga-LLZO|LMO cells **d)** and **g)** without interlayer, **e)** and **h)** with LTO interlayer as well as **f)** and **i)** with TiO_2 interlayer.

Discussion of Electrochemical Results

The galvanostatic cycling tests of the Ga-LLZO|LMO samples without and with LTO or TiO_2 interlayer show just polarization effects when cycled between 3.1 V and 4.4 V vs. Li/Li^+, even with a low current density of 1 µA/cm² (**Fig. 7.16a**). Even though crystalline LMO and Ga-LLZO without $La_2Zr_2O_7$ impurity phases could be detected in the GIXRD (**Fig. 7.13**), the charge transfer resistances seem to be quite high so that a high overpotential for the Li^+ extraction reaction at ca. 4.00 V during charge might shift the reaction above 4.4 V. However, the high initial charge capacity of > 200 µAh/cm² indicates a high degree of side reactions, particularly, at ca. 3 V (**Fig. 7.16b**). By widening the potential window to a lower potential limit of 2.0 V vs. Li/Li^+, the Ga-LLZO cells can be cycled and redox plateaus can be observed during charge and discharge, especially, in the potential range around ca. 3 V (**Fig. 7.17 d-f**, **Fig. 7.19 d-f** and **Fig. 7.20 g-i**). Most of these side reactions are irreversible, which results in a low coulombic efficiency at the beginning (**Fig. 7.18b**) and a capacity fade with cycle number (**Fig. 7.18a**). However, the voltage profiles stabilize (**Fig. 7.19 a-c**) and the coulombic efficiencies increase up to 98 % in cycle 100 for LMO_{700}, in cycle 35 for $LTO_{<10nm}LMO_{700}$ and in cycle 43 for $TiO_{<10nm}LMO_{700}$ (**Fig. 7.18b**). Although the two days' rest due to maintenance of the battery cycler causes self-discharge, the voltage profiles afterward are the same as before the rest step, except for higher capacities and a lower capacity fade for the $LTO_{<10nm}LMO_{700}$ sample. In addition, the differential capacity plots of all three samples are comparable (**Fig. 7.20 g-i**). The determined voltage ranges incl. the converted charges of cycle 350 are summarized in **Table 7.7**. They can be distinguished into three ranges, whereby the second range most likely includes two redox peaks (**Fig. 7.20 g-i**). A discussion about the probable reaction mechanisms and a comparison with the literature are done in the following. However, since post-mortem analyses could not be done in this study, the discussion is very hypothetical but might give a theoretical basis for further studies.

Firstly, the intrinsic electrochemical stability of LLZO needs to be considered. Cyclic voltammetry measurements are reported, which show electrochemical windows of LLZO up to 6 V vs. Li/Li^+.[221,222] However, these measurements were performed with high scan rates of > 1 mV/s, which might cause a shift of the reaction potential to higher voltages in case of slow reaction kinetics. Han et al.[223] executed cyclic voltammetry measurements with scan rates of 0.01 mV/s and could demonstrate an oxidation onset at ca. 4.0 V vs. Li/Li^+. The same group, Zhu et al.[224], published a principle study based on the thermodynamical calculations of potential onsets, phase equilibria and decomposition energies. The authors could calculate an intrinsic LLZO decomposition starting at 2.91 V with a low decomposition energy of - 10 meV/atom (**Table 7.6**). The low decomposition energy explains the discrepancy in the experimental results, as a high overpotential is expected due to slow reaction kinetics.[223,224] The phase equilibria, to which the LLZO tends, consists of Li_2O_2, La_2O_3 and $Li_6Zr_2O_7$. At higher potentials (5 V), even oxygen release and the formation of $La_2Zr_2O_7$ are possible (**Table 7.6**). The decomposition energy is about - 530 meV/atom, thus, a very favorable process, which would explain

$La_2Zr_2O_7$ as the main impurity phase in the LLZO synthesis and under electrochemical operation.[78,167,186,225,226]

In addition to the intrinsic stability, Zhu et al.[224] calculated the chemical and electrochemical stability of LLZO in combination with $LiCoO_2$ (LCO). Since no publications about the combination with the spinel LMO have been published so far, the computational results of Zhu et al.[224] might give some findings, which probably can be transferred to the combination of LLZO and LMO. For instance, the chemical phase equilibrium of LLZO and LCO indicates the tendency of the overlithiation of the active material. It consists of La_2O_3, $Li_6Zr_2O_7$ and Li_5CoO_4. Thus, the Li/Co ratios are 5 for Li_5CoO_4 and 1 for $LiCoO_2$. The overlithiation has also been shown in a computational study of Miara et al.[131], who calculated a phase equilibrium of La_2O_3, $La_2Zr_2O_7$ and Li_2CoO_3, thus a Li/Co ratio of 2. The authors additionally demonstrated the phase equilibrium of LLZO and the layered $LiMnO_2$, which consists of La_2O_3, $La_2Zr_2O_7$ and Li_2MnO_3. Consequently, the calculated phase equilibria in both studies indicate that the decomposition of LLZO is supported by the possibility of Li^+ release.

This is also depicted in the calculations of the electrochemical oxidation onset for the LLZO|LCO interface since no mixed phases between LLZO and LCO can be found in the phase equilibria up to 3.99 V (**Table 7.6**). Consequently, the changes in the crystalline structures are based on the diffusion of Li^+. Here, it is important to mention, that the electrochemical calculations consider an electrochemically stable interface at the Li/Li^+ reservoir on the anode side.[224]

The first calculated potential range between 2.00 V and 2.57 V is based on the chemical phase equilibrium (**Table 7.6**). The further oxidation (similar to charge processes) between 2.57 V and 2.81 V of the active material goes along with the delithiation of the $LiCoO_2$ so that the Li/Co ratio of the $Li_7Co_5O_{12}$ is 1.4. This is followed by the delithiation of $Li_6Zr_2O_7$ to $La_2Zr_2O_7$ up to 3.50 V. Afterwards, the phase equilibrium between 3.50 V and 3.99 V shows the delithiated state of the layered $Li_{0.5}CoO_2$ in addition to oxygen release. Above 3.99 V, further O_2 formation and the first mixed phase $LaCoO_2$ can be determined (**Table 7.6**).

In conclusion, the computational study of Zhu et al.[224] showed that the LLZO material tends to release its Li to reach a thermodynamical equilibrium. In combination with a Li incorporating material like the $LiCoO_2$ active material, the decomposition leads to an overlithiation to Li_5CoO_4 or $Li_7Co_5O_{12}$ and the formation of La_2O_3, $Li_6Zr_2O_7$ or $La_2Zr_2O_7$. Consequently, the calculated potential onset of 2.00 V is lower than the intrinsic decomposition onset at 2.91 V. Nevertheless, the oxidation states of Co in Li_5CoO_4 and $Li_7Co_5O_{12}$ are 3+ and 4+. Thus, it can be assumed that a lithiation and delithiation can take place, which indicates the reversibility and cycle-ability of the active material in the calculated potential ranges. However, the formation of the non-conductive La_2O_3, $La_2Zr_2O_7$ and $LaCoO_3$ would result in a Li-ion blocking layer with ongoing decomposition causing a high charge transfer resistance, which has been reported in experimental studies.[186,220]

Table 7.6 Calculated potential onset and corresponding calculated phase equilibria for LLZO as well as LLZO in combination with $LiCoO_2$. Reprinted with permission from Zhu et al.[224] (2016). © 2016 The Royal Society of Chemistry.

	Calculated Potential Onset vs. Li/Li$^+$	**Calculated Phase Equilibria**	**Calculated Decomposition Energy meV per atom**
Intrinsic Electrochemical Stability of LLZO			
	2.91 V	Li_2O_2, La_2O_3, $Li_6Zr_2O_7$	- 10
	5.00 V	O_2, La_2O_3, $La_2Zr_2O_7$	- 530
Electrochemical Stability of LLZO | $LiCoO_2$ interface			
	2.00 V - 2.57 V	La_2O_3, $Li_6Zr_2O_7$, Li_5CoO_4	- 9
	2.57 V - 2.81 V	La_2O_3, $Li_6Zr_2O_7$, $Li_7Co_5O_{12}$ ($Li_{2.3}Co_{1.7}O_4$)	- 13
	2.81 V - 3.50 V	La_2O_3, $La_2Zr_2O_7$, $Li_7Co_5O_{12}$ ($Li_{2.3}Co_{1.7}O_4$)	- 72
	3.50 V - 3.99 V	La_2O_3, $La_2Zr_2O_7$, $Li_{0.5}CoO_2$, O_2	- 137
	3.99 V - 5.00 V	$LaCoO_3$, $La_2Zr_2O_7$, O_2	- 656

Table 7.7 Redox regions obtained from differential capacity plots (**Fig. 7.20 g-i**) and corresponding converted capacities (**Fig. 7.20 d-f**) of cycle 350 for all samples.

	Potential Range 1	**Potential Range 2 Probably Two Peaks**	**Potential Range 3**
LMO_{700}			
Charge	2.00 V - 2.99 V (1.07 µAh/cm^2)	2.99 V - 4.04 V (3.99 µAh/cm^2)	> 4.04 V (1.89 µAh/cm^2)
Discharge	2.00 V - 2.90 V (4.55 µAh/cm^2)	2.90 V - 4.18 V (2.29 µAh/cm^2)	
$LTO_{<10nm}LMO_{700}$			
Charge	2.00 V - 2.66 V (0.54 µAh/cm^2) Peak at 2.86 V (1.25 µAh/cm^2)	3.03 V - 4.00 V (5.41 µAh/cm^2)	Peak at 4.18 V (1.52 µAh/cm^2) > 4.29 V (0.69 µAh/cm^2)
Discharge	2.00 V - 2.86 V (5.75 µAh/cm^2) incl. peak at 2.28 V (2.61 µAh/cm^2)	2.86 V - 4.22 V (3.33 µAh/cm^2)	
$TiO_{<10nm}LMO_{700}$			
Charge	2.00 V - 2.90 V (0.91 µAh/cm^2)	2.90 V - 4.40 V (7.11 µAh/cm^2)	
Discharge	2.00 - 2.90 V (5.00 µAh/cm^2) incl. shoulder < 2.28 V (2.19 µAh/cm^2)	2.92 V - 4.22 V (2.92 µAh/cm^2)	

Comparing the results of the computational study of Zhu et al.[223] (**Table 7.6**) and the experimental results of the Ga-LLZO|LMO cells of this study (**Table 7.7**), it becomes evident that the various potential ranges are very similar. Thus, the possibility of overlithiation of the $LiMn_2O_4$ spinel structure needs to be considered. The formation of $Li_{1+x}Mn_2O_4$ is well known in literature accompanied by a crystal structure change to a rock salt phase for $0 < x < 1$.[23,24] A further lithiation to $Li_{1+x}Mn_2O_4$ with $1 < x < 3$ is also possible, which results in a change to a layered structure.[23] The open circuit voltages for both species are reported as 3.0 V and 1.2 V vs. Li/Li^+, respectively.[23,227] The formation of $Li_7Mn_5O_{12}$ (similar to $Li_7Co_5O_{12}$, **Table 7.6**) is also reported by Thackerey et al.[23], which can be written as $Li_{2.3}Mn_{1.7}O_4$. The tendency of the formation of $Li_{2+\delta}Mn_{2-\delta}O_4$ ($0 < \delta < 0.33$) is supported by the Jahn-Teller distortion of the Mn^{3+} (**Chapter 2.1**: Cathode Active Materials). It has been reported, that by discharging $LiMn_2O_4$ to 2.0 V vs. Li/Li+, it is electrochemically possible to lithiate the $LiMn_2O_4$ to $Li_2Mn_2O_4$. This reaction is reversible and its average potential is about 3 V vs. Li/Li^+.[23,24]

Comparing the reported knowledge with the results of this study, indications of overlithiation after crystallization of the Ga-LLZO on top of coated and uncoated LMO can be found. The formation of the Mn_2O_3 observed via GIXRD (**Fig. 7.13**) suggests the formation of $Li_{2+\delta}Mn_{2-\delta}O_4$ ($0 < \delta < 0.33$). The only LMO reflection (hkl 111 at ca. 18.72°) cannot be used to distinguish $LiMn_2O_4$ from $Li_2Mn_2O_4$ since the positions of their hkl 111 reflections are quite similar and its variation is within the expected error of the used measurement set-up.[23] Thackeray et al.[23] also reported the position of the hkl 311 reflection of $Li_2Mn_2O_4$ at ca. 32.98° ($Li_2Mn_2O_4$, ICSD 380299), so that this reflection superposes with the Mn_2O_3 reflection at 32.92° within the expected error range (**Fig. 7.13**). Nevertheless, the Li^- and GaO^- signal trends of the ToF-SIMS measurements suggested a concentration gradient from $Li_{6.25}Ga_{0.25}La_3Zr_2O_{12}$ at the surface to $Li_7La_3Zr_2O_{12}$ at the interface to LMO (**Fig. 7.15 a-c**). Additionally, the signal of Li^- is highest in the LMO layer. Consequently, the increasing trend of the Li^- signal from the LLZO surface into the LMO layer supports the overlithiation argument. Therefore, it can be assumed that overlithiated $Li_2Mn_2O_4$ and $Li_{2.3}Mn_{1.7}O_4$ exist after crystallization. This would explain the significant reaction at ca. 3.0 V in the initial charge step (delithiation), which consumes > 200 µAh/cm² of charge (**Fig. 7.16b**). The high charge capacity cannot be solely explained by the $Li_2Mn_2O_4$ delithiation so that a reaction of Ga-LLZO to $Li_6Zr_2O_7$, $La_2Zr_2O_7$ or La_2O_3 (**Table 7.6**) is also suggested. Additional phase transitions cannot be excluded, particularly, since the differential capacity plots of the first couple of cycles show many redox reactions during charge and discharge until a stable trend for the voltage profiles occurs (**Fig. 7.17 d-f**).

These stable trends can be distinguished in three potential ranges (**Table 7.7**), which are comparable and independent from the interlayer material. The first potential range during charge between 2.00 V and ca. 2.99 V is most likely a polarization effect due to the formation of the electrochemical double-layer or space-charge layer at the interface Ga-LLZO|LMO, as a low amount of charge is converted. The second potential range during charge between 3.00 V and 4.00 V shows the highest charge conversion for all samples. The comparison with the computational studies of Zhu et al.[224] (**Table 7.6**) and the results of Thackeray et al.[23] indicates that in this range the delithiation of overlithiated $Li_2Mn_2O_4$ and $Li_{2.3}Mn_{1.7}O_4$ takes place in addition to the formation of $Li_6Zr_2O_7$ and $La_2Zr_2O_7$. The shape of the curve also suggests two redox peaks in this potential range (**Fig. 7.20 g-i**), which accurately fits with the computational results (**Table 7.6**). Above 4.0 V, the most reasonable reaction might be the further decomposition of Ga-LLZO to $La_2Zr_2O_7$ and La_2O_3 as well as the O_2 formation. A reaction of LLZO with LMO or the further delithiation of $LiMn_2O_4$ is also thinkable. Considering the reversibility of these reactions and the correlation of the potential ranges during charge with them during discharge, it appears obvious that the second potential ranges of charge and discharge belong together. The discharge capacity is lower than the charge capacity, which can be explained by the irreversible formation of $La_2Zr_2O_7$ and La_2O_3 besides the reversible lithiation of the LMO active material, as the second discharge potential range might fit with the delithiation of spinel LMO. However, the potential range of the overlithiation of $Li_{1+x}Mn_2O_4$ is below 3 V and a high amount of charge is convert in this range during discharge (**Table 7.7**).[23,24] That indicates that further phase conversions take place during charge and discharge in addition to the listed computational results (**Table 7.6**) since an overlithiation of $Li_{1+x}Mn_2O_4$ is not expected in the second potential range during discharge. Thus, the reactions of the second charge potential range are most likely a combination of the first and second discharge potential ranges.

In conclusion, the material system appears to be very complex due to the many possibilities of LMO crystal phases and lithiation states.[23] Its chemical stability after cycling is also not given, since the two days' rest results in self-discharge (**Fig. 7.20 a-c**), which indicates elemental diffusion processes during rest. Interestingly, the open circuit voltage after rest is ca. 1.2 V, which is in accordance with the open circuit potential of $Li_{1+x}Mn_2O_4$ with $1 < x < 3$.[23,227] That might suggest a tendency of Li diffusion into the LMO layer during rest. The complexity is furthermore increased by the interlayer materials since the $LTO_{<10nm}LMO_{700}$ sample shows additional sharp peaks in the first charge and discharge potential ranges (**Table 7.7**). These peaks cannot be reasonably associated with reactions. Even though the interlayer samples show a more stable trend and higher capacities than the LMO_{700} sample (**Fig. 7.18a**), the chemical instability during rest as well as the evident continuous formation of electrical isolating impurity phases such as $La_2Zr_2O_7$ or La_2O_3 makes the cell unusable for battery applications so far. By considering the overlithiation of the LMO active material during the crystallization process, it is probably possible to design a cell on basis of Ga-LLZO and overlithiated $Li_2Mn_2O_4$, which operates at 3 V vs. Li/Li^+. For instance, the preparation of a $Li_2Mn_2O_4$ thin-layer as a basis for the Ga-LLZO deposition should be considered. Additionally, LTO should be used as an interlayer to prevent Ga interdiffusion into the LMO layer. For a better understanding of the phase changes, in situ XRD measurements during galvanostatic cycling should be performed. Post-mortem analyses via GIXRD, ToF-SIMS or a depth profile XPS could also give more information about the changes in crystal structure and oxidation states of the Ga-LLZO and LMO during cycling.

7.6 Summary and Conclusion of the Investigation into the SSE/Cathode Interface

This study investigated the general functionality of sol-gel-based cathode LMO thin-films in LIPON TF-SSB cells and the impact of TiO_2 and LTO interlayers on the cell performance. Secondly, these coated LMO thin-films were used in Ga-LLZO TF-SSBs in order to inhibit the elemental diffusion during the crystallization of Ga-LLZO on top of the coated and uncoated LMO cathode thin-films.

In the beginning, coated and uncoated LMO double-layer thin-films were tested in liquid electrolyte cells as reference cells to the TF-SSB cells. However, liquid electrolyte decomposition and Mn dissolution need to be considered, particularly, in long-term cycling tests over 1,000 cycles (**Fig. 7.7**). It could be shown that LTO has excellent protection characteristics against these side effects, which results in significant lower capacity fade (just 2 % over 1,000 cycles for $LTO_{<10nm}LMO_{700}$, **Fig. 7.7b**), thus, longer cycle lives for LTO coated LMO than TiO_2 coated (26 % capacity fade, **Fig. 7.7b**) and pure LMO_{700} thin-films (18 % capacity fade, **Fig. 7.7b**). A significant impact on the cycling-ability has the crystallization temperature of LMO. The samples annealed at 600 °C show significantly poorer cycling behavior (**Fig. 7.7a**) than the samples annealed at 700 °C (**Fig. 7.7b**), which can be correlated with the crystallinity of LMO. On the one hand, the amorphous LMO phase might tend to a higher Mn dissolution. On the other hand, higher amounts of carbonate and hydroxide residues from the sol-gel solution might remain after the crystallization at 600 °C, which enhances the electrolyte decomposition. A further effect of the crystallinity can be seen for the rate capabilities (**Table 7.2**). The samples annealed at 700 °C show poorer rate capabilities than the samples annealed at 600 °C. This indicates that the electronic and ionic resistance within the LMO layer increases with the crystallinity of the LMO thin-film.

Effects of the carbonate and hydroxide residues as well as of the higher ionic and electronic resistances of the LMO_{700} samples can also be observed for the LIPON TF-SSB cells. The LMO_{700} samples with and without interlayers showed polarization effects even at a current density of 10 $\mu A/cm^2$ so that no capacity could be obtained (**Fig. 7.9b**). The LMO_{600} samples could be cycled and showed higher capacities than the liquid electrolyte cells (**Fig. 7.9a**). Furthermore, the cycle lives, defined as the cycle number where 80 % of the initial discharge is reached, of the LIPON TF-SSB cells are below 220 cycles (**Table 7.5**), which is not in accordance with the literature, where LIPON|LMNO cells with cycle lives of over 10,000 cycles are reported.[52] Since the reported cells are prepared and tested in inert gas atmosphere without exposure to air during and between every single preparation step, it is evident that the sol-gel-based preparation and crystallization in air atmosphere have an impact on the cycling performance. The carbonate and hydroxide residues might react with the LIPON SEE during cycling, which results in a continuous formation of a blocking layer at the interface of LIPON and LMO. Conclusively, sol-gel-based active materials are not sufficient for TF-SSBs unless a purification step after crystallization is inserted. This is highly recommended for further studies.

Nevertheless, the rate capability tests of the LIPON|LMO_{600} TF-SSB cells with and without LTO and TiO_2 interlayers give information about the impact of the interlayer thickness and interlayer material. The pure LMO_{600} and the $LTO_{<10nm}LMO_{600}$ samples show the best rate capability followed by the thicker LTO interlayer (ca. 20nm) sample and the thin TiO_2 (< 10 nm) interlayer sample (**Fig. 7.9e**). No capacity could be obtained for the TiO_2 interlayer sample with an interlayer thickness of ca. 20 nm. Consequently, the thin LTO interlayer is most feasible for incorporation in TF-SSBs.

The target system was the TF-SSB based on Ga-LLZO and LMO. Since Ga-LLZO was crystallized at 650 °C on top of LMO, the functionality of TiO_2 and LTO interlayer (< 10 nm) as interdiffusion barrier should be tested. It could be shown that the crystallization temperature of LMO has also an impact on the crystallization behavior of Ga-LLZO (**Fig. 7.12**). The most common impurity phase $La_2Zr_2O_7$ could be observed when Ga-LLZO was crystallized on LMO_{600}, which was crystallized at 600 °C. Using LMO_{700} as substrate results in no formation of $La_2Zr_2O_7$ but the formation of Mn_2O_3 for all samples. No Ga-LLZO reflections could be observed for the pure LMO_{700} sample (**Fig. 7.12a**). However, the samples with TiO_2 and LTO interlayer show crystalline Ga-LLZO (**Fig. 7.13**). Additionally, both interlayers suppress Ga diffusion into LMO, which could be observed for the pure LMO samples (**Fig. 7.15**). However, Mn diffusion into Ga-LLZO could not be inhibited. Additionally, a Li concentration gradient could be observed, which starts with a low amount of Li at the surface of Ga-LLZO and increases to the interface to LMO. The highest amount of Li can be detected in the LMO layer. This is accompanied by the exact opposite trend for Ga, which compensates for the Li depletion at the Ga-LLZO surface (**Fig. 7.15**). This leads to the main finding of this study: the overlithiation of the LMO layer. The galvanostatic cycling gives many indications for this overlithiation. Firstly, the high initial charge capacity with a significant plateau at ca. 3.0 V (**Fig. 7.16b**), which is the redox potential of the delithiation of $Li_2Mn_2O_4$. Secondly, the cells cannot be cycled between 3.1 V and 4.4 V vs. Li/Li^+. The cells are activated below 3.0 V by discharging to 2.0 V, which indicates the lithiation of $LiMn_2O_4$ to $Li_2Mn_2O_4$. The existence of Mn_2O_3 indicates also the formation of $Li_{2+\delta}Mn_{2-\delta}O_4$ ($0 < \delta < 0.33$), which is induced by the Jahn-Teller distortion of Mn^{3+}. The hypothesis of overlithiation is also supported by the computational calculations of the phase equilibria of LLZO done by Zhu et al.[224] (**Table 7.6**). The authors could show that the tendency of LLZO decomposition is supported by the possibility of Li release. Since LMO has many overlithiated states, it can be assumed that the overlithiation takes place during the crystallization process, so that the potential ranges of redox reactions are most likely associated with the lithiation and delithiation of $Li_{1+x}Mn_2O_4$ (**Table 7.7**). There are no indications for the redox reaction of spinel LMO at 3.95 V and 4.1 V vs. Li/Li^+. However, the first cycles of the samples with and without interlayers show many redox plateaus and peaks during charge and discharge (**Fig. 7.17 d-f**), which indicates a very complex electrochemical system and many side reactions. Most of them are irreversible. These redox plateaus stabilize with cycle number and three potential ranges could be identified (**Table 7.7**), which could partly be associated with reactions reported in literature (**Table 7.6**). It could be shown that Ga-LLZO decomposes with cycle number, which causes the formation of non-conductive $La_2Zr_2O_7$, La_2O_3 and also the formation of O_2 is likely. Consequently, all cells show a capacity fade with cycle number (**Fig. 7.18a**). However, LTO shows the lowest capacity fade, followed by TiO_2. The pure LMO cells showed the poorest cycle stability. Even though the exact reaction mechanisms cannot be deduced from the available data, it is evident that the overlithiation of LMO during the crystallization process has the most significant impact on the electrochemical behavior. In addition, the further decomposition of Ga-LLZO during cycling is the main loss mechanism. A more precise interpretation requires further tests, particularly, post-mortem GIXRD or XPS measurements. At the current state, these Ga-LLZO TF-SSBs are not sufficient for battery application.

8 Summary and Conclusion of Ph.D. Thesis and Outlook

8.1 English Summary, Conclusion and Outlook

Summary and Conclusion

This Ph.D. thesis has addressed several main issues in current ASSB research within four studies. Ceramic ASSBs are meant to enable the implementation of Li-metal anodes and high voltage cathode materials, which would increase energy density, power density, life time as well as safety aspects in comparison with commercially available liquid electrolyte LiBs. In this thesis, several scientific questions arising on the cathode side of ASSBs have been focused on. With respect to the target system of a ternary composite bulk cathode consisting of ceramic active material, ceramic SSE and an electrically conductive component, studies about the thermal stabilities of these components and their impact on the electrochemical performance have been conducted. As described in **Chapter 2.2**, particulate bulk cathode composites have to fulfill electrochemical, chemical, mechanical and structural requirements in order to compete with commercial LiBs. Particularly, the production process requires high-temperature sintering to obtain firmly bonded contacts in order to maximize the electrochemically active area, charge transfer and ionic conduction. However, interdiffusion, intermixing and decomposition of the initial components during sintering result in low-performing ASSBs so far. The formation of non-conductive or electrochemically inactive mixed phases decreases significantly the cell performance.

In this context, these side reactions during high-temperature treatment have been investigated in order to gain a better understanding of these mechanisms and to enable a better controlling of the manufacturing process as well as to simplify the choice of material combinations for future ASSB applications. The thesis is structured in four parts. The first two parts deal with the thermal stability of the ceramic SSE LATP in combination with various active materials and with the validation of a probable improvement of the sintering process due to liquid phase sintering of LATP by adding the sintering additive Li_3PO_4. In the third and fourth parts, the impact of interdiffusion, intermixing and decomposition on the electrochemical performance of TF-SSBs based on the active material LMO and the ceramic SSE Ga-LLZO has been investigated.

The investigation into the thermal stabilities of LATP in combination with Mn-based active materials of each structural class (olivine, layered and spinel) revealed the impact of the structure type and the associated oxidation states of Mn on the tendency for intermixing and decomposition (**Chapter 4**). The possibility of the reduction of Mn^{3+} and Mn^{4+} in the spinel LMO-s to lower valent Mn^{2+} species such as Mn_3O_4, $MnTiO_3$ or LMP along with the oxidation of O^{2-}, which causes O_2 outgassing, are the main driving forces for the decomposition of the initial components and the formation of mixed phases with lower Gibbs free energies. The spinel LMO-s and the layered LMO-l with oxidation state 3+ for Mn showed, consequently, the complete decomposition of the initial LATP and active material up to a sintering temperature of 650 °C. In contrast, the LMP, which contains Mn^{2+}, showed no significant decomposition and intermixing with LATP and the powder mixture remained thermally stable up to 800 °C. The formation of a low amount of an oxy-phosphate ($Li_{1-x}Mn_{x/2}TiOPO_4$) at 680 °C could be traced back to carbonates, which are residues of the sol-gel syntheses or were formed during storage of the initial powders. However, this assumption must be verified in further studies. Nonetheless, the combination of LATP and LMP can be considered thermally stable, so that Ag was added as an electrically conductive component. Ag has no impact on the thermal stability and the material combination of LATP, LMP and Ag is a promising basis for further electrochemical studies and the optimization of the composite composition with respect to microstructural properties such as percolation, tortuosity, grain sizes, porosity, cracks or volume changes of the active material during electrochemical operation.

The optimization of the composite bulk cathode can be supported by liquid phase sintering, which has been investigated in the second part of the thesis (**Chapter 5**). Li_3PO_4 as a sintering additive for ceramic LATP accelerated the densification process of LATP through liquid phase sintering. The sinter neck formation temperature could be reduced by 50 °C and the start of densification appeared at temperatures, which were 150 °C lower than without the sintering additive. This led to high grain boundary conductivities at low sintering temperatures. The Li_3PO_4-containing samples sintered at 800 °C showed comparable ionic conductivities (ca. 2×10^{-4} S/cm) like the samples without sintering additive annealed at 1000 °C reported in literature. In addition, microstructural characteristics could be correlated with the measured electrical properties. The formation of the secondary phases $LiTiOPO_4$ and $AlPO_4$, pores, grain size distribution and cracks have an impact on the grain boundary conductivity, which is the performance-limiting factor of ceramic SSEs. Secondary phases, pores and cracks interrupt the percolation network for Li-ion conduction. However, the grain size distribution is the major influencing factor. Low grain sizes increase the number of contact areas between grains so that the possibility of well-aligned lattice planes of two neighboring grains and so the possibility of Li-ion hopping from one grain to another grain increases. It could be shown that the Li_3PO_4-containing samples sintered at 700 °C with a porosity of 26 % and grain size distribution of 2 - 6 µm has just a slightly lower grain boundary conductivity than the 800 °C sintered samples with ca. 7 % porosity and grain sizes between 6 µm and 18 µm. This is a promising finding for bulk cathode composites, in which the pores can be considered as filled with active material. It indicates that the ionic conduction through the composite layer can be still high when small grain sizes are conducted. Li_3PO_4 can also support the grain size control since it limited the grain growth of LATP to a maximum of 25 µm at 900 °C and 950 °C, which is significantly smaller than the > 60 µm grains of the pure LATP samples sintered at 950 °C. Further optimization cycles regarding sintering duration and temperature should be conducted on basis of this study in order to find the best parameters for even higher ionic conductivities. These parameters can be a good basis for the manufacturing of bulk composite cathodes and Li_3PO_4 should be tested as an additive for a LMP, LATP and Ag composite cathode.

In the third and fourth parts of this study, the impact of interdiffusion, intermixing and decomposition on the electrochemical cell performance could be investigated by means of TF-SSBs. TF-SSB manufacturing has been performed by subsequent layer deposition and crystallization of a LMO cathode and LIPON or Ga-LLZO SSE on top of a stainless-steel substrate (StSt). Consequently, the third part deals with the thermal stability of a sol-gel deposited LMO thin-film on top of StSt (**Chapter 6**). It could be shown that the StSt elements Cr, Al and Fe diffuse in the LMO layer and substitute Mn and Li in the spinel structure of LMO enabled by the interdiffusion of Li and Mn into StSt. The interdiffusion and substitution led to the formation of AB_2O_4 (A or B = Mn, Al, Cr, Fe) and $LiMnXO_4$ (X = Al, Cr, Fe) spinels, which decreases significantly the discharge capacity due to lower utilization and it increases the polarization of the cell due to Li depletion at the surface and the formation of an insulating layer, which significantly increases the charge transfer resistance. Consequently, the cells show just polarization effects and no capacity could be obtained so that the interdiffusion must be inhibited. Pt and Au are often used as interdiffusion barriers between cathode and substrate in literature. In addition to Pt and Au, ITO has been introduced in this study and a comprehensive comparison of these interlayers has been conducted. ITO exhibited the best blocking characteristics for interdiffusion even at an elevated temperature of 700 °C for the LMO crystallization so that these cells showed the highest discharge capacities. In contrast, Au did not inhibit the interdiffusion at all at 700 °C and its cells polarized. Pt inhibited the StSt element diffusion but diffuses into LMO. In addition, Pt is electrochemically not stable, so that it dissolves into the liquid electrolyte at the operation potentials of LMO. Conclusively, the first-time introduction of ITO as an interdiffusion barrier has successfully and significantly improved the cell performance of the LMO cathode layer in liquid electrolyte thin-film batteries. This is very important for the subsequent investigation into the thermal stability of the cathode thin-film in combination with ceramic SSE thin-films, as the cathode-current collector interface can be neglected.

These LMO thin-films on top of ITO|StSt samples have been used to investigate the impact of interdiffusion between Ga-LLZO and LMO on the electrochemical performance in the fourth part of this thesis (**Chapter 7**). As interdiffusion and intermixing were expected during the Ga-LLZO crystallization, LTO and TiO_2 interlayers of ≤ 20 nm were investigated as probable interdiffusion barriers between the cathode and SSE. The sol-gel-based LTO and TiO_2 coatings on LMO also allowed the investigation of the capability of these coatings to suppress liquid electrolyte decomposition and CEI formation as well as to suppress Mn dissolution from LMO during long-term cycling. The LTO-coated samples showed the best protection characteristics, thus, the longest cycle life and best capacity retentions. However, the poor cycling stability of the pure and TiO_2-coated LMO samples as well as the dependency between cycling stability and crystallization temperature of LMO suggested already an impact of the carbonate and hydroxide residues remained from the sol-gel deposition on the cell performance. This became clearer in the electrochemical investigation into the general functionality of the interlayers in LIPON TF-SSBs. The LIPON SSE is amorphous and does not require a crystallization process after sputter deposition so that interdiffusion can be neglected. However, the long-term cycling tests revealed very poor cycling stabilities of these TF-SSB full cells. This is in significant contrast to the literature, where cycling lives of LIPON-based TF-SSBs of over 10,000 cycles are reported. These TF-SSBs are prepared by means of PVD processes in highly impurity-free conditions resulting in highly impurity-free TF-SSBs. The results obtained within this study suggest that carbonates and hydroxides remaining from sol-gel deposition react with the LIPON SSE and form an insulating layer, which significantly affects the cell performance and cycle life. Consequently, sol-gel-based cathodes are not sufficient for TF-SSB applications so far. A further purification step after LMO crystallization must be validated. Nevertheless, it could be shown, that the cells with thin LTO interlayers (< 10 nm) have a better rate capability than the TiO_2 interlayers or thicker LTO interlayers (ca. 20 nm), which can be explained by the higher Li-ion diffusivity of LTO than TiO_2 and the higher ionic resistance due to thicker layers. Thus, the implementation of thin LTO interlayers (< 10 nm) in Ga-LLZO-based TF-SSBs appears to be feasible.

Ga-LLZO was crystallized at 650 °C on top of LMO thin-films with and without LTO and TiO_2 interlayers (< 10 nm). It could be shown, that the crystallization temperature, thus, the crystallinity of LMO has an effect on the Ga-LLZO crystallization, since the impurity phase $La_2Zr_2O_7$ could be determined for samples based on LMO crystallized at 600 °C. The LMO thin-films crystallized at 700 °C did not show $La_2Zr_2O_7$ impurity phases. However, Mn_2O_3 could be determined for all samples even with interlayers. This indicates already the main finding of this study, which is the overlithiation of LMO during the Ga-LLZO crystallization process. Mn diffusion into the Ga-LLZO layer could be determined for all samples along with an increasing concentration gradient of Li from the surface of Ga-LLZO into the LMO layer. The concentration gradient of Ga showed an exact opposite trend compensating for the charge in the crystal lattice caused by Li depletion at the surface. Mn seems to form Mn_2O_3 within the Ga-LLZO layer and is substituted by Li in the LMO ($LiMn_2O_4$) layer forming $Li_{1+x}Mn_2O_4$ ($1 \leq x \leq 3$) and $Li_{2+\delta}Mn_{2-\delta}O_4$ ($0 < \delta < 0.33$). This was confirmed in the electrochemical tests, which showed a pronounced redox plateau at ca. 3.0 V vs. Li/Li^+ in the initial cycle. This redox potential corresponds to the redox potential of overlithiated LMO reported in literature. The overlithiation of the LMO causes a very complex electrochemical system with many various reversible and irreversible redox reactions during galvanostatic cycling. The redox plateaus for LMO at ca. 4.1 V vs. Li/Li^+ could not be observed and most of the charge is converted around ca. 3.0 V during charge and discharge. The comparison of the electrochemically obtained results with computational calculations in literature indicates that Ga-LLZO decomposes during charge, which would explain the strong capacity fade with cycle number. Even though the samples with LTO interlayer showed the best cycling behavior, these cells are not sufficient for TF-SSB applications. Since the overlithiation of LMO based on Li diffusion is the main reason for the negative change in the electrochemistry of the cell, interlayer will not help to improve the cell performance of these cells. Blocking of the Li diffusion to prevent the overlithiation during preparation would also result in polarization of the cell during operation.

In conclusion, this Ph.D. thesis showed the complexity of the thermal processes on the cathode side during the manufacturing of ASSBs and its complex impact on the electrochemical processes. The range of probable material combinations is large and the tested material combinations in this thesis revealed that further detailed research is required to achieve competitive ASSBs, particularly, with oxidic or phosphatic SSEs. However, some of the presented results give confidence that ceramic ASSBs are realizable.

Outlook

The combination of the olivine LMP, phosphatic LATP and Ag is promising for further electrochemical characterization with respect to structural characteristics such as percolation, tortuosity, grain sizes, porosity, cracks or volume changes of the active material during electrochemical operation. A first study of our collaboration partners at the Center of Excellence in Transportation Electrification and Energy Storage (Hyrdo-Québec) on an analogical material system based on $LiFePO_4$, $Li_{1.5}Al_{0.5}Ge_{1.5}(PO_4)_3$ and carbon black showed the principle cyclability of these composite cathodes with high utilization in the first ten cycles.[228] However, carbon black combusted at high temperatures and the cells were cycled at 80 °C because of high charge transfer and ion conduction resistances. Further optimization with respect to smaller grain sizes must be done. Hereby, the addition of the sintering additive Li_3PO_4 might help, since it limits the grain growth and a decrease in sintering temperature might be possible. The target bulk cathode composite should have grain sizes of < 1 µm, particularly because of the low ionic and electrical conductivities of LMP and LFP. The mixing and composition of the single components must be optimized for good percolation of the Li-on and electron transport networks required for high utilization of the composite layer. Additionally, based on the presented foundation and findings of the sintering additive investigation, further fundamental research on the impact of the sintering additive on the bulk conductivity and grain boundary activation energies should be conducted. The understanding of the change in lattice stoichiometry due to the formation of secondary phases and the change in the nature of the grain boundaries might probably help to engineer ceramic SSEs with improved ionic conductivities.

In the field of TF-SSBs, the excellent blocking characteristics of the ITO interdiffusion barrier between the active material and stainless-steel substrate could already be proven for NMC811 active materials in collaboration with our partners at EMPA, which reported an increase in cell performance by using the ITO-coated substrates presented in this study.[229] However, sol-gel-based preparation of TF-SSBs appears not to be sufficient for battery application. Impurities that remained from the dip-coating and crystallization process should be removed by a purification process in order to validate the cycling stability in long-term cycling tests in LIPON TF-SSBs. The combination of Ga-LLZO and LMO is not very promising due to the overlithiation of LMO during Ga-LLZO crystallization. Even though an overlithiated LMO TF-SSB with Ga-LLZO operating at ca. 3.0 V vs. Li/Li^+ is thinkable, these cells would not enhance the energy and power densities, so that a focus on other material combinations is highly recommended.

8.2 Deutsche Zusammenfassung, Fazit und Ausblick

Zusammenfassung und Fazit

Diese Dissertation hat sich in vier Studien mit mehreren Hauptthemen der aktuellen Festkörperbatterieforschung (engl.: all solid-state battery, ASSB) befasst. Keramische Festkörperbatterien sollen die Implementierung von Li-Metallanoden und Hochvoltkathodenmaterialien ermöglichen, die die Energiedichte, die Leistungsdichte, die Lebensdauer sowie Sicherheitsaspekte im Vergleich zu kommerziell erhältlichen Li-Ionenbatterien (LiBs) mit flüssigen Elektrolyten erhöhen würden. In dieser Thesis wurden mehrere wissenschaftliche Fragestellungen untersucht, die sich auf der Kathodenseite der ASSB ergeben. In Hinblick auf das Zielsystem einer ternären Kompositkathode, bestehend aus keramischen Aktivmaterial, keramischen Festkörperelektrolyt (engl.: solid-state electrolyt, SSE) und elektrisch leitender Komponente, wurden Studien über die thermische Stabilität dieser Komponenten und ihre Auswirkung auf die elektrochemische Leistung durchgeführt. Wie in **Kapitel 2.2** beschrieben, müssen partikuläre Kathodenkomposite elektrochemische, chemische, mechanische und strukturelle Anforderungen erfüllen, um mit kommerziellen LiBs konkurrieren zu können. Insbesondere erfordert der Produktionsprozess ein Hochtemperatursintern, um eine stoffschlüssige Anbindung zu erhalten, damit die elektrochemisch aktive Fläche, der Ladungstransfer und die Ionenleitung maximiert werden können. Interdiffusion, Vermischung und Zersetzung der Ausgangskomponenten während des Sinterns führen jedoch bisher zu ASSBs mit geringen Leistungen. Die Bildung nicht-leitender oder elektrochemisch inaktiver Mischphasen verschlechtert die Leistung der Zellen erheblich.

In diesem Zusammenhang wurden diese Nebenreaktion während der Hochtemperaturbehandlung untersucht, um ein besseres Verständnis dieser Mechanismen zu erlangen, eine bessere Steuerung des Herstellungsprozesses zu ermöglichen sowie die Auswahl von Materialkombinationen für zukünftige ASSB-Anwendungen zu erleichtern. Die Arbeit ist in vier Teile gegliedert. Die ersten beiden Teile befassen sich mit der thermischen Stabilität des keramischen SSEs LATP in Kombination mit verschiedenen Aktivmaterialien und mit der Validierung einer möglichen Verbesserung des Sinterprozesses von LATP durch Flüssigphasensintern hervorgerufen durch die Zugabe des Sinteradditivs Li_3PO_4. Im dritten und vierten Teil wurden die Auswirkungen von Interdiffusion, Vermischung und Zersetzung auf die elektrochemische Leistung von Dünnschicht-Festkörperbatterien (engl.: thin-film solid-state batteries, TF-SSBs) auf der Grundlage des Aktivmaterials LMO und des keramischen SSE Ga-LLZO untersucht.

Die Untersuchung der thermischen Stabilität von LATP in Kombination mit Mn-basierenden Aktivmaterialien jeder Strukturklasse (Olivin, Schichtoxide und Spinell) zeigte den Einfluss des Strukturtyps und der damit verbundenen Oxidationsstufe von Mn auf die Tendenz zur Durchmischung und Zersetzung (**Kapitel 4**). Die Möglichkeit der Reduktion von Mn^{3+} und Mn^{4+} in den Spinell LMO-s zu geringerwertigen Mn^{2+} Spezies wie Mn_3O_4, $MnTiO_3$ oder LMP, zusammen mit der Oxidation von O^{2-}, die eine O_2-Ausgassung verursacht, sind die Haupttriebkräfte für die Zersetzung der Ausgangskomponenten und für die Bildung von Mischphasen mit niedrigeren Freien Gibbs Energien. Der Spinell LMO-s und das Schichtoxid LMO-l mit der Oxidationsstufe 3+ für Mn zeigten folglich die vollständige Zersetzung des ursprünglichen LATPs und der Aktivmaterialien bis zu einer Sintertemperatur von 650 °C. Im Gegensatz dazu zeigte der Olivin LMP, die Mn^{2+} enthalten, keine signifikante Zersetzung und Vermischung mit LATP und die Pulvermischung blieb bis 800 °C thermisch stabil. Die Bildung einer geringen Menge eines Oxyphosphats ($Li_{1-x}Mn_{x/2}TiOPO_4$) bei 680 °C könnte auf Karbonate zurückzuführen sein, welche die Rückstände aus der Sol-Gel Synthese sind oder während der Lagerung der Ausgangsstoffe gebildet wurden. Diese Vermutung muss jedoch in weiteren Studien überprüft werden. Nichtsdestotrotz kann die Kombination aus LATP und LMP als thermisch stabil angesehen werden, sodass Ag als elektrisch leitende Komponente hinzugefügt wurde. Ag hat keinen Einfluss auf die thermische Stabilität und die Materialkombination aus LATP, LMP und Ag ist eine vielversprechende Grundlage für weitere elektrochemische Studien und für die Optimierung der Kompositzusammensetzung im Hinblick auf mikrostrukturelle Eigenschaften wie Perkolation, Tortuosität, Korngrößen, Porosität, Risse oder Volumenänderung des Aktivmaterials während des elektrochemischen Prozesses.

Die Optimierung der Kompositkathode kann durch Flüssigphasensintern unterstützt werden, was im zweiten Teil der Arbeit untersucht wurde (**Kapitel 5**). Li_3PO_4 als Sinteradditiv für keramisches LATP beschleunigt den Verdichtungsprozess von LATP durch Flüssigphasensintern. Die Temperatur der Sinterhalsbildung konnte um 50 °C gesenkt werden und der Beginn der Schrumpfung trat bei Temperaturen auf, die 150 °C niedriger waren als ohne Sinteradditiv. Die bei 800 °C gesinterten Li_3PO_4-haltigen Proben zeigten vergleichbare Ionenleitfähigkeiten (ca. 2×10^{-4} S/cm) wie die in der Literatur beschriebenen, bei 1000 °C gesinterten Proben ohne Sinteradditiv. Darüber hinaus konnten die mikrostrukturellen Merkmale mit den gemessenen elektrischen Eigenschaften korreliert werden. Die Bildung der Sekundärphasen $LiTiOPO_4$ und $AlPO_4$, Poren, Korngrößenverteilung und Risse wirken sich auf die Korngrenzleitfähigkeit aus, die der leistungsbegrenzende Faktor von keramischen SSEs ist. Sekundärphasen, Poren und Risse unterbrechen das Perkolationsnetzwerk für die Li-Ionenleitung. Die Korngrößenverteilung ist jedoch der wichtigste Einflussfaktor. Kleine Korngrößen erhöhen die Anzahl der Kontaktflächen zwischen den Körnern, sodass die Möglichkeit gut ausgerichteter Gitterebenen zweier benachbarter Körner und damit die Möglichkeit des Li-Ionen-Hoppings von einem Korn zum anderen zunimmt. Es konnte gezeigt werden, dass die bei 700 °C gesinterten Li_3PO_4-haltigen Proben mit einer Porosität von 26 % und einer Korngrößenverteilung von 2 - 6 µm nur eine etwas geringere Korngrenzleitfähigkeit aufweisen als die bei 800 °C gesinterten Proben mit ca. 7 % Porosität und Korngrößen zwischen 6 µm und 18 µm. Dies ist eine vielversprechende Erkenntnis für Kompositkathoden, bei denen die Poren als mit Aktivmaterial gefüllt angesehen werden können. Es deutet darauf hin, dass die Ionenleitung durch die Kompositschicht bei kleinen Korngrößen noch hoch sein kann. Li_3PO_4 kann auch bei der Kontrolle der Korngrößeneinstellung unterstützen, da es das Kornwachstum von LATP bei 900 °C und 950 °C auf maximal 25 µm begrenzt, was deutlich geringer ist als die > 60 µm großen Körner der bei 950 °C gesinterten reinen LATP Proben. Auf der Grundlage dieser Studie sollten weitere Optimierungszyklen hinsichtlich Sinterdauer und Sintertemperatur durchgeführt werden, um die besten Parameter für noch höhere Ionenleitfähigkeiten zu finden. Diese Parameter können eine gute Grundlage für die Herstellung von Kompositkathoden sein. Li_3PO_4 sollte als Sinteradditiv für eine LMP, LATP und Ag basierende Kompositkathode getestet werden.

Im dritten und vierten Teil der Dissertation konnten die Auswirkungen von Interdiffusion, Vermischung und Zersetzung auf die elektrochemische Zellleistung anhand von TF-SSBs untersucht werden. Die Herstellung von TF-SSBs erfolgt durch aufeinanderfolgende Schichtabscheidung und Kristallisation von LMO Kathoden und LIPON oder Ga-LLZO SSEs auf einem Edelstahlsubstrat (engl.: stainless-steel, StSt). Folglich befasst sich der dritte Teil mit der thermischen Stabilität eines durch Sol-Gel abgeschiedenen LMO-Dünnfilms auf StSt (**Kapitel 6**). Es konnte gezeigt werden, dass die StSt-Elemente Cr, Al und Fe in die LMO-Schicht diffundieren und Mn und Li in der Spinellstruktur von LMO ersetzen, was durch die Interdiffusion von Mn und Li in StSt ermöglicht wird. Die Interdiffusion und die Substitution führen zur Bildung von AB_2O_4 (A oder B = Mn, Al, Cr, Fe) und $LiMnXO_4$ (X = Al, Cr, Fe) Spinellen, was die Entladekapazität aufgrund der geringeren Nutzbarkeit deutlich verringert und die Polarisierung der Zelle erhöht. Dies geschieht durch die Li-Verarmung an der Oberfläche und die dadurch induzierte Bildung einer isolierenden Schicht, die den Ladungstransferwiderstande deutlich erhöht. Folglich zeigten die Zellen ausschließlich Polarisationseffekte und es konnte keine Kapazität erzielt werden, sodass die Interdiffusion verhindert werden muss. Pt und Au werden in der Literatur häufig als Interdiffusionsbarrieren zwischen Kathode und Substrat verwendet. In dieser Studie wurde zusätzlich zu Pt und Au auch ITO eingeführt und ein umfassender Vergleich dieser Zwischenschichten durchgeführt. ITO zeigte selbst bei einer erhöhten Temperatur von 700 °C für die LMO Kristallisation die besten Blockiereigenschaften für die Interdiffusion, sodass diese Zellen die höchsten Entladekapazitäten aufwiesen. Im Gegensatz dazu hemmte Au die Interdiffusion bei 700 °C überhaupt nicht und dessen Zellen polarisierten. Pt hemmte die Diffusion der StSt-Elemente, aber diffundierte selbst ins LMO. Darüber hinaus ist Pt elektrochemisch nicht stabil, sodass es sich bei den Betriebspotentialen von LMO in den flüssigen Elektrolyten löst. Zusammenfassend lässt sich sagen, dass die erstmalige Einführung von ITO als Interdiffusionsbarriere die Zellleistung der LMO Kathodenschichten in Flüssigelektrolyt-Dünnschichtbatterien erfolgreich und deutlich verbessert hat. Dies ist sehr wichtig für die anschließende Untersuchung der thermischen Stabilität der Kathoden-Dünnschicht in Kombination mit keramischen SSE-Dünnschichten, da die Grenzfläche zwischen Kathode und Stromableiter-Substrat vernachlässigt werden kann.

Diese LMO-Dünnschichten auf ITO|StSt Proben wurden im vierten Teil dieser Arbeit verwendet, um die Auswirkungen der Interdiffusion zwischen Ga-LLZO und LMO auf die elektrochemische Leistung zu untersuchen (**Kapitel 7**). Da während der Ga-LLZO Kristallisation Interdiffusion und Vermischung zu erwarten waren, wurden LTO und TiO_2 Zwischenschichten mit ≤ 20 nm als mögliche Interdiffusionsbarriere zwischen Kathode und SSE untersucht. Die auf Sol-Gel basierenden LTO und TiO_2 Beschichtungen auf LMO ermöglichen auch die Untersuchung der Tauglichkeit dieser Beschichtungen die

Flüssigelektrolytzersetzung und CEI-Bildung zu unterdrücken sowie die Mn-Auswaschung aus LMO während langfristigen Zyklisierens zu verhindern. Die LTO-beschichteten Proben zeigten die besten Schutzeigenschaften, folglich, die längste Zyklenlebensdauer und die beste Kapazitätserhaltung. Die schlechte Zyklenstabilität der reinen und der TiO_2-beschichteten LMO Proben sowie die Abhängigkeit zwischen Zyklenstabilität und Kristallisationstemperatur deuten jedoch bereits auf einen Einfluss der von der Sol-Gel-Abscheidung verbliebenen Karbonatrückstände auf die Zellleistung hin. Dies wurde bei der elektrochemischen Untersuchung der allgemeinen Funktionalität der Zwischenschichten in LIPON TF-SSBs noch deutlicher. Der LIPON SSE ist amorph und erfordert keine Kristallisationsprozess nach der Sputterabscheidung, so dass Interdiffusionsprozesse vernachlässigt werden können. Die Langzeit-Zyklentests zeigten jedoch eine sehr schlechte Zyklenstabilität dieser TF-SSB-Vollzellen. Dies steht in deutlichem Gegensatz zur Literatur, in der von Lebensdaueren von TF-SSBs auf LIPON Basis von über 10,000 Zyklen berichtet werden. Diese TF-SSBs werden mittels physikalischer Gasphasenabscheidung unter hochgradig verunreinigungsfreien Bedingungen hergestellt, was zu hochgradig verunreinigungsfreien TF-SSBs führt. Die im Rahmen dieser Studie erzielten Ergebnisse deuten darauf hin, dass Karbonate und Hydroxide, die bei der Sol-Gel-Abscheidung zurückbleiben, mit dem LIPON SSE reagieren und eine Isolierschicht bilden, die die Zellleistung und die Lebensdauer erheblich beeinträchtigt. Folglich sind Kathoden auf Sol-Gel-Basis für TF-SSB Anwendungen bisher nicht ausreichend. Ein weiterer Reinigungsschritt nach der LMO Kristallisation muss validiert werden. Dennoch konnte gezeigt werden, dass die Zellen mit dünnen LTO-Zwischenschichten (< 10 nm) eine bessere Ratenfähigkeit aufweisen als die TiO_2-Zwischenschichten oder dicker LTO-Zwischenschichten (ca. 20 nm), was sich durch die höhere Li-Ionendiffusivität von LTO gegenüber TiO_2 und den höheren Ionenwiderstand aufgrund dickerer Schichten erklären lässt. Somit scheint die Implementierung von dünnen LTO-Zwischenschichten (< 10 nm) in Ga-LLZO-basierenden TF-SSB machbar zu sein.

Ga-LLZO wurde bei 650 °C auf LMO-Dünnschichten mit und ohne LTO und TiO_2 Zwischenschichten (< 10 nm) kristallisiert. Es konnte gezeigt werden, dass die Kristallisationstemperatur, folglich die Kristallinität von LMO, einen Einfluss auf die Ga-LLZO Kristallisation hat, da die Verunreinigungsphase $La_2Zr_2O_7$ für Proben auf Basis von 600 °C kristallisierten LMO-Dünnfilmen bestimmt werden konnte. Die bei 700 °C kristallisierten LMO-Dünnfilme wiesen keine $La_2Zr_2O_7$ Phasen auf. Mn_2O_3 konnte jedoch für alle Proben, auch mit Zwischenschichten, bestimmt werden. Dies deutet bereits auf die Haupterkenntnis dieser Studie hin, nämlich die Überlithiierung von LMO während des Ga-LLZO Kristallisationsprozesses. Die Diffusion von Mn in die Ga-LLZO Schicht konnte für alle Proben zusammen mit einem zunehmenden Konzentrationsgradienten von Li von der Oberfläche von Ga-LLZO in die LMO-Schicht festgestellt werden. Der Konzentrationsgradient von Ga zeigte einen genauen entgegengesetzten Trend, wodurch die durch die Li-Verarmung an der Oberfläche freien Ladungen im Kristallgitter des Ga-LLZOs kompensiert werden. Mn scheint innerhalb der Ga-LLZO Schicht Mn_2O_3 zu bilden und wird in der LMO-Schicht ($LiMn_2O_4$) durch Li ersetzt, wodurch $Li_{1+x}Mn_2O_4$ ($1 \leq x \leq 3$) und $Li_{2+\delta}Mn_{2-\delta}O_4$ ($0 < \delta < 0.33$) entstehen. Dies wurde in den elektrochemischen Tests bestätigt, welche ein ausgeprägtes Redoxplateau bei ca. 3.0 V vs. Li/Li^+ im ersten Zyklus aufweisen. Dieses Redoxpotential entspricht dem in der Literatur angegebenen Redoxpotential von überlithiierten LMO. Die Überlithiierung des LMOs verursacht ein sehr komplexes elektrochemisches System mit vielen verschiedene reversiblen und irreversiblen Redoxreaktionen während des galvanostatischen Zyklisierens. Das Redoxplateau für LMO bei ca. 4.1 V vs. Li/Li^+ konnte nicht beobachtet werden und der größte Teil der Ladung wird bei ca. 3.0 V vs. Li/Li^+ während des Ladens und Entladens umgesetzt. Der Vergleich der elektrochemischen Ergebnisse mit Berechnungen in der Literatur deutet darauf hin, dass sich Ga-LLZO während des Ladens zersetzt, was den starken Kapazitätsabfall mit Zyklenzahl erklären würde. Obwohl die Proben mit LTO-Zwischenschicht das beste Zyklenverhalten zeigten, sind diese Zellen für TF-SSB Anwendungen nicht ausreichend. Da die Überlithiierung von LMO aufgrund der Li-Diffusion der Hauptgrund für die negative Veränderung in der Elektrochemie der Zelle ist, wird die Zwischenschicht nicht dazu beitragen, die Zellleistung dieser Zellen zu verbessern. Eine Blockierung der Li-Diffusion zur Verhinderung der Überlithiierung während der Herstellung würde auch zu einer Polarisation der Zelle während des Betriebs führen. Ein Zellkonzept aus überlithiierten LMO in Kombination mit Ga-LLZO betrieben bei 3.0 V mit geringerer Zersetzung von Ga-LLZO und besserer Zyklenstabilität ist denkbar. Allerdings würden diese Zellen keinen Vorteil hinsichtlich Energie- und Leistungsdichte im Vergleich zu kommerziellen Flüssigelektrolyt-LiBs bringen.

Zusammenfassend lässt sich sagen, dass diese Doktorarbeit die Komplexität der thermischen Prozesse auf der Kathodenseite während der Herstellung von ASSBs und ihre komplexen Auswirkungen auf die elektrochemischen Prozesse gezeigt hat. Die Bandbreite möglicher Materialkombinationen ist groß und die in dieser Arbeit getesteten Materialkombinationen zeigten, dass weitere detaillierte Forschung erforderlich ist, um wettbewerbsfähige ASSBs umzusetzen, insbesondere mit oxidischen oder phosphatischen SSEs. Einige der vorgestellten Ergebnisse stimmen jedoch zuversichtlich, das keramische ASSBs realisierbar sind.

Ausblick

Die Kombination aus olivinen LMP, phosphathaltigen LATP und Ag ist vielversprechend für die weitere elektrochemische Charakterisierung unter Berücksichtigung struktureller Merkmale wie Perkolation, Tortuosität, Korngröße, Porosität, Risse oder Volumenänderung des Aktivmaterials während der elektrochemischen Prozesse. Eine erste Studie unserer Kooperationspartner am Center of Excellence in Transportation Electrification and Energy Storage (Hyrdo-Québec) über ein analoges Materialsystems basierend auf $LiFePO_4$ (LFP), $Li_{1.5}Al_{0.5}Ge_{1.5}(PO_4)_3$ und Ruß zeigte die prinzipielle Zyklisierbarkeit dieser Kompositkathoden mit einer hohen Nutzbarkeit in den ersten zehn Zyklen.[228] Allerdings verbrannte teilweise der Ruß bei der Herstellung und die Zelle wurden bei 80 °C zyklisiert, da diese einen hohen Ladungstransfer- und Ionleitwiderstand aufwiesen. Weiter Optimierungen hinsichtlich kleinerer Korngrößen müssen vorgenommen werden. Dabei könnte die Zugabe des Sinteradditivs Li_3PO_4 helfen, da es das

Kornwachstum begrenzt und die Sintertemperatur herabsetzt. Die angestrebte Kompositkathode sollte Korngrößen von < 1 µm aufweisen, insbesondere wegen der geringen ionischen und elektrischen Leitfähigkeiten von LMP und LFP. Die Mischung und Zusammensetzung der einzelnen Komponenten muss für eine gute Perkolation der Li-Ionen- und Elektronentransportnetzwerke optimiert werden, die für eine hohe Nutzbarkeit der Kompositschicht erforderlich sind. Darüber hinaus sollten auf Grundlage der vorgestellten Erkenntnisse und Ergebnisse der Untersuchung des Sinteradditivs weitere grundlegende Untersuchungen zu der Auswirkung des Sinteradditivs auf die Bulkleitfähigkeit und auf die Korngrenzaktivierungsenergie durchgeführt werden. Das Verständnis über die Veränderung der Gitterstöchiometrie durch die Bildung der Sekundärphasen und über die Veränderung der Beschaffenheit der Korngrenzen könnte möglicherweise dazu beitragen, keramische SSEs mit verbesserter Ionenleitfähigkeit zu entwickeln.

Im Bereich der TF-SSBs konnte die hervorragende Sperrwirkung der ITO-Interdiffusionsbarriere zwischen Aktivmaterial und Edelstahlsubstrat bereits für NCM811 Aktivmaterialien in Zusammenarbeit mit unseren Partnern an der EMPA nachgewiesen werden, die eine Steigerung der Zellleistung durch der in dieser Arbeit vorgestellten ITO-beschichteten Substrate publizierten.[229] Die Sol-Gel basierende Herstellung von TF-SSBs scheint jedoch für die Anwendung in Batterien nicht ausreichend zu sein. Verunreinigungen, die bei der Tauchbeschichtung und Kristallisation zurückbleiben, sollten durch einen Reinigungsprozess entfernt werden, um die Zyklenstabilität in Langzeitzyklentests in LIPON TF-SSBs zu überprüfen. Die Kombination von Ga-LLZO und LMO ist aufgrund der Überlithiierung von LMO während der Ga-LLZO Kristallisation nicht sehr vielversprechend. Auch wenn eine überlithiierte LMO TF-SSB mit Ga-LLZO bei ca. 3.0 V denkbar ist, würden diese Zellen die Energie- und Leistungsdichte nicht erhöhen, sodass ein Fokus auf andere Materialkombinationen dringend empfohlen wird.

9 Experimental Part

9.1 Experimental Part of Study on Thermal Stabilities of LATP in Combination with various Mn-based Active Materials

Powder Synthesis

The powders of $Li_{1.3}Al_{0.3}Ti_{1.7}(PO_4)_3$ (LATP), $LiMn_2O_4$ (LMO-s) and $LiMnPO_4$ (LMP) were synthesized via sol-gel formulations. The crystallization temperatures and durations were particularly chosen in order to obtain particle sizes less than 1 µm. Since $LiMnO_2$ (LMO-l) and nano-sized Ag particles could not be synthesized, these powders were purchased from Sigma Aldrich® (LMO-l: < 1 µm) and Nanografi® (Ag: 48 - 78 nm).

LATP Synthesis

LATP was synthesized by subsequent dissolving stoichiometric amounts of lithium acetate dihydrate, alumina nitrate nonahydrate and ammonium dihydrogen phosphate in a 1:1 mixture of ethanol and 1-methoxy-2-propanol, to which concentrated nitric acid was added. Titanium (IV) butoxide was added to acetyl acetone in a second vessel. This solution was stirred for 30 min in order to obtain a complete complex formation. Afterward, the two solutions were mixed and stirred for further 30 min. The obtained sol-gel solution was dried overnight at 80 °C. A drying oven was used to accelerate the drying process. The temperature was stepwise increased depending on the solvent content to finally 120 °C until a very dry, amorphous LATP powder was obtained. The amorphous powder was crystallized at 800 °C for 5 h in an alumina crucible and afterward ball-milled at 400 rpm for 40 min.

LMP Synthesis

For the LMP synthesis, stoichiometric amounts of lithium acetate dihydrate, manganese (II) acetate tetrahydrate and ammonium dihydrogen phosphate were subsequently dissolved in a 1:1 mixture of ethanol and 1-methoxy-2-propanol with additional concentrated nitric acid. The solution was stirred for 30 min. Then, the solution was dried overnight like the LATP solution and afterward crystallized at 600 °C for 5 h in an alumina crucible. The crystallized LMP powder was ball-milled at 400 rpm for 40 min.

LMO-s Synthesis

Stochiometric amounts of lithium acetylacetonate and manganese (II) acetate tetrahydrate were dissolved in ethanol. The solution was stirred for 30 min. Then, the solution was dried overnight like the LATP and LMP solutions. Afterward, the amorphous powder was crystallized at 600 °C for 5 h in an alumina crucible. The crystallized LMO-s powder was ball-milled at 400 rpm for 40 min.

Powder Mixtures, Pellet Preparation and Form Integrity Tests

Powder mixtures of 1:1 vol% of LATP and the various active materials were mixed in a mortar. In the case of the LMP, LATP and Ag mixture the ratio was 1:1:1 vol%. Pellets of 0.25 g of these powder mixtures were pressed with 90 kN. The pellets had a thickness of about 0.7 mm and a diameter of 14.85 mm. Before these pellets were used in the HT-XRD measurements, they were stepwise sintered until an obvious shrinkage could be observed. These form integrity tests are important since the deformation of the pellet during the HT-XRD measurements falsifies the results.

HT-XRD incl. Rietveld Refinement

High-temperature X-ray diffraction spectroscopy measurements (HT-XRD) were performed at the University of Darmstadt in collaboration with the group of Prof. Oliver Clemens. A Bruker D8 advance® diffractometer with Cu K_α radiation and Bragg-Brentano geometry was used. A high-temperature sample holder chamber (Anton Paar®) with a controlled argon atmosphere was used inside the diffractometer. A calibration of the temperature profile of the chamber was conducted by means of a standardized and defined MgO sample. The pellets of the powder mixtures were placed inside the chamber. The heating rate was 3 K/min and the first diffractogram was measured at 500 °C. The diffractograms were collected between 2θ values of 14° and 54°. The temperature was kept constant during the 15 min XRD scan. Scans were performed every 25 °C and the heating rate between the scans was 3 K/min. The maximum temperature determined by the form integrity tests was held for 1 h with four scans for LMO-s and LMO-l. For the LMP and LATP powder mixture, a holding step of 4 h with 16 scans was chosen. After the holding step, the sample was cooled down with 3 K/min to room temperature with scans every 25 °C until 500 °C.

The XRD diffractograms were analyzed via Rietveld refinement using the TOPAS V6 software (Bruker®). The phase fractions of the different components were analyzed by refining only the lattice parameters and crystalline size parameters.

DSC-TG incl. MS

The differential scanning calorimetry and thermogravimetry analysis (DSC-TG) measurements were performed on a Netzsch® STA 449 C Jupiter set-up. 20 mg of a powder mixture was heated up to 1000 °C with a heating rate of 10 K/min. An alumina crucible was used in argon atmosphere. Evaporation and combustion products were analyzed in a Netzsch® M 403 C Aeolos mass spectrometer (MS).

SEM/EDS

Scanning electron microscopy incl. energy dispersive X-ray spectroscopy (SEM/EDS) was performed on polished cross sections of pellets of the powder mixtures. For these measurements, separate pellets were pressed and sintered at 800 °C for 2 h in argon atmosphere. The heating rate was 5 K/min. Cross sections were prepared by polishing one edge of the pellets with a

HITACHI® IM4000 ion milling system. A ZEISS® Auriga 60 microscope was used to obtain the SEM images. An AMETEK® EDAX Octane Elect Plus analytical system was used to measure the EDS spectra.

9.2 Experimental Part of Study on the Sintering Additive Li_3PO_4 for LATP

Powder Synthesis

LATP was synthesized by subsequent dissolving stoichiometric amounts of lithium acetate dihydrate, alumina nitrate nonahydrate and ammonium dihydrogen phosphate in a 1:1 mixture of ethanol and 1-methoxy-2-propanol, to which concentrated nitric acid was added. Titanium (IV) butoxide was added to acetyl acetone in a second vessel. This solution was stirred for 30 min in order to obtain a complete complex formation. Afterward, the two solutions were mixed and stirred for further 30 min. The obtained sol-gel solution was dried overnight at 80 °C. A drying oven was used to accelerate the drying process. The temperature was stepwise increased depending on the solvent content to finally 120 °C until a very dry, amorphous LATP powder was obtained. The amorphous powder was crystallized at 800 °C for 5 h in an alumina crucible and afterward ball-milled at 400 rpm for 40 min.

Adding of Li_3PO_4, Preparation of Pellets and Sintering

Li_3PO_4 (SigmaAldrich®, CAS: 10377-52-3) was added to the LATP powder with 3 vol%, 5 vol% and 10 vol% ratios. The DAC 400.1 VAC-P speedmixer of Hauschild® was used to mix the powder mixture at 1000 rpm for 10 min. Green bodies for the TOM measurements were prepared by pressing pellets with 2000 kN. The diameter of these pellets was 11 mm and the thicknesses ca. 2 mm. For the EIS measurements, 0.5 g of the powders were pressed into pellets at 80 kN. Their thicknesses were about 1.4 mm and the diameters were 16 mm. Sintering of these pellets for the TOM and EIS measurements was performed with 5 K/min in ambient air atmosphere. The final sintering temperature was between 650 °C and 950 °C. The final sintering temperature at the end of the heating ramp was held for 24 h. Afterward, the furnace cooled down at a rate of ca. 2 K/min.

XRD

The X-ray diffractograms were collected by means of a PANalytical® Empyrean diffractometer with Cu K_α radiation and Bragg-Brentano geometry. LATP pellets with and without Li_3PO_4 sintered at 900 °C were ground to powder. These powders were measured between 15° and 60° 2θ with a step size of 0.02° and a scan duration per step of 5 s.

TOM and Water Saturation (Archimedes Principle)

A thermal-optical measurement device (TOM) of the Group of Prof. Raether was used to analyze the sintering behavior. TOM and porosity measurements happened in collaboration with the Center for High-Temperature Materials and Design (HTL, Bayreuth), in particular in collaboration with Jens Baber. The pellets were placed into the TOM heating chamber. The heating rate was 5 K/min. Thermal diffusivity and the relative thickness were measured every 50 °C until the holding step of the final temperature, where every 30 min data was collected. After sintering, the furnace cooled down with ca. 2 K/min. These sintered pellets were characterized by means of water saturation based on the Archimedes principle to obtain the porosity. The masses of a pellet were determined in completely dry condition, immersed in a flask of water and afterward from the wet pellet. The mass of the wet pellet minus the mass of the dry pellet and then divided by the difference of the mass of the wet pellet and the mass determined immersed in water result in the porosity of the pellet.

SEM/EDS

SEM images were taken from the pellets, which were measured via temperature-dependent EIS (see below). SEM images were collected using a ZEISS® Auriga 60 microscope with an accelerating voltage of 5 kV and a backscattered electron detector. Cross sections were obtained by polishing the pellets with a JEOL® SM-0910 cross-section polisher in an argon atmosphere. The lower and upper limits of the grain size distribution were determined by means of the ImageJ® software. The EDS spectrum of the LATP pellet with 5 vol% Li_3PO_4 sintered at 950 °C was measured by using an AMETEK® EDAX Octane Elect Plus analytical system.

EIS

For the electrical impedance spectroscopy (EIS), the pellets were sputtered with round gold electrodes (diameter 10 mm). These pellets were dried under vacuum (10^{-2} mbar) at 120 °C for 10 h and transferred into an argon-filled glovebox ($H_2O < 1$ ppm and $O_2 < 1$ ppm). Pouch cells were assembled in the glovebox in order to avoid the influence of humidity during the EIS measurement. A VMP-300 galvanostat of Biologic® was used to conduct the EIS measurements. The frequency range was 7 MHz to 1 HZ and the amplitude was 50 mV. The measurements at room temperature and the preparation of the pellets were carried out in triplicates in order to examine the reproducibility. Since good reproducibility could be achieved, one representative pellet of each sintering temperature and Li_3PO_4 content was measured by temperature-dependent EIS in the temperature range between -20 °C and 60 °C in 10 °C steps. Afterward, these pellets were additionally used to examine the microstructure via SEM.

9.3 Experimental Part of Study on the Current Collector/Cathode Interface

Preparation of Substrate and Interlayers

The base substrate was a heat-resistant ferritic chrome steel (StSt) with 20 wt% Cr and 5 wt% Al and a thickness of 30 µm (1.4767, X8CrAl 20-5, H + S Präzesionsfolien GmbH). It was cut into 5 x 5 cm² samples. Au and Pt were sputtered via DC sputtering (Bulzer® Union 040) on top of the StSt substrate. In an argon atmosphere with a pressure of 0.1 mbar, the distance between the sample and target was set to 7 cm and a sputter current of 40 mA was used. The deposition time was 10 min for Au and 15 min for Pt to achieve similar layer thicknesses of ca. 100 nm. ITO layers were deposited onto StSt via sol-gel dip-coating. The sol-gel solution was obtained by dissolving indium (III) acetate and diethanolamine in 1-butanol. The solution was refluxed for 10 min. Subsequently, ethoxy acetic acid and tin (II) 2-ethylhexanoate were added and refluxed for a further 1 h. By means of a rotary evaporator, the solvent was removed. Then the sol was adjusted to a defined solid content of 4.6 wt% by adding 1-butanol. ITO layer deposition via dip-coating equipment was conducted in a controlled air atmosphere with 25 % relative humidity at 25 °C. The withdraw velocity corresponding to 100 nm films was found to be 200 mm/min. The ITO gel films after dip-coating were crystallized rapidly at 600 °C for 10 min. The electrical sheet resistivity of these films was ca. 25 mΩcm.

Preparation of LMO Thin-Films

The LMO layers were deposited on the various substrates via dip-coating from a LMO sol. Stoichiometric amounts of lithium acetylacetone and manganese (II) acetate tetrahydrate were dissolved into a solution of 2-(2-methoxyethoxy) acetic acid and ethanol. The mixture was stirred for 30 min under reflux at 120 °C. The solid content was 10 wt%. The dip-coating was conducted in a controlled air atmosphere with 25 % relative humidity at 25 °C. The substrate was immersed for 10 s in the sol and then it was withdrawn with a velocity of 50 mm/min. The LMO gel films on the substrates were dried immediately for 30 min at 180 °C. Finally, the LMO films were crystallized rapidly at 600 °C for 1 h or 700 °C for 1 h in ambient air atmosphere. The cooling process was opening the furnace at the set temperature and removing the samples so that the cooling was rapid to room temperature.

SEM

SEM images have been taken on a ZEISS® Supra 25 microscope. The accelerating voltage was usually set to 2.5 kV. Cross-sections were prepared by embedding the samples in an epoxy resin and polishing them by means of a JOEL® SM-0910 cross-section polisher in argon atmosphere.

ToF-SIMS

Time-of-flight secondary ion mass spectrometry (ToF-SIMS) was performed on a ToF.SIMS5 system from IONTOF® in collaboration with our partners of the group of Y. E. Romanyuk at Swiss Federal Laboratories of Material Science and Technology (EMPA, Switzerland). Sputtering was performed at a 300 x 300 µm² area at the sample surface with a Cs^+ sputtering ion beam with an acceleration voltage of 1 kV and a current of 50 nA. Compositional depth-profiles were measured by means of an analysis ion source of Bi^+ primary ions with an acceleration voltage of 25 kV and a current of 2 pA on a 100 x 100 µm² area within the sputtering crater.

GIXRD

Grazing-incidence XRD (GIXRD) was performed on a PANalytical® Empyrean diffractometer with Cu K_α radiation and a fixed incidence angle of 0.5°. The diffractograms were measured between 15° and 60° 2θ with a step size of 0.02° and a scan duration per step of 5 s.

XPS

X-ray photoelectron spectroscopy (XPS) was performed with a monochromatic Al K_α radiation (Surface Science Instruments®, S-Probe). Scans were done with 32 eV pass energy resulting in high-resolution scans with full-width half maximum of 1 eV. The scans were calibrated to the C_{1s} peak at 284.60 eV.

Cell Assembly

After LMO crystallization, the backside of the coated StSt substrate must be polished in order to remove the oxide layer formed during the annealing. Round cathodes with a diameter of 16 mm (2.01 cm² area) were cut. These electrodes were dried under vacuum (10^{-2} mbar) at 110 °C for 10 h and transferred into an argon-filled glovebox (H_2O < 1 ppm and O_2 < 1 ppm). Pouch cells were assembled with a Whatman GF/F glass separator and Li-metal as anode. The liquid electrolyte consists of a 1:1 vol% mixture of ethylene carbonate (EC) and dimethyl carbonate (DMC) with 1 M $LiPF_6$ (LP30, BASF®).

GCPL & EIS

Galvanostatic cycling with potential limits (GCPL) and electrochemical impedance spectroscopy (EIS) were performed on a VMP-300 galvanostat (Biologic®) in a temperature-controlled climatic chamber (Memmert® IPP260^{PLUS}) at 25 °C. After a rest step of 12 h for acclimatization, GCPL measurement was conducted with a current density of 30 µA/cm² between 4.4 V vs. Li/Li^+ and 3.2 V vs. Li/Li^+ for 24 cycles. Constant voltage steps were performed after each constant current charge step at 4.4 V for 5 min or a current density limit of 0.5 µA/cm. After the 24th cycle, the cells were charged to 4.4 V with 30 µA/cm² and then a constant voltage step was conducted at 4.4 V for either 3 h or until a current density limit of 0.75 µA/cm² was reached in order to obtain quasi-stable conditions for the following EIS measurements. Immediately after the constant voltage step, EIS measurements were performed at 4.4 V in the frequency range between 1 MHz and 1 mHz with an amplitude of 5 mV. Two cells of each parameter set were tested.

The rate capability tests were conducted on a battery cycler (Maccor® 4000) with the same test protocol for each cycle as described above. The current densities were varied between 200 µA/cm² and 10 µA/cm².

Optimization of Preparation and ITO Interlayers

In order to investigate the limits of the ITO|StSt substrates with respect to interdiffusion and electrochemical performance, a few parameters in the preparation of the LMO|ITO|StSt samples had been changed. The crystallization temperatures of 600 °C, 700 °C and additionally 800 °C should be tested so that a thicker StSt substrate of 100 µm instead of 30 µm was used in order to withstand the thermal tensions at 800 °C. For the ITO deposition, a lower withdrawal velocity of 50 mm/min was used to obtain thinner layers of ca. 50 nm. The ITO layers were rapidly crystallized at 600 °C for 10 min. In order to investigate the interdiffusion processes as a function of the ITO layer thickness, up to a maximum of four ITO interlayers were dip-coated subsequently. After each dip-coating process, the layers were crystallized. The electrochemical performance was measured with the same cell assembly, rate capability test and cycling protocol as described above. Two cells of each parameter set had been measured.

9.4 Experimental Part of Study on the Cathode/SSE Interface

Preparation of LMO Double-Layer Thin-Films and LTO or TiO_2 Coatings

LMO|ITO|StSt thin-film cathodes were prepared by the same procedure as described above (**Chapter 9.3**). However, for this study, double LMO layers were used. A single LMO layer was deposited via dip-coating from a sol solution and subsequently dried at 300 °C for 30 min. Then a second LMO layer was deposited and dried at 300 °C for 30 min. Finally, the layer stacks were crystallized either at 600 °C for 1 h or 700 °C for 1 h.

LTO and TiO2 coatings were dip-coated from sol solutions.

The LTO sol was prepared by dissolving stoichiometric amounts of lithium acetate and titanium (IV) isopropoxide in a mixture of ethanol and acetic acid. 37% (w/w) hydrochloric acid was added. The solution with a solid content of 5.6 wt% was stirred for at least 2 h. It was further diluted with ethanol in a volume ratio of 1:3.

For the TiO2 sol, titanium acetyl acetonate was synthesized in a first step by slowly dissolving titanium ethoxide in acetyl acetonate and subsequent evaporation of the solvent at 100 °C for 5 h by using a rotary evaporator operating at a pressure of 40 mbar. The titanium acetyl acetonate powder was dissolved in a mixture of ethanol and 1,5-pentandiol (90:10 wt%), which results in a solid content of 6 wt%. The sol was then diluted with ethanol in a volume ratio of 1:3.

These sols were used to prepare the coatings on top of the LMO double-layers via dip-coating. Two withdraw velocities were used: 50 mm/min for thinner layers (< 10 nm) and 200 mm/min for thicker layers (ca. 20 nm). The coatings were rapidly crystallized at 600 °C for 10 min in ambient air.

LIPON Preparation

LIPON was deposited on top of the LMO cathodes with and without LTO or TiO_2 interlayers in collaboration with our partners at the Swiss Federal Laboratories of Material Science and Technology (EMPA, Switzerland) in cooperation with the group of Yaroslav E. Romanyuk. An Orion RF magnetron sputtering system of AJA International Inc.® was used. The amorphous LIPON SSE was deposited via co-sputtering of Li_3PO_4 and Li_2O at a power of 100 W and 120 W, respectively. This happened in combination with a 50 sccm N_2 gas flow at a pressure of 0.4 Pa. A sputter time of ca. 16 h resulted in a LIPON layer thickness of ca. 1 µm.

Ga-LLZO Preparation

Ga-LLZO was deposited on top of the LMO cathodes with and without LTO or TiO_2 interlayers in collaboration with our partners at the Swiss Federal Laboratories of Material Science and Technology (EMPA, Switzerland) in cooperation with the group of Yaroslav E. Romanyuk. An Orion RF magnetron sputtering system of AJA International Inc.® was used. The Ga-LLZO SSE was deposited following the procedure described by Sastre et al.[78,186] $Li_{6.25}Ga_{0.25}La_3Zr_2O_{12}$ and Li_2O targets were used for co-sputtering at powers of 62 W and 180 W, respectively, in a 50 sccm Ar and 1 sccm Ar:O_2 gas flow at a pressure of 0.3 Pa. Afterwards the Ga-LLZO were crystallized at 650 °C for 1 h in a controlled O_2 atmosphere with a heating and cooling rate of 10 K/min.

SEM

SEM images have been taken on a ZEISS® Supra 25 microscope. The accelerating voltage was usually set to 2.5 kV. Cross-sections were prepared by embedding the samples in an epoxy resin and polishing them by means of a JOEL® SM-0910 cross-section polisher in argon atmosphere.

GIXRD

Grazing-incidence XRD (GIXRD) was performed on a Bruker® D8 Discover diffractometer with Cu K_α radiation and a fixed incidence angle of 2°. The diffractograms were measured between 15° and 60° 2θ with a step size of 0.02° and a scan duration per step of 5 s.

ToF-SIMS

Time-of-flight secondary ion mass spectrometry (ToF-SIMS) was performed on a ToF.SIMS5 system from IONTOF® in collaboration with our partners of the group of Y. E. Romanyuk at Swiss Federal Laboratories of Material Science and Technology (EMPA, Switzerland). Sputtering was performed at a 300 x 300 µm² area at the sample surface with a Cs^+ sputtering ion beam with an acceleration voltage of 2 kV and a current of 110 nA. Compositional depth-profiles were measured by means of an analysis ion source of Bi^+ primary ions with an acceleration voltage of 25 kV and a current of 1.2 pA on a 50 x 50 µm² area within the sputtering crater.

Cell Assembly

The coated LMO cathodes and the Ga-LLZO @ coated LMO samples were electrochemically characterized in liquid electrolyte cells. The backside of the coated StSt substrate must be polished in order to remove the oxide layer formed during the annealing. Because of the thicker StSt substrate (100 µm), the samples were cut in 1 x 1 cm² instead of punching out round samples. These electrodes were dried under vacuum (10^{-2} mbar) at 120 °C for 12 h and transferred into an argon-filled glovebox (H_2O < 1 ppm and O_2 < 1 ppm). Pouch cells were assembled with a Whatman GF/F glass separator and Li-metal as anode. The liquid electrolyte consists of a 1:1 vol% mixture of ethylene carbonate (EC) and dimethyl carbonate (DMC) with 1 M $LiPF_6$ (LP30, BASF®).

The LIPON samples were tested in an ASSB full cell set-up. The full cells were prepared in a Nexped system by Angstrom Engineering® by depositing 2 µm Li and 200 nm Cu through a mask on top of the LIPON layer. The mask led to circular cells with a diameter of 1 mm (0.00785 cm² electrode area). The assembling and electrochemical characterization had been done in a glovebox at the Swiss Federal Laboratories of Material Science and Technology (EMPA, Switzerland) in collaboration with the group of Y. E. Romanyuk.

Electrochemical Characterization of coated LMO and LIPON Full Cells

The electrochemical characterizations of the LIPON cells were performed on a VMP-300 galvanostat (Biologic®) at the Swiss Federal Laboratories of Material Science and Technology (EMPA, Switzerland) in collaboration with the group of Y. E. Romanyuk. The rate capability tests of the coated LMO cells were performed on a battery cycler (Maccor® 4000) at the Fraunhofer ISC. The rate capability tests and long-term cycling tests were performed at 25 °C after a 12 h rest step for acclimatization.

Rate Capability Tests

The GCPL test procedure for the rate capability tests included potential limits of 4.4 V vs. Li/Li^+ and 3.1 V vs. Li/Li^+. No constant voltage step after the constant current charge step was performed. The current densities were varied between 10 µA/cm² and 400 µA/cm² after each 5th cycle.

Long-Term Cycling Tests

Long-term cycling tests were performed via GCPL within the potential limits of 4.4 V vs. Li/Li^+ and 3.1 V vs. Li/Li^+ for 1,000 cycles. No constant voltage step after the constant current charge step was performed. The chosen current densities were deduced from the rate capability tests and were 100 µA/cm² for the coated and uncoated LMO samples annealed at 600 °C and 10 µA/cm² for the coated and uncoated LMO samples annealed at 700 °C. The LIPON samples with and without interlayer on top of 600 °C annealed LMO were tested with 100 µA/cm².

Electrochemical Characterization of Ga-LLZO Cells

Since the first GCPL tests of the Ga-LLZO cells showed just polarization in the potential range of 4.4 V vs. Li/Li^+ and 3.1 V vs. Li/Li^+ at a current density of 1 µA/cm², the lower potential limit was set to 2.0 V vs. Li/Li^+. As the first initial cycles in the first tests showed already side reactions, five formation cycles were introduced with 5 µA/cm² and a constant voltage step after charge with the end criteria of either 3 h or a current density limit of 0.2 µA/cm². These formation steps were meant to let CEI or SEI formation complete. Afterward, long-term cycling at 1 µA/cm² without a constant voltage step was conducted.

10 Appendix

10.1 List of Figures

Fig. 2.1 Schematics of LiBs consisting of $LiMO_2$ (M = transition metal such as Mn, Ni, Co) as cathode and graphite in full cell design as well as Li-metal in half cell design as anodes. The listed redox reactions are insertion/extraction reactions for the $LiMnO_2$ and graphite as well as Li plating and stripping on the Li-metal. Adapted from T. B Reddy and D. Linden: Linden's handbook of batteries (2011, 4th ed., McGraw-Hill).[5] 4

Fig. 2.2 Cell voltage as a function of operating current including the fractions of the three loss mechanisms. Adapted from T. B Reddy and D. Linden: Linden's handbook of batteries (2011, 4th ed., McGraw-Hill).[5] 6

Fig. 2.3 Crystal structures reprinted from Julien et al.[13] (published under CC-BY license in MDPI: *inorganics* 2014) of the three common active material types on the left: the Li-ions in green and the MO_6 octahedrons in blue for $LiCoO_2$, in purple for $LiMn_2O_4$ and in brown for $LiFePO_4$. On the right: the value ranges of the Li diffusivity D_{Li} and electrical conductivity σ_{el}.[15] 10

Fig. 2.4 **a)** d-orbital splitting regarding the crystal field theory including the corresponding $Mn^{4+}O_6$ and $Mn^{3+}O_6$ octahedrons, latter exhibits Jahn-Teller distortion, which induces further splitting of the e_g and t_{2g} energy levels. **b)** Discharge profile of $Li_xMn_2O_4$ for the lithiation between $0 < x < 2$ reprinted with permission from Goodenough et al.[19]. © American Chemical Society 2013. 11

Fig. 2.5 Scheme of the ASSB concept regarding the various ionic conductivities σ_i of the SSE on the atomic, micro and macro scale as well as the interaction of the cathode particles and SSE defined by the area-specific resistances (ASR_i) and contact losses (pores in black) on the device scale. These resistances are summed up in the total device impedance (Z_{SSB}) of the ASSB. Reprinted by permission from Springer Nature: Nature Materials, Famprikis et al.[7] (2019): © Springer Nature 2019. 16

Fig. 2.6 Important properties of ternary composite cathodes consisting of cathode active material, ceramic SSE and electrically conductive additive. 17

Fig. 2.7 **a)** Evolution of the chemical potential of Li μ_{Li} (right axis) and the corresponding electrode potentials (V, left axis) across the SSE in contact with anode and cathode. Accumulation and depletion of Li-ions (opposite of vacancy depletion and accumulation) form space-charge layers (comparable to double layer formation in liquid electrolytes) and concentration gradients, which can directly lead to decomposition of the SSE and/or reaction with the electrodes. Reprinted by permission from Springer Nature: Nature Materials, Famprikis et al.[7] (2019): © Springer Nature 2019. 17

Fig. 2.8 Schemes of a thin-film solid-state battery (TF-SSB, left) and a bulk ASSB (right) including protecting interlayer (Interface layer) against electrochemical or chemical decomposition and intermixing. Given cell thicknesses are without current collectors. 19

Fig. 2.9 a) Total ionic conductivities of the various SSE material classes. Ionic conductivity of a liquid electrolyte (EC:DMC, 1 M $LiPF_6$) marked with the dashed line. Reprinted with permission from Bachman et al.[63] (2016). © 2016 American Chemical Society. 21

Fig. 2.10 a) Crystal lattice structure of rhombohedral LATP. Reprinted with permission from Epp et al.[66] (published under CC BY 3.0 license in Royal Society of Chemistry: *Phys. Chem. Chem. Phys.* 2015). 23

Fig. 2.11 Curve of relative density during the sintering process consisting of the heating ramp and subsequent isothermal holding step at maximum temperature.[86] SEM images represent microstructures of the three sintering stages. Three SEM images, which demonstrate appropriately the sintering stages, are chosen carefully from **Chapter 5**.............................. 25

Fig. 2.12 Ion conduction through crystal lattice and grain boundaries (GB) including simplified energy levels and activation energies $E_{a,b}$ and $E_{a,gb}$ for ion hopping within the crystal lattice and over grain boundaries, respectively. Brick-Layer model for ion conduction representing grains with thickness d_g and grain boundaries with thickness d_{gb}. Serial conduction through grains and grain boundaries on the right bottom. Parallel conduction along grain boundaries on the left bottom.. 31

Fig. 3.1 a) Diffraction of X-rays at lattice planes of a unit cell. **b)** Various orientations for lattice planes adapted from Carter and Norton (2007).[90] **c)** X-ray diffraction pattern of $LiMn_2O_4$ (ICSD 85398)... 34

Fig. 3.2 Bragg-Brentano Geometry usually used for powder samples as well as grazing-incidence geometry with fixed incidence angle γ for thin-film samples................................ 35

Fig. 3.3 a) Set-up of a thermal-optical measurement device. Reprinted by permission from Elsevier: Journal of European Ceramic Society, Baber et al.[121] (2007) © Elsevier 2007. **b)** Determination of shrinkage of sample pellet by means of the CCD camera. 36

Fig. 3.4 a) Scheme of ToF-SIMS set-up. **b)** SEM image of sputtering crater via sputtering ion beam and measurement region via analysis ion beam. 37

Fig. 3.5 a) Alternating voltage and phase-shifted (Φ) alternating current response. **b)** Nyquist plot of impedance Z^* in imaginary numbers at particular ω. **c)** Nyquist plot of RC component obtained by scanning through ω.. 39

Fig. 3.6 a) Dimensions of SSE pellet required for the determination of the ionic conductivity. **b)** Theoretical Nyquist plot consisting of two semicircles for bulk and grain boundary conduction of Li-ions in ceramic SSEs. **c)** Experimentally obtained Nyquist plot of a LATP SSE pellet measured at room temperature. 41

Fig. 3.7 a) Nyquist plot of a battery cell with the internal resistance R_{Ω}, the semicircles of the RC components for the insulating layer (corresponding to R_{In}) and for the charge transfer (corresponding to R_{CT}) as well as the Warburg impedance W_0. **b)** The corresponding equivalent circuit. 42

Fig. 3.8 Plots obtained from GCPL analysis of a $LiMn_2O_4$ thin-film cell with liquid electrolyte and Li-metal anode. **a)** Potential and current as a function of time **b)** Voltage profile of one cycle. **c)** Charge and discharge capacities as well as coulombic efficiencies as a function of cycle number. **d)** Differential capacity plots of the voltage profile presented in **b)**. 44

Fig. 4.1 Manufacturing of bulk cathode composites can result in decomposition and intermixing of the initial components. AM = active material; SSE = solid-state electrolyte. 46

Fig. 4.2 Experimental plan of the investigation of the thermal stabilities of LATP in combination with various Mn-based active materials. Experimental steps (green), parameters (red) and measured properties (orange) 49

Fig. 4.3 SEM images of the starting powders: **a)** LATP, **b)** LMO-s, **c)** LMO-l and **d)** LMP. Particle size distributions are comparable and particle sizes are < 1 µm. Published by and reprinted from Rumpel et al.[130] (published under CC-BY license in Royal Society of Chemistry: *Materials Advances* 2022). 50

Fig. 4.4 Characterization of starting powders LATP (dark green), LMO-s (blue), LMO-l (red) and LMP (light green): **a)** XRD patterns and **b)** DSC-TG profiles. Published by and reprinted from Rumpel et al.[130] (published under CC-BY license in Royal Society of Chemistry: *Materials Advances* 2022). 51

Fig. 4.5 Results of the DSC-TG and MS analyses of a 1:1 vol% LMO-s + LATP powder mixture measured in argon atmosphere with 10 K/min. Published by and reprinted from Rumpel et al.[130] (published under CC-BY license in Royal Society of Chemistry: *Materials Advances* 2022). 52

Fig. 4.6 Selected HT-XRD patterns and their Rietveld refinements of the LMO-s + LATP pellet sintered in argon atmosphere at 500 °C, 700 °C and 900 °C. Additionally, the XRD pattern of the pristine LMO-s + LATP powder is presented. Published by and reprinted from Rumpel et al.[130] (published under CC-BY license in Royal Society of Chemistry: *Materials Advances* 2022). 54

Fig. 4.7 Weight percentages wt% of crystalline phases obtained by Rietveld refinement of the LMO-s + LATP pellet as a function of the annealing temperature. Heating up to 900 °C with 3 K/min, holding step at 900 °C for 1 h, and afterward cooling with 3 K/min to 30 °C. Published by and reprinted from Rumpel et al.[130] (published under CC-BY license in Royal Society of Chemistry: *Materials Advances* 2022). 54

Fig. 4.8 a) SEM cross-section and **b)** EDS analyses of a LMO-s + LATP pellet sintered for 2 h at 800 °C in argon atmosphere. Published by and reprinted from Rumpel et al.[130] (published under CC-BY license in Royal Society of Chemistry: *Materials Advances* 2022). 55

Fig. 4.9 Results of the DSC-TG and MS analyses of a 1:1 vol% LMO-l + LATP powder mixture measured in argon atmosphere with 10 K/min. Published by and reprinted from Rumpel et al.[130] (published under CC-BY license in Royal Society of Chemistry: *Materials Advances* 2022). 57

Fig. 4.10 Selected HT-XRD patterns and their Rietveld refinements of the LMO-l + LATP pellet sintered in argon atmosphere at 500 °C, 700 °C and 1000 °C. Additionally, the XRD pattern of the pristine LMO-l + LATP powder is presented. Published by and reprinted from Rumpel et al.[130] (published under CC-BY license in Royal Society of Chemistry: *Materials Advances* 2022). 59

Fig. 4.11 Weight percentages wt% of crystalline phases obtained by Rietveld refinement of the LMO-l + LATP pellet as a function of the annealing temperature. Heating up to 1000 °C with 3 K/min, holding step at 1000 °C for 1 h, and afterward cooling with 3 K/min to 30 °C. Published by and reprinted from Rumpel et al.[130] (published under CC-BY license in Royal Society of Chemistry: *Materials Advances* 2022)... 59

Fig. 4.12 a) SEM cross-section and **b)** EDS analyses of a LMO-l + LATP pellet sintered for 2 h at 800 °C in argon atmosphere. Published by and reprinted from Rumpel et al.[130] (published under CC-BY license in Royal Society of Chemistry: *Materials Advances* 2022). 60

Fig. 4.13 Results of the DSC-TG and MS analyses of a 1:1 vol% LMP + LATP powder mixture measured in argon atmosphere with 10 K/min. Published by and reprinted from Rumpel et al.[130] (published under CC-BY license in Royal Society of Chemistry: *Materials Advances* 2022). 63

Fig. 4.14 Selected HT-XRD patterns and their Rietveld refinements of the LMP + LATP pellet sintered in argon atmosphere at 500 °C, 700 °C and 800 °C. Additionally, the XRD pattern of the pristine LMP + LATP powder is presented. Published by and reprinted from Rumpel et al.[130] (published under CC-BY license in Royal Society of Chemistry: *Materials Advances* 2022). 64

Fig. 4.15 Weight percentages wt% of crystalline phases obtained by Rietveld refinement of the LMP + LATP pellet as a function of the annealing temperature. Heating up to 800 °C with 3 K/min, holding step at 800 °C for 4 h, and afterward cooling with 3 K/min to 30 °C. Published by and reprinted from Rumpel et al.[130] (published under CC-BY license in Royal Society of Chemistry: *Materials Advances* 2022). 64

Fig. 4.16 a) SEM cross-section and **b)** EDS analyses of a LMP + LATP pellet sintered for 2 h at 800 °C in argon atmosphere. Published by and reprinted from Rumpel et al.[130] (published under CC-BY license in Royal Society of Chemistry: *Materials Advances* 2022). 65

Fig. 4.17 Results of the DSC-TG and MS analyses of **a)** 1:1:1 vol% LMP + LATP + Ag powder mixture and **b)** pure Ag powder measured in argon atmosphere with 10 K/min. Published by and reprinted from Rumpel et al.[130] (published under CC-BY license in Royal Society of Chemistry: *Materials Advances* 2022). 70

Fig. 4.18 HT-XRD patterns and their Rietveld refinements of the LMP + LATP + Ag pellet measured at RT before and after sintering in argon atmosphere at 800 °C for 4 h with a heating and cooling rate of 3 K/min. Published by and reprinted from Rumpel et al.[130] (published under CC-BY license in Royal Society of Chemistry: *Materials Advances* 2022). 71

Fig. 4.19 Weight percentages wt% of crystalline phases obtained by Rietveld refinement of the LMP + LATP + Ag pellet as a function of the annealing temperature. Heating up to 800 °C with 3 K/min, holding step at 800 °C for 4 h, and afterward cooling with 3 K/min to 30 °C. Published by and reprinted from Rumpel et al.[130] (published under CC-BY license in Royal Society of Chemistry: *Materials Advances* 2022). 72

Fig. 4.20 **a)** SEM cross-section and **b)** EDS analyses of a LMP + LATP + Ag pellet sintered for 2 h at 800 °C in argon atmosphere. EDS energies for Ag are in accordance with literature.[146] Published by and reprinted from Rumpel et al.[130] (published under CC-BY license in Royal Society of Chemistry: *Materials Advances* 2022). 73

Fig. 5.1 Li-ion migration through LATP microstructure can be hindered by cracks, pores and secondary phases, which depend on the sintering behavior of LATP. 76

Fig. 5.2 Experimental plan of the investigation of Li_3PO_4 as sintering additive for LATP. Experimental steps (green), parameters (red) and measured properties (orange). 79

Fig. 5.3 XRD patterns of all powder mixtures sintered as pellets at 900 °C for 24 h. Pure LATP (dark green), LATP + 3 vol% Li_3PO_4 (light green), LATP + 5 vol% Li_3PO_4 (red) and LATP + 10 vol% Li_3PO_4 (blue). Published by and reprinted from Rumpel et al.[148] (published under CC-BY license in Royal Society of Chemistry: *Materials Advances* 2022). 80

Fig. 5.4 **a)** SEM cross-section and **b)** corresponding EDS analyses of a LATP + 5 vol% Li3PO4 sample sintered at 950 °C for 24 h. Published by and reprinted from Rumpel et al.[148] (published under CC-BY license in Royal Society of Chemistry: *Materials Advances* 2022). 81

Fig. 5.5 Thermal diffusivities, relative densities and temperature profiles as a function of time of **a)** the pure LATP samples sintered between 800 °C and 950 °C and **b)** the LATP + 5 vol% Li_3PO_4 samples sintered between 600 °C and 950 °C. Published by and reprinted from Rumpel et al.[148] (published under CC-BY license in Royal Society of Chemistry: *Materials Advances* 2022). 83

Fig. 5.6 Thermal diffusivities and relative densities of the pure LATP (green) and the LATP + 5 vol% Li_3PO_4 (red) pellets sintered at 900 °C. The heating ramp is plotted as a function of temperature and the following holding step as a function of time. The courses during the heating ramp are representative of the further pellets. Published by and reprinted from Rumpel et al.[148]

(published under CC-BY license in Royal Society of Chemistry: *Materials Advances* 2022). 83

Fig. 5.7 Values of shrinkage at the end of sintering and the porosity as a function of sintering temperature of **a)** the pure LATP samples and **b)** LATP + 5 vol% Li_3PO_4 samples. Published by and reprinted from Rumpel et al.[148] (published under CC-BY license in Royal Society of Chemistry: *Materials Advances* 2022). 84

Fig. 5.8 SEM cross-sections of the pure LATP pellets sintered at **a)** 850 °C, **b)** 900 °C and **c)** 950 °C and LATP + 5 vol% Li_3PO_4 pellets sintered at **d)** 650 °C, **e)** 700 °C, **f)** 750 °C, **g)** 800 °C, **h)** and **k)** 850 °C, **i)** and **l)** 900 °C and **j)** 950 °C. The sintering time was 24 h. Accelerating voltage was 5 kV. A backscattered electron detector was used to obtain a higher contrast. Published by and reprinted from Rumpel et al.[148] (published under CC-BY license in Royal Society of Chemistry: *Materials Advances* 2022). 85

Fig. 5.9 SEM cross-sections with higher magnification of LATP + 5 vol% Li_3PO_4 samples sintered at **a)** 650 °C, **b)** 700 °C and **c)** 750 °C. 86

Fig. 5.10 Nyquist plots including fits of **a)** samples sintered at 900 °C for 24 h. **b)** Fit of EIS data of a pure LATP pellet sintered at 900 °C for 24 h using the given equivalent circuit. Published by and reprinted from Rumpel et al.[148] (published under CC-BY license in Royal Society of Chemistry: *Materials Advances* 2022). 87

Fig. 5.11 Bulk conductivities σ_b of the samples sintered at various sintering temperatures. Published by and reprinted from Rumpel et al.[148] (published under CC-BY license in Royal Society of Chemistry: *Materials Advances* 2022). 89

Fig. 5.12 Grain boundary conductivities σ_{gb} of the samples sintered at various sintering temperatures. Published by and reprinted from Rumpel et al.[148] (published under CC-BY license in Royal Society of Chemistry: *Materials Advances* 2022). 90

Fig. 5.13 Grain boundary capacitances C_{gb} of the samples sintered at various sintering temperatures. Published by and reprinted from Rumpel et al.[148] (published under CC-BY license in Royal Society of Chemistry: *Materials Advances* 2022). 91

Fig. 5.14 Arrhenius plots obtained from the temperature-dependent EIS measurements of **a)** pure LATP, **b)** LATP + 3 vol% Li_3PO_4, **c)** LATP + 5 vol% Li_3PO_4 and **d)** LATP + 10 vol% Li_3PO_4. Solid lines represent the linear fits. Published by and reprinted from Rumpel et al.[148] (published under CC-BY license in Royal Society of Chemistry: *Materials Advances* 2022). 92

Fig. 5.15 Grain boundary activation energies $E_{a,gb}$ of the samples sintered at various sintering temperatures. Published by and reprinted from Rumpel et al.[148] (published under CC-BY license in Royal Society of Chemistry: *Materials Advances* 2022). 94

Fig. 5.16 Comparison of grain boundary conductivity σ_{gb} and porosity of the LATP + 5 vol% Li_3PO_4 samples. 97

Fig. 5.17 Comparison of grain boundary conductivity σ_{gb} and grain size of the LATP + 5 vol% Li_3PO_4 samples. 99

Fig. 6.1 Interdiffusion processes between StSt current collector and LMO thin-film can occur during the high-temperature manufacturing process of TF-SSBs. 103

Fig. 6.2 Experimental plan of the investigation into the cathode / current collector interface. Experimental steps (green), parameters (red) and measured properties (orange). 106

Fig. 6.3 SEM cross-sections of **a)** LMO @ StSt (LS700), **b)** LMO @ ITO (LIS700), **c)** LMO @ Pt (LPS700) and **d)** LMO @ Au (LAS700) annealed at 700 °C for 1 h. LMO layer thicknesses are approx. 160 nm. Layer thicknesses of Pt, Au and ITO are approx. 100 nm. Published by and reprinted from Rumpel et al.[168] (published under CC-BY license in Royal Society of Chemistry: *Materials Advances* 2021). 108

Fig. 6.4 Top view SEM images of the LMO layers annealed at 600 °C on **a)** StSt, **b)** ITO, **c)** Pt and **g)** Au as well as annealed at 700 °C on **d)** StSt, **e)** ITO, **f)** Pt and **h)** Au. Published by and reprinted from Rumpel et al.[168] (published under CC-BY license in Royal Society of Chemistry: *Materials Advances* 2021). 109

Fig. 6.5 ToF-SIMS depth profiles of 600 °C annealed samples: **a)** LMO @ StSt, **c)** LMO @ ITO, **e)** LMO @ Pt and **g)** LMO @ Au; as well as 700 °C annealed samples: **b)** LMO @ StSt, **d)** LMO @ ITO, **f)** LMO @ Pt and **h)** LMO @ Au. Sputter time is normalized to 1 for the interface between LMO and interlayer. LMO elements (Li^- and MnO^-) in green, StSt elements (AlO^- and CrO^-) in red and interlayer elements (InO^-, Pt^-, PtO^-, Au^- and AuO^-) in blue. Published by and reprinted from Rumpel et al.[168] (published under CC-BY license in Royal Society of Chemistry: *Materials Advances* 2021). 111

Fig. 6.6 a) GIXRD patterns of LMO on top of StSt (red) and ITO (cyan) and **b)** GIXRD patterns of LMO on top of Pt (blue) and Au (green). **c)** Analysis of the shifts of the reflection positions of all samples: LIS600 is set as a benchmark. Published by and reprinted from Rumpel et al.[168] (published under CC-BY license in Royal Society of Chemistry: *Materials Advances* 2021). 113

Fig. 6.7 XPS data of LMO @ StSt and LMO @ ITO samples annealed at 600 °C and 700 °C. **a)** Mn $2p_{3/2}$ region and **b)** Fe $2p_{1/2}$ and Fe $2p_{3/2}$ region. Published by and reprinted from Rumpel et al.[168] (published under CC-BY license in Royal Society of Chemistry: *Materials Advances* 2021). 114

Fig. 6.8 Voltage profiles of 600 °C annealed samples: **a)** LMO @ StSt, **c)** LMO @ ITO, **e)** LMO @ Pt and **g)** LMO @ Au; as well as 700 °C annealed samples: **b)** LMO @ StSt, **d)** LMO @ ITO, **f)** LMO @ Pt and **h)** LMO @ Au. The color gradient starts with green for cycle 1 and ends with red for cycle 24. Current density: 30 µA/cm². Potential limits: 3.2 V and 4.4 V vs. Li/Li^+. Published by and reprinted from Rumpel et al.[168] (published under CC-BY license in Royal Society of Chemistry: *Materials Advances* 2021). 115

Fig. 6.9 GCPL results of the LMO@StSt (red), LMO@Pt (blue), LMO@Au (green) and LMO@ITO (cyan) samples. **a)** Voltage profile of cycle 24 at 30 µA/cm² and **b)** discharge capacities as a function of cycles at 30 µA/cm². Published by and reprinted from Rumpel et al.[168] (published under CC-BY license in Royal Society of Chemistry: *Materials Advances* 2021). 116

Fig. 6.10 GCPL results of the LMO@StSt (red), LMO@Pt (blue), LMO@Au (green) and LMO@ITO (cyan) samples. **a)** Coulombic efficiencies of cycle 24 and **b)** discharge capacities during the rate capability test. Published by and reprinted from Rumpel et al.[168] (published under CC-BY license in Royal Society of Chemistry: *Materials Advances* 2021). 117

Fig. 6.11 GCPL results of the LMO@StSt (red), LMO@Pt (blue), LMO@Au (green) and LMO@ITO (cyan) samples. **a)** and **b)** Differential capacity plots of cycle 24 (representative cells). Published by and reprinted from Rumpel et al.[168] (published under CC-BY license in Royal Society of Chemistry: *Materials Advances* 2021). 118

Fig. 6.12 Current decay during the CV step @ 4.4 V vs. Li/Li^+ for 3 h. Published by and reprinted from Rumpel et al.[168] (published under CC-BY license in Royal Society of Chemistry: *Materials Advances* 2021). 120

Fig. 6.13 Comparison of Nyquist plots of the samples annealed at **a)** 600 °C and **b)** 700 °C. Published by and reprinted from Rumpel et al.[168] (published under CC-BY license in Royal Society of Chemistry: *Materials Advances* 2021). 120

Fig. 6.14 Nyquist plots of the EIS data incl. fits using the equivalent circuit: **a)** LS600, **b)** LIS600, **c)** LPS600, **d)** LS700, **e)** LIS700, **f)** LPS700, **g)** LAS600, **f)** LAS700 and **i)** the used equivalent circuit. Published by and reprinted from Rumpel et al.[168] (published under CC-BY license in Royal Society of Chemistry: *Materials Advances* 2021). 122

Fig. 6.15 Photographs of 5 x 5 cm² LMO/ITO/StSt samples annealed at 700 °C for 1 h on **a)** a 30 µm StSt foil and **b)** a 100 µm StSt foil. 127

Fig. 6.16 SEM cross-sections of LMO @ ITO @ StSt samples with various ITO interlayer thicknesses annealed at 700 °C for 1 h. a) 1x ITO, b) 2x ITO, c) 3x ITO and d) 4x ITO interlayer. 127

Fig. 6.17 Top view SEM images of the LMO/ITO/StSt samples with 4x ITO interlayer annealed at a) 600 °C for 1 h, b) 700 °C for 1 h and c) 800 °C for 1 h. 128

Fig. 6.18 Voltage profiles of cycle 73 at 30 µA/cm² of samples with various interlayers and annealing temperatures: a) 600 °C for 1 h, b) 700 °C for 1 h, c) 800 °C for 1 h and d) the corresponding discharge capacities. 129

Fig. 6.19 Differential capacity plots of cycle 73 at 30 µA/cm² of samples with various interlayers and annealing temperatures: a) 600 °C for 1 h, b) 700 °C for 1 h, c) 800 °C for 1 h and d) the corresponding overvoltages. 130

Fig. 6.20 Discharge capacities of the rate capability tests as a function of the cycle number of samples with various interlayers and annealing temperatures: a) 600 °C for 1 h, b) 700 °C for 1 h, c) 800 °C for 1 h and d) comparison of the discharge capacities of cycle 81 at 10 µA/cm². 132

Fig. 7.1 Interdiffusion processes between Ga-LLZO SSE and LMO thin-film cathode can occur during the high-temperature manufacturing process of TF-SSBs........ 135

Fig. 7.2 Experimental plan of the investigation into the SSE / cathode interface. Experimental steps (green), parameters (red) and measured properties (orange). 138

Fig. 7.3 SEM top view images of LMO single layers annealed at 600 °C: **a)** without coating, **b)** and **c)** LTO and TiO_2 coatings deposited with 50 mm/min withdrawal velocity, **d)** and **e)** LTO and TiO_2 coatings deposited with 200 mm/min withdrawal velocity. 140

Fig. 7.4 GIXRD diffractograms of double-layer LMO samples on ITO|StSt without coating (green), with TiO2 coating (red) and with LTO coating (blue). **a)** LMO layers annealed at 600 °C and **b)** LMO layers annealed at 700 °C........ 141

Fig. 7.5 Electrochemical data obtained from rate capability tests of liquid electrolyte cells (LP 30, EC:DMC 1:1 vol%, 1 M $LiPF_6$). Voltage profiles of all samples with and without LTO and TiO_2 coatings on top of LMO_{600} at **a)** 10 µA/cm² (cycle 35) and **c)** 100 µA/cm² (cycle 20) as well as on top of LMO_{700} at **b)** 10 µA/cm² (cycle 35) and **d)** 100 µA/cm² (cycle 20). Discharge capacities during rate capability tests for **e)** coatings on LMO_{600} and **f)** coatings on LMO_{700}. 143

Fig. 7.6 Voltages profiles of long-term cycling tests in liquid electrolyte cells over 1,000 cycles. LMO_{600} samples tested at 100 µA/cm² **a)** without coating, **c)** with < 10 nm LTO coating and **e)** with < 10 nm TiO_2 coating. LMO_{700} samples tested at 10 µA/cm² **b)** without coating, **d)** with < 10 nm LTO coating and **f)** with < 10 nm TiO_2 coating........ 145

Fig. 7.7 Discharge capacities as a function of cycle number for the **a)** LMO_{600} samples and **b)** LMO_{700} samples tested in liquid electrolyte cells over 1,000 cycles. Corresponding coulombic efficiencies as a function of cycle number for the **c)** LMO_{600} samples and **d)** LMO_{700} samples. 147

Fig. 7.8 SEM cross-section of a LIPON @ LMO_{600} full cell with Li anode and Cu current collector........ 149

Fig. 7.9 Electrochemical data obtained from rate capability tests of LIPON full cells. Voltage profiles of all samples with and without LTO and TiO_2 interlayers between LIPON and LMO_{600} at **a)** 10 µA/cm² (cycle 35) and **c)** 100 µA/cm² (cycle 20) as well as between LIPON and LMO_{700} at **b)** 10 µA/cm² (cycle 35) and **d)** 100 µA/cm² (cycle 20). Discharge capacities during rate capability tests of samples with and without **e)** interlayers between LIPON and LMO_{600} and **f)** interlayers between LIPON and LMO_{700}........ 151

Fig. 7.10 Voltages profiles of long-term cycling tests in LIPON full cells over 1,000 cycles. LMO_{600} samples tested at 100 µA/cm² **a)** without interlayer, **b)** with < 10 nm LTO interlayer and **c)** with < 10 nm TiO_2 interlayer. 152

Fig. 7.11 **a)** Discharge capacities as a function of cycle number of the long-term cycling tests of the LIPON|Interlayer|LMO_{600} full cells and **b)** corresponding coulombic efficiencies as a function of the cycle number. 153

Fig. 7.12 GIXRD diffractograms of Ga-LLZO crystallized at 650 °C on top of **a)** pure LMO and **b)** LTO coated LMO. 156

Fig. 7.13 GIXRD diffractograms of Ga-LLZO crystallized at 650 °C on top of LMO_{700} with and without LTO and TiO_2 interlayer. 156

Fig. 7.14 SEM cross-sections of Ga-LLZO|LMO thin-film stacks **a)** without interlayer, **b)** with LTO (< 10 nm) interlayer and **c)** with TiO2 (< 10 nm) interlayer. 157

Fig. 7.15 ToF-SIMS depth profiles of Ga-LLZO|LMO thin-film stacks **a)** without interlayer, **b)** with LTO (< 10 nm) interlayer and **c)** TiO_2 (< 10 nm) interlayer. 159

Fig. 7.16 Voltage profiles Ga-LLZO|LMO cells: **a)** second cycle of cells cycled between 3.1 V and 4.4 V; **b)** initial cycles of cells cycled between 2.0 V and 4.4 V. 160

Fig. 7.17 Voltage profiles and corresponding differential capacity plots of the initial five cycles at 5 µA/cm² of the Ga-LLZO|LMO cells **a)** and **d)** without interlayer, **b)** and **e)** with LTO interlayer as well as **c)** and **f)** with TiO_2 interlayer. 161

Fig. 7.18 GCPL results of the Ga-LLZO|LMO cells with and without interlayer cycled with 1 µA/cm² between 2.0 V and 4.4 V: **a)** Discharge capacities as a function of cycle number and **b)** the corresponding coulombic efficiencies. 163

Fig. 7.19 Voltage profiles and corresponding differential capacity plots of the cycles 6 - 200 at 1 µA/cm² of the Ga-LLZO|LMO cells **a)** and **d)** without interlayer, **b) and e)** with LTO interlayer as well as **c)** and **f)** with TiO_2 interlayer. 165

Fig. 7.20 Voltage profiles of the last cycles before and the first cycles after the maintenance and two days' rest of Ga-LLZO|LMO cells **a)** without interlayer, **b)** with LTO interlayer and **c)** with TiO_2 interlayer. 167

10.2 List of Tables

Table 2.1 Electrochemical characteristics of selected cathode active materials adapted from Nitta et al.[14] 9

Table 2.2 Summary of SSE materials. Reprinted by permission from Springer Nature: Nature Materials, Manthiram et al.[46] (2017): © Springer Nature 2017. 20

Table 4.1 Summary of the results and findings of the analyses of the thermal stability of LMO-s and LATP. DSC Peak positions: 564 °C (P1), 645 °C (P2), 803 °C (P3), 862 °C (P4) and 916 °C (P5). 56

Table 4.2 Summary of the results and findings of the analyses of the thermal stability of LMO-l and LATP. DSC Peak positions: 662 °C (P1), 707 °C (P2), 816 °C (P3) and 915 °C (P4)... 62

Table 4.3 Summary of the results and findings of the analyses of the thermal stability of LMP and LATP. DSC Peak positions: 777 °C (P1) and 872 °C (P2). 67

Table 4.4 Comparison of remaining components after cooling of the 1:1 vol% powder mixtures of various active materials and LATP. 69

Table 6.1 Designation of the samples. 107

Table 6.2 Electrochemical results obtained from galvanostatic cycling. Published by and reprinted from Rumpel et al.[168] (published under CC-BY license in Royal Society of Chemistry: *Materials Advances* 2021). 119

Table 6.3 The ohmic resistance R_{Ω}, insulating layer resistance R_{In} and charge transfer resistance R_{CT} obtained by fitting the EIS data with the equivalent circuit shown in **Fig. 6.14**. Published by and reprinted from Rumpel et al.[168] (published under CC-BY license in Royal Society of Chemistry: *Materials Advances* 2021). 123

Table 7.1 Designation of the samples. 139

Table 7.2 Electrochemical results obtained from rate capability tests of liquid electrolyte cells. LMO_{600} and LMO_{700} samples without and with LTO and TiO_2 coatings. 144

Table 7.3 Electrochemical results obtained from long-term cycling tests in liquid electrolyte cells. LMO_{600} and LMO_{700} samples without and with LTO and TiO_2 coatings. 147

Table 7.4 Electrochemical results obtained from rate capability tests of LIPON full cells. LMO_{600} and LMO_{700} samples without and with LTO and TiO_2 interlayers. 152

Table 7.5 Electrochemical results obtained from long-term cycling of LIPON full cells. LMO_{600} samples without and with LTO and TiO_2 interlayers. 153

Table 7.6 Calculated potential onset and corresponding calculated phase equilibria for LLZO as well as LLZO in combination with $LiCoO_2$. Reprinted with permission from Zhu et al.[223] (2016). © 2016 The Royal Society of Chemistry. 170

Table 7.7 Redox regions obtained from differential capacity plots (**Fig. 7.20 g-i**) and corresponding converted capacities (**Fig. 7.20 d-f**) of cycle 350 for all samples. 170

11 References

1. J. Janek and W. G. Zeier, “A solid future for battery development,” Nat Energy **1** (9), 1167 (2016).
2. R. A. Huggins, *Advanced Batteries. Materials Science Aspects* (Springer US, Boston, MA, 2009).
3. J.-K. Park, ed., *Principles and applications of lithium secondary batteries* (Wiley-VCH, Weinheim, 2012).
4. T. B. Reddy and D. Linden, eds., *Linden's handbook of batteries*, 4th ed. (McGraw-Hill, New York, 2011).
5. Y.-S. Hu, “Batteries: Getting solid,” Nat Energy **1** (4), 652 (2016).
6. T. Famprikis, P. Canepa, J. A. Dawson, M. S. Islam, and C. Masquelier, “Fundamentals of inorganic solid-state electrolytes for batteries,” Nature materials **18** (12), 1278–1291 (2019).
7. W. Hou, X. Guo, X. Shen, K. Amine, H. Yu, and J. Lu, “Solid electrolytes and interfaces in all-solid-state sodium batteries: Progress and perspective,” Nano Energy **52**, 279–291 (2018).
8. K. Kerman, A. Luntz, V. Viswanathan, Y.-M. Chiang, and Z. Chen, “Review—Practical Challenges Hindering the Development of Solid State Li Ion Batteries,” J. Electrochem. Soc. **164** (7), A1731-A1744 (2017).
9. S. Randau, D. A. Weber, O. Kötz, R. Koerver, P. Braun, A. Weber, E. Ivers-Tiffée, T. Adermann, J. Kulisch, W. G. Zeier, F. H. Richter, and J. Janek, “Benchmarking the performance of all-solid-state lithium batteries,” Nat Energy **5** (3), 259–270 (2020).
10. Y. Zhu, X. He, and Y. Mo, “First principles study on electrochemical and chemical stability of solid electrolyte-electrode interfaces in all-solid-state Li-ion batteries,” Journal of Materials Chemistry A **4** (9), 3253–3266 (2016).
11. A. J. Bard and L. R. Faulkner, *Electrochemical methods. Fundamentals and applications* (John Wiley & Sons, New York, 1980).
12. C. H. Hamann, A. Hamnett, and W. Vielstich, *Electrochemistry*, 2., completely rev. and updated edition (Wiley-VCH, Weinheim, 2007).
13. C. M. Julien, A. Mauger, K. Zaghib, and H. Groult, “Comparative Issues of Cathode Materials for Li-Ion Batteries,” Inorganics **2** (1), 132–154 (2014).
14. N. Nitta, F. Wu, J. T. Lee, and G. Yushin, “Li-ion battery materials: present and future,” Materials Today **18** (5), 252–264 (2015).
15. M. Park, X. Zhang, M. Chung, G. B. Less, and A. M. Sastry, “A review of conduction phenomena in Li-ion batteries,” Journal of Power Sources **195** (24), 7904–7929 (2010).

16. C. Liu, Z. G. Neale, and G. Cao, "Understanding electrochemical potentials of cathode materials in rechargeable batteries," Materials Today **19** (2), 109–123 (2016).
17. M. Binnewies, M. Finze, M. Jäckel, P. Schmidt, H. Willner, and G. Rayner-Canham, *Allgemeine und Anorganische Chemie* (Springer Berlin Heidelberg, Berlin, Heidelberg, 2016).
18. L. Beyer and J. Angulo Cornejo, *Koordinationschemie* (Vieweg+Teubner Verlag, Wiesbaden, 2012).
19. J. B. Goodenough and K.-S. Park, "The Li-ion rechargeable battery: a perspective," Journal of the American Chemical Society **135** (4), 1167–1176 (2013).
20. J. B. Goodenough and Y. Kim, "Challenges for Rechargeable Li Batteries," Chem. Mater. **22** (3), 587–603 (2010).
21. F. Kong, R. C. Longo, M.-S. Park, J. Yoon, D.-H. Yeon, J.-H. Park, W.-H. Wang, S. KC, S.-G. Doo, and K. Cho, "Ab initio study of doping effects on LiMnO 2 and Li 2 MnO 3 cathode materials for Li-ion batteries," J. Mater. Chem. A **3** (16), 8489–8500 (2015).
22. M. Tuccillo, O. Palumbo, M. Pavone, A. B. Muñoz-García, A. Paolone, and S. Brutti, "Analysis of the Phase Stability of LiMO2 Layered Oxides (M = Co, Mn, Ni)," Crystals **10** (6), 526 (2020).
23. Michael M. Thackeray, "Manganese oxides for lithium batteries," Progress in Solid State Chemistry **25** (1-2), 1–71 (1997).
24. G. Vitins and K. West, "Lithium Intercalation into Layered LiMnO2," J. Electrochem. Soc. **144** (8), 2587–2592 (1997).
25. C. Li, H. P. Zhang, L. J. Fu, H. Liu, Y. P. Wu, E. Rahm, R. Holze, and H. Q. Wu, "Cathode materials modified by surface coating for lithium ion batteries," Electrochimica Acta **51** (19), 3872–3883 (2006).
26. N. H. Kwon, J. Conder, M. Srout, and K. M. Fromm, "Surface Modifications of Positive-Electrode Materials for Lithium Ion Batteries," Chimia **73** (11), 880–893 (2019).
27. A.-H. Marincaş and P. Ilea, "Enhancing Lithium Manganese Oxide Electrochemical Behavior by Doping and Surface Modifications," Coatings **11** (4), 456 (2021).
28. A. Gutierrez, N. A. Benedek, and A. Manthiram, "Crystal-Chemical Guide for Understanding Redox Energy Variations of M 2+/3+ Couples in Polyanion Cathodes for Lithium-Ion Batteries," Chem. Mater. **25** (20), 4010–4016 (2013).
29. T. Muraliganth and A. Manthiram, "Understanding the Shifts in the Redox Potentials of Olivine LiM 1− y M y PO 4 (M = Fe, Mn, Co, and Mg) Solid Solution Cathodes," J. Phys. Chem. C **114** (36), 15530–15540 (2010).

30. Q. Lu, Y. Jie, X. Meng, A. Omar, D. Mikhailova, R. Cao, S. Jiao, Y. Lu, and Y. Xu, “Carbon materials for stable Li metal anodes: Challenges, solutions, and outlook,” Carbon Energy **3** (6), 957–975 (2021).
31. C. P. Sandhya, B. John, and C. Gouri, “Lithium titanate as anode material for lithium-ion cells: a review,” Ionics **20** (5), 601–620 (2014).
32. J. Lu, Z. Chen, F. Pan, Y. Cui, and K. Amine, “High-Performance Anode Materials for Rechargeable Lithium-Ion Batteries,” Electrochem. Energ. Rev. **1** (1), 35–53 (2018).
33. D. Ma, Z. Cao, and A. Hu, “Si-Based Anode Materials for Li-Ion Batteries: A Mini Review,” Nano-micro letters **6** (4), 347–358 (2014).
34. D. Lin, Y. Liu, and Y. Cui, “Reviving the lithium metal anode for high-energy batteries,” Nature nanotechnology **12** (3), 194–206 (2017).
35. J.-G. Zhang, W. Xu, and W. A. Henderson, *Lithium Metal Anodes and Rechargeable Lithium Metal Batteries* (Springer International Publishing, Cham, 2017).
36. J. Landesfeind, J. Hattendorff, A. Ehrl, W. A. Wall, and H. A. Gasteiger, “Tortuosity Determination of Battery Electrodes and Separators by Impedance Spectroscopy,” J. Electrochem. Soc. **163** (7), A1373-A1387 (2016).
37. S. Hess, M. Wohlfahrt-Mehrens, and M. Wachtler, “Flammability of Li-Ion Battery Electrolytes: Flash Point and Self-Extinguishing Time Measurements,” J. Electrochem. Soc. **162** (2), A3084-A3097 (2015).
38. D. Aurbach, “Review of selected electrode–solution interactions which determine the performance of Li and Li ion batteries,” Journal of Power Sources **89** (2), 206–218 (2000).
39. K. Edström, T. Gustafsson, and J. O. Thomas, “The cathode–electrolyte interface in the Li-ion battery,” Electrochimica Acta **50** (2-3), 397–403 (2004).
40. N. Boaretto, I. Garbayo, S. Valiyaveettil-SobhanRaj, A. Quintela, C. Li, M. Casas-Cabanas, and F. Aguesse, “Lithium solid-state batteries: State-of-the-art and challenges for materials, interfaces and processing,” Journal of Power Sources **502** (7179), 229919 (2021).
41. N. Boaretto, L. Meabe, M. Martinez-Ibañez, M. Armand, and H. Zhang, “Review—Polymer Electrolytes for Rechargeable Batteries: From Nanocomposite to Nanohybrid,” J. Electrochem. Soc. **167** (7), 70524 (2020).
42. J. W. Fergus, “Ceramic and polymeric solid electrolytes for lithium-ion batteries,” Journal of Power Sources **195** (15), 4554–4569 (2010).
43. B. John and G. Cheruvally, “Polymeric materials for lithium-ion cells,” Polym. Adv. Technol. **28** (12), 1528–1538 (2017).

44. Y. Takeda, N. Imanishi, and O. Yamamoto, “Developments of the Advanced All-Solid-State Polymer Electrolyte Lithium Secondary Battery,” Electrochemistry **77** (9), 784–797 (2009).

45. J. G. Kim, B. Son, S. Mukherjee, N. Schuppert, A. Bates, O. Kwon, M. J. Choi, H. Y. Chung, and S. Park, “A review of lithium and non-lithium based solid state batteries,” Journal of Power Sources, 299–322 (2015).

46. A. Manthiram, X. Yu, and S. Wang, “Lithium battery chemistries enabled by solid-state electrolytes,” Nat. Rev. Mater. **2** (4), 16103 (2017).

47. M. Pasta, D. Armstrong, Z. L. Brown, J. Bu, M. R. Castell, P. Chen, A. Cocks, S. A. Corr, E. J. Cussen, E. Darnbrough, V. Deshpande, C. Doerrer, M. S. Dyer, H. El-Shinawi, N. Fleck, P. Grant, G. L. Gregory, C. Grovenor, L. J. Hardwick, J. T. S. Irvine, H. J. Lee, G. Li, E. Liberti, I. McClelland, C. Monroe, P. D. Nellist, P. R. Shearing, E. Shoko, W. Song, D. S. Jolly, C. I. Thomas, S. J. Turrell, M. Vestli, C. K. Williams, Y. Zhou, and P. G. Bruce, “2020 roadmap on solid-state batteries,” J. Phys. Energy **2** (3), 32008 (2020).

48. D. H. S. Tan, A. Banerjee, Z. Chen, and Y. S. Meng, “From nanoscale interface characterization to sustainable energy storage using all-solid-state batteries,” Nature nanotechnology **15** (3), 170–180 (2020).

49. G. Yang, C. Abraham, Y. Ma, M. Lee, E. Helfrick, D. Oh, and D. Lee, “Advances in Materials Design for All-Solid-state Batteries: From Bulk to Thin Films,” Applied Sciences **10** (14), 4727 (2020).

50. T. Zhang, W. He, W. Zhang, T. Wang, P. Li, Z. Sun, and X. Yu, “Designing composite solid-state electrolytes for high performance lithium ion or lithium metal batteries,” Chem. Sci. **334** (14), 928 (2020).

51. F. Zheng, M. Kotobuki, S. Song, M. O. Lai, and L. Lu, “Review on solid electrolytes for all-solid-state lithium-ion batteries,” Journal of Power Sources **389**, 198–213 (2018).

52. J. Li, C. Ma, M. Chi, C. Liang, and N. J. Dudney, “Solid electrolyte: The key for high-voltage lithium batteries,” Advanced Energy Materials **5** (4), 1401408 (2015).

53. P. Daubinger, M. Schelter, R. Petersohn, F. Nagler, S. Hartmann, M. Herrmann, and G. A. Giffin, “Impact of Bracing on Large Format Prismatic Lithium-Ion Battery Cells during Aging,” Advanced Energy Materials **12** (10), 2102448 (2022).

54. A. Bielefeld, D. A. Weber, and J. Janek, “Modeling Effective Ionic Conductivity and Binder Influence in Composite Cathodes for All-Solid-State Batteries,” ACS applied materials & interfaces **12** (11), 12821–12833 (2020).

55. Y. Zhu, X. He, and Y. Mo, “Origin of Outstanding Stability in the Lithium Solid Electrolyte Materials: Insights from Thermodynamic Analyses Based on First-Principles Calculations,” ACS Applied Materials and Interfaces **7** (42), 23685–23693 (2015).

56. A. C. Luntz, J. Voss, and K. Reuter, “Interfacial Challenges in Solid-State Li Ion Batteries,” Journal of Physical Chemistry Letters **6** (22), 4599–4604 (2015).

57. R. C. Xu, X. H. Xia, S. Z. Zhang, D. Xie, X. L. Wang, and J. P. Tu, “Interfacial challenges and progress for inorganic all-solid-state lithium batteries,” Electrochimica Acta **284**, 177–187 (2018).

58. Y. Qi, L. G. Hector, C. James, and K. J. Kim, “Lithium Concentration Dependent Elastic Properties of Battery Electrode Materials from First Principles Calculations,” J. Electrochem. Soc. **161** (11), F3010-F3018 (2014).

59. B. Wang, J. B. Bates, F. X. Hart, B. C. Sales, R. A. Zuhr, and J. D. Robertson, “Characterization of Thin-Film Rechargeable Lithium Batteries with Lithium Cobalt Oxide Cathodes,” J. Electrochem. Soc. **143** (10), 3203–3213 (1996).

60. N.J. Dudney, “Solid-state thin-film rechargeable batteries,” Materials Science and Engineering: B **116** (3), 245–249 (2005).

61. N.J. Dudney and B.J. Neudecker, “Solid state thin-film lithium battery systems,” Current Opinion in Solid State and Materials Science **4** (5), 479–482 (1999).

62. N. J. Dudney and Y.-I. Jang, “Analysis of thin-film lithium batteries with cathodes of 50 nm to 4 µm thick LiCoO2,” Journal of Power Sources, 300–304 (2003).

63. J. C. Bachman, S. Muy, A. Grimaud, H.-H. Chang, N. Pour, S. F. Lux, O. Paschos, F. Maglia, S. Lupart, P. Lamp, L. Giordano, and Y. Shao-Horn, “Inorganic Solid-State Electrolytes for Lithium Batteries: Mechanisms and Properties Governing Ion Conduction,” Chemical reviews **116** (1), 140–162 (2016).

64. Y. Ren, K. Chen, R. Chen, T. Liu, Y. Zhang, and C.-W. Nan, “Oxide Electrolytes for Lithium Batteries,” J. Am. Ceram. Soc. **98** (12), 3603–3623 (2015).

65. R. DeWees and H. Wang, “Synthesis and Properties of NaSICON-type LATP and LAGP Solid Electrolytes,” ChemSusChem **12** (16), 3713–3725 (2019).

66. V. Epp, Q. Ma, E.-M. Hammer, F. Tietz, and M. Wilkening, “Very fast bulk Li ion diffusivity in crystalline Li(1.5)Al(0.5)Ti(1.5)(PO4)3 as seen using NMR relaxometry,” Physical chemistry chemical physics : PCCP **17** (48), 32115–32121 (2015).

67. N. V. Kosova, E. T. Devyatkina, A. P. Stepanov, and A. L. Buzlukov, “Lithium conductivity and lithium diffusion in NASICON-type Li1+xTi2–xAlx(PO4)3 (x= 0; 0.3) prepared by mechanical activation,” Ionics **14** (4), 303–311 (2008).

68. J. Wolfenstine, D. Foster, J. Read, and J. L. Allen, “Rate-controlling species for the sintering of LiTi2(PO4)3,” Journal of Power Sources **182** (2), 626–629 (2008).

69. H. Aono, E. Sugimoto, Y. Sadaoka, N. Imanaka, and G.-y. Adachi, “Ionic Conductivity of LiTi 2 (PO 4) 3 Mixed with Lithium Salts,” Chem. Lett. **19** (3), 331–334 (1990).

70. H. AONO, E. SUGIMOTO, Y. SADAOKA, N. IMANAKA, and G. ADACHI, “Electrical property and sinterability of LiTi2(PO4)3 mixed with lithium salt (Li3PO4 or Li3BO3),” Solid State Ionics **47** (3-4), 257–264 (1991).
71. K. Arbi, W. Bucheli, R. Jiménez, and J. Sanz, “High lithium ion conducting solid electrolytes based on NASICON Li 1+x Al x M 2−x (PO 4) 3 materials (M = Ti, Ge and 0 ≤ x ≤ 0.5),” Journal of the European Ceramic Society **35** (5), 1477–1484 (2015).
72. K. Waetzig, A. Rost, U. Langklotz, B. Matthey, and J. Schilm, “An explanation of the microcrack formation in Li 1.3 Al 0.3 Ti 1.7 (PO 4) 3 ceramics,” Journal of the European Ceramic Society **36** (8), 1995–2001 (2016).
73. T. Hupfer, E. C. Bucharsky, K. G. Schell, A. Senyshyn, M. Monchak, M. J. Hoffmann, and H. Ehrenberg, “Evolution of microstructure and its relation to ionic conductivity in Li1+xAlxTi2−x(PO4)3,” Solid State Ionics **288**, 235–239 (2016).
74. M. M. Raju, F. Altayran, M. Johnson, D. Wang, and Q. Zhang, “Crystal Structure and Preparation of Li7La3Zr2O12 (LLZO) Solid-State Electrolyte and Doping Impacts on the Conductivity: An Overview,” Electrochem **2** (3), 390–414 (2021).
75. K. Meier, T. Laino, and A. Curioni, “Solid-State Electrolytes: Revealing the Mechanisms of Li-Ion Conduction in Tetragonal and Cubic LLZO by First-Principles Calculations,” J. Phys. Chem. C **118** (13), 6668–6679 (2014).
76. M. Matsui, K. Takahashi, K. Sakamoto, A. Hirano, Y. Takeda, O. Yamamoto, and N. Imanishi, “Phase stability of a garnet-type lithium ion conductor Li7La3Zr2O12,” Dalton transactions (Cambridge, England : 2003) **43** (3), 1019–1024 (2014).
77. C. A. Geiger, E. Alekseev, B. Lazic, M. Fisch, T. Armbruster, R. Langner, M. Fechtelkord, N. Kim, T. Pettke, and W. Weppner, “Crystal chemistry and stability of "Li7La3Zr2O12" garnet: a fast lithium-ion conductor,” Inorganic chemistry **50** (3), 1089–1097 (2011).
78. J. Sastre, A. Priebe, M. Döbeli, J. Michler, A. N. Tiwari, and Y. E. Romanyuk, “Lithium Garnet Li 7 La 3 Zr 2 O 12 Electrolyte for All-Solid-State Batteries: Closing the Gap between Bulk and Thin Film Li-Ion Conductivities,” Adv. Mater. Interfaces, 2000425 (2020).
79. J. Sastre, T.-Y. Lin, A. N. Filippin, A. Priebe, E. Avancini, J. Michler, A. N. Tiwari, Y. E. Romanyuk, and S. Buecheler, “Aluminum-Assisted Densification of Cosputtered Lithium Garnet Electrolyte Films for Solid-State Batteries,” ACS Appl. Energy Mater. **2** (12), 8511–8524 (2019).
80. C. Galven, J.-L. Fourquet, M.-P. Crosnier-Lopez, and F. Le Berre, “Instability of the Lithium Garnet Li 7 La 3 Sn 2 O 12 : Li + /H + Exchange and Structural Study,” Chem. Mater. **23** (7), 1892–1900 (2011).

81. W.-G. Wang, X.-P. Wang, Y.-X. Gao, J.-F. Yang, and Q.-F. Fang, “Investigation on the stability of Li5La3Ta2O12 lithium ionic conductors in humid environment,” Front. Mater. Sci. China **4** (2), 189–192 (2010).

82. J. D. LaCoste, A. Zakutayev, and L. Fei, “A Review on Lithium Phosphorus Oxynitride,” J. Phys. Chem. C **125** (7), 3651–3667 (2021).

83. X. Yu, J. B. Bates, G. E. Jellison, and F. X. Hart, “A Stable Thin-Film Lithium Electrolyte: Lithium Phosphorus Oxynitride,” J. Electrochem. Soc. **144** (2), 524–532 (1997).

84. V. Lacivita, N. Artrith, and G. Ceder, “Structural and Compositional Factors That Control the Li-Ion Conductivity in LiPON Electrolytes,” Chem. Mater. **30** (20), 7077–7090 (2018).

85. N. Suzuki, T. Inaba, and T. Shiga, “Electrochemical properties of LiPON films made from a mixed powder target of Li3PO4 and Li2O,” Thin Solid Films **520** (6), 1821–1825 (2012).

86. H. Salmang, H. Scholze, and R. Telle, *Keramik (German Edition)* (Springer, Dordrecht, 2007).

87. Q. Yin, B. Zhu, and H. Zeng, *Microstructure, property and processing of functional ceramics* (Metallurgical Industry Press; Springer Verlag, Berlin, 2009).

88. Z. Z. Fang, *Sintering of advanced materials. Fundamentals and processes* (Woodhead Pub, Oxford, Philadelphia, PA, 2010).

89. S.-J. L. Kang, *Sintering. Densification, grain growth, and microstructure* (Elsevier, Amsterdam, 2005).

90. C. B. Carter and M. G. Norton, *Ceramic materials. Science and engineering* (Springer, New York, 2007).

91. B. V. L'vov, *Thermal decomposition of solids and melts. New thermochemical approach to the mechanism, kinetics, and methodology* (Springer, New York, 2007).

92. Q. Jiang and Z. Wen, *Thermodynamics of materials* (Higher Education Press/ Springer-Verlag, Beijing, Heidelberg, 2011).

93. P. Stephan, K. Schaber, K. Stephan, and F. Mayinger, *Thermodynamik* (Springer Berlin Heidelberg, Berlin, Heidelberg, 2010).

94. M. Zhao, L. Song, and X. Fan, *The boundary theory of phase diagrams and its application. Rules for phase diagram construction with phase regions and their boundaries* (Springer; Science Press, Berlin, New York, Beijing, 2009).

95. W. D. Callister and D. G. Rethwisch, *Materials science and engineering. An introduction*, Ninth edition (Wiley, Hoboken, NJ, 2014).

96. S. Breuer, D. Prutsch, Q. Ma, V. Epp, F. Preishuber-Pflügl, F. Tietz, and M. Wilkening, "Separating bulk from grain boundary Li ion conductivity in the sol–gel prepared solid electrolyte Li 1.5 Al 0.5 Ti 1.5 (PO 4) 3," J. Mater. Chem. A **3** (42), 21343–21350 (2015).

97. E. Barsoukov and J. R. Macdonald, *Impedance spectroscopy. Theory, experiment, and applications*, 2nd ed. (Wiley-Interscience, Hoboken N.J., 2005).

98. C. Ma, K. Chen, C. Liang, C.-W. Nan, R. Ishikawa, K. More, and M. Chi, "Atomic-scale origin of the large grain-boundary resistance in perovskite Li-ion-conducting solid electrolytes," Energy Environ. Sci. **7** (5), 1638 (2014).

99. R. Bouchet, P. Knauth, and J.-M. Laugier, "Theoretical Analysis of IS of Polycrystalline Materials with Blocking or Conducting Grain Boundaries: From Microcrystals to Nanocrystals," Solid State Ionics **150** (7), E348 (2003).

100. R. Bouchet, P. Knauth, and J.-M. Laugier, "Theoretical analysis of the impedance spectra of electroceramics Part 2: isotropic grain boundaries," J Electroceram **16** (3), 229–238 (2006).

101. J. Fleig, "Inhomogeneous current distributions at grain boundaries and electrodes and their impact on the impedance," Solid State Ionics **113-115** (1-2), 739–747 (1998).

102. J. Fleig, "The influence of non-ideal microstructures on the analysis of grain boundary impedances," Solid State Ionics **131** (1-2), 117–127 (2000).

103. J. Fleig and J. Maier, "A Finite Element Study on the Grain Boundary Impedance of Different Microstructures," J. Electrochem. Soc. **145** (6), 2081–2089 (1998).

104. J. Fleig and J. Maier, "The impedance of ceramics with highly resistive grain boundaries: validity and limits of the brick layer model," Journal of the European Ceramic Society **19** (6-7), 693–696 (1999).

105. J. Fleig and J. Maier, "Finite-Element Calculations on the Impedance of Electroceramics with Highly Resistive Grain Boundaries: I, Laterally Inhomogeneous Grain Boundaries," J. Am. Ceram. Soc. **82** (12), 3485–3493 (1999).

106. N. J. Kidner, N. H. Perry, T. O. Mason, and E. J. Garboczi, "The Brick Layer Model Revisited: Introducing the Nano-Grain Composite Model," J American Ceramic Society **91** (6), 1733–1746 (2008).

107. P. Knauth, "Ionic and electronic conduction in nanostructured solids: Concepts and concerns, consensus and controversies," Solid State Ionics **177** (26-32), 2495–2502 (2006).

108. J. Maier, "Ionic conduction in space charge regions," Progress in Solid State Chemistry **23** (3), 171–263 (1995).

109. Indris, Heitjans, Roman, and Bunde, "Nanocrystalline versus microcrystalline Li(2)O:B(2)O3 composites: anomalous ionic conductivities and percolation theory," Physical review letters **84** (13), 2889–2892 (2000).

110. R. E. Dinnebier, ed., *Powder diffraction*. Theory and practice, Repr (Royal Society of Chemistry, Cambridge, 2009).

111. V. K. Pecharsky and P. Y. Zavalij, *Fundamentals of powder diffraction and structural characterization of materials* (Springer US, Boston, MA, 2005).

112. B. E. Warren, *X-ray diffraction*, Dover edition, unabridged and corrected republication of the work originally published in 1969 by Addison-Wesley Publishing Company (Dover Publications Inc, New York, 1990).

113. R. W. Cheary, A. A. Coelho, and J. P. Cline, "Fundamental parameters line profile fitting in laboratory diffractometers," J. Res. Natl. Inst. Stand. Technol. **109** (1), 1 (2004).

114. R. J. Hill and C. J. Howard, "Quantitative phase analysis from neutron powder diffraction data using the Rietveld method," J Appl Crystallogr **20** (6), 467–474 (1987).

115. W. A. Dollase, "Correction of intensities for preferred orientation in powder diffractometry: application of the March model," J Appl Crystallogr **19** (4), 267–272 (1986).

116. W.I.F. David, "Powder diffraction: Least-squares and beyond," J. Res. Natl. Inst. Stand. Technol. **109** (1), 107 (2004).

117. L. B. McCusker, R. B. von Dreele, D. E. Cox, D. Louer, and P. Scardi, "Rietveld refinement guidelines,".

118. B. H. Toby, "R factors in Rietveld analysis: How good is good enough?," Powder Diffr. **21** (1), 67–70 (2006).

119. R. A. Young, ed., *The Rietveld method* (Oxford Univ. Press, Oxford, 1995).

120. F. Raether, R. Hofmann, G. Müller, and H. J. Sölter, "A Novel Thermo-Optical Measuring System for the in situ Study of Sintering Processes," Journal of Thermal Analysis and Calorimetry **53** (3), 717–735 (1998).

121. J. Baber, A. Klimera, and F. Raether, "In situ measurement of dimensional changes and temperature fields during sintering with a novel thermooptical measuring device," Journal of the European Ceramic Society **27** (2-3), 701–705 (2007).

122. F. Raether and R. Springer, "In-Situ Measurement of Neck Formation During Sintering of Alumina by a Novel Thermo-Optical Measuring Device," Adv. Eng. Mater. **2** (11), 741–744 (2000).

123. L. Stanciu, D. Quach, C. Faconti, J. R. Groza, and F. Raether, "Initial Stages of Sintering of Alumina by Thermo-Optical Measurements," J American Ceramic Society **90** (9), 2716–2722 (2007).

124. L. Stanciu, D. Quach, C. Faconti, J. R. Groza, and F. Raether, “Initial Stages of Sintering of Alumina by Thermo-Optical Measurements,” J American Ceramic Society **90** (9), 2716–2722 (2007).

125. W. J. Parker, R. J. Jenkins, C. P. Butler, and G. L. Abbott, “Flash Method of Determining Thermal Diffusivity, Heat Capacity, and Thermal Conductivity,” Journal of Applied Physics **32** (9), 1679–1684 (1961).

126. A. Adriaens, L. van Vaeck, and F. Adams, “Static secondary ion mass spectrometry (S-SIMS) Part 2: material science applications,” Mass Spectrom. Rev. **18** (1), 48–81 (1999).

127. A. Benninghoven, “Chemical Analysis of Inorganic and Organic Surfaces and Thin Films by Static Time-of-Flight Secondary Ion Mass Spectrometry (TOF-SIMS),” Angew. Chem. Int. Ed. Engl. **33** (10), 1023–1043 (1994).

128. B. W. Schueler, “Microscope imaging by time-of-flight secondary ion mass spectrometry,” Microsc. Microanal. Microstruct. **3** (2-3), 119–139 (1992).

129. L. van Vaeck, A. Adriaens, and R. Gijbels, “Static secondary ion mass spectrometry (S-SIMS) Part 1: methodology and structural interpretation,” Mass Spectrom. Rev. **18** (1), 1–47 (1999).

130. M. Rumpel, F. Nagler, L. Appold, W. Stracke, A. Flegler, O. Clemens, and G. Sextl, “Thermal stabilities of Mn-based active materials in combination with the ceramic electrolyte LATP for ASSB bulk cathodes,” Mater. Adv. **3** (9), 4015–4025 (2022).

131. L. J. Miara, W. D. Richards, Y. E. Wang, and G. Ceder, “First-Principles Studies on Cation Dopants and Electrolyte|Cathode Interphases for Lithium Garnets,” Chemistry of Materials **27** (11), 4040–4047 (2015).

132. L. Miara, A. Windmüller, C.-L. Tsai, W. D. Richards, Q. Ma, S. Uhlenbruck, O. Guillon, and G. Ceder, “About the Compatibility between High Voltage Spinel Cathode Materials and Solid Oxide Electrolytes as a Function of Temperature,” ACS applied materials & interfaces **8** (40), 26842–26850 (2016).

133. M. Gellert, E. Dashjav, D. Grüner, Q. Ma, and F. Tietz, “Compatibility study of oxide and olivine cathode materials with lithium aluminum titanium phosphate,” Ionics **24** (4), 1001–1006 (2018).

134. B. Ammundsen, P. B. Aitchison, G. R. Burns, D. J. Jones, and J. Rozière, “Proton insertion and lithium-proton exchange in spinel lithium manganates,” Solid State Ionics **97** (1-4), 269–276 (1997).

135. I. A. Shkrob, J. A. Gilbert, P. J. Phillips, R. Klie, R. T. Haasch, J. Bareño, and D. P. Abraham, “Chemical Weathering of Layered Ni-Rich Oxide Electrode Materials: Evidence for Cation Exchange,” J. Electrochem. Soc. **164** (7), A1489-A1498 (2017).

136. M. E. Brown, “Handbook of Thermal Analysis and Calorimetry. Volume 1, Principles and Practice,”.

137. P. Haines, *Principles of Thermal Analysis and Calorimetry* (Royal Society of Chemistry, Cambridge, 2002).

138. O. Clemens, R. Haberkorn, and H. P. Beck, “New phases in the system LiMnVO4–Mn3(VO4)2,” Journal of Solid State Chemistry **184** (10), 2640–2647 (2011).

139. O. Clemens, R. Haberkorn, M. Springborg, and H. P. Beck, “On Aliovalent Substitution on the Li Site in LiMPO 4 : an -X-ray Diffraction Study of the Systems LiMPO 4 -M 1.5 PO 4 (= Li x M 1.5- x /2 PO 4 ; M = Ni, Co, Fe, Mn),” Z. anorg. allg. Chem. **640** (1), 173–183 (2014).

140. U. Müller, *Anorganische Strukturchemie*, 6., aktualisierte Aufl., unveränd. Nachdr (Vieweg + Teubner, Wiesbaden, 2009).

141. K. Yan, Z. Lu, H.-W. Lee, F. Xiong, P.-C. Hsu, Y. Li, J. Zhao, S. Chu, and Y. Cui, “Selective deposition and stable encapsulation of lithium through heterogeneous seeded growth,” Nat Energy **1** (3), 359 (2016).

142. Nanografi, “Ag(silver) Nanoparticles 48-78nm _ CAS.No: 7440-22-4 _ Safety Data Sheet,” (2017).

143. H. M. Schadel and C. E. Birchenall, “The vapor pressure of silver,” JOM **2** (9), 1134–1138 (1950).

144. M. Ohring, *Materials science of thin films. Deposition and structure*, 2nd ed. (Academic Press, San Diego, CA, 2002).

145. Peter M. Martin, ed., *Handbook of deposition technologies for films and coatings*. Science, applications and technology, 3rd ed. (Elsevier, Amsterdam, Boston, 2010).

146. C. H. Macgillavry, G. D. Rieck, and Lonsdale K., eds., *Physical and chemical tables*, 2. ed., repr (Reidel, Dordrecht, 1985).

147. N. A. N. Mohamad, N. A. Arham, J. Junaidah, A. Hadi, and S. A. Idris, “Green Synthesis of Ag, Cu and AgCu Nanoparticles using Palm Leaves Extract as the Reducing and Stabilizing Agents,” IOP Conf. Ser.: Mater. Sci. Eng. **358**, 12063 (2018).

148. K. Waetzig, A. Rost, C. Heubner, M. Coeler, K. Nikolowski, M. Wolter, and J. Schilm, “Synthesis and sintering of Li1.3Al0.3Ti1.7(PO4)3 (LATP) electrolyte for ceramics with improved Li+ conductivity,” Journal of Alloys and Compounds **818** (2), 153237 (2020).

149. M. Rumpel, L. Appold, J. Baber, W. Stracke, A. Flegler, and G. Sextl, “Impact of the sintering additive Li 3 PO 4 on the sintering behaviour, microstructure and electrical properties of a ceramic LATP electrolyte,” Mater. Adv. **3** (22), 8157–8167 (2022).

150. H. Aono, Y. Sadaoka, G. y. Adachi, E. Sugimoto, and N. Imanaka, “Ionic Conductivity of the Lithium Titanium Phosphate (Li<inf>1+</inf>xMxTi<inf>2</inf>-x(PO<inf>4</inf>)<inf>3</inf> M = Al, Sc, Y, and La) Systems,” Journal of the Electrochemical Society **136** (2), 590–591 (1989).

151. H. Aono, Y. Sadaoka, G. y. Adachi, E. Sugimoto, and N. Imanaka, “Ionic conductivity and sinterability of lithium titanium phosphate system,” Solid State Ionics **40-41**, 38–42 (1990).

152. H. Aono, E. Sugimoto, Y. Sadaoka, N. Imanaka, and G.-y. Adachi, “Ionic Conductivity of Solid Electrolytes Based on Lithium Titanium Phosphate,” J. Electrochem. Soc. **137** (4), 1023–1027 (1990).

153. K. G. Schell, E. C. Bucharsky, F. Lemke, and M. J. Hoffmann, “Effect of calcination conditions on lithium conductivity in Li1.3Ti1.7Al0.3(PO4)3 prepared by sol-gel route,” Ionics **23** (4), 821–827 (2017).

154. X. Liu, J. Fu, and C. Zhang, “Preparation of NASICON-Type Nanosized Solid Electrolyte Li1.4Al0.4Ti1.6(PO4)3 by Evaporation-Induced Self-Assembly for Lithium-Ion Battery,” Nanoscale research letters **11** (1), 551 (2016).

155. C. R. Mariappan, C. Yada, F. Rosciano, and B. Roling, “Correlation between microstructural properties and ionic conductivity of Li1.5Al0.5Ge1.5(PO4)3 ceramics,” Journal of Power Sources **196** (15), 6456–6464 (2011).

156. S. D. Jackman and R. A. Cutler, “Effect of microcracking on ionic conductivity in LATP,” Journal of Power Sources **218**, 65–72 (2012).

157. K. Chen, M. Huang, Y. Shen, Y. Lin, and C. W. Nan, “Enhancing ionic conductivity of Li0.35La0.55TiO3 ceramics by introducing Li7La3Zr2O12,” Electrochimica Acta **80**, 133–139 (2012).

158. K. Chen, M. Huang, Y. Shen, Y. Lin, and C. W. Nan, “Improving ionic conductivity of Li0.35La0.55TiO3 ceramics by introducing Li7La3Zr2O12 sol into the precursor powder,” Solid State Ionics **235** (71), 8–13 (2013).

159. T. Hupfer, E. C. Bucharsky, K. G. Schell, and M. J. Hoffmann, “Influence of the secondary phase LiTiOPO 4 on the properties of Li 1+x Al x Ti 2−x (PO 4) 3 (x = 0; 0.3),” Solid State Ionics **302**, 49–53 (2017).

160. Y. Kobayashi, Tabuchi, Mitsuharu, and Nakamura, Osamu, “Ionic conductivity enhancement in LiTi2(PO4)3-based composite electrolyte by the addition of lithium nitrate,” Journal of Power Sources **68** (2), 407–411 (1997).

161. A. MEI, X. WANG, Y. FENG, S. ZHAO, G. LI, H. GENG, Y. LIN, and C. NAN, “Enhanced ionic transport in lithium lanthanum titanium oxide solid state electrolyte by introducing silica,” Solid State Ionics **179** (39), 2255–2259 (2008).

162. A. Mei, X.-L. Wang, J.-L. Lan, Y.-C. Feng, H.-X. Geng, Y.-H. Lin, and C.-W. Nan, “Role of amorphous boundary layer in enhancing ionic conductivity of lithium–lanthanum–titanate electrolyte,” Electrochimica Acta **55** (8), 2958–2963 (2010).

163. K. Waetzig, C. Heubner, and M. Kusnezoff, “Reduced Sintering Temperatures of Li+ Conductive Li1.3Al0.3Ti1.7(PO4)3 Ceramics,” Crystals **10** (5), 408 (2020).

164. H. Keiser, K. D. Beccu, and M. A. Gutjahr, “Abschätzung der porenstruktur poröser elektroden aus impedanzmessungen,” Electrochimica Acta **21** (8), 539–543 (1976).

165. J. T. S. Irvine, D. C. Sinclair, and A. R. West, “Electroceramics: Characterization by Impedance Spectroscopy,” Adv. Mater. **2** (3), 132–138 (1990).

166. S. Duluard, A. Paillassa, L. Puech, P. Vinatier, V. Turq, P. Rozier, P. Lenormand, P.-L. Taberna, P. Simon, and F. Ansart, “Lithium conducting solid electrolyte Li1.3Al0.3Ti1.7(PO4)3 obtained via solution chemistry,” Journal of the European Ceramic Society **33** (6), 1145–1153 (2013).

167. M. Rawlence, A. N. Filippin, A. Wäckerlin, T.-Y. Lin, E. Cuervo-Reyes, A. Remhof, C. Battaglia, J. L. M. Rupp, and S. Buecheler, “Effect of Gallium Substitution on Lithium-Ion Conductivity and Phase Evolution in Sputtered Li7-3 xGa xLa3Zr2O12 Thin Films,” ACS applied materials & interfaces **10** (16), 13720–13728 (2018).

168. P. Hofmann, F. Walther, M. Rohnke, J. Sann, W. G. Zeier, and J. Janek, “LATP and LiCoPO4 thin film preparation – Illustrating interfacial issues on the way to all-phosphate SSBs,” Solid State Ionics **342**, 115054 (2019).

169. M. Rumpel, M. Machhaus, J. Sastre, S. Ziegler, X. Chen, A. Flegler, Y. E. Romanyuk, and G. A. Giffin, “How interdiffusion affects the electrochemical performance of LiMn 2 O 4 thin films on stainless steel,” Mater. Adv. **2** (7), 2289–2298 (2021).

170. L. Baggetto, R. R. Unocic, N. J. Dudney, and G. M. Veith, “Fabrication and characterization of Li–Mn–Ni–O sputtered thin film high voltage cathodes for Li-ion batteries,” Journal of Power Sources **211**, 108–118 (2012).

171. J. H. Kim, J. Park, J. Y. Cheong, A. Song, K.-B. Chung, Y. C. Park, I.-D. Kim, Y. J. Kim, K. Park, and H.-S. Kim, “Suppressed ionic contamination of LiNi0.5Mn1.5O4 with a Pt/ITO/stainless steel multilayer current collector,” Ceramics International **44** (16), 20093–20104 (2018).

172. M. Gellert, K. I. Gries, J. Sann, E. Pfeifer, K. Volz, and B. Roling, “Impedance spectroscopic study of the charge transfer resistance at the interface between a LiNi0.5Mn1.5O4 high-voltage cathode film and a LiNbO3 coating film,” Solid State Ionics **287**, 8–12 (2016).

173. M. Gellert, K. I. Gries, J. Zakel, A. Ott, S. Spannenberger, C. Yada, F. Rosciano, K. Volz, and B. Roling, “LiNi0.5Mn1.5O4 Thin-Film Cathodes on Gold-Coated Stainless

Steel Substrates: Formation of Interlayers and Electrochemical Properties," Electrochimica Acta **133**, 146–152 (2014).

174. S. Komaba, N. Kumagai, M. Baba, F. Miura, N. Fujita, H. Groult, D. Devilliers, and B. Kaplan, "Preparation of Li-Mn-O thin films by r.f.-sputtering method and its application to rechargeable batteries," J Appl Electrochem **30** (10), 1179–1182 (2000).

175. A. N. Filippin, T.-Y. Lin, M. Rawlence, T. Zünd, K. Kravchyk, J. Sastre-Pellicer, S. G. Haass, A. Wäckerlin, M. V. Kovalenko, and S. Buecheler, "Ni–Al–Cr superalloy as high temperature cathode current collector for advanced thin film Li batteries," RSC Adv. **8** (36), 20304–20313 (2018).

176. M. Roeder, A. B. Beleke, U. Guntow, J. Buensow, A. Guerfi, U. Posset, H. Lorrmann, K. Zaghib, and G. Sextl, "Li4Ti5O12 and LiMn2O4 thin-film electrodes on transparent conducting oxides for all-solid-state and electrochromic applications," Journal of Power Sources **301**, 35–40 (2016).

177. K. E. Sickafus, J. M. Wills, and N. W. Grimes, "Structure of spinel," Journal of the American Ceramic Society **82** (12), 3279–3292 (1999).

178. E. Barsoukov, *Impedance Spectroscopy. Theory, Experiment, and Applications*, 2nd ed. (John Wiley & Sons Incorporated, Hoboken, 2005).

179. M.-L.-P. Le, P. Strobel, C. V. Colin, T. Pagnier, and F. Alloin, "Spinel-type solid solutions involving Mn4+ and Ti4+:Crystal chemistry, magnetic and electrochemical properties," Journal of Physics and Chemistry of Solids **72** (2), 124–135 (2011).

180. T.-F. Yi, T.-T. Wei, Y. Li, Y.-B. He, and Z.-B. Wang, "Efforts on enhancing the Li-ion diffusion coefficient and electronic conductivity of titanate-based anode materials for advanced Li-ion batteries," Energy Storage Materials **26**, 165–197 (2020).

181. N. Takami, K. Hoshina, and H. Inagaki, "Lithium Diffusion in Li 4/3 Ti 5/3 O 4 Particles during Insertion and Extraction," J. Electrochem. Soc. **158** (6), A725-A730 (2011).

182. L. Kavan, J. Procházka, T. M. Spitler, M. Kalbáč, M. Zukalová, T. Drezen, and M. Grätzel, "Li Insertion into Li[sub 4]Ti[sub 5]O[sub 12] (Spinel)," J. Electrochem. Soc. **150** (7), A1000 (2003).

183. F. Wunde, F. Berkemeier, and G. Schmitz, "Lithium diffusion in sputter-deposited Li4Ti5O12 thin films," Journal of Power Sources **215**, 109–115 (2012).

184. H. Lindström, S. Södergren, A. Solbrand, H. Rensmo, J. Hjelm, A. Hagfeldt, and S.-E. Lindquist, "Li + Ion Insertion in TiO 2 (Anatase). 1. Chronoamperometry on CVD Films and Nanoporous Films," J. Phys. Chem. B **101** (39), 7710–7716 (1997).

185. H. Lindström, S. Södergren, A. Solbrand, H. Rensmo, J. Hjelm, A. Hagfeldt, and S.-E. Lindquist, "Li + Ion Insertion in TiO 2 (Anatase). 2. Voltammetry on Nanoporous Films," J. Phys. Chem. B **101** (39), 7717–7722 (1997).

186. J. Sastre, X. Chen, A. Aribia, A. N. Tiwari, and Y. E. Romanyuk, “Fast charge transfer across the Li7La3Zr2O12 solid electrolyte / LiCoO2 cathode interface enabled by an interphase-engineered all-thin-film architecture,” ACS applied materials & interfaces, 36196–36207 (2020).

187. C. M. Julien, A. Mauger, H. Groult, and K. Zaghib, “Surface modification of positive electrode materials for lithium-ion batteries,” Thin Solid Films **572**, 200–207 (2014).

188. F. Mao, W. Guo, and J. Ma, “Research progress on design strategies, synthesis and performance of LiMn 2 O 4 -based cathodes,” RSC Adv. **5** (127), 105248–105258 (2015).

189. T. R. Somo, T. E. Mabokela, D. M. Teffu, T. K. Sekgobela, B. Ramogayana, M. J. Hato, and K. D. Modibane, “A Comparative Review of Metal Oxide Surface Coatings on Three Families of Cathode Materials for Lithium Ion Batteries,” Coatings **11** (7), 744 (2021).

190. G. Xu, Z. Liu, C. Zhang, G. Cui, and L. Chen, “Strategies for improving the cyclability and thermo-stability of LiMn 2 O 4 -based batteries at elevated temperatures,” J. Mater. Chem. A **3** (8), 4092–4123 (2015).

191. D. H. Jang and S. M. Oh, “Electrolyte Effects on Spinel Dissolution and Cathodic Capacity Losses in 4 V Li / Li x Mn2 O 4 Rechargeable Cells,” J. Electrochem. Soc. **144** (10), 3342–3348 (1997).

192. M. Metzger, B. Strehle, S. Solchenbach, and H. A. Gasteiger, “Hydrolysis of Ethylene Carbonate with Water and Hydroxide under Battery Operating Conditions,” J. Electrochem. Soc. **163** (7), A1219-A1225 (2016).

193. Y. Kim, “Mechanism of gas evolution from the cathode of lithium-ion batteries at the initial stage of high-temperature storage,” J Mater Sci **48** (24), 8547–8551 (2013).

194. S. E. Renfrew and B. D. McCloskey, “Residual Lithium Carbonate Predominantly Accounts for First Cycle CO2 and CO Outgassing of Li-Stoichiometric and Li-Rich Layered Transition-Metal Oxides,” Journal of the American Chemical Society **139** (49), 17853–17860 (2017).

195. S. E. Sloop, J. B. Kerr, and K. Kinoshita, “The role of Li-ion battery electrolyte reactivity in performance decline and self-discharge,” Journal of Power Sources **119-121** (8), 330–337 (2003).

196. L. Yang, B. Ravdel, and B. L. Lucht, “Electrolyte Reactions with the Surface of High Voltage LiNi[sub 0.5]Mn[sub 1.5]O[sub 4] Cathodes for Lithium-Ion Batteries,” Electrochem. Solid-State Lett. **13** (8), A95 (2010).

197. J. Sicklinger, M. Metzger, H. Beyer, D. Pritzl, and H. A. Gasteiger, “Ambient Storage Derived Surface Contamination of NCM811 and NCM111: Performance Implications and Mitigation Strategies,” J. Electrochem. Soc. **166** (12), A2322-A2335 (2019).

198. D.-H. Cho, C.-H. Jo, W. Cho, Y.-J. Kim, H. Yashiro, Y.-K. Sun, and S.-T. Myung, “Effect of Residual Lithium Compounds on Layer Ni-Rich Li[Ni 0.7 Mn 0.3]O 2,” J. Electrochem. Soc. **161** (6), A920-A926 (2014).

199. J. Kim, H. Lee, H. Cha, M. Yoon, M. Park, and J. Cho, “Prospect and Reality of Ni-Rich Cathode for Commercialization,” Adv. Energy Mater. **8** (6), 1702028 (2018).

200. G. V. Zhuang, G. Chen, J. Shim, X. Song, P. N. Ross, and T. J. Richardson, “Li2CO3 in LiNi0.8Co0.15Al0.05O2 cathodes and its effects on capacity and power,” Journal of Power Sources **134** (2), 293–297 (2004).

201. C. Lai, W. Ye, H. Liu, and W. Wang, “Preparation of TiO2-coated LiMn2O4 by carrier transfer method,” Ionics **15** (3), 389–392 (2009).

202. F. Mattelaer, P. M. Vereecken, J. Dendooven, and C. Detavernier, “The Influence of Ultrathin Amorphous ALD Alumina and Titania on the Rate Capability of Anatase TiO 2 and LiMn 2 O 4 Lithium Ion Battery Electrodes,” Adv. Mater. Interfaces **4** (13), 1601237 (2017).

203. K. A. Walz, C. S. Johnson, J. Genthe, L. C. Stoiber, W. A. Zeltner, M. A. Anderson, and M. M. Thackeray, “Elevated temperature cycling stability and electrochemical impedance of LiMn2O4 cathodes with nanoporous ZrO2 and TiO2 coatings,” Journal of Power Sources **195** (15), 4943–4951 (2010).

204. C. Zhang, X. Liu, Q. Su, J. Wu, T. Huang, and A. Yu, “Enhancing Electrochemical Performance of LiMn 2 O 4 Cathode Material at Elevated Temperature by Uniform Nanosized TiO 2 Coating,” ACS Sustainable Chem. Eng. **5** (1), 640–647 (2017).

205. J. Li, Y. Zhu, L. Wang, and C. Cao, “Lithium titanate epitaxial coating on spinel lithium manganese oxide surface for improving the performance of lithium storage capability,” ACS applied materials & interfaces **6** (21), 18742–18750 (2014).

206. D.-Q. Liu, X.-Q. Liu, and Z.-Z. He, “The elevated temperature performance of LiMn2O4 coated with Li4Ti5O12 for lithium ion battery,” Materials Chemistry and Physics **105** (2-3), 362–366 (2007).

207. M. Sachs, M. Gellert, M. Chen, H. J. Drescher, S. R. Kachel, H. Zhou, M. Zugermeier, M. Gorgoi, B. Roling, and J. M. Gottfried, “LiNi<inf>0.5</inf>Mn<inf>1.5</inf>O<inf>4</inf>high-voltage cathode coated with Li<inf>4</inf>Ti<inf>5</inf>O<inf>12</inf>: A hard X-ray photoelectron spectroscopy (HAXPES) study,” Physical Chemistry Chemical Physics **17** (47), 31790–31800 (2015).

208. J. Yao, C. Shen, P. Zhang, C. A. Ma, D. H. Gregory, and L. Wang, “Spinel-Li3.5+xTi5O12 coated LiMn2O4 with high surface Mn valence for an enhanced cycling performance at high temperature,” Electrochemistry Communications **31**, 92–95 (2013).

209. T.-F. Yi, J. Shu, Y.-R. Zhu, A.-N. Zhou, and R.-S. Zhu, “Structure and electrochemical performance of Li4Ti5O12-coated LiMn1.4Ni0.4Cr0.2O4 spinel as 5V materials,” Electrochemistry Communications **11** (1), 91–94 (2009).

210. D. Guan, J. A. Jeevarajan, and Y. Wang, “Enhanced cycleability of LiMn2O4 cathodes by atomic layer deposition of nanosized-thin Al2O3 coatings,” Nanoscale **3** (4), 1465–1469 (2011).

211. D. Guan and Y. Wang, “Ultrathin surface coatings to enhance cycling stability of LiMn2O4 cathode in lithium-ion batteries,” Ionics **19** (1), 1–8 (2013).

212. W.-K. Kim, D.-W. Han, W.-H. Ryu, S.-J. Lim, and H.-S. Kwon, “Al2O3 coating on LiMn2O4 by electrostatic attraction forces and its effects on the high temperature cyclic performance,” Electrochimica Acta **71**, 17–21 (2012).

213. M. Gellert, K. I. Gries, J. Sann, E. Pfeifer, K. Volz, and B. Roling, “Impedance spectroscopic study of the charge transfer resistance at the interface between a LiNi<inf>0.5</inf>Mn<inf>1.5</inf>O<inf>4</inf> high-voltage cathode film and a LiNbO<inf>3</inf> coating film,” Solid State Ionics **287**, 8–12 (2016).

214. F. Han, J. Yue, C. Chen, N. Zhao, X. Fan, Z. Ma, T. Gao, F. Wang, X. Guo, and C. Wang, “Interphase Engineering Enabled All-Ceramic Lithium Battery,” Joule **2** (3), 497–508 (2018).

215. T. Kato, T. Hamanaka, K. Yamamoto, T. Hirayama, F. Sagane, M. Motoyama, and Y. Iriyama, “In-situ Li7La3Zr2O12/LiCoO2 interface modification for advanced all-solid-state battery,” Journal of Power Sources **260**, 292–298 (2014).

216. T. Liu, Y. Ren, Y. Shen, S.-X. Zhao, Y. Lin, and C.-W. Nan, “Achieving high capacity in bulk-type solid-state lithium ion battery based on Li 6.75 La 3 Zr 1.75 Ta 0.25 O 12 electrolyte: Interfacial resistance,” Journal of Power Sources **324**, 349–357 (2016).

217. S. Ohta, S. Komagata, J. Seki, T. Saeki, S. Morishita, and T. Asaoka, “All-solid-state lithium ion battery using garnet-type oxide and Li3BO3 solid electrolytes fabricated by screen-printing,” Journal of Power Sources **238**, 53–56 (2013).

218. K. Park, B.-C. Yu, J.-W. Jung, Y. Li, W. Zhou, H. Gao, S. Son, and J. B. Goodenough, “Electrochemical Nature of the Cathode Interface for a Solid-State Lithium-Ion Battery: Interface between LiCoO 2 and Garnet-Li 7 La 3 Zr 2 O 12,” Chem. Mater. **28** (21), 8051–8059 (2016).

219. D. Wang, Q. Sun, J. Luo, J. Liang, Y. Sun, R. Li, K. Adair, L. Zhang, R. Yang, S. Lu, H. Huang, and X. Sun, “Mitigating the Interfacial Degradation in Cathodes for High-Performance Oxide-Based Solid-State Lithium Batteries,” ACS applied materials & interfaces **11** (5), 4954–4961 (2019).

220. A. A. Delluva, J. Dudoff, G. Teeter, and A. Holewinski, “Cathode Interface Compatibility of Amorphous LiMn2O4 (LMO) and Li7La3Zr2O12 (LLZO) Characterized with

Thin-Film Solid-State Electrochemical Cells," ACS applied materials & interfaces **12** (22), 24992–24999 (2020).

221. T. Thompson, S. Yu, L. Williams, R. D. Schmidt, R. Garcia-Mendez, J. Wolfenstine, J. L. Allen, E. Kioupakis, D. J. Siegel, and J. Sakamoto, "Electrochemical Window of the Li-Ion Solid Electrolyte Li 7 La 3 Zr 2 O 12," ACS Energy Lett. **2** (2), 462–468 (2017).

222. S. Ohta, T. Kobayashi, and T. Asaoka, "High lithium ionic conductivity in the garnet-type oxide Li7−X La3(Zr2−X, NbX)O12 (X=0–2)," Journal of Power Sources **196** (6), 3342–3345 (2011).

223. F. Han, Y. Zhu, X. He, Y. Mo, and C. Wang, "Electrochemical Stability of Li 10 GeP 2 S 12 and Li 7 La 3 Zr 2 O 12 Solid Electrolytes," Adv. Energy Mater. **6** (8), 1501590 (2016).

224. Y. Zhu, X. He, and Y. Mo, "First principles study on electrochemical and chemical stability of solid electrolyte–electrode interfaces in all-solid-state Li-ion batteries," J. Mater. Chem. A **4** (9), 3253–3266 (2016).

225. A. J. Samson, K. Hofstetter, S. Bag, and V. Thangadurai, "A bird's-eye view of Li-stuffed garnet-type Li 7 La 3 Zr 2 O 12 ceramic electrolytes for advanced all-solid-state Li batteries," Energy Environ. Sci. **12** (10), 2957–2975 (2019).

226. C. Wang, K. Fu, S. P. Kammampata, D. W. McOwen, A. J. Samson, L. Zhang, G. T. Hitz, A. M. Nolan, E. D. Wachsman, Y. Mo, V. Thangadurai, and L. Hu, "Garnet-Type Solid-State Electrolytes: Materials, Interfaces, and Batteries," Chemical reviews **120** (10), 4257–4300 (2020).

227. M. M. Thackeray, W.I.F. David, P. G. Bruce, and J. B. Goodenough, "Lithium insertion into manganese spinels," Materials Research Bulletin **18** (4), 461–472 (1983).

228. A. Paolella, W. Zhu, G. Bertoni, A. Perea, H. Demers, S. Savoie, G. Girard, N. Delaporte, A. Guerfi, M. Rumpel, H. Lorrmann, G. P. Demopoulos, and K. Zaghib, "Toward an All-Ceramic Cathode–Electrolyte Interface with Low-Temperature Pressed NASICON Li 1.5 Al 0.5 Ge 1.5 (PO 4) 3 Electrolyte," Adv. Mater. Interfaces **7** (12), 2000164 (2020).

229. A. Aribia, J. Sastre, X. Chen, M. H. Futscher, M. Rumpel, A. Priebe, M. Döbeli, N. Osenciat, A. N. Tiwari, and Y. E. Romanyuk, "Unlocking Stable Multi-Electron Cycling in NMC811 Thin-Films between 1.5 – 4.7 V," Advanced Energy Materials **4**, 2201750 (2022).

12 Acknowledgments

First, I would like to thank all students, technicians, engineers and scientists, who have supported me in finalizing this thesis and further projects besides the Ph.D. thesis.

Jonathan Henzel, Wladislav Maier, Katharina Nuss, Nathan Krug, Michael Machhaus, Felix Nagler, Lavinia Appold, Simon Ziegler and Johannes Nowarra had done extraordinary work during their master theses and bachelor theses or as assistant researchers and interns. I deeply appreciate their assistance in building up the research field, implementing measurement routines and carrying out proper and detailed lab work. Good luck and great success in your next stations in industry or academia and life in general.

Further, I like to thank Vilija Anfimovaite, Werner Stracke, Oliver Schüßler, Andreas Gronbach, Martina Kapuschinski, Ajana Gebel, Detlev Uhl, Richard Olsowski and Angelika Schmitt, who supported partly the Ph.D. work but in particular the practical work in industry and research projects besides the Ph.D. thesis, I had to manage. Thank you very much for your reliable and dependable work, which allowed me to gain more space for the Ph.D. topics.

I also thank all Ph.D. students at the FZEB for fruitful and deep discussions: Paul Wulfert-Holzmann, Lukas Gold, Begüm Bozkaya, Philip Daubinger, Mario Weller, Michael Hofmann, Mara Göttlinger, Sven Macher and Lukas Niklaus. I truly appreciate the enthusiasm and support in creating the group „Anonyme Elektrochemiker“ as a platform for electrochemical discussions and knowledge transfer. I think we can be pretty proud of our political involvement and the creation of the basis for the code of conduct for doctoral supervision at Fraunhofer ISC.

In particular, I like to thank Prof. Gerhard Sextl for his supervision, discussions and assistance, especially, during the implementation of the code of conduct and at the end of the Ph.D. thesis. Without his support, the finalization of three publications and the Ph.D. thesis in parallel would not have been possible.

In addition to all colleagues at the Fraunhofer ISC, I like to thank the external partners, who enabled the possibility to expand the set of measurement techniques and contributed their knowledge and experience in their specific fields to interpretations and discussions.

I thank Prof. Oliver Clemens formerly from TU Darmstadt for the possibility of measuring the material combinations via HT-XRD.

I thank Jens Barber and Dr. Andreas Nöth from Fraunhofer HTL for the possibility of measuring the sintering behavior of the LATP material via the thermal-optical measurement device. I am also thankful for the discussions and input regarding handling and analyzing ceramic materials.

I thank Dr. Yaroslav Romanyuk, Jordi Sastre and Abdessalem Aribia from EMPA for the constructive collaboration, discussions and scientific exchange as well as the support with materials and measurement techniques in the field of thin-film solid-state batteries. Without this collaboration, the successful completion of this topic would not have been possible.

Finally, I thank my family and all my friends for all the emotional support during the Ph.D. thesis. I will not list your names here, you know that you are meant when you read this. Thank you all. However, I like to thank, particularly, Daniela Quattländer, Lea Goldan and Paul Wulfert-Holzmann as well as two old friends Fabian Grunert and Paul Stapor, who have stood closely by my side not only emotionally but also with scientific advice, and I am deeply thankful for this. Thank you, for listening, supporting and everything.